Montanuniversitaet Leoben
Chair of Thermal Processing Technology

PhD Thesis

with title

Experimental Investigations and CFD Simulations on Particle Depositions in Gas Cyclone Separators

Author:
ir. J.J.H. Houben

October 2011

Promotion committee:
Univ.-Prof. Dipl.-Ing. Dr.techn. H. Raupenstrauch
Chair of Thermal Processing Technology
Montanuniversitaet Leoben

Ao.Univ.-Prof. Dipl.-Ing. Dr.techn. Ch. Weiß
Institute of Process Technology and Industrial Environmental Protection
Montanuniversitaet Leoben

Sinds de universiteiten waren gedemocratiseerd, wat inhield dat hij bijna elke week vele uren moest vergaderen om mensen die niets afwisten van de zaken waar ze over praatten, de gelegenheid te geven van hun democratische recht gebruik te maken er toch het hoogste woord over te voeren, ergerde hij zich. (W.F. Hermans 1975 [59])

Eidesstattliche Erklärung

Ich erkläre an Eides statt, dass ich die vorliegende Doktorarbeit selbstständig und ohne fremde Hilfe verfasst, andere als die angegebenen Quellen und Hilfsmittel nicht benutzt und die benutzten Quellen wörtlich und inhaltlich entnommenen Stellen als solche erkenntlich gemacht habe.

I declare in lieu of oath that I wrote this thesis and performed the associated research myself, using only literature cited in this volume.

ir. Joseph, Johannes Hubertus Houben
October 2011

Abstract

Wall depositions form a problem in the practical use of cyclone separators because they influence the separation efficiency, product quality and pressure drop. Furthermore, cleaning efforts are needed more often with decreasing efficiencies in time and financial effort as a consequence.

From the literature, it is examined which forces and energies have a significant contribution to the phenomenon of particle-wall adhesion, that is described by one of the two distinguished deposition models, based on conservation of energy and on the equilibrium of forces and moments, respectively. These models are implemented into computation fluid dynamics (CFD) simulations, using the commercial software package ANSYS Fluent 13.0. In the simulations, the flow field of the continuous phase is described with the Reynolds Stress Turbulence Model. Particle trajectories of the dispersed phase are calculated within a Lagrangian reference frame, for which the Discrete Phase Model with the one-way coupling and the discrete random walk model with random eddy lifetime are used. The deposition criteria are described in user defined boundary conditions.

The results of the depositions found in these simulations are compared to experiments performed with a test cyclone in respect, of the relative deposited mass, positions and particle size distributions.

A new model is introduced, since with the original deposition models large differences between the simulations and experiments are found. This model adapts the particle-wall impact velocity and probability in such a way that it is able to predict these quantities better, resulting in more realistic depositions during the simulations.

Kurzfassung

Wandablagerungen in Zyklonabscheidern sind in der Praxis problematisch, da sie den Abscheidegrad, die Produktqualität und den Druckverlust beeinflussen. Eine regelmäßige Reinigung des Zyklons wird notwendig, mit abnehmender Zeiteffizienz und höheren Kosten als Folge.

Es wird mit Modellen aus der Literatur eruiert, welche Kräfte und Energien einen signifikanten Anteil an der Partikel-Wand-Haftung in Zyklonen haben. Diese Haftung kann mit zwei unterschiedlichen Modellen, die auf Energieerhaltung bzw. dem Gleichgewicht aus Kräften und Momenten beruhen, beschrieben werden. Die Modelle wurden in "Computational Fluid Dynamics" (CFD) Simulationen im kommerziellen Software Packet ANSYS Fluent 13.0 implementiert. In diesen Simulationen wird das Geschwindigkeitsfeld der kontinuierlichen Phase mit dem "Reynolds Stress Turbulence Model" dargestellt. Die Berechnung der Partikelbahnen beruht auf der Langrange-Betrachtung. Als Phasenkupplung wird die Einwegkupplung verwendet und turbulente Partikelbewegungen werden mit dem "Discrete Random Walk" Modell, mit einer willkürlichen Wirbelexistenzzeit, erläutert. Die Ablagerungskriterien werden in vom Benutzer definierten Randbedingungen festgelegt.

Die Ergebnisse von den in den Simulationen gefundenen Ablagerungen werden mit den Ablagerungen aus Versuchen verglichen. Die relative abgelagerte Masse, sowie die Positionen und Korngrößeverteilungen der Ablagerungen, dienen hierbei als Vergleichskriterien.

Da bei Simulationen mit den originalen Ablagerungsmodellen große Unterschiede zwischen Versuchs- und Simulationsergebnissen festgestellt wurden, wurde ein neues Modell entwickelt. Dieses Modell adaptiert die Aufprallgeschwindigkeit von Partikeln an der Wand und die Wahrscheinlichkeit, mit der es zu einem Aufprall kommt. Mit dem neuen Modell werden Wandablagerungen im Zyklon physikalisch korrekter vorhergesagt.

Contents

1 Introduction and Overview

The first patent of a gas cyclone separator dates from the year 1886. It was granted to the American citizen O. M. Morse from the Knickerbocker Company [11, 66]. Advantages of the use of a cyclone for gas cleaning are the low investment costs, high reliability (since there are no moving parts in its basic design) and its resistance against high temperatures and pressure fluctuations [8].

Since the middle of the last century people tried to predict the cyclone's separation efficiency and pressure drop. In the beginning, this was done by the use of experimental data and dimensionless scaling parameters [7, 104, 106, 131, 141]. Some of the models developed include the influence of the solid loading on the cyclone performance.

In the 1980s, the first computational fluid dynamics (CFD) simulations on cyclone separators were performed using the finite element method [28]. It turned out that, due to the high rotation of the flow field, the Reynold stress model (RSM) was the simplest turbulence model able to predict the flow field of the continuous phase in an accurate way. CFD proofed to be a strong tool for cyclone design optimisation as a compensation for expensive and time intensiv experiments.

Although cyclone separators are not new and have successfully been used in industrial applications for many years, some basics on the working principle are still not understood.

One of the problems in practice is the formation and growth of wall depositions. Wall depositions have a similar effect as wall roughness and reduce the separation efficiency as well as the pressure drop of a cyclone separator [78]. Since high collection efficiencies are desired, extra cleaning efforts are needed. During this cleaning, whole processes cannot be operated, which results in decreasing efficiencies of time, energy and financial effort. The cleaning is necessary because some products tend to deteriorate and other to congest [6]. Also the depositions may flake off again in irregular times intervals, which causes different product qualities and quantities in case of batch conveying [94]. In food industries, it is important to avoid food decomposition.

Until now, research and development were more focussed on simplifying the cleaning procedure than on prevention. Methods for prevention are coating the cyclone wall with polymers [80], using a cylindrical design with a polished wall [11, 105] or to change the geometry for example by using a baffle [26]. Removing of depositions can be achieved by installing extra stirrers, which can scrap the deposition from the wall [11], cyclone cleaning by water sprays [38], to implement a double cyclone wall, of which the inner one is flexible and vibrates by varying the pressure between the walls [80], for example.

Other authors discovered that the cyclone geometry influences the depositions: the depositions in the upper part appeared to be independent on the outlet geometry although the use of a vortex stabiliser, in the form of a Chinese hat, could lower the place of the depositions [112, 114, 115].

This PhD-thesis compares experimental investigations on limestone depositions in gas cyclones with CFD simulations, in which several physical particle sticking criteria are implemented.

Therefore, it combines each of the three aspects, *theoretical modelling*, *experimental investigations* and *numerical simulations*.

The "experiment" is the aspect that needs to be explained. The question is, why and under which conditions depositions are formed?

Theoretical models are made to describe physical processes with mathematical equations. However, it is not always possible to test these models directly in an experiment. For example, it may be almost impossible to test a sticking criterion by letting a particle with a certain diameter collide with a wall under a defined angle and with a prescribed velocity in complex geometry such as a cyclone. Therefore, the link between *theory* and *experiment* is relatively weak and sometimes hard to prove.

Simulations give an indirect method to couple experiments with theoretical models. CFD gives the possibility to calculate the flow field of the continuous phase and particle trajectories of the dispersed phase in a cyclone numerically. The validity of the models can be proofed for simple cases for which experimental data are available. If the models turn out to predict the physics in a more or less correct way, they may also be implemented for more sophisticated applications and geometries.

In this thesis, the experiments are explained by the implementation of the physical models in the commercial CFD package ANSYS Fluent 13.0 by means of user defined functions (UDFs).

The chapters in thesis can be gathered into three segments:

Ch. 2-8: A short introduction explaining the working principle of cyclone separators is given. Also an overview of depositions in cyclone separators mentioned in the literature is discussed, as well as depositions in other industrial applications. Forces and energies are compared in respect of their relevance for particle sticking of limestone at steel or at other limestone particles. Also fluid-dynamical forces are discussed. With an adhesion map, it is shown what kind of contact may be expected for the limestone particles. From the forces, energies and the adhesion map, criterions for particles sticking are derived. Finally, an introduction into computational fluid dynamics with a view to cyclone separators is presented.

Ch. 9: Depositions in a test cyclone are systematically investigated, with the solid loading and the volume flow rate as variable quantities. Relative deposited masses and particle size distributions are distinguished and statistically evaluated for several parts of the cyclone.

Ch. 10-12: The flow field in the cyclone separator is calculated with the commercial software ANSYS Fluent 13.0 and discussed in regard with the critical areas for depositions. The deposition models, introduced in Ch. 7, are implemented with user defined functions (UDFs). Also a model for a physically correcter prediction of the particle-wall impact velocities and probabilities is introduced and implemented into the deposition models.

2 Cyclone Separator Design and Working Principle

Cyclones are used to separate a dispersed phase (liquid or solid) from a continuous phase (gas or liquid). This is achieved by the centrifugal force due to the difference in density between the phases. The geometry of the used cyclone and the denomination of its parts are presented in Fig. A.1 in App. A.

The two phase flow enters the cyclone through the inlet. Due to the cyclone's geometry, the mixture is brought into rotation and the denser phase is forced into the direction of the wall. In the cyclone body the flow in the boundary layer points downwards and the particles move to the dust outlet. Gravity is known to play only a minor role for the particle trajectories and thus for the separation efficiency as well [8]. As a consequence, the orientation of the cyclone separator does not influence its performance. The dispersed phase can whether be collected in a dustbin or carried away using one of the several known underflow configurations, such as a rotary lock, a screw extruder discharge, a flapper valve, a counter weighted valve, a submerged dipleg or a submerged 'J-bend' [66].

It is also possible to equip a cyclone with a vertical tube section (also called "downcomer tube"), in which particle agglomeration is improved. This leads to a better total separation efficiency, which is mainly caused by a higher grade efficiency of small particles [113]. The geometry C, used in this study and described by Obermair and Staudinger [113], is equipped with such a downcomer tube.

The continuous phase builds an outer vortex, which ends somewhere at the cyclone wall, usually in the conical part but sometimes in the cylindrical body or at the bottom of the dustbin. The distance from the cyclone's roof to this position is known as the natural vortex length [64]. The continuous phase forms a second smaller vortex of opposite direction in the cyclone's centre and leaves it through the vortex finder. This stream is called the overflow and contains some small, not separated particles. About 10% of the overflow comes from the continuous phases volume flow rate that immediately leaks through the vortex finder [107]. This phenomenon is known as lip-leakage [66]. Because of the high swirling flow in the inner vortex, the dynamic pressure of the continuous phase is much larger over the outlet than over the inlet cross section. This results in a pressure drop over the cyclone. A part of this pressure drop can be regained by the the use of a scroll outlet, which lowers the rotational velocity of the overflow.

The last part, which is distinguished, is the cyclone's roof, which is a simple flat round plate, covering the cyclone's body.

2.1 Inlet Geometries

Cyclone separators can be equipped with various inlet geometries which are different in performance, and production- and operation costs [66], although the latter quantity is proportional

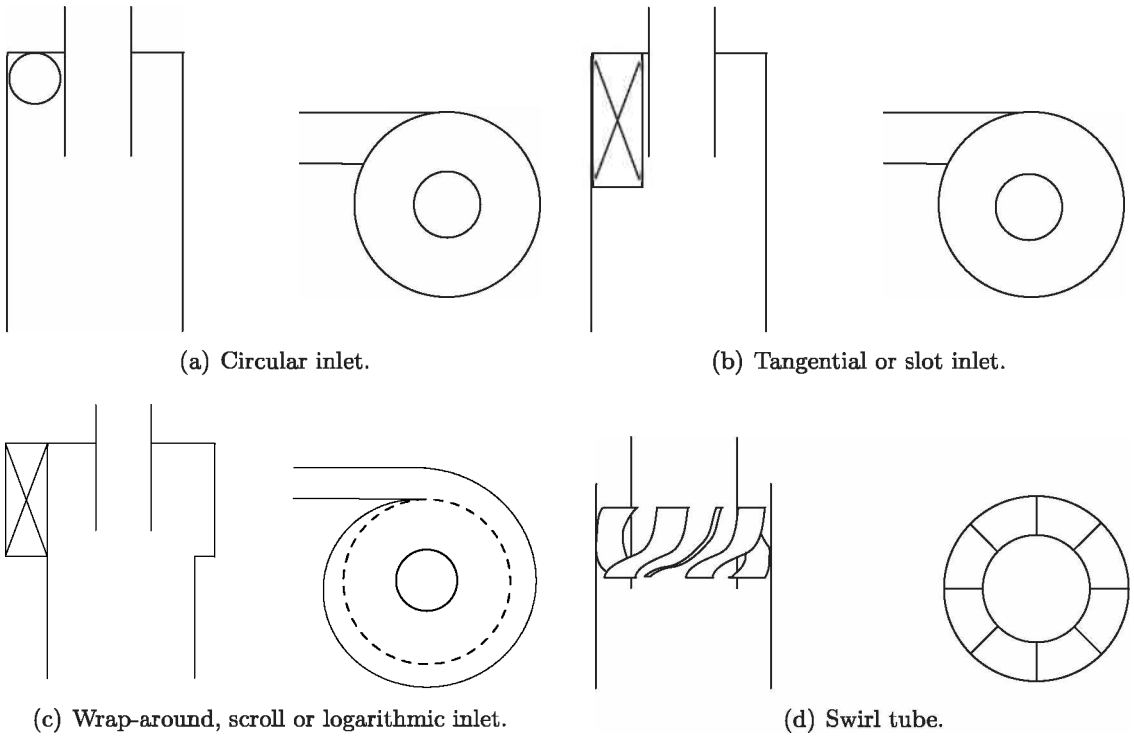

(a) Circular inlet.

(b) Tangential or slot inlet.

(c) Wrap-around, scroll or logarithmic inlet.

(d) Swirl tube.

Figure 2.1: *Inlet configurations (redrawn from [66]).*

to the total pressure drop in the cyclone. This total pressure drop is the sum of the pressure drops caused by the friction at the wall and that in the the vortex finder [109]. The latter one is in general five to 10 times larger [109]. The simplest one is the circular pipe inlet as shown in Fig. 2.1(a). The major disadvantage of this type is the existence of dead zones near the cyclone's roof. However, they are cheap to produce and no round to rectangular transition part is needed.

More complicate to construct is the tangential inlet configuration, shown in Fig. 2.1(b), which gives a better separation efficiency. For this type, a transition part is needed if the feed comes from a circular duct. A tangential inlet is used for the experiments and simulations in this work.

In the scroll inlet (Fig. 2.1(c)), the radius of the outer wall decreases with increasing angle. Therefore, it combines the high angular momentum of a cyclone of another type, with a body larger in diameter, with a smaller geometry. For so called wrap-around cyclones, the spiral inlet is over the full angle of 360°. Other scrolls with angles of 270° or 180° are also used in practice and are more compact and cheaper. Scroll inlets are more sensitive for depositions at the horizontal surfaces [89].

The last type is a cyclone with an axial inlet with swirl vanes in Fig. 2.1(d). They are very compact. If this type of cyclone does not have a conical but only a cylindrical part, it is called a swirl tube.

2.2 Separation Characteristics

In Fig. 2.2, a schematic view of any separation equipment is shown to demonstrate the mass and volume flow rates in the cyclone separator. The used symbols are [136]:

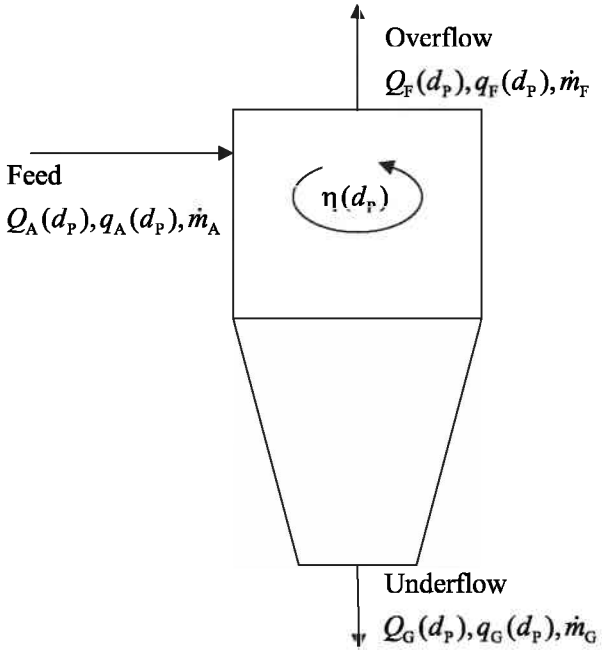

- Indices A, F, G	feed, overflow, underflow; (from German "**A**ufgabegut", "**F**eingut" and "**G**robgut");
- $Q_A(d_P)$, $Q_F(d_P)$, $Q_G(d_P)$	mass distribution functions $Q_3(d_P)$ of these flows;
- $\dot{V}_A$, $\dot{V}_F$, $\dot{V}_G$	volume flow rates of the mixtures ($m^3\,s^{-1}$);
- $\dot{m}_A$, $\dot{m}_F$, $\dot{m}_G$	total mass flow rates ($kg\,s^{-1}$);
- $\dot{m}_A(d_P)$, $\dot{m}_F(d_P)$, $\dot{m}_G(d_P)$	mass flow rates as function of the particle diameter.

Figure 2.2: *Mass balances in a separator [136].*

The mass flow rates of the feed, underflow and overflow for a specific particle diameter, d_P, are calculated from the total mass flow rates and their probability density functions

$$\dot{m}_A(d_P) = \dot{m}_A q_A(d_P) = \dot{m}_A \frac{dQ_A(d_P)}{dd_P}, \tag{2.1a}$$

$$\dot{m}_G(d_P) = \dot{m}_G q_G(d_P) = \dot{m}_G \frac{dQ_G(d_P)}{dd_P}, \tag{2.1b}$$

$$\dot{m}_F(d_P) = \dot{m}_F q_F(d_P) = \dot{m}_F \frac{dQ_F(d_P)}{dd_P}. \tag{2.1c}$$

Furthermore, conservation of mass and volume for an incompressible flow (i.e. in case the Mach number Ma < 0.1 and therefore no density variations exist) are given

$$\dot{m}_\mathrm{A} = \dot{m}_\mathrm{G} + \dot{m}_\mathrm{F}, \tag{2.2}$$
$$\dot{V}_\mathrm{A} = \dot{V}_\mathrm{G} + \dot{V}_\mathrm{F}. \tag{2.3}$$

Without particle agglomeration or size reduction by milling within the separation equipment, also the masses per particle diameter are conserved

$$\dot{m}_\mathrm{A}\left(d_\mathrm{P}\right) = \dot{m}_\mathrm{G}\left(d_\mathrm{P}\right) + \dot{m}_\mathrm{F}\left(d_\mathrm{P}\right). \tag{2.4}$$

The ratio of the total mass of the underflow and that of the feed is known as the total separation efficiency and is defined as

$$\eta_\mathrm{tot} = \frac{\dot{m}_\mathrm{G}}{\dot{m}_\mathrm{A}} = \frac{\dot{m}_\mathrm{G}}{\dot{m}_\mathrm{G} + \dot{m}_\mathrm{F}}. \tag{2.5}$$

In a similar way the separation efficiency of any particle diameter is defined, which can be calculated by one of the following three ways

$$\eta\left(d_\mathrm{P}\right) = \frac{\dot{m}_\mathrm{G}\left(d_\mathrm{P}\right)}{\dot{m}_\mathrm{A}\left(d_\mathrm{P}\right)}, \tag{2.6a}$$
$$= \eta_\mathrm{tot}\frac{q_\mathrm{G}\left(d_\mathrm{P}\right)}{q_\mathrm{A}\left(d_\mathrm{P}\right)} = \eta_\mathrm{tot}\frac{\mathrm{d}Q_\mathrm{G}\left(d_\mathrm{P}\right)}{\mathrm{d}Q_\mathrm{A}\left(d_\mathrm{P}\right)}, \tag{2.6b}$$
$$= 1 - \left(1 - \eta_\mathrm{tot}\right)\frac{q_\mathrm{F}\left(d_\mathrm{P}\right)}{q_\mathrm{A}\left(d_\mathrm{P}\right)} = 1 - \left(1 - \eta_\mathrm{tot}\right)\frac{\mathrm{d}Q_\mathrm{F}\left(d_\mathrm{P}\right)}{\mathrm{d}Q_\mathrm{A}\left(d_\mathrm{P}\right)}. \tag{2.6c}$$

The separation efficiencies in Eq. (2.6a)-(2.6c) are also known as the grade efficiency. Two important features of a separation equipment are:

a. *Cut size*, $d_{\mathrm{P},50}$: The cut size is defined as the particle diameter, that has a separation probability of exactly 50% and thus an equal probability to leave the cyclone with the over- or underflow. This means that:

$$\eta(d_{\mathrm{P},50}) \equiv 50\%, \tag{2.7a}$$
$$\dot{m}_\mathrm{G}(d_{\mathrm{P},50}) \equiv \dot{m}_\mathrm{F}(d_{\mathrm{P},50}). \tag{2.7b}$$

b. *Sharpness of cut*, κ: The sharpness of cut is a parameter that indicates the steepness of the grade efficiency separation curve. It is defined as

$$\kappa_{\mathrm{i}/100-\mathrm{i}} = \frac{d_{\mathrm{P,i}}}{d_{\mathrm{P},100-\mathrm{i}}}, \tag{2.8}$$

where the index i is the percentage of the cumulative particle size distribution function. Common values for i are 10, 25 and 35%. The sharpness of cut becomes 1 for an ideal separator.

In Fig. 2.3, three typical separation curves are shown as function of the particle diameter, made dimensionless with the cut size, $d_{\mathrm{P},50}$. For an ideal separator, the function for the grade

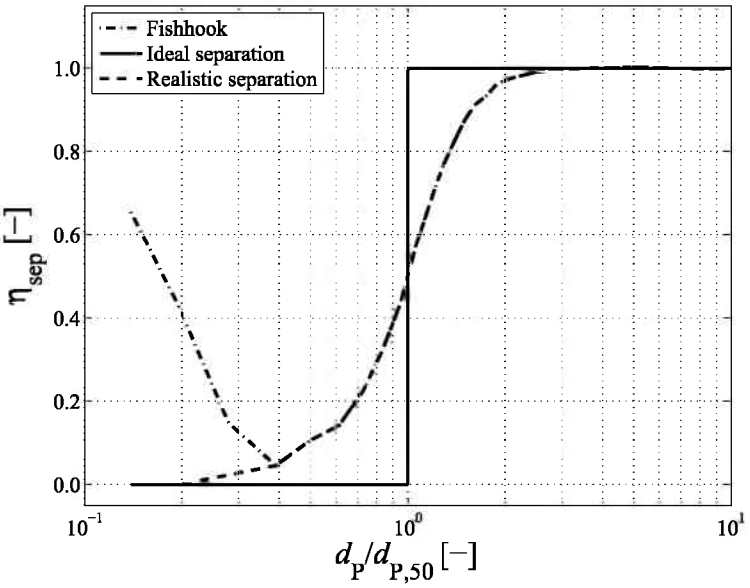

Figure 2.3: *Grade efficiency curves, η_{sep}, for a non-ideal separator with a fishhook, for an ideal separator and for a non-ideal separator without fishhook, as function of the particle diameter, made dimensionless with the cut size, $d_{P,50}$.*

efficiency equals a step function, i.e zero for all particle diameter smaller than the cut size, undefined for the particle diameter which exactly equals the cut size and unity for all particle diameters larger than the cut size. For a non-ideal separator, the separation curve shows the typical S-shape. However, sometimes very small particles are better separated than slighter larger ones. This phenomenon is known as fishhook and can occur in a cyclone separator because of agglomeration of small particles for example.

3 Experimental Observations on Depositions

Depositions in gas cyclones have not been described yet in detail in the literature. More data are available for other applications such as fibre filters, heat exchangers and pipe flows. An overview about depositions in these applications is given in the following sections.

3.1 Depositions in Cyclone Separators

In literature some rules of thumb are described to prevent depositions as well as some equipments for cyclone cleaning. Most are in form of patents. Although depositions have been noticed in experiments, they have not been investigated in detail yet.

3.1.1 Depositions around the Natural Vortex Length

According to the 2nd Helmholtz vortex theorem the strength of a vortex is constant over its length. This means that a vortex cannot end in a frictionless fluid itself and must whether form a closed structure (e.g. a torus) or end on a surface (e.g. a wall) [118]. In a cyclone separator the primary vortex cannot have an infinite length and since a closed structure is not possible because of the geometry, the vortex must end on a surface. This surface might be the cyclone's wall (i.e the cylindrical or conical part), the downcomer tube or the bottom of the dust collector. When a vortex stabilisator is used, the vortex can end here as well. For very high friction, it may be theoretically possible that the vortex is decelerated downwards and ends in free space. However, measurements of Muschelknautz and Krambrock [108] showed that this will not occur, which is confirmed by Peng et al. [118]. Consequently, in practice, the primary vortex will end at a certain position at the wall and a secondary, induced vortex will arise in the lower part of the cyclone. The distance from the bottom of the vortex finder to this position is called the natural vortex length [65]. Alternatively it can be measured downwards starting from the roof [64]. Usually the outer vortex will end in the conical part (cyclone body) or vertical tube section [64]. The natural length of the vortex should be ideally larger or equal to the physical length of the cyclone, because in the region below the natural vortex length the separation of solids is known to be much lower than above [43]. However, the vortex should not end in the dustbin to prevent re-entrainment from separated particles. Hoffmann et al. [63] found that a ratio of the vortex length to the cyclone body diameter, L_c/D_{cb}, larger than 5.65 led to dramatically lower separation efficiencies.

The position of natural vortex length can be measured in transparant cyclones with tracer particles, as shown in Fig. 3.1(a), by making the vortex visible with a strobe [118]. Alternatively, wall pressure fluctuations can be measured and transformed with a fast Fourier transformation (FFT) into frequencies [41, 118]. Two frequency peaks can be distinguished from which two the lower one indicates the position of the end of the outer vortex and the higher one the beginning of the inner vortex. Gao et al. noticed that in their test cyclone both

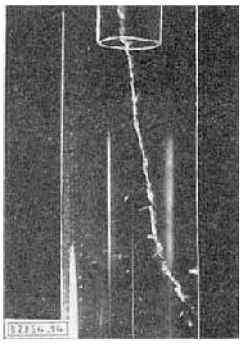

(a) The end of the natural vortex made visible in a transparant cyclone with tracer particles and a strobe [108].

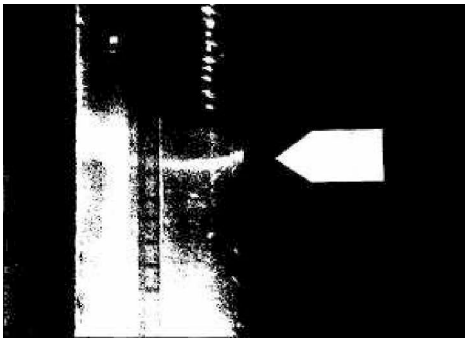

(b) The formation of a closed ring in the vertical tube section as indication of the end of the outer vortex [64].

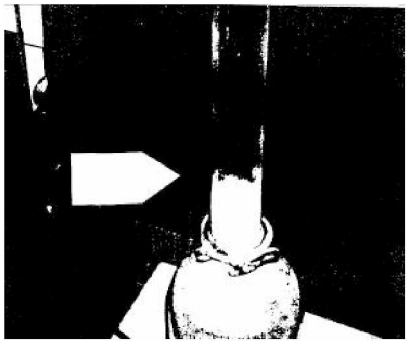

(c) A sudden increase of the depositions on this position [64].

Figure 3.1: *Features of the natural vortex length and the depositions noticed there.*

vortices end and arise on an azimuthal of 270°, measured in positive flow direction from the inlet [41].

Hoffmann et al. [64] report "a sudden transition in the amount of dust deposits on the wall" in the vertical tube section, which is also known from practice. In other experiments this dust ring gained a thickness of almost 0.5 cm [63]. The lowest point of these deposits indicates the end of the vortex. Hoffmann et al. observed that for increasing solid loading as well as for increasing inlet velocities, under otherwise similar conditions, the position of the end of the vortex rises. A narrower vortex finder, which has the same effect as a higher wall roughness, decreased the position. Also Gil et. al [43] noticed a similar ring in their experiments, this time in the vertical tube section.

In literature, several models are mentioned for the estimation of the natural length of the vortex, which are mentioned in Tab. 3.1. All models are only a function of the cyclone's geometry, neglecting velocity or solid loading conditions. If the natural vortex length is calculated according to the equations in Tab. 3.1 and compared with the length between the bottom of the vortex finder and the dust outlet of the cyclone used in the experiments in Ch. 9 (807 mm from App. A), only the models of Alexander and Bryant et al. give values within the same range [64, 123]. The model of Zhongli et al. predicts a length that is several times larger than the height of the test cyclone [64]. Therefore, the last model does not seem to be able to predict the natural vortex length for the cyclone used in the experiments described in Ch. 9.

Gil et al. [43], however, found a dependency on both the inlet velocity and solid loading as well. They observed that the end of the vortex could be examined by measuring the pressure profile in the vertical tube section. A higher solid loading resulted in a faster decreasing pressure and therefore in a higher position of the vortex end. Also a lower inlet velocity had the same effect. This corresponds to experiments, where higher solid loadings resulted in decreasing tangential velocities because of higher wall friction.

3.1.2 Cleaning Devices

Cyclones are often cleaned continuously or in certain time intervals [38]. One of the cleaning methods is injecting a spray of water by which depositions are removed from the wall. This

Table 3.1: *Models to calculate the natural vortex length, L_c, and its values for the test cyclone's geometry with: D_{vf}, the vortex finder diameter, D_{cb}, the diameter of the cyclone body and a and b, the width and height of the inlet respectively. The vertical distance between the bottom of the vortex finder and the dust exits equals 0.807 m.*

Author	Equation	L_c [m]
Alexander 1949 [64]	$\frac{L_c}{D_{cb}} = 2.3\frac{D_{vf}}{D_{cb}}\left(\frac{D_{cb}^2}{a_{in}b_{in}}\right)^{1/3}$	0.721
Bryant et al. 1983 [123]	$\frac{L_c}{D_{cb}} = 2.26\left(\frac{D_{vf}}{D_{cb}}\right)^{-1}\left(\frac{D_{cb}^2}{a_{in}b_{in}}\right)^{-0.5}$	0.747
Zhongli et al. 1991 [64]	$\frac{L_c}{D_{cb}} = 2.4\left(\frac{D_{vf}}{D_{cb}}\right)^{-2.25}\left(\frac{D_{cb}^2}{a_{in}b_{in}}\right)^{-0.361}$	3.924

application is often found in large cyclones. There, the solid deposits are caught up in airtight containers. The wall is at least partly wetted and the injection of liquid can be continuously or at periodic time intervals [70].

The same cleaning principle could also be achieved in smaller cyclones when a film of water covered the whole wall and a slightly negative pressure drop at the solid outlet was created [38]. The scrubbing liquid is injected in pulses using a peristaltic pump. A certain part of it evaporates in the air or leaves the cyclone directly via the cyclone's roof with the overflow by lip-leakage.

Also Yang and Yoshida [152] observed a decrease of wall depositions after a mist injection. Particles are forced to the wall by the mist droplets, where they are washed downwards. As a consequence, the separation efficiency is influenced in a positive way. They found that the washing effect was dependent on the cyclone's geometry and the position of the nozzle.

Also mechanical cleaning devices are used in practice:

- To prevent fouling of extremely cohesive or adhesive products, the inner wall of the cyclone can be made of a flexible material as shown in Fig. 3.2(a) [94] . If the magnitude of the volume flow rate of the continuous phase is pulsed by a pneumatic conveyer, located upstream of the separator, the depositions are vibrated from the wall. This wall should be made of an antistatic, electrical conductive and corrosion-resistant material, such as an elastomeric polymer (e.g. PU, PVC or PE). A decrease of the deposited mass of two different iron oxides in the range of 91.2 to 92.8% was obtained in experiments. Also the thickness of the depositions decreased from 8 mm to a value below the measurable range.

  Alternatively the pressure between the stiff cyclone's outer wall and the elastic jacket can be varied with an external compressor, if the continuous flow is not pulsating (Fig. 3.3(a)) [11].

- Mechanical strikers are used to scratch off the depositions from the wall as shown in Fig. 3.3(b) [11]. A shaft with an external driving is needed, which results in a more complicated geometry with seals. Therefore, the danger of leaks of the continuous phase through these faulty positions exists. Possible positions of the striker are the cylindrical part of the cyclone or the vortex finder. The movements may be rotating or translating and pulsating.

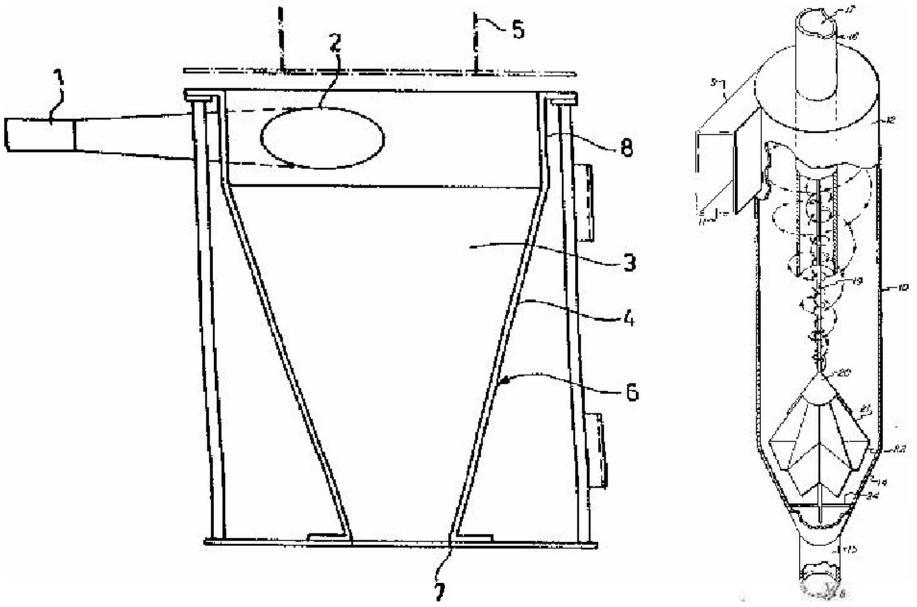

(a) Elastic cyclone wall [94]. (b) Baffle [26].

Figure 3.2: *Constructions to prevent cyclone fouling.*

3.1.3 Prevention of Depositions

To prevent depositions at the height of the natural vortex length, as described in Sec. 3.1.1, the cyclone can be provided with baffles, with two to ten fins attached (Fig. 3.2(b)) [26]. These baffles reduce the spin of the gas-solid mixture and therefore lessen the material transport towards the wall. This results in less fouling in the cone region. A decrease in the rate of fouling in the range of a factor 2 to 45 compared to conventional cyclones is claimed.

Furthermore, it is known that the use of cylindrical cyclones with a polished surface has a positive effect on lowering the depositions. For strong cohesive materials, it is also recommended to build cyclones with a large ratio of the diameter of the cylindrical body to inner diameter of the vortex finder, i.e. $D_{cb}/D_{vf} >> 1$ [11].

Cyclone separators with a logarithmic inlet geometry tend more to fouling than those with a slot inlet [7]. The quadratical cross sectional areas should be smooth to avoid deposition areas and regions of dead ends [6].

Besides polishing, coatings are also implemented [7, 105]. Muschelknautz [105] states furthermore, as a rule of thumb for general depositions, that neither the inlet velocity nor the centripetal acceleration in the near wall area should exceed a value of 10 m/s and 200 m/s^2, respectively. If these conditions are met, large, hard particles will rebound after a collision with the wall.

3.2 Depositions in Other Industrial Applications

Many researchers have studied depositions in other industrial applications than cyclone separators. In some applications the depositions are necessary and in other they should be avoided. In fibre filters for example, depositions are essential for the cleaning of the gas. In heat exchangers, fouling decreases the effectiveness of the heat transfer between the media.

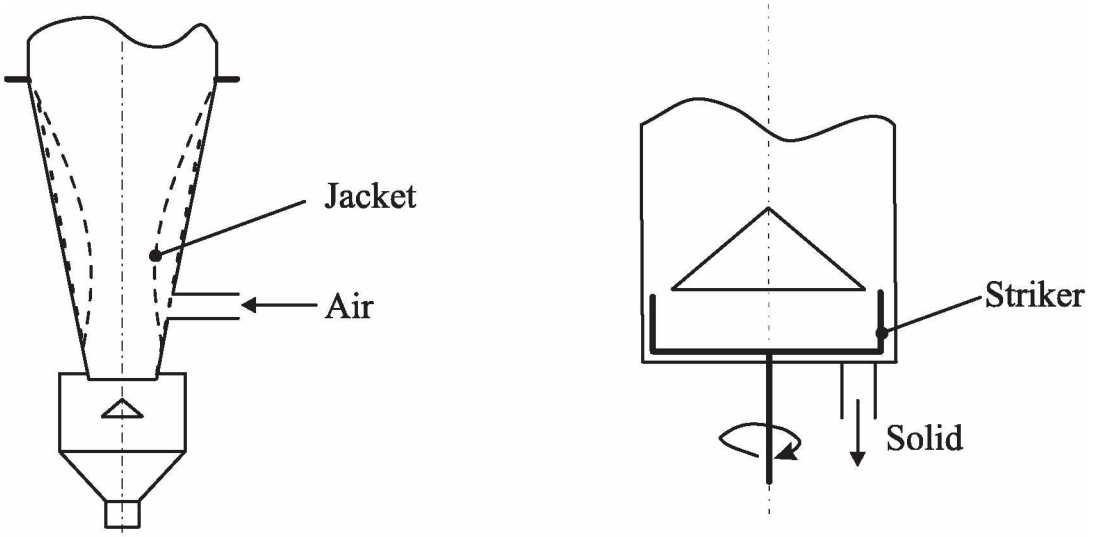

(a) Elastic jacket. (b) Striker.

Figure 3.3: *Mechanical cyclone cleaning devices [11].*

3.2.1 Deposition in Channels

According to Young and Leeming [154], the flux of particles to the wall per unit area, J_w, in a turbulent pipe flow is made dimensionless in the dimensionless deposition velocity

$$V_{dep+} = \frac{J_w}{\rho_{Pm} u_*}, \tag{3.1}$$

where, ρ_{Pm} is the mass concentration of particles in the main flow. In Eq. (3.1), the friction velocity is defined as

$$u_* = \sqrt{\frac{\tau_w}{\rho_g}}. \tag{3.2}$$

The wall shear stress is calculated from the dynamic viscosity of the carrier fluid, μ_g and the derivative of the wall tangential fluid velocity, u_t, to the wall normal vector, $\vec{n}$

$$\tau_w = \mu_g \frac{du_t}{d\vec{n}}. \tag{3.3}$$

It is obvious that τ_w is still a function of the fluid velocity in Eq. (3.3). Also the particle relaxation time, τ_P, is made dimensionless by

$$\tau_{P+} = \frac{\tau_P u_*^2}{\nu_g}, \tag{3.4}$$

where, the particle relaxation time is given by

$$\tau_P = \frac{C_c \rho_P d_P^2}{18 \mu_g}. \tag{3.5}$$

The Cunningham correction factor is determined with Eq. (3.6):

$$C_c = 1 + Kn \left[2.514 + 0.8 \exp\left(-0.55/Kn\right)\right], \tag{3.6}$$

in which the Knudsen number, Kn, is the quotient of mean free path of the carrier gas, λ_g, and particle diameter, d_P

$$\mathrm{Kn} = \frac{\lambda_g}{d_P}. \tag{3.7}$$

Three types of deposition regions are distinguished for different regimes of τ_{P+}, as shown in Fig. 3.4. The particle transport in the single regimes are characterised by the following physical behaviour as described by Young and Leeming [154]. Fits, which are made from experimental data, for the dimensionless deposition velocity are given by Masuda et al. [96]:

a. *Diffusional deposition regime:* The particle movement is dominated by Brownian motion in the near wall region and/or turbulent gradient diffusion caused from eddies further away. The fit of the dimensionless deposition velocity reads:

$$V_{dep+} = 0.065 \cdot \mathrm{Sc}^{-2/3}, \text{ for } \tau_{P+} < 0.2. \tag{3.8}$$

Here, the Schmidt number, Sc, is defined as [154]

$$\mathrm{Sc} = \frac{\nu_g}{D_P}. \tag{3.9}$$

D_P is the particle Brownian diffusion coefficient, which can be calculated with the Einstein equation

$$D_P = R_P T \tau_P, \tag{3.10}$$

in which, R_P is the quotient of the Boltzmann constant, k_b and particle mass m_p:

$$R_P = \frac{k_b}{m_p}. \tag{3.11}$$

The absolute temperature, T, is assumed to be isothermal. Eq. (3.8)-(3.10) predict higher values of V_{dep+} for increasing values of τ_P, although measurements show the opposite as can be observed in Fig. 3.4 [154].

b. *Diffusion-impaction regime:* Particles have significant inertia to interact with turbulent eddies. The particles are transported by gradient diffusion up to one stopping distance from the wall, where they are assumed to have gained enough momentum to reach it. The fit for the dimensionless deposition velocity is given by:

$$V_{dep+} = 3.5 \times 10^{-4} \tau_{P+}^2, \text{ for } 0.2 < \tau_{P+} < 20. \tag{3.12}$$

c. *Inertia-moderated regime:* Particles respond less to turbulence and have got enough energy from eddies located far away from the wall to reach the wall directly. The domain for the intertia-moderated regime and the fit for the dimensionless deposition velocity are:

$$V_{dep+} = 0.18, \text{ for } \tau_{P+} > 20. \tag{3.13}$$

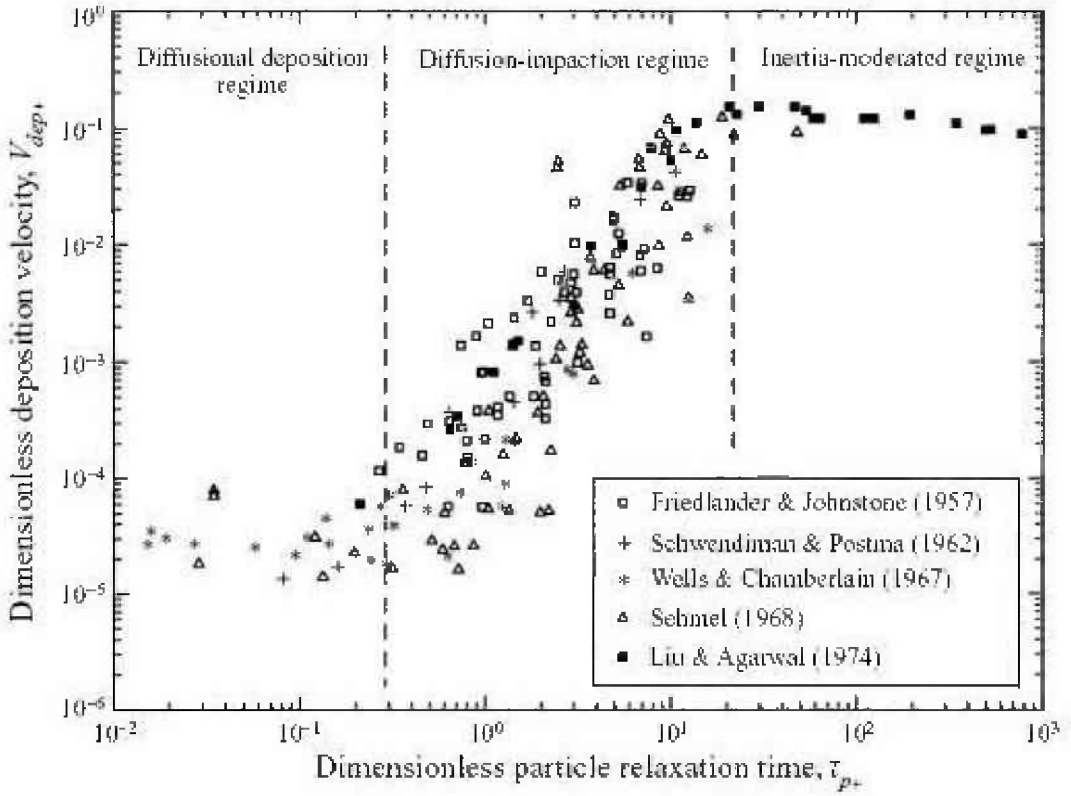

Figure 3.4: *The three different particle deposition regimes, with, τ_{P+}, the dimensionless particle relaxation time and V_{dep+}, the dimensionless deposition velocity [154].*

In this thesis, the following ranges for the wall shear stress, calculated in the CFD simulations in Ch. 11, and for the particle diameter, measured from the feed, are considered:

$$0 < \tau_{\mathrm{w}} < 10 \text{ Pa}, \tag{3.14a}$$

$$0.1 < d_{\mathrm{P}} < 100 \ \mu\text{m}. \tag{3.14b}$$

Therefore, the dimensionless particle relaxation time can be theoretically in a range of

$$0 < \tau_{\mathrm{P}+} < \mathcal{O}(10^4). \tag{3.15}$$

This range covers all three regimes, as shown in Fig. 3.4. Therefore, it is difficult to predict the behaviour of the mixture. Due to the formation of strands, it might be possible that also smaller particles act like larger ones. Small particles could as a result fall in the inertia-moderated regime since they are captured within the wakes of larger particles. This phenomena has been observed in experiments with cyclone separators [106].

Another interesting aspect is that, for a constant friction velocity, a higher flux of particles is predicted with an increasing particle concentration. It is also known that the concentration of particles in the region close to the cyclone's wall increases for increasing volume flow rates due to centrifugal forces. However, in the experiments discussed in Ch. 9, there is an unambiguous negative correlation between the deposited mass and the volume flow rate. This behaviour leads to the following two hypotheses:

a. The deposition model in Eq. (3.1)-(3.4), which was developed for an axial pipe flow, is not suitable to predict the deposition in a strong swirling flow, such as found in a cyclone separator. Here, other mechanisms than Brownian and turbulent diffusion could be responsible for the transport of particles towards the wall;

b. The model describes the transport of particles towards the wall correctly, but these particles do not meet a specific sticking criterion and reflect. Two different sticking criterions, based on respectively energy conservation on the one side and force and moment equilibrium on the other side are discussed in Ch. 7. A model for a better prediction of the particle impact velocity is treated in Ch. 10.

3.2.2 Physical Parameters Influencing Depositions

The sticking behaviour of particles after colliding with a solid wall has been described in mathematical models by several authors for different applications. Hiller and Löffler [60] investigated the sticking of particles on fibre filters and mention that the sticking fraction, h, is a function of the following dimensionless numbers:

$$h = h\left(\mathrm{Stk}, \mathrm{Re}_{\mathrm{D}}, \mathrm{Fr}_{\mathrm{P}}, \mathrm{S}, e_{\mathrm{pl}}^2, \mathrm{H}\right). \tag{3.16}$$

The following dimensionless numbers describe the transport of particles to the wall:

$$\mathrm{Stk} = \frac{\rho_\mathrm{P}}{\rho_\mathrm{g}} \frac{d_\mathrm{P}^2 u_\mathrm{in}}{18 \nu_\mathrm{g} D_\mathrm{cb}}, \tag{3.17a}$$

$$\mathrm{Re_D} = \frac{u_\mathrm{in} D_\mathrm{cb}}{\nu_\mathrm{g}}, \tag{3.17b}$$

$$\mathrm{Fr_P} = \frac{u_\mathrm{in}^2}{d_\mathrm{P} g} \frac{\rho_\mathrm{g}}{\rho_\mathrm{P}}. \tag{3.17c}$$

In Eq. (3.17a)-(3.17c), $\mathrm{Re_D}$ and $\mathrm{Fr_P}$ are the Reynolds and Froude number respectively, as defined by Derksen et al. [36] for a cyclone separator. The Froude number, $\mathrm{Fr_P}$, gives the influence of gravity, which is only important at high solid loadings, where mass effects become important [66]. The Stokes number, Stk, gives the ratio between the stopping distance of a particle and the characteristic dimensions of an obstacle.

Other parameters describe the material properties:

$$\mathrm{S} = \frac{\rho_\mathrm{P}}{\rho_\mathrm{g}}, \tag{3.17d}$$

$$e_\mathrm{pl}^2 = \frac{E_\mathrm{kin,1} - E_\mathrm{pl}}{E_\mathrm{kin,1}}, \tag{3.17e}$$

$$\mathrm{H} = \frac{p''_\mathrm{vdW}}{p_\mathrm{pl}}. \tag{3.17f}$$

The density ratio, S, does not change for a constant gas density, i.e. for low Mach numbers. Therefore, it will be treated as a constant for the temperature range of the performed experiments (Ch. 9). In the literature, constant values for the plastic coefficient of restitution, e_pl, are mentioned which vary from 0.4 to 0.9 [14, 57, 73, 126]. The plastic coefficient of restitution is related to the energy stored in plastic deformation after collision, E_pl and the kinetic energy of the particle before collision, $E_\mathrm{kin,1}$. Alternatively, it can be calculated from the adhesion energy, which is explained in Sec. 5.5. The ratio of the van der Waals pressure, p''_vdW, and yield stress of the softer material in contact, p_pl, is denoted with the symbol H and is also kept constant during the experiments. Material properties of the used limestone are found in Tab. 9.1.

4 Forces Working on a Particle

The forces on a particle in a fluid, whose domain is bounded by a wall, can be divided into:

- forces between particles,
- the force, a particle experiences from the fluid velocity,
- the force, the particle acts on the wall, when it is at the contact distance from the wall,
- the force, a particle acts on the fluid and
- the force, the wall acts on a particle.

The last two types of interactions are not be taken into account in this thesis. In Sec. 4.1 the particle-particle forces and particle-wall forces are discussed as well as an overview of the calculation methods. Flow forces are discussed in Sec. 4.1.5. It is also shown which forces are relevant for wall depositions of limestone on a wall of steel in a cyclone separator.

4.1 Particle-Particle and Particle-Wall Forces

Adhesion forces are divided into a short range part describing chemical reactions and a long range part described by van der Waals forces [129]. The long range forces vanish rapidly beneath a distance of 1 Å.

The van der Waals forces are proportional to z^{-2} for a sphere in contact with a flat surface or between two spheres and proportional to z^{-3}, between two flat surfaces. Here z denotes the distance between the two bodies in contact. In Fig. 4.1 a realistic interaction between a spherical particle and a plane wall is given such as five models from literature of modelling the contact.

The work of adhesion, γ, is calculated from integrating the interaction pressure, $\sigma(z)$, (i.e. the interaction force per unit contact area) from infinity up to the distance at zero contact, z_0:

$$\gamma = \int_{z_0}^{\infty} \sigma(z)\,\mathrm{d}z. \tag{4.1}$$

γ is divided into the amount of work performed by short range forces, w_1, and that by (the long range) van der Waals force, w_2

$$\gamma = w_1 + w_2. \tag{4.2}$$

The works of adhesion have by definition the dimension $m\,t^{-2}$, or expressed in SI units $\mathrm{kg\,s^{-2}}$. This means, they have the same dimension as energy per unit area ($\mathrm{J\,m^{-2}}$) or force per unit length ($\mathrm{N\,m^{-1}}$), which is known to be the dimension of surface tension.

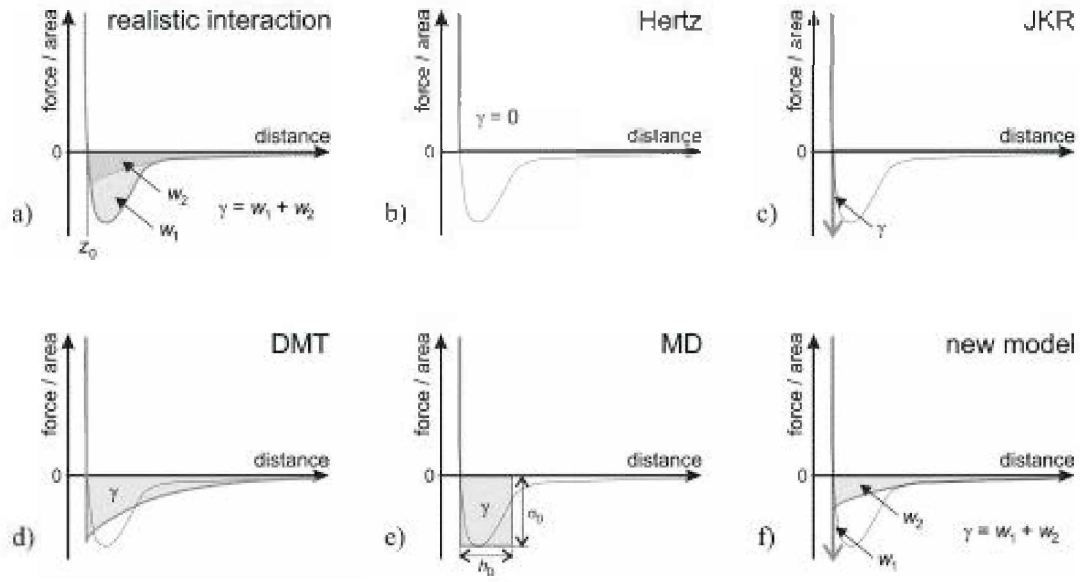

Figure 4.1: *Particle-wall interaction force with distinction between the work done by short range forces (w_1) and the long range van der Waals force (w_2) for a realistic interaction and five models, where the "new model" equals the proposal of Schwarz [129].*

Another way to describe the contact between two bodies is the total free energy of adhesion (ΔG_{ij}^{tot}). This energy exists of an apolar Lifshitz van der Waals (ΔG_{ij}^{LW}) and a polar acid-base component, ΔG_{ij}^{AB} [144, 146]:

$$\Delta G_{ij}^{tot} = \Delta G_{ij}^{LW} + \Delta G_{ij}^{AB}. \tag{4.3}$$

For the cohesion of one material in air or vacuum (i.e. $i = j$ and in case both bodies in contact are spherical), the surface tension γ_i follows from

$$\gamma_i^{tot} = -\frac{1}{2}\Delta G_{ii}^{tot}. \tag{4.4}$$

This surface tension is the sum of several, more or less independent, forces:

$$\gamma_i^{tot} = \sum_j \gamma_i^j. \tag{4.5}$$

These forces are for example of the type of dispersion-, polar-, induction-, H-bonding- and metallic interactions [144].

Similar as in Eq. (4.3), the surface tension (or surface free energy per unit area) is divided into an apolar (γ_{ij}^{LW}) and a polar (γ_{ij}^{AB}) component [146]:

$$\gamma_{ij}^{tot} = \gamma_{ij}^{LW} + \gamma_{ij}^{AB}. \tag{4.6}$$

which gives the same result as Eq. (4.2).

The calculation of the free energy of adhesion and cohesion in air (or vacuum) or with a fluid as interface is presented in Sec. 5.3.1.

4.1.1 Lifshitz-van der Waals Forces

The long-range interaction between molecules is known as the *van der Waals force* [121]. This force is the consequence of the fluctuating movement of negative electrons around a positive nucleus in an atom. This induces constant changing dipole moments and electric fields. The van der Waals forces are the result of the interactions between such magnetics fields. The van der Waals force reaches over distances much larger than the London distance and the range covered by the Lifshitz theory, which is from 1 nm to 100 nm. The van der Waals force consists of three parts [145], which are:

a. *Keesom-orientation force* from randomly orienting dipole-dipole interactions,

b. *Debeye-induction force* from randomly orienting interactions between dipoles and induced dipoles,

c. *London-dispersion force* from fluctuating dipole-induced dipole interactions.

From these parts, the first two are the result of molecules which have permanent dipole movements. Although limestone is a mixture of salts, as can be seen in Tab. 9.1, and thus a dipole, only the London-dispersion force will be taken into account because this force is generally larger than the other two forces [121, 145].

The van der Waals energy E_{vdW} is then calculated from ΔG^{LW} [76]:

$$\begin{aligned} E_{\mathrm{vdW}} &= \Delta G^{\mathrm{LW}} \pi r_0^2 \\ &= -2\gamma^{\mathrm{LW}} \pi r_0^2. \end{aligned} \tag{4.7}$$

The van der Waals part in the free energy of adhesion between the materials in contact, ΔG^{LW}, is calculated in detail in Sec. 5.3.1. The contact radius, r_0, is estimated from the adhesion map as explained in Sec. 6.7.

The van der Waals force follows from differentiating the van der Waals energy with respect to the position, x

$$F_{\mathrm{vdW}} = -\frac{\mathrm{d}E_{\mathrm{vdW}}}{\mathrm{d}x}. \tag{4.8}$$

From Johnson et al. [76], it is known that

$$x \approx \frac{r_0^2}{r^*}, \tag{4.9}$$

where, r^*, is the reduced radius (introduced in Sec. 6.3). After substitution of Eq. (4.9) into Eq. (4.8), the latter one becomes

$$F_{\mathrm{vdW}} \approx 2\pi\gamma^{\mathrm{LW}} r^*. \tag{4.10}$$

The van der Waals force is made dimensionless in form of the dimensionless critical pull-off force, $\bar{P}$ [75]

$$\bar{P} = \frac{F_{\mathrm{vdW}}}{\pi\gamma^{\mathrm{LW}} r^*}. \tag{4.11}$$

The critical pull-off force can vary, dependent on the type of contact, between the following values

$$1.5 \leq \bar{P} \leq 2.0. \tag{4.12}$$

The lower boundary in Eq. (4.12) is known to be the upper boundary of DMT-regime and the upper one that for lower boundary of the JKR-regime. Details about the validity of these regimes are discussed in Ch. 6.

F_{vdW} can also be expressed as function of the Hamaker constant, A, or Lifshitz van der Waals constant, $\hbar\varpi$, which are discussed in Sec. 5.3.1.6 and 5.3.1.7, respectively. The cohesive Hamaker constant follows from the following conversion of the specific surface energy of the material with index "1", γ_1

$$A_{11} = \gamma_1 \left(24\pi z_0^2\right). \tag{4.13}$$

The relation between the Hamaker and the Lifshitz van der Waals constant reads:

$$\hbar\varpi_{\mathrm{ij}} \equiv \frac{4\pi}{3} A_{\mathrm{ij}} \tag{4.14}$$

The van der Waals interaction forces between two spheres (with radius R), a sphere and a flat and two flats, with contact area, A_{c}, of the same material respectively are [121, 144]:

$$F_{\mathrm{s-s}}^{\mathrm{LW}} = \frac{A_{11}R}{12z_0^2} = \frac{\hbar\varpi_{11}}{16\pi z_0^2}R, \tag{4.15a}$$

$$F_{\mathrm{s-f}}^{\mathrm{LW}} = \frac{A_{11}R}{6z_0^2} = \frac{\hbar\varpi_{11}}{8\pi z_0^2}R, \tag{4.15b}$$

$$\frac{F_{\mathrm{f-f}}^{\mathrm{LW}}}{A_{\mathrm{c}}} = \frac{A_{11}}{6\pi z_0^3} = \frac{\hbar\varpi_{11}}{8\pi^2 z_0^3}, \tag{4.15c}$$

where the indices s and f denote a sphere and a flat surface respectively.

4.1.2 Polar Electron Acceptor-Donator Interactions

Beside the apolar van der Waals force, polar, but not electrostatic, forces play a role in colloidal interactions. These polar force typically exists in many nonmetallic condensed materials, which may be liquid or solid [144]. If this interaction is attractive, it is called "hydrophobic interaction" and if repulsive "hydration pressure". These polar interactions are major based on Lewis acid-base interactions, i.e. on electron acceptance and donation and include the hydrogen-bonding type. Between two materials 1 and 2, respectively acting as electron acceptor and donor and vica versa, the polar component of the free energy of interaction is given by:

$$\begin{aligned} \Delta G_{12}^{\mathrm{AB}} &= -2\left(\sqrt{\gamma_1^+\gamma_2^-} + \sqrt{\gamma_1^-\gamma_2^+}\right) \\ &= \gamma_{12}^{\mathrm{AB}} - \gamma_1^{\mathrm{AB}} - \gamma_2^{\mathrm{AB}}, \end{aligned} \tag{4.16}$$

which is always attractive, and therefore per definition negative. The polar interfacial tension between two materials, γ_{12}^{AB} in Eq. (4.16), is given by

$$\begin{aligned}\gamma_{12}^{AB} &= 2\left(\sqrt{\gamma_1^+\gamma_1^-}+\sqrt{\gamma_2^+\gamma_2^-}-\sqrt{\gamma_1^+\gamma_2^-}-\sqrt{\gamma_1^-\gamma_2^+}\right) \\ &= 2\left(\sqrt{\gamma_1^+}-\sqrt{\gamma_2^+}\right)\left(\sqrt{\gamma_1^-}-\sqrt{\gamma_2^-}\right),\end{aligned} \tag{4.17}$$

where,

$$2\sqrt{\gamma_1^+\gamma_1^-} = \gamma_1^{AB}, \tag{4.18}$$

$$2\sqrt{\gamma_2^+\gamma_2^-} = \gamma_2^{AB}. \tag{4.19}$$

In Eq. (4.16)-(4.18) the superscripts "+" and "–" denote the electron acceptor and donator respectively. The adhesion force due to electron acceptance/donation follows similar to Eq. (4.10)

$$F_{vdW,ij} = c\pi\gamma_{ij}^{AB}r^*, \tag{4.20}$$

where, the indices ij can take the value 12, 13 or 23 for accounting the force between material respectively 1 and 2 with or without the interface 3. The constant c in Eq. (4.20) has a value between 1.5 and 2.0, as in Eq. (4.12).

4.1.3 Capillary Forces

Capillary forces originate from a liquid layer between a particle and a wall or between particles. They are important because moist powders tend to stick to metal walls [121].

However, Podczeck [121] mentions that moisture condensation only occurs if the relative air humidity exceeds the critical value of 50%. In Eq. (4.27)-(4.30b) it is demonstrated with the Kelvin equation how the smaller curvature of the meniscus is dependent of this relative humidity. For lower values, no capillary forces exist. Nevertheless, moist can work as a plasticiser for the particle's material, resulting in a larger contact area, and therefore in a larger total Lifshitz-van der Waals and/or acid-base force.

The calculation procedure for the capillary force between a spherical particle and a flat wall and that for the capillary interaction between two spherical particles is given below.

4.1.3.1 Particle-Wall

A spherical particle in contact with a plane is shown in Fig. 4.2(a) [31]. The contact angle between the particle and the fluid is denoted by θ_P and that between the wall and fluid by θ_w. The coordinates of the contact point between the particle and the meniscus can be expressed in these contact angles and radius of the smaller meniscus curvature, r, with the following

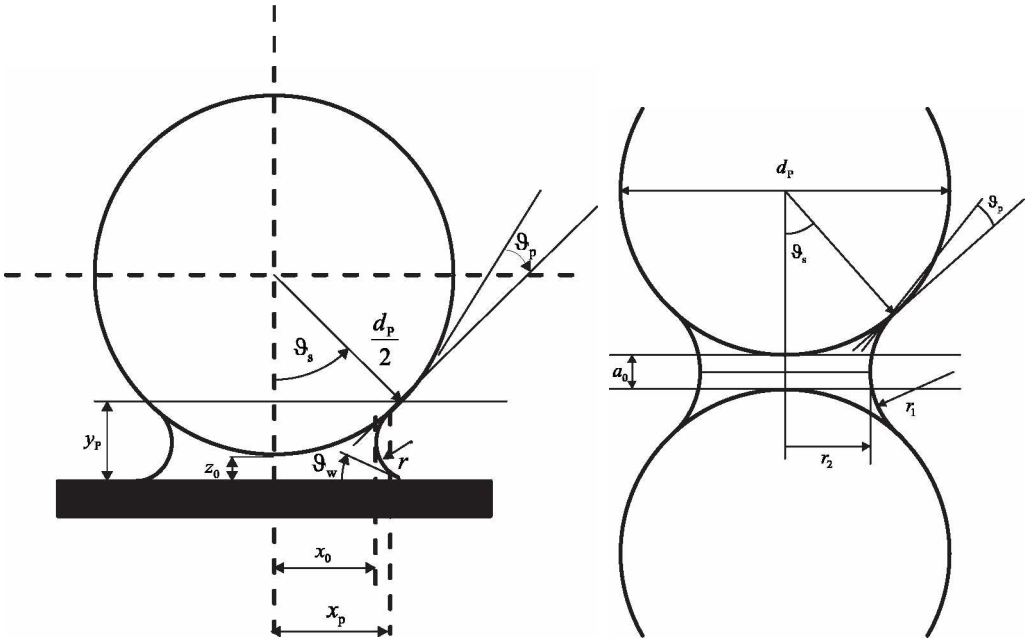

(a) A particle in contact with a flat, wetted surface showing a liquid meniscus [31].

(b) Two particles of same diameter in contact with a liquid bridge in between [119].

Figure 4.2: *Liquid bridges: a particle with diameter d_P is at a contact distance, z_0, from the wall or at a distance a_0 from its neighbouring particle. The contact angles between the fluid and the particle is denoted by θ_p, that between the fluid and the wall by θ_w and the wetting angle by θ_s. The meniscus curvatures are x_0 and r for the particle-wall contact and r_1 and r_2 for the particle-particle contact. The coordinates of the contact point are (x_p, y_p).*

equation

$$x_\mathrm{p} = \frac{d_\mathrm{P}}{2} \sin\theta_\mathrm{s}, \tag{4.21a}$$

$$y_\mathrm{p}\left(x_\mathrm{P}\right) = r\cos\left(\theta_\mathrm{p} + \theta_\mathrm{s}\right) + r\cos\theta_\mathrm{w}, \tag{4.21b}$$

or written in another way as

$$r = \frac{y_\mathrm{p}\left(x_\mathrm{p}\right)}{\cos\left(\theta_\mathrm{p} + \theta_\mathrm{s}\right) + \cos\theta_\mathrm{w}}. \tag{4.22}$$

The total capillary force, F_C, is divided into a part due to the capillary pressure difference, Δp, and a part due to the vertical component of the surface tension, γ_L [31]. The capillary pressure difference force is denoted by F_A and the force due to the surface tension by F_S. Expressions for both forces are given by:

$$F_\mathrm{A} = -\pi x_0^2 \Delta p, \tag{4.23a}$$

$$F_\mathrm{S} = 2\pi x_0 \gamma_\mathrm{L} \sin\left(\theta_\mathrm{p} + \theta_\mathrm{s}\right). \tag{4.23b}$$

Both forces work on a circle with radius x_0, which is the inner curvature of the meniscus ($x_0 \approx x_\mathrm{p} - r$ [137]). The total capillary force then reads

$$F_\mathrm{C} = F_\mathrm{A} + F_\mathrm{S} = -\pi x_0^2 \Delta p + 2\pi x_0 \gamma_\mathrm{L} \sin\left(\theta_\mathrm{p} + \theta_\mathrm{s}\right). \tag{4.24}$$

The pressure difference in Eq. (4.24) is calculated by means of the Young-Laplace equation [31, 119]

$$\Delta p = \gamma_\mathrm{L} \left(\frac{1}{x_0} - \frac{1}{r}\right), \tag{4.25}$$

where, the radius of the smaller curvature, r, has to be considered negative due to the shape of the meniscus [137]. The Kelvin radius, r_K, can be expressed as function of the meniscus curvatures:

$$r_\mathrm{K} = \left(\frac{1}{x_0} + \frac{1}{r}\right)^{-1}, \tag{4.26}$$

or, alternatively, as a function of the relative humidity [74]:

$$\begin{aligned} r_\mathrm{K} &= \frac{\gamma_\mathrm{L} V_\mathrm{m}}{R_\mathrm{u} T \log\left(p/p_\mathrm{s}\right)}, \\ &= \frac{\gamma_\mathrm{L}}{p_\mathrm{tot} \log\left(p/p_\mathrm{s}\right)}. \end{aligned} \tag{4.27}$$

In Eq. (4.27), γ_L is the vapour/liquid surface tension, V_m, the molar volume, R_u, the universal gas constant, T, the absolute temperature and p, p_s and p_tot, the vapour, saturation and total pressure respectively. The quotient of the vapour and saturation pressure gives the relative humidity, RH:

$$\mathrm{RH} = \frac{p}{p_\mathrm{s}}. \tag{4.28}$$

Eq. (4.26) is simplified to

$$r \approx r_\mathrm{K} = \frac{\gamma_\mathrm{L} V_\mathrm{m}}{R_\mathrm{u} T \log(\mathrm{RH})}, \tag{4.29}$$

since $r << x_0$ for small distances between the particle and surface, z_0, compared to the particle's diameter [74, 137]. This also means, that $x_\mathrm{p} \approx x_0$ and that x_0 can be replaced by x_p in Eq. (4.23)-(4.29) without making large errors.

Israelachvili [74] gives for water at 20 °C a value of 0.54 nm for the factor $\frac{\gamma_\mathrm{L} V_\mathrm{m}}{R_\mathrm{u} T}$. With a relative humidity (p/p_s) ranging from 10 to 90%, r_K has therefore a value around 1 nm. This is in the same order of magnitude as the distance at zero contact, z_0, and about three orders of magnitude smaller than the particle's diameter. Because $r << x_0$ (and therefore neglecting the $1/x_0$-term in Eq. (4.25)) and considering Eq. (4.29), the following factors are replaced in Eq. (4.24)

$$x_0 \approx x_\mathrm{p} = \frac{d_\mathrm{p}}{2} \sin\theta_\mathrm{s}, \tag{4.30a}$$

$$\Delta p \approx \frac{\gamma_\mathrm{L}}{r} \approx \frac{R_\mathrm{u} T \log(p/p_\mathrm{s})}{\gamma_\mathrm{L} V_\mathrm{m}}. \tag{4.30b}$$

The value of Δp is negative because of the geometry of the meniscus. The explicit expression for the capillary force then reads:

$$F_\mathrm{C} = -\pi \frac{d_\mathrm{p}^2}{4} \sin^2\theta_\mathrm{s} \frac{\gamma_\mathrm{L} R_\mathrm{u} T \log(p/p_\mathrm{s})}{\gamma_\mathrm{L} V_\mathrm{m}} + \pi d_\mathrm{P} \gamma_\mathrm{L} \sin\theta_\mathrm{s} \sin(\theta_\mathrm{p} + \theta_\mathrm{s}). \tag{4.31}$$

The maximal capillary force, that is theoretically possible, follows for $\theta_\mathrm{p} = 0$ and $\theta_\mathrm{s} = \pi/2$;

$$F_\mathrm{C,max} = \pi \frac{d_\mathrm{p}^2}{4} \frac{\gamma_\mathrm{L} R_\mathrm{u} T \log(p/p_\mathrm{s})}{\gamma_\mathrm{L} V_\mathrm{m}} + \pi d_\mathrm{P} \gamma_\mathrm{L}. \tag{4.32}$$

Realistic contact angles are calculated with the Young's equation [84]

$$\begin{aligned} \gamma_\mathrm{L} \cos\theta &= \gamma_\mathrm{S} - \gamma_\mathrm{SL}, \\ \gamma_\mathrm{L}(1 + \cos\theta) &= 2\sqrt{\gamma_\mathrm{L}^\mathrm{LW} \gamma_\mathrm{S}^\mathrm{LW}} + \sqrt{\gamma_\mathrm{L}^+ \gamma_\mathrm{S}^-} + \sqrt{\gamma_\mathrm{L}^- \gamma_\mathrm{S}^+}, \end{aligned} \tag{4.33}$$

with, γ_L, the surface energy of the liquid (i.e. water), γ_S, that of the solid (limestone or steel) and γ_SL, that of the interface. From the data in Tab. 4.1 the contact angles between limestone and water and steel and water respectively are

Table 4.1: *Values for the Lifshitz-van der Waals term γ^{LW}, Lewis-acid term γ^+ and Lewis-base γ^- term for limestone, steel and water [84, 122].*

material	γ^{LW} [mJ/m^2]	γ^+ [mJ/m^2]	γ^- [mJ/m^2]
limestone	42.62	1.64	14.52
steel	37.42	0.06	13.94
water	21.8	25.5	25.5

$$\theta_P = \operatorname{acos}\left(\frac{2\sqrt{\gamma_w^{LW}\gamma_l^{LW}} + \sqrt{\gamma_w^+\gamma_l^-} + \sqrt{\gamma_w^-\gamma_l^+}}{\gamma_w} - 1\right) = 79.0°, \tag{4.34}$$

$$\theta_w = \operatorname{acos}\left(\frac{2\sqrt{\gamma_w^{LW}\gamma_s^{LW}} + \sqrt{\gamma_w^+\gamma_s^-} + \sqrt{\gamma_w^-\gamma_s^+}}{\gamma_w} - 1\right) = 86.5°, \tag{4.35}$$

where, the indices w, l and s denote the material properties of water, limestone and steel respectively.

The wetting angle, θ_s, is calculated from the equilibrium of the wall normal coordinate from the contact between particle at a contact distance of $z_0 = 0.4$ nm from the wall and fluid, as expressed in Eq. (4.21b):

$$\begin{aligned} y_p(x_p) &= z_0 + \frac{d_P}{2}(1 - \cos\theta_s) \\ &= r\cos(\theta_p + \theta_s) + r\cos\theta_w. \end{aligned} \tag{4.36}$$

From Eq. (4.34), (4.35) and (4.36), it follows that the wetting angle must be between $\theta_s = 40.9°$ and $\theta_s = 45.0°$ for a rigid particle that is at a distance of 0.4 nm from the wall. Furthermore, it is only stable for relative humidities above 50% for a particle at the contact distance from the wall. This is approved by Podzceck [121]. Schubert gives a wetting angle of $\theta_s = 20°$ as a realistic value [128].

4.1.3.2 Particle-Particle

For the system particle-particle, the two capillary forces, comparable to those for the particle-wall contact system as defined in Eq. (4.23), are given by [119]:

$$F_A = \Delta p \frac{\pi}{4} d_P^2 \sin^2\theta_s = \gamma_L\left(\frac{1}{r_1} - \frac{1}{r_2}\right)\frac{\pi}{4}d_P^2\sin^2\theta_s, \tag{4.37a}$$

$$F_S = \gamma_L \frac{\pi}{2} d_P \sin\theta_s \sin(\theta_s + \theta_p). \tag{4.37b}$$

The sum of the components, defined in Eq. (4.37a) and (4.37b) then reads

$$F_C = \gamma_L \pi d_P \sin\theta_s \left[\sin(\theta_s + \theta_p) + \frac{d_P}{4}\left(\frac{1}{r_1} - \frac{1}{r_2}\right)\sin\theta_s\right]. \tag{4.38}$$

Also here, the maximum force follows for $\theta_\mathrm{p} = 0$ and $\theta_\mathrm{s} = \pi/2$:

$$\begin{aligned} F_{\mathrm{C,max}} &= \gamma_\mathrm{L}\pi d_\mathrm{P}\left[1 + \frac{d_\mathrm{P}}{4}\left(\frac{1}{r_1} - \frac{1}{r_2}\right)\right] \\ &= \gamma_\mathrm{L}\pi d_\mathrm{P}\left[1 + \frac{d_\mathrm{P}}{4}\left(\frac{\gamma_\mathrm{L} V_\mathrm{m}}{R_\mathrm{u} T \log\left(p/p_\mathrm{s}\right)}\right)^{-1}\right]. \end{aligned} \tag{4.39}$$

4.1.4 Electrostatic Forces

The electrostatic forces are divided into a part, which results from the formation of a double-layer in the contact zone, and a part, which results from the interaction of a charge with its image. Derjaguin et al. mention that the contribution of the image force is negligible small compared to the double-layer force in the total electrostatic force [33].

4.1.4.1 Electrical Forces

Electrical forces, or *electric double-layer forces*, are the consequence of the difference in contact potential between two particles or a particle and a surface [121]. They only occur for small particles with less than 5 μm in diameter, which are in a dry environment. The force is given by [33]

$$F_\mathrm{el} = 2\pi\sigma_\mathrm{A}^2 A, \tag{4.40}$$

where, σ_A is the surface density of charge in $\left[\mathrm{N}^{1/2}\,\mathrm{m}^{-1}\right]$ and A is the contact area. The electrostatic force between a flat plate and a spherical particle then becomes [82, 128]

$$F_{\mathrm{el,s-f}} = \pi\epsilon_\mathrm{r}\epsilon_0 V_\mathrm{e}^2 \frac{r^*}{z_0}, \tag{4.41a}$$

$$F_{\mathrm{el,s-f}} = \frac{2\pi}{\epsilon_\mathrm{r}\epsilon_0}\phi_{\mathrm{e},1}\phi_{\mathrm{e},2} r^{*2}, \tag{4.41b}$$

where, Eq. (4.41a) is for an electrical insulator and Eq. (4.41b) for a conductor. For the contact between two spheres with radius R_1 and R_2 respectively, the equations become

$$F_{\mathrm{el,s-s}} = \frac{1}{2}\pi\epsilon_\mathrm{r}\epsilon_0 V_\mathrm{e}^2 \frac{r^*}{z_0}, \tag{4.42a}$$

$$F_{\mathrm{el,s-s}} = \frac{\pi}{\epsilon_\mathrm{r}\epsilon_0}\frac{\phi_{\mathrm{e},1}\phi_{\mathrm{e},2} r^{*2}}{\left(1 + \frac{z_0}{R_1+R_2}\right)^2}. \tag{4.42b}$$

In Eq. (4.41)-(4.42), ϵ_r is the dielectric constant of the intermediate medium, which becomes unity for vacuum. The vacuum permittivity equals $\epsilon_0 = 8.855 \times 10^{-12}\ \left[\frac{\mathrm{As}}{\mathrm{Vm}}\right]$. Schubert gives values for the contact electrical potential, V_e, between 0.1 and 0.7 V and a maximum for the surface charge of $\phi_{\mathrm{e,max}} = 1.6 \times 10^{-5}\ \left[\frac{\mathrm{C}}{\mathrm{m}^2}\right]$ [128].

4.1.4.2 Coulomb Forces

Coulomb forces, or *electrostatic image forces*, are important for non-conductive particles larger than 5 μm and arise from the excess of charges [121]. It is one of the strongest forces and much stronger than most chemical binding forces [74]. The force between two charges q_1 and q_2 reads

$$F_{\mathrm{ES}} = \frac{q_1 q_2}{4\pi\epsilon_0\epsilon_\mathrm{r} r^2}, \tag{4.43}$$

where, ϵ_0 and ϵ_r are the vacuum and relativ permittivity respectively, and r is the distance between the charges. A particle close to the wall will feel its image as in a mirror and therefore r will take the value of twice the particle-wall distance, l_0, by which Eq. (4.43) becomes [72]:

$$F_{\mathrm{ES}} = \frac{q_{\mathrm{P},1}^2}{16\pi\epsilon_0\epsilon_\mathrm{r} l_0^2}. \tag{4.44}$$

For the calculation of the particle charges before and after colliding with a wall ($q_{\mathrm{P},1}$ and $q_{\mathrm{P},2}$ respectively), the following models, which are summarised in Tab. 4.2, are compared:

- Derjaguin et al. [34] only gives an expression for $q_{\mathrm{P},2}$ as function of the particle diameter, impact velocity, w_P, and the ratio between the charge density at equilibrium and the characteristic time, $\frac{\sigma_\mathrm{e}}{T_\mathrm{e}}$, which has the value of $1.5 \times 10^6 \left[\mathrm{C}^{-1}\,\mathrm{s}^{-1}\right]$.
- For the model of Matsuyama and Yamamoto [97], the particle charge before and after collision are dependent on the equilibrium charge, q_e and the charge of a neutral particle after collision, q_0. The first one was measured for quartz particles by Heinl and Bohnet [57] and the latter one is proportional to the factor $\frac{\epsilon_\mathrm{r}-1}{\epsilon_\mathrm{r}+2}$ according to Schütz [127]. By applying the value of the dielectric constant [135], the equation of Heinl and Bohnet for quartz could be rewritten for limestone.
- Lianze et al. [91] give an expression for the calculation of $q_{\mathrm{P},1}$ as function of (among other quantities) the time constant for diffusion charging, τ_d (neglecting field charging) and the time elapsed since the last collision, t. The latter one is calculated from the inter-particle collision time, which is defined in Eq. (8.107). As simplification, particles are only assumed to collide with particles of the same size, i.e. $d_\mathrm{P} = d_{\mathrm{P,max}}$, with a maximal relative velocity, $\Delta w_{\mathrm{P,max}}$, that equals the maximal gas velocity in the computational domain in the CFD-simulation in Sec. 8.1. Charging is assumed to happen by diffusion only, since an external electrical field is absent. The time constant by diffusion charging is then calculated from the number density of ions in space, n_i, which is calculated from the solid loading at the cyclone's inlet and the rms value of the thermal velocity of the ions, C_i. The particle charge after an elastic collision, $q_{\mathrm{P},2}$, is calculated from the collision time, τ_c, which is a function of the particle diameter, velocity and material properties, the charge relaxation time, τ_q, and $q_{\mathrm{P},1}$. The particle charge after colliding with the wall, $q_{\mathrm{P},2}$ follows from $q_{\mathrm{P},1}$, the collision time, τ_c, and the charge relaxation time, τ_q.

The Coulomb force of a particle after collision on a (not-grounded) wall follows from substituting l_0 by z_0, the contact distance, in Eq. (4.44) and thus reads

$$F_{\mathrm{ES}} = \frac{q_{\mathrm{P},2}^2}{16\pi\epsilon_0\epsilon_\mathrm{r} z_0^2}, \tag{4.45}$$

Table 4.2: *Models for the calculation of the Coulomb force for particle-wall collision (with indices P,1 and P,2 denoting the particles charge before and after collision respectively).*

author	dimension	equation	unit
Derjaguin et al. [34]	particle charge after collision	$q_{\mathrm{P},2} = 15.3 \left[\frac{d_\mathrm{P}}{2}\right]^3 w_\mathrm{P}^{3/5} \frac{\sigma_\mathrm{e}}{T_\mathrm{e}} \left[\frac{\rho_\mathrm{P}\left(1-\nu^2\right)}{Y}\right]^{-4/5}$	C
		$\frac{\sigma_\mathrm{e}}{T_\mathrm{e}} = 1.5 \times 10^6$	$\mathrm{C\,m^{-1}\,s^{-1}}$
Matsuyama and Yamamoto [97, 57]	particle charge after collision	$q_{\mathrm{P},2} = \frac{q_0}{q_\mathrm{e}} \left(q_\mathrm{e} - q_{\mathrm{P},1}\right)$	C
	particle charge before collision	$q_{\mathrm{P},1} = 1.5 \times 10^{-11} d_\mathrm{P}$	C
	particle charge of a neutral particle	$q_0 = 10 \times 10^{-6} d_\mathrm{P}^2$	C
	equilibrium charge	$q_\mathrm{e} = 9\pi\epsilon_0 d_\mathrm{P}$	C
Lianze et al. [151, 91, 100]	particle charge before collision	$q_{\mathrm{P},1} = \frac{2\pi d_\mathrm{P} \epsilon_0 k_\mathrm{B} T}{e} \ln\left(1 + \frac{t}{\tau_\mathrm{d}}\right)$	C
	particle charge after collision	$q_{\mathrm{P},2} = q_{\mathrm{P},1} \exp\left(-\frac{\tau_\mathrm{c}}{\tau_\mathrm{q}}\right)$	C
	time constant for diffusion charging	$\tau_\mathrm{d} = \frac{8\epsilon_0 k_\mathrm{B} T}{d_\mathrm{P} C_\mathrm{i} n_\mathrm{i} e^2}$	s
	charge relaxation time	$\tau_\mathrm{q} = \rho_\mathrm{q} \epsilon_0 \epsilon_\mathrm{r}$	s
	collision time	$\tau_\mathrm{c} = 2.87 \left(\frac{m^{*2}}{r^* Y^{*2} w_\mathrm{P}}\right)^{1/5}$	s
	thermal velocity of ion	$C_\mathrm{i} = \sqrt{\frac{k_\mathrm{B} T}{m_\mathrm{i}}}$	$\mathrm{m\,s^{-2}}$
	reduced mass	$m^* \approx m_\mathrm{P} = \frac{\pi \rho_\mathrm{P} d_\mathrm{p}^3}{6}$	kg
	reduced Young's modulus	$Y^* = \left[\left(1-\nu_1^2\right)/Y_1 + \left(1-\nu_2^2\right)/Y_2\right]^{-1}$	$\mathrm{N\,m^{-2}}$
	number density of ions in space	$n_\mathrm{i} = \frac{\mu_\mathrm{e} \rho_\mathrm{g}}{m_\mathrm{i}}$	$\mathrm{m^{-3}}$
	ion mass	$m_\mathrm{i} = m_\mathrm{P}$	kg
	time since the last collision [134]	$t = \left(\frac{\pi}{4} \left(d_{\mathrm{p,min}} + d_{\mathrm{p,max}}\right)^2 \Delta w_{\mathrm{P,max}} N_\mathrm{P}\right)^{-1}$	s

and is shown in Fig. 4.3(a). For a small particle with a diameter of 0.1 μm, the differences between the three models are in the order of seven orders of magnitude. For a relative large particle of 100 μm, this difference even becomes 30 orders of magnitude. Another interesting feature is that the Coulomb forces increase for an increasing particle diameter in the models of and Derjaguin et al. and Matsuyama and Yamamoto, whereas they decrease in the model of Lianze et al. The Coulomb force directly at the wall is relative high compared to the Coulomb force experienced at a distance of half the cyclone diameter, which is the largest particle-wall distance that is possible in the domain, as can be seen from Fig. 4.3(b). This shows the importance of grounding the walls in a cyclone separator, to assure particle charges are neutralised rapidly after a collision with the wall.

4.1.5 Comparison of Adhesion Forces

Podzcek [121] writes that "under normal experimental conditions", i.e. in absence of a high-voltage field and at close distances between the contiguous bodies, Lifshitz-van der Waals forces are about 10 times larger than electrical forces and at least 10 times larger than electrostatic image forces. These proportions are still valid if capillary forces are present. Furthermore, the electrostatic forces play a major role in deposition although the van der Waals force is responsible for the adhesion strength. This is confirmed by Schubert [128], who states that the electrostatic forces are responsible for the transport of particles to the wall and the van der Waals forces for the adhesion strength. In Fig. 4.4(a), 4.4(c) and 4.4(e) this is made visible for the contact between a spherical, limestone particle and a flat steel wall and for the contact between two spherical, limestone particles (Fig. 4.4(b), 4.4(d) and 4.4(f)).

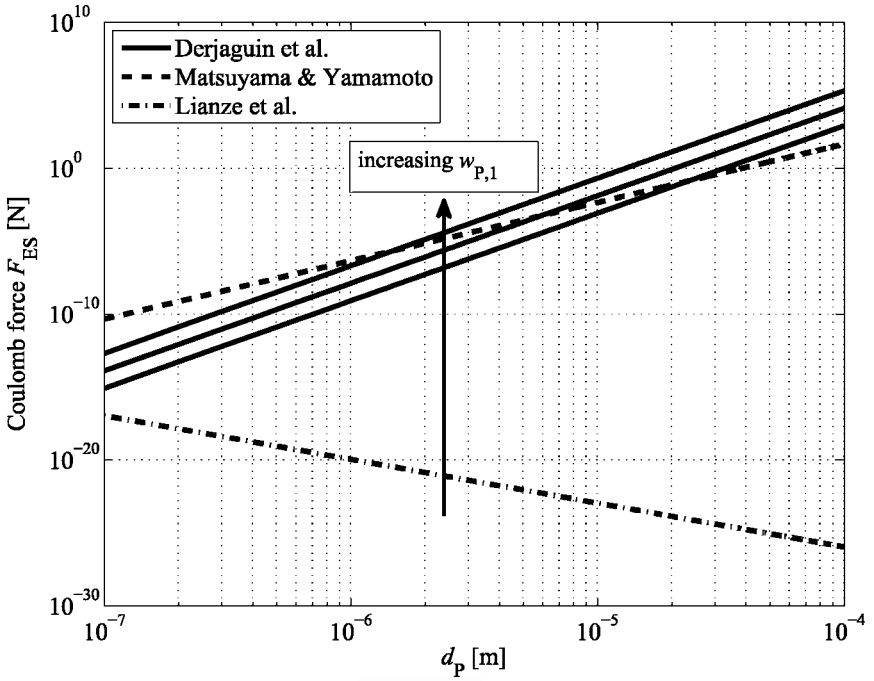

(a) Prediction of the Coulomb force, F_{ES}, defined in Eq. (4.45) with the models as mentioned in Tab. 4.2 for impact velocities of 0.1; 1 and 10 m/s for a particle in contact with the wall at a distance of $l_0 = z_0 = 0.4$ nm.

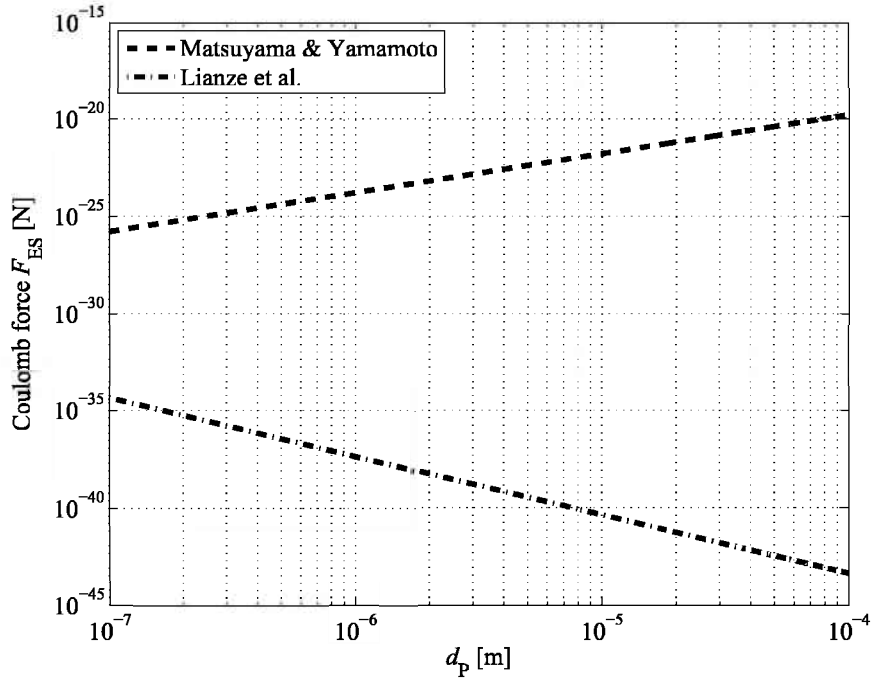

(b) Prediction of the Coulomb force, F_{ES}, defined in Eq. (4.44) for a particle at a distance of half the cyclone diameter ($l_0 = 0.2$ m). The model of Derjaguin et al. is not included because of the zero particle velocity.

Figure 4.3: *Coulomb force for a particle in contact with the wall (top) and a particle at a distance of half the cyclone diameter (bottom) calculated with the models summarised in Tab. 4.2.*

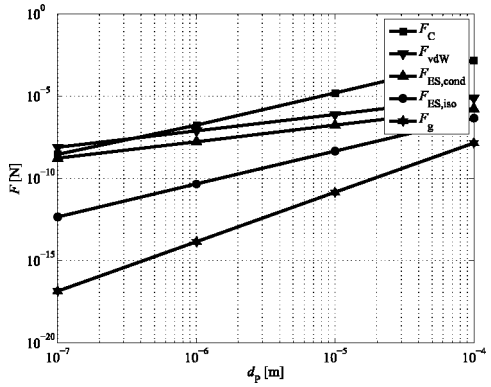

(a) Forces of a particle in contact with the wall for $\theta_s = 5°$.

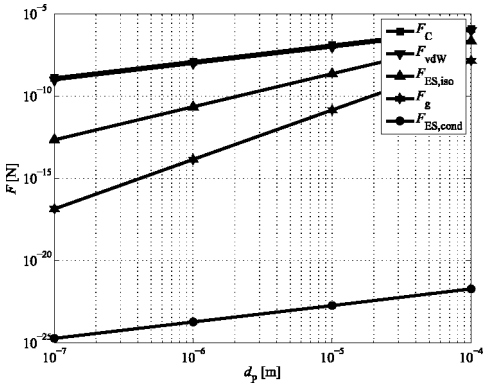

(b) Forces between two limestone particles of identic diameter for $\theta_s = 5°$.

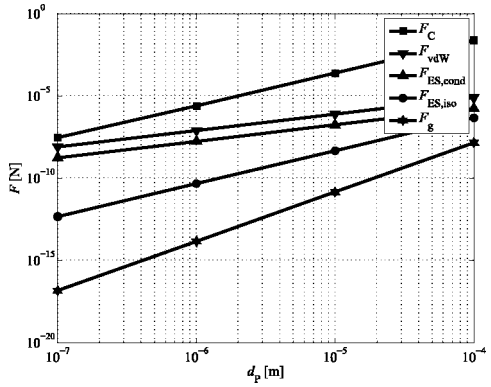

(c) Forces of a particle in contact with the wall for $\theta_s = 20°$.

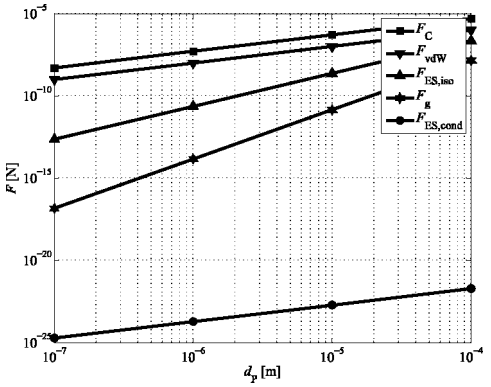

(d) Forces between two limestone particles of identic diameter for $\theta_s = 20°$.

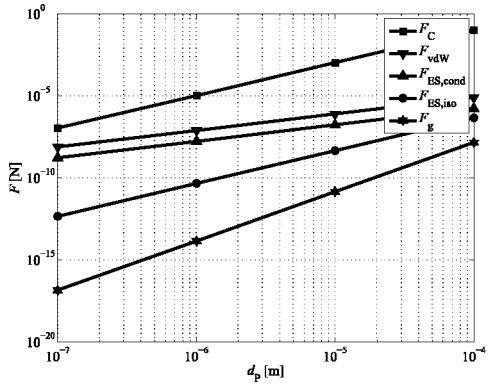

(e) Forces of a particle in contact with the wall for $\theta_s = 45°$.

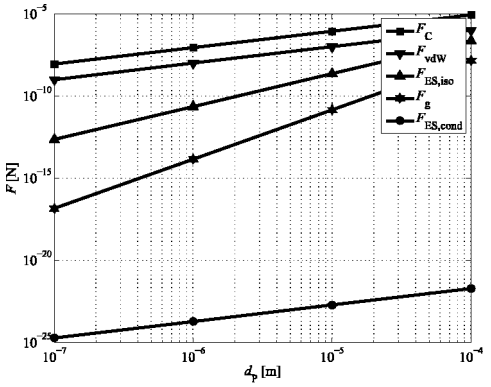

(f) Forces between two limestone particles of identic diameter $\theta_s = 45°$.

Figure 4.4: *Comparison of adhesion forces: F_{vdW}, van der Waals force ($\hbar\varpi = 6.28 \times 10^{-19}$ J for limestone particle-steel wall contact and $\hbar\varpi = 1.59 \times 10^{-19}$ J for limestone particle-particle contact), F_C, capillary force (for θ_s=5, 20 and 45° and a relative humidity of 50%), electrostatic force ($F_{es,iso}$ for an insulator and $F_{es,cond}$ for a conductor, for a contact electrical potential of $V_e = 0.7$ V and a surface charge of $\phi_e = 1.6 \times 10^{-5}$ C/m^2) and F_g, gravity ($\rho_P = 2770$ kg/m^3) at a contact distance of $z_0 = 0.4$ nm.*

For the particle-wall contact, the capillary force is theoretical 3 times larger than the van der Waals force for a wetting angle $\theta_s = 5°$ and a particle of 0.1 μm in diameter. For particles larger than 1 μm, the capillary force is negligible.

However, most of the situations are instable, since the the wetting angle will be in practice much smaller than the one needed for this stable situation ($\theta_s = [40 - 45]\,°$, as discussed in Sec. 4.1.3.1). For all other forces, it is clear that the van der Waals force is dominant over the whole range of diameters considered. It is a factor five larger than the maximal possible electrostatic force (i.e for a conductor) and at least two orders of magnitude larger than gravity. For a larger value of the wetting angle $\theta_s = 20°$, the capillary force is dominant over whole the particle diameter range.

In case of the particle-particle contact, the capillary force seems to be dominant, however it is still in the same order of magnitude as the van der Waals force for a wetting angle of $\theta_s = 5°$. The contact force between conductors is over 10 orders of magnitude smaller than those between isolating materials, from which the latter one becomes comparable to the van de Waals force for particles of 100 μm, which is a factor two larger than the maximal particle size of the feed. Also between particles, the gravity is negligible small. A higher relative humidity leads to a smaller capillary force as is demonstrated in Fig. 4.5. The explanation for this behaviour is that with increasing ratio p/p_s, the pressure in Eq. (4.30b) decreases. However, vapour adsorption at the particle's and wall's surface might occur and therefore the water film thickness will change with increasing humidity.

From the considerations made, the particle-wall contact force will be further considered to be based on van der Waals forces only in this thesis. Also capillary forces could play a role in the contact between a particle and wall on the one side and between particles on the other side, but are neglected for simplicity and because the relative humidity during the experiments never exceeded the critical value of 50%. Electrostatic forces and gravity are small, without exception.

4.2 Fluid-Dynamic Forces

Since the particle's movement through the flow field is described with the Euler-Lagrange particle tracking model (see Ch. 8), which is based on Newtons 2nd law of motion, analytical expressions for relevant forces are implemented into the ANSYS Fluent 13.0 simulations if needed by user defined functions (UDF). An overview of possible forces and a comparison of their magnitudes is given in the following sections.

4.2.1 Drag Force

For the calculation of the drag force two situations are distinguished:

a. if a particle is far away enough from the wall, standard equations for the drag force as implemented in ANSYS Fluent 13.0 are used;

b. a particle in contact with the wall will approximately behave like being in a shear flow. Therefore, models from literature are introduced and calculated with UDFs.

Both situations are discussed in the following two paragraphs.

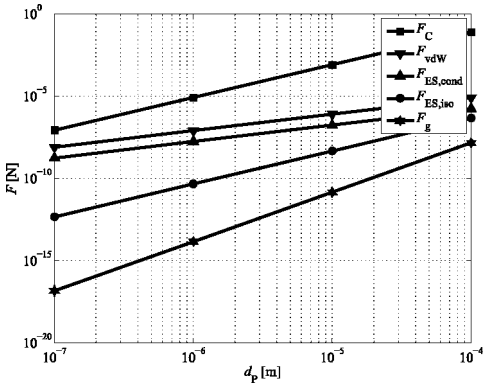

(a) Particle-surface, $RH = 10\%$.

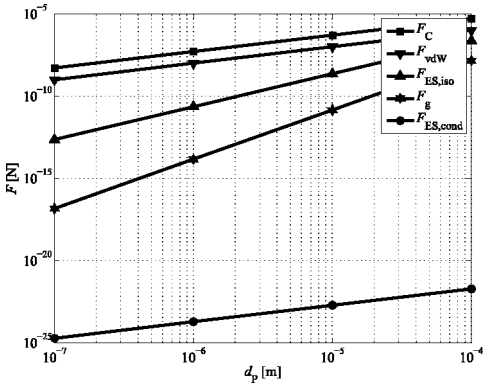

(b) Particle-particle, $RH = 10\%$.

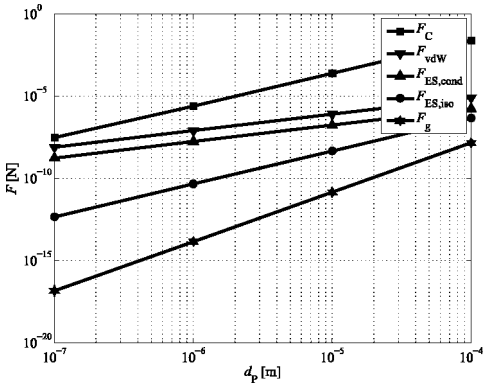

(c) Particle-surface, $RH = 50\%$.

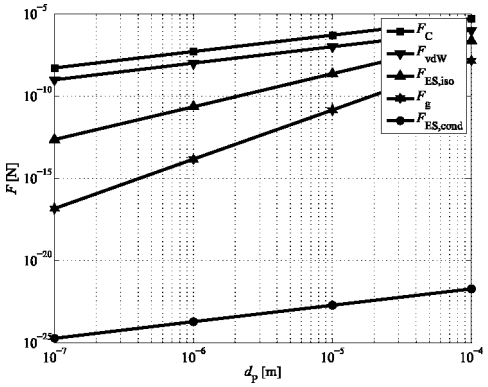

(d) Particle-particle, $RH = 10\%$.

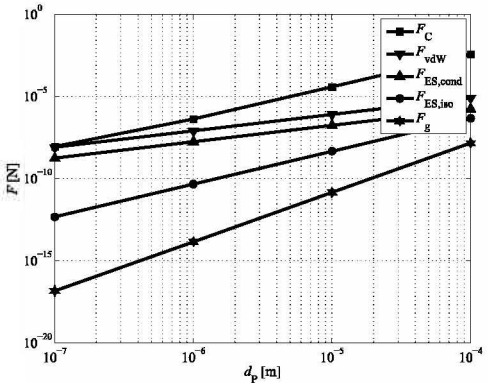

(e) Particle-surface, $RH = 90\%$.

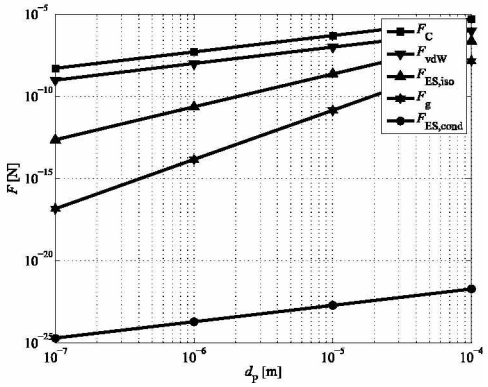

(f) Particle-surface, $RH = 90\%$.

Figure 4.5: *Comparison of adhesion forces: F_{vdW}, van der Waals force ($\hbar\varpi = 6.28 \times 10^{-19}$ J for limestone particle-steel wall contact and $\hbar\varpi = 1.59 \times 10^{-19}$ J for limestone particle-particle contact), F_{C}, capillary force (for $\theta_{\mathrm{S}} = 20°$ and a relative humidity of 10%, 50% and 90%), electrostatic force ($F_{\mathrm{es,iso}}$ for an insulator and $F_{\mathrm{es,cond}}$ for a conductor) (for a contact electrical potential of $V = 0.7$ V and a surface charge of $\phi = 1.6 \times 10^{-5}$ C/m^2) and F_{g} gravity ($\rho_{\mathrm{P}} = 2770$ kg/m^3) at a contact distance of $z_0 = 0.4$ nm.*

4.2.1.1 Drag Force in the Core Region

In ANSYS Fluent 13.0 [39] the drag force is given by the following expression

$$\vec{F}_{\mathrm{D}} = \frac{18\mu_{\mathrm{g}}}{\rho_{\mathrm{P}} d_{\mathrm{p}}^2} \frac{C_{\mathrm{D}} \mathrm{Re}_{\mathrm{P}}}{24}, \tag{4.46}$$

where, Re_{P} is the relative particle Reynold number, which is defined as:

$$\mathrm{Re}_{\mathrm{P}} = \frac{\rho_{\mathrm{g}} d_{\mathrm{P}} \left| w_{\mathrm{P}} - u_{\mathrm{g}} \right|}{\mu_{\mathrm{g}}}. \tag{4.47}$$

The drag coefficient for perfect spherical particles is given by:

$$C_{\mathrm{D}} = a_1 + \frac{a_2}{\mathrm{Re}_{\mathrm{P}}} + \frac{a_3}{\mathrm{Re}_{\mathrm{P}}^2}, \tag{4.48}$$

where, the values of a_1, a_2 and a_3 are given by Morsi and Alexander [103] as a function of Re_{P}, whose value has to be in the range of $0.1 - 5 \times 10^4$.

For non-spherical particles, i.e. the sphericity, ϕ, is smaller than unity, ANSYS Fluent 13.0 uses the following expression from Haider and Levenspiel [55]

$$C_{\mathrm{D}} = \frac{24}{\mathrm{Re}_{\mathrm{P}}} \left(1 + b_1 {\mathrm{Re}_{\mathrm{P}}}^{b_2}\right) + \frac{b_3 \mathrm{Re}_{\mathrm{P}}}{b_4 + \mathrm{Re}_{\mathrm{P}}}, \tag{4.49}$$

where, b_{1-4} are functions of the sphericity, which are found in the literature [39, 55]:

$$b_1 = \exp\left(2.3288 - 6.4581\phi + 2.4486\phi^2\right), \tag{4.50a}$$
$$b_2 = 0.0964 + 0.5565\phi, \tag{4.50b}$$
$$b_3 = \exp\left(4.905 - 13.8944\phi + 18.4222\phi^2 - 10.2599\phi^3\right), \tag{4.50c}$$
$$b_4 = \exp\left(1.4681 + 12.2584\phi - 20.7322\phi^2 + 15.8855\phi^3\right). \tag{4.50d}$$

The ranges of sphericities and particle Reynolds numbers for which Eq. (4.49) is valid are

$$0 < \mathrm{Re}_{\mathrm{P}} < 2.6 \times 10^5 \tag{4.51a}$$
$$0.026 < \phi < 1. \tag{4.51b}$$

The sphericity of a particle is defined to Wadell as the ratio between the real particle's surface, A_{S} and the surface of a sphere with the same volume, A_{s} [5]

$$\phi = \frac{A_{\mathrm{s}}}{A_{\mathrm{S}}}. \tag{4.52}$$

Gronald [53] measured a value of 0.8 for the sphericity for the limestone particles, which are from the same brand as used in the experiments in this thesis.

4.2.1.2 Drag Force near the Wall

Abd-Elhady [1] gives the following equation for a particle resting on a flat plate in a cross flow

$$F_{\mathrm{D,AW}} = C_{\mathrm{D}} \frac{\rho_{\mathrm{g}}}{16} u_{\mathrm{g,t}} d_{\mathrm{P}}^2, \tag{4.53}$$

where, the tangential fluid velocity, $u_{\mathrm{g,t}}$, has to be determined at a distance of one particle radius from the wall. The drag coefficient is a function of the particle Reynolds number according to Al-Hayes and Winterton (who actually recommended it for bubbles) [4]

$$C_{\mathrm{D}} = \begin{cases} 1.22 & 20 < \mathrm{Re_P} < 400, \\ {}^{24}/_{\mathrm{Re_P}} & 4 < \mathrm{Re_P} < 20\ . \end{cases} \tag{4.54}$$

The lower value for the domain of $\mathrm{Re_P}$, for which Eq. (4.54) is valid, should not be taken too strictly since it equals the theoretical viscous drag on a solid, spherical particle [4].

Another function for the drag force in a shear flow is provided by O'Neill [116] and Goldman et al. [45]

$$F_{\mathrm{D,ON}} = 6\pi\mu_{\mathrm{g}} \left(\frac{\mathrm{d}u_{\mathrm{g,t}}}{\mathrm{d}\vec{n}} \right) \frac{d_{\mathrm{P}}^2}{4} f \tag{4.55}$$

$$T_{\mathrm{D,ON}} = -4\pi\mu_{\mathrm{g}} \left(\frac{\mathrm{d}u_{\mathrm{g,t}}}{\mathrm{d}\vec{n}} \right) \frac{d_{\mathrm{P}}^3}{8} g, \tag{4.56}$$

where, the dimensionless coefficient of force, f, and couple, g, have a value of 1.7009 and 0.943993, respectively. It should be noticed that the torque in Eq. (4.56) acts independent of the force in Eq. (4.55). From the torque on the particle, $T_{\mathrm{D,ON}}$, it follows that the wall normal position where the drag force acts as a point force is located at a distance of

$$r_{\mathrm{D,T}} = \frac{2g}{3f} d_{\mathrm{P}} \approx 0.19 d_{\mathrm{P}} \tag{4.57}$$

from the wall. Therefore, the total effective arm is

$$r_{\mathrm{D}} = r + r_{\mathrm{D,T}} \approx 1.4 r_{\mathrm{P}} = 0.7 d_{\mathrm{P}}, \tag{4.58}$$

which is also used by several other authors [71, 130, 132, 156].

Goldman et al. [45] give values for the dimensionless drag force and moment on a particle in a shear flow as function of the ratio of particle-wall distance and diameter, ${}^{h}/_{r_{\mathrm{P}}}$, which are shown in Tab. 4.3. It should be noticed that for a particle close to the wall, the dimensionless drag force and moment become close to the values of O'Neill [116]:

$$F_{\mathrm{x}}^{\mathrm{s}*}\left({}^{h}/_{r_{\mathrm{P}}} = 0\right) \equiv \frac{F_{\mathrm{x}}^{\mathrm{s}}}{6\pi\mu_{\mathrm{g}} r_{\mathrm{P}} h \frac{\mathrm{d}u_{\mathrm{g,t}}}{\mathrm{d}\vec{n}}} \left({}^{h}/_{r_{\mathrm{P}}} = 0\right) = 1.7005 \approx f, \tag{4.59}$$

$$F_{\mathrm{y}}^{\mathrm{s}*}\left({}^{h}/_{r_{\mathrm{P}}} = 0\right) \equiv \frac{T_{\mathrm{y}}^{\mathrm{s}}}{4\pi\mu_{\mathrm{g}} r_{\mathrm{P}}^3 \frac{\mathrm{d}u_{\mathrm{g,t}}}{\mathrm{d}\vec{n}}} \left({}^{h}/_{r_{\mathrm{P}}} = 0\right) = 0.94399 \approx g. \tag{4.60}$$

Table 4.3: *Dimensionless force and torque on a particle in a shear flow near a wall with, h, the wall distance and* $\alpha = \cosh^{-1}(h/r_P)$*, the bipolar coordinate parameter [45].*

α	h/r_P	F_x^{S*}	F_y^{S*}
∞	∞	1.0000	1.00000
3.0	10.0677	1.0587	0.99981
2.0	3.7622	1.1671	0.99711
1.5	2.3524	1.2780	0.99010
1.0	1.5431	1.4391	0.97417
0.5	1.1276	1.6160	0.95374
0.3	1.0453	1.6682	0.94769
0.1	1.005004	1.6969	0.94442
0.08	1.003202	1.6982	0.94427
0	1.0000	1.7005	0.94399

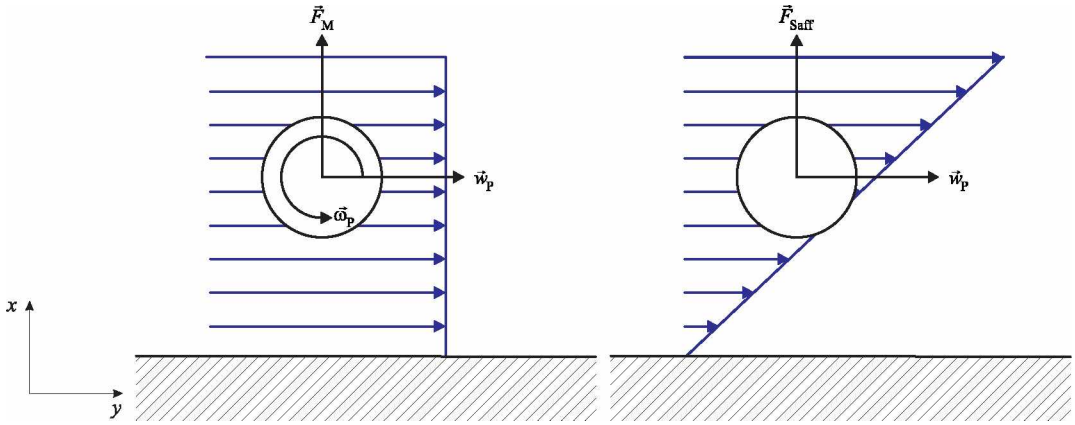

(b) Magnus force for a particle rotating in a uniform flow.

(c) Saffman force for a particle in a flow with a velocity gradient.

Figure 4.6: *Magnus and Saffman force working on a particle.*

4.2.2 Centrifugal Force

A particle rotating on a circle with radius r_i and velocity $w_{P,i}$ experiences a centrifugal force. This force is perpendicular to the particle's path and points outwards. Its magnitude is given by [7]

$$F_z = m_P \frac{w_{P,i}^2}{r_i}. \tag{4.61}$$

The centrifugal force is a fictitious force and the result of the sum of several forces working on a particle. Therefore, extra modelling in ANSYS Fluent 13.0 is not needed.

4.2.3 Magnus Force

At the moment a sphere rotates in an uniform flow profile, it will experience a different relative velocity at its top and its bottom (see Fig. 4.6(b)). Therefore, a pressure difference originates and thus, a lift force perpendicular to the fluid velocity arises. This is the same effect as topspin known from tennis [25]. An expression for laminar, uniform flows (i.e. $Re_P << 1$ and

$\mathrm{Re}_\omega = \frac{\omega_\mathrm{P} d_\mathrm{P}^2}{\nu_\mathrm{g}} << 1$) is given by [147]

$$\vec{F}_\mathrm{M} = k_\mathrm{M} \rho_\mathrm{g} \left(\frac{d_\mathrm{P}}{2}\right)^3 (\vec{\omega_\mathrm{g}} \times \vec{\omega_\mathrm{P}}), \tag{4.62}$$

with

$$k_\mathrm{M} = 0.534 \mathrm{Re}_\omega{}^{-0.64} \mathrm{Re}_\mathrm{P}{}^{0.715}. \tag{4.63}$$

Since, particle rotation is not taken into account in ANSYS Fluent 13.0 in the default settings, the Magnus force has to be modelled using user defined functions (UDFs). Therefore, the particle rotation vector is calculated with a proposal of Brenn et al. [13]

$$\vec{\omega}_\mathrm{P} = \frac{1}{2} \nabla \times \vec{u}_\mathrm{g} + \left(\vec{\omega}_{\mathrm{P},0} - \frac{1}{2} \nabla \times \vec{u}_{\mathrm{g},0}\right) \exp\left(-\frac{60 \mu_\mathrm{g}}{\rho_\mathrm{P} d_\mathrm{P}^2} \Delta t\right), \tag{4.64}$$

where the subscript 0 indicates the values before the time step, Δt. In this thesis, the particles are assumed to enter the the cyclone without rotation and gain their rotation from the rotation of the continuous phase.

4.2.4 Saffman Lift Force

In a shear flow a particle experiences a force due to the difference in static pressure on both sides of the particle. This force is known as the Saffman-lift force [125] and is shown in Fig. 4.6(c). Its magnitude is given by

$$F_\mathrm{Saff} = 1.61 \rho_\mathrm{g} \nu_\mathrm{g}^{1/2} d_\mathrm{P}^2 (u_\mathrm{g} - w_\mathrm{P}) \left|\frac{\mathrm{d}u_\mathrm{g}}{\mathrm{d}x}\right|^{1/2} \mathrm{sgn}\left(\frac{\mathrm{d}u_\mathrm{g}}{\mathrm{d}x}\right), \tag{4.65}$$

with x denoting the wall-normal coordinate direction, being positive when pointing away from the wall. In ANSYS Fluent 13.0, a standard option for the calculation of the Saffman lift force is included.

4.2.5 Lift Force on a Particle in a Shear Flow

Leighton and Acrivos [86] give the following expression for the lift force on a particle touching a wall in a shear flow

$$F_\mathrm{L,LA} = 9.22 \left(\frac{\mathrm{d}u_\mathrm{g,t}}{\mathrm{d}\vec{n}}\right)^2 \frac{\rho_\mathrm{g} d_\mathrm{P}^4}{16}. \tag{4.66}$$

Another equation is given by Cleaver and Yates [23]:

$$F_\mathrm{L,CY} = 60.87 \mu_\mathrm{g} \left(\frac{d_\mathrm{P}}{2}\right)^3 C_\mathrm{E}, \tag{4.67}$$

where, the constant C_E is defined by the following function of the friction velocity

$$C_{\mathrm{E}} \approx 0.01 \frac{u_*^3}{\nu_{\mathrm{g}}^2}. \tag{4.68}$$

Substitution of Eq. (4.68) into Eq. (4.67) finally gives

$$\begin{aligned} F_{\mathrm{L,CY}} &= 0.076 \rho_{\mathrm{g}} \nu_{\mathrm{g}}^2 \left(\frac{d_{\mathrm{P}} u_*}{\nu_{\mathrm{g}}} \right)^3 \\ &= 0.076 \rho_{\mathrm{g}} \sqrt{\nu_{\mathrm{g}}} \left(\frac{\mathrm{d}u_{\mathrm{g,t}}}{\mathrm{d}\vec{n}} \right)^{3/2} d_{\mathrm{P}}^3. \end{aligned} \tag{4.69}$$

When comparing Eq. (4.66) and (4.67), it is noticed that both models differ from their proportionality to the particle diameter and the wall normal gradient of the tangential velocity.

4.2.6 Turbophoresis Force

Turbophoresis forces arise because of the non-uniformity of the turbulent flow field (i.e. because of the gradient in the fluctuating part of the gas velocity). Varaksin [147] gives the following expression:

$$\vec{F}_{\mathrm{Tu}} = -\frac{1}{2} \rho_{\mathrm{P}} \frac{\pi d_{\mathrm{P}}^3}{6} \frac{\mathrm{d}\overline{u'^2_{\mathrm{g,x}}}}{\mathrm{d}x}. \tag{4.70}$$

Turbophoresis dominates the particle's dynamic behaviour in the diffusion-impaction and inertia-moderated regimes [154]. In large eddy simulation turbophoresis is underestimated if subgrid effects are not taken into account. This can be avoided by applying an inverse filtering model [83]. However, this means that turbophorsis is still difficult to predict with a RANS-turbulence model. Furthermore, the particle diameter will in the same order of magnitude as or up to three orders smaller than the Kolmogorov length scale, which is introduced in Eq. (8.82).

4.2.7 Added Mass Force

When a particle is accelerated in respect to its relative velocity in a flow, it will also change the velocity of a certain mass of the surrounding fluid [79]. Since the total momentum should be reserved, this leads to a deceleration of the particle. The force responsible for this phenomena is called the added mass force and is expressed by

$$\vec{F}_{\mathrm{Add}} = \frac{m_{\mathrm{P}}}{2} \left(\frac{\mathrm{d}u_{\mathrm{g}}}{\mathrm{d}t} - \frac{\mathrm{d}w_{\mathrm{P}}}{\mathrm{d}t} \right). \tag{4.71}$$

In one-way coupled Euler-Lagrange simulations, i.e. (quasi) steady state, it is not possible to take the added mass force into account since the acceleration of the fluid is not considered.

4.2.8 Basset Force

The boundary layer around a particle, that is accelerated in a flow, needs some time to get used to the new relative velocity. The viscous effects during this time are described by the

Basset (history) force, whose expression is given by [79]

$$\vec{F}_{\mathrm{Bas}} = \frac{3}{2} d_{\mathrm{P}}^2 \sqrt{\pi \rho_{\mathrm{g}} \mu_{\mathrm{g}}} \int_{t_0}^{t} \frac{\frac{\mathrm{d}u_{\mathrm{g}}}{\mathrm{d}t} - \frac{\mathrm{d}w_{\mathrm{P}}}{\mathrm{d}t}}{\sqrt{t - t'}} \mathrm{d}t'. \tag{4.72}$$

The Basset force vanishes in steady state simulations.

4.2.9 Thermophoretic Force

A particle in a flow with a temperature gradient experiences a force into the colder direction, because the molecules of the carrier gas act more on the heater side. This phenomena is called thermophoresis and is physically described, for particles with low thermal conductivity, λ_{P}, by [147]

$$F_{\mathrm{T}} = -\frac{4.5 \rho_{\mathrm{g}} \nu_{\mathrm{g}}^2 d_{\mathrm{P}} \lambda_{\mathrm{g}}}{T \left(2\lambda_{\mathrm{g}} + \lambda_{\mathrm{P}}\right)} \frac{\partial T}{\partial x}. \tag{4.73}$$

In a flow without temperature gradients, the thermophoretic force disappears because the factor $\frac{\partial T}{\partial x}$ becomes zero for this situation.

4.2.10 Pressure Gradient Force

Similar to the Saffman lift force and the Magnus force, also a particle in any static pressure gradient field will experience a netto force. This pressure gradient force is given by [79]:

$$F_{\mathrm{PG}} = -V_{\mathrm{P}} \nabla p, \tag{4.74}$$

where, V_{P}, is the particle volume.

4.2.11 Gravitational Force and Buoyancy

The gravitational force is given by:

$$\vec{F}_{\mathrm{g}} = \rho_{\mathrm{P}} \frac{\pi}{6} d_{\mathrm{P}}^3 \vec{g}, \tag{4.75}$$

where, $|\vec{g}|$ is the magnitude of the gravitational constant. For a wall with normal vector $\vec{n}$ pointing into the flow field, $\vec{g}$ can be divided into a parallel and normal wall component:

$$g_{\perp} = |\vec{g}| \, \vec{g} \cdot \vec{n}, \tag{4.76a}$$

$$g_{\parallel} = \vec{g} - |\vec{g}| \, \vec{g} \cdot \vec{n}. \tag{4.76b}$$

Buoyancy is calculated similar as is in Eq. (4.75)

$$\vec{F}_{\mathrm{b}} = \rho_{\mathrm{g}} \frac{\pi}{6} d_{\mathrm{P}}^3 \vec{g}, \tag{4.77}$$

which is however neglectable small compared to gravity since the particle density is much larger than the fluid density.

4.2.12 Comparison of Fluid-Dynamic Forces

For a particle in contact with the wall, the Saffman lift force is dominant in wall normal and the drag force in wall tangential direction. Further details are presented in Ch. 11, where the forces are determined by CFD.

An interesting point is that the following fluid-dynamic forces are a function of the wall shear rate $\frac{\mathrm{d}u_{\mathrm{g,t}}}{\mathrm{d}\vec{n}}$:

- the drag forces, both in Eq. (4.53) and (4.55);
- the Saffmann lift force in Eq. (4.65);
- the lift forces in a shear flow in Eq. (4.66) and (4.67).

In a laminar boundary flow this velocity gradient can be expressed as function of the mean velocity of the main flow, $\bar{u}_{\mathrm{g}}$, and the friction coefficient, λ_{s}, [124]

$$\frac{\mathrm{d}u_{\mathrm{g,t}}}{\mathrm{d}\vec{n}} = \frac{\lambda_{\mathrm{s}}}{8}\frac{\bar{u}_{\mathrm{g}}^{\,2}}{\nu_{\mathrm{g}}}. \tag{4.78}$$

The friction coefficient is given by the following function of the solid loading, μ_{e} [107]:

$$\lambda_{\mathrm{s}} = \lambda_0\left(1 + 2\sqrt{\mu_{\mathrm{e}}}\right), \tag{4.79}$$

where, the friction coefficient for a clean gas, λ_0, is a function of the cyclone's Reynolds number and wall roughness and has to be determined from literature [107].

All the forces containing the wall shear rate thus become a function of the solid loading. For increasing solid loading, the magnitude of the drag and lift forces increases as well. For a solid loading up to 0.008 kg/kg, the difference in the friction coefficient is up to 18% compared to that for a clean gas. The drag force according to O'Neill is proportional to the wall shear rate, and thus will vary in the same range. The Lift force according to Leighton and Acrivos (Eq. (4.66)) will differ up to 39% and that of Cleaver and Yates (Eq. (4.69)) up to 28%.

5 Relevant Energies Stored in Particles

A particle travelling through a fluid can have several sources of energy. Kinetic energy is stored in rigid body translation, E_{kin}, or rotation, E_{rot}. Electrostatic energy, $E_{\mathrm{el\,st}}$, is caused by an electromagnetic field in which a particle has a certain charge. This charge can change by collisions between particles or by collisions of a single particle with a wall. Between interfaces, such as a particle and a solid wall, energy is stored in the adhesion energy, E_{ad} (sometimes expressed in term of the van der Waals energy, E_{vdW}), which can be calculated in several ways. Also a certain amount of energy, E_{l}, can be lost into heat due to friction after a collision. If the kinetic energy due to rotation is neglected, the following energy balance is set up for a particle *before* and *after* colliding with a wall, denoted with an index 1 and 2 respectively [90]:

$$E_{\mathrm{kin},1} + E_{\mathrm{el\,st},1} = E_{\mathrm{ad}} + E_{\mathrm{el\,st},2} + E_{\mathrm{l}} \ . \tag{5.1}$$

The single terms in Eq. (5.1) are discussed in the following sections.

5.1 Kinetic Energy

The kinetic energy of a particle with mass, m_{P}, travelling with velocity, $w_{\mathrm{P,i}}$, is given by

$$E_{\mathrm{kin,i}} = \frac{1}{2} m_{\mathrm{P}} w_{\mathrm{P,i}}^2, \tag{5.2}$$

in which the index i indicates if the velocity is before a collision with a wall ($i = 1$) or after ($i = 2$). If the particle is spherical, the mass is expressed by

$$m_{\mathrm{P}} = \frac{\pi}{6} \rho_{\mathrm{P}} d_{\mathrm{P}}^3, \tag{5.3}$$

by which Eq. (5.2) becomes

$$E_{\mathrm{kin,i}} = \frac{\pi}{12} \rho_{\mathrm{P}} d_{\mathrm{P}}^3 w_{\mathrm{P,i}}^2. \tag{5.4}$$

5.2 Rotational Energy

Rotational kinetic energy is expressed by:

$$E_{\mathrm{rot}} = \frac{I_{\mathrm{P}} \omega_{\mathrm{P}}^2}{2}, \tag{5.5}$$

where, I_{P} is the moment of inertia around the axis of rotation and ω_{P}, the angular velocity of the particle.

5.3 Adhesion Energy

The interaction force between a particle and a surface contains two parts [129]:

1. a long-range part that is often described by van der Waals forces and

2. a short-range part describing chemical reactions such as hydrogen bounds [145].

These forces act between an infinite distance and the distance at zero contact (z_0) and can be a function of the distance between the particle and the surface. The work of adhesion performed by these adhesion forces is then described by the following integral

$$W_{\mathrm{ad}} = \int_{z_0}^{\infty} F_{\mathrm{ad}} \mathrm{d}z. \tag{5.6}$$

The work of adhesion can be calculated from the surface energy (for which several models are available to calculate the contact area) or alternatively by using the Lifshitz-van der Waals or Hamaker theory. It is possible to convert the models into each other, but the values of some parameters have considerable uncertainties causing differences in the surface energy larger than one order of magnitude.

5.3.1 Surface Energy

The adhesion energy, E_{ad}, expressed in terms of the work of adhesion per unit area, ΔG, is given by

$$E_{\mathrm{ad}} = \Delta G \pi r_0^2. \tag{5.7}$$

In Eq. (5.7), r_0 represents the contact radius, which is dependent on the nature of the contact and discussed in detail in Ch. 6. Four situations for the calculation of the work of adhesion can be distinguished:

a. adhesion between two different materials in air or vacuo;

b. cohesion of one material in air or vacuo;

c. adhesion between two different materials immersed in a liquid;

d. cohesion of one material immersed in a liquid.

These situations are discussed in detail below.

5.3.1.1 Two Different Materials in Air or Vacuo

The total interaction energy between two materials in air or a vacuo consists out of an apolar Lifshitz van der Waals part ($\Delta G_{12}^{\mathrm{LW}}$) and a polar acid-base part ($\Delta G_{12}^{\mathrm{AB}}$) as already introduced in Eq. (4.3) [144]:

$$\Delta G_{12}^{\mathrm{tot}} = \Delta G_{12}^{\mathrm{LW}} + \Delta G_{12}^{\mathrm{AB}}. \tag{5.8}$$

In Eq. (5.8), the Lifshitz van der Waals and the acid-base part are respectively given by

$$\Delta G_{12}^{\mathrm{LW}} = \gamma_{12}^{\mathrm{LW}} - \gamma_1^{\mathrm{LW}} - \gamma_2^{\mathrm{LW}}, \tag{5.9}$$

$$\Delta G_{12}^{\mathrm{AB}} = -2\left(\sqrt{\gamma_1^+\gamma_2^-} + \sqrt{\gamma_1^-\gamma_2^+}\right). \tag{5.10}$$

Here, the term $\gamma_{12}^{\mathrm{LW}}$ is computed from

$$\begin{aligned}\gamma_{12}^{\mathrm{LW}} &= \left(\sqrt{\gamma_1^{\mathrm{LW}}} - \sqrt{\gamma_2^{\mathrm{LW}}}\right)^2 \\ &= \gamma_1^{\mathrm{LW}} + \gamma_2^{\mathrm{LW}} - 2\sqrt{\gamma_1^{\mathrm{LW}}\gamma_2^{\mathrm{LW}}}.\end{aligned} \tag{5.11}$$

In Eq. (5.11), γ_1^{LW} and γ_2^{LW} are the Lifshitz van der Waals contributions to the surface tensions of the materials in contact and $\gamma_{12}^{\mathrm{LW}}$ that of the interface between the materials 1 and 2.

The polar part, which contains an electron-acceptor, γ_i^+ and an electron-donor, γ_i^+, can be written as:

$$\Delta G_{12}^{\mathrm{AB}} = \gamma_{12}^{\mathrm{AB}} - \gamma_1^{\mathrm{AB}} - \gamma_2^{\mathrm{AB}}, \tag{5.12}$$

where, the contribution of the interface has already been introduced in Eq. (4.17) and those of both, pure materials in Eq. (4.18) and (4.19).

After combining Eq. (5.8)-(5.11), (4.17), (4.18) and (4.19), the total free energy of adhesion is finally written as

$$\begin{aligned}\Delta G_{12}^{\mathrm{tot}} &= \gamma_{12}^{\mathrm{tot}} - \gamma_1^{\mathrm{tot}} - \gamma_2^{\mathrm{tot}} \\ &= -2\left(\sqrt{\gamma_1^{\mathrm{LW}}\gamma_2^{\mathrm{LW}}} + \sqrt{\gamma_1^+\gamma_2^-} + \sqrt{\gamma_1^-\gamma_2^+}\right).\end{aligned} \tag{5.13}$$

All material parameters used in Eq. (5.13) for limestone, steel and water are given in Tab. 4.1.

5.3.1.2 One Material in Air or Vacuo

The cohesion of one single material in air of vacuo follows from Eq. (5.13), where in this case the index 2 equals the index 1:

$$\begin{aligned}\Delta G_{11}^{\mathrm{tot}} &= -2\left(\gamma_1^{\mathrm{LW}} + 2\sqrt{\gamma_1^+\gamma_1^-}\right) \\ &= -2\left(\gamma_1^{\mathrm{LW}} + \gamma_1^{\mathrm{AB}}\right).\end{aligned} \tag{5.14}$$

5.3.1.3 Two Different Materials Immersed in a Liquid

When a small layer of water forms an interface (indicated by the index 3) between the limestone particle and the steel wall, Eq. (5.8) becomes

$$\Delta G_{132}^{\mathrm{tot}} = \Delta G_{132}^{\mathrm{LW}} + \Delta G_{132}^{\mathrm{AB}}, \tag{5.15}$$

where the two terms are given by

$$\Delta G_{132}^{LW} = \gamma_{12}^{LW} - \gamma_{13}^{LW} - \gamma_{23}^{LW}, \tag{5.16}$$

$$\Delta G_{132}^{AB} = \gamma_{12}^{AB} - \gamma_{13}^{AB} - \gamma_{23}^{AB}. \tag{5.17}$$

After calculating γ_{ij}^{LW} and γ_{ij}^{AB} as in Eq. (5.11) and (4.17) for all combinations of i and j, an explicit function for ΔG_{132}^{tot} is found [143]

$$\begin{aligned}\Delta G_{132}^{tot} = 2\Big[&\sqrt{\gamma_1^{LW}\gamma_3^{LW}} + \sqrt{\gamma_2^{LW}\gamma_3^{LW}} - \sqrt{\gamma_1^{LW}\gamma_2^{LW}} - \gamma_3^{LW} \\ &+\sqrt{\gamma_3^+}\left(\sqrt{\gamma_1^-} + \sqrt{\gamma_2^-} - \sqrt{\gamma_3^-}\right) \\ &+\sqrt{\gamma_3^-}\left(\sqrt{\gamma_1^+} + \sqrt{\gamma_2^+} - \sqrt{\gamma_3^+}\right) - \sqrt{\gamma_1^+\gamma_2^-} - \sqrt{\gamma_1^-\gamma_2^+}\Big].\end{aligned} \tag{5.18}$$

5.3.1.4 One Material Immersed in a Liquid

After substitution of $\gamma_2^{LW} = \gamma_1^{LW}$, $\gamma_2^+ = \gamma_1^+$ and $\gamma_2^- = \gamma_1^-$ in Eq. (5.18), the cohesion of one single material in a fluid is found. Its expression reads:

$$\begin{aligned}\Delta G_{131}^{tot} &= -2\gamma_{131}^{tot} \\ &= -2\left(\sqrt{\gamma_1^{LW}} - \sqrt{\gamma_3^{LW}}\right)^2 - 4\left(\sqrt{\gamma_1^+\gamma_1^-} + \sqrt{\gamma_3^+\gamma_3^-} - \sqrt{\gamma_1^+\gamma_3^-} - \sqrt{\gamma_1^-\gamma_3^+}\right).\end{aligned} \tag{5.19}$$

5.3.1.5 Comparison of the Free Energy of Adhesion for Several Systems

Using the data from Tab. 4.1, the specific surface energies for the four systems are calculated and summarised in Tab. 5.1. It should be noticed that the influence of water as interface is much larger than that of the materials in contact, which increases only slightly for the limestone-limestone system compared to limestone-steel.

The total free energy of cohesion of limestone in a dry environment (i.e. the sum of the van der Waals and acid base parts), ΔG_{11}^{tot}, is 14.8% larger than the adhesion between limestone and steel, ΔG_{12}^{tot}. With water as interface, this difference becomes -5.9% from the ratio between ΔG_{131}^{tot} and ΔG_{132}^{tot} and thus negative.

The cohesion of limestone decreases with 75.7%, when a sheet of water forms an interface. The adhesion between limestone and steel increases with 90.3% with water as interface, compared to the contact in air or vacuo.

For the contribution of the Lifshitz van der Waals and the acid-base part to the total free energy of adhesion, it is clear from the data in Tab. 4.1 that in air or vacuo the Lifshitz van der Waals part is dominant and in a moist environment the acid-base part.

5.3.1.6 Hamaker Approach

The free energy of adhesion between a spherical particle and a flat wall can also be expressed as function of the Hamaker-constant in air or in a vacuo, A_{11}, by the following expression [56, 144]:

Table 5.1: *Free energy of adhesion for the systems limestone-limestone and limestone-steel for vacuo/air and water as interface.*

	air/vacuo	water
limestone-steel	$\Delta G_{12}^{\text{tot}} = -91.3\ \text{mJ/m}^2$ $\Delta G_{12}^{\text{LW}} = -79.9\ \text{mJ/m}^2$ $\Delta G_{12}^{\text{AB}} = -11.4\ \text{mJ/m}^2$	$\Delta G_{132}^{\text{tot}} = -27.1\ \text{mJ/m}^2$ $\Delta G_{132}^{\text{LW}} = -5.4\ \text{mJ/m}^2$ $\Delta G_{132}^{\text{AB}} = -21.7\ \text{mJ/m}^2$
limestone-limestone	$\Delta G_{11}^{\text{tot}} = -104.8\ \text{mJ/m}^2$ $\Delta G_{11}^{\text{LW}} = -85.2\ \text{mJ/m}^2$ $\Delta G_{11}^{\text{AB}} = -19.5\ \text{mJ/m}^2$	$\Delta G_{131}^{\text{tot}} = -25.5\ \text{mJ/m}^2$ $\Delta G_{131}^{\text{LW}} = -6.9\ \text{mJ/m}^2$ $\Delta G_{131}^{\text{AB}} = -18.6\ \text{mJ/m}^2$

$$\begin{aligned} \Delta G_{11}^{\text{LW}}(z_0) &= -2\gamma_1^{\text{LW}} \\ &= -\frac{A_{11}}{12\pi}\frac{1}{z_0^2} \end{aligned} \tag{5.20}$$

in which z_0 is the distance at zero contact, which is constant and has a value around 4.0×10^{-10} m [102]. Other ratios between A_{11} and γ_1^{LW} for liquids are given by [144]:

$$\frac{A_{11}}{\gamma_{11}^{\text{LW}}} = \text{const.} = 3.01 \times 10^{-18}\ \text{m}^2, \tag{5.21a}$$

$$\frac{A_{11}}{\gamma_{11}^{\text{LW}}} = \text{const.} = 1.51 \times 10^{-18}\ \text{m}^2. \tag{5.21b}$$

From these ratios, smaller values for z_0 of respectively 2.0×10^{-10} m and 1.4×10^{-10} follow after substitution in Eq. (5.20).

The calculation of the combined Hamaker constant between two materials, A_{12}, can be made within an accuracy of 5% from the following equation [81, 148]

$$A_{12} = \sqrt{A_{11}A_{22}}. \tag{5.22}$$

The Hamaker constant between two materials and an interface follows from

$$A_{132} = \left(\sqrt{A_{11}} - \sqrt{A_{33}}\right)\left(\sqrt{A_{22}} - \sqrt{A_{33}}\right), \tag{5.23}$$

which can be simplified by introducing a correction factor c (which equals 1.6 for water) in the following expression [148]

$$A_{132} = c\left(A_{12} + A_{33} - A_{13} - A_{23}\right). \tag{5.24}$$

Here, A_{132} can be simplified if material 1 equals material 3, resulting in similar equations as Eq. (5.23) and Eq. (5.24)

$$A_{131} = \left(\sqrt{A_{11}} - \sqrt{A_{33}}\right)^2, \tag{5.25}$$

$$A_{131} = c\left(A_{11} + A_{33} - 2A_{13}\right). \tag{5.26}$$

The Hamaker constant is converted to the Lifshitz-van der Waals constant, $\hbar\varpi$, and van der Waals pressure, $p"_{\mathrm{vdW}}$, by the following equations [149]

$$\hbar\varpi = \frac{4\pi}{3}A, \tag{5.27}$$

$$p"_{\mathrm{vdW}} = \frac{A}{6\pi z_0^3}. \tag{5.28}$$

5.3.1.7 Lifshitz Approach

For materials, for which optical data are available, the Liftshitz-van der Waals constant, $\hbar\varpi$ can be calculated from experimental data. For two bodies of material 1 and 2, included in a third medium 3, $\hbar\varpi$ is calculated from [81]

$$\hbar\varpi = \hbar\int_0^\infty \frac{\epsilon_1(i\xi)-\epsilon_3(i\xi)}{\epsilon_1(i\xi)+\epsilon_3(i\xi)}\cdot\frac{\epsilon_2(i\xi)-\epsilon_3(i\xi)}{\epsilon_2(i\xi)+\epsilon_3(i\xi)}, \tag{5.29}$$

where

$$\epsilon_{\mathrm{i}}(i\xi) = 1+\frac{2}{\pi}\int_0^\infty \frac{\epsilon_{\mathrm{i}}"(\omega)\,\omega\mathrm{d}\omega}{\xi^2+\omega^2}. \tag{5.30}$$

$\epsilon_{\mathrm{i}}"$ is the imaginary part of the complex dielectric constant, ω is the angular frequency of photon energy $E=\hbar\omega$ and $\hbar\equiv\frac{h_{\mathrm{P}}}{2\pi}$, i.e. Planck's constant, h_{P}, divided by the factor 2π.

5.3.2 Van der Waals Energy without Deformation

Löffler and Muhr [90] give an expression for particles with a small deformation in respect to their radius. The change in the van der Waals energy is found by integrating the product of the van der Waals pressure, $p"_{\mathrm{vdW}}$, and deformed area, A_{def}, over the distance to the wall z, i.e. the result equals the amount of work acted by the van der Waals force:

$$E_{\mathrm{vdW}} = \int_{z_0}^\infty p"_{\mathrm{vdW}}A_{\mathrm{def}}\mathrm{d}z. \tag{5.31}$$

As can be noticed, Eq. (5.31) is integrated between the distance at contact, z_0, and an infinite large distance from the wall. If the deformation is assumed only to be caused by van der Waals forces, the contact area equals

$$A_{\mathrm{def}} = \pi r_0^2 = \frac{F_{\mathrm{vdW},0}}{p_{\mathrm{pl}}}, \tag{5.32}$$

with, p_{pl}, the plastic yield stress of the softer material, i.e. limestone in case of limestone-steel contact. The van der Waals attractive force reads as already introduced in Eq. (4.15b)

$$F_{\mathrm{vdW},0} = \frac{\hbar\varpi}{16\pi z_0^2}d_{\mathrm{P}}. \tag{5.33}$$

as already defined in Eq. (4.15b). After combining Eq. (5.31)-(5.33) the van der Waals energy between a flat plate and a not deformed sphere is given by

$$E_{\mathrm{vdW},0} = \frac{\hbar\varpi^2 d_{\mathrm{P}}}{256\pi^3 z_0^4 p_{\mathrm{pl}}}. \tag{5.34}$$

Table 5.2: *Material properties of limestone, steel and water [58, 84, 101, 110, 122, 140, 151].*

	value			unit
	limestone	*steel*	*water*	
$\hbar\varpi$	1.59×10^{-19}	6.28×10^{-19} [a]		J
p_{pl}	3.5×10^{8}			$\mathrm{N\,m^{-2}}$
z_0	4.0×10^{-10}			m
ρ_{P}	2.770×10^{3}			$\mathrm{kg\,m^{-3}}$
Y	$3 \times 10^{10} - 1.50 \times 10^{11}$ [b]	1.5×10^{11}		$\mathrm{N\,m^{-2}}$
ν	0.25-0.28 [b]	0.25		[-]
γ^{LW}	42.62	37.24	21.8	$\mathrm{mJ\,m^{-2}}$
γ^{+}	1.64	6×10^{-2}	25.5	$\mathrm{mJ\,m^{-2}}$
γ^{-}	14.52	13.94	25.5	$\mathrm{mJ\,m^{-2}}$
ϵ_0	8.85×10^{-12}			$\mathrm{As\,(Vm)^{-1}}$
ϵ_{r}	7.7	3.00×10^{2}		[-]
ρ_{q}	$1 \times 10^{7} - 1 \times 10^{12}$ [b]	9.7×10^{-8}		Ωm

[a] Value from contact between limestone and metals [101].
[b] Mean values used in simulations: $Y = 9.0 \times 10^{10}\ \mathrm{N\,m^{-2}}$; $\nu = 0.265$; $\rho_{\mathrm{q}} = 5.0 \times 10^{11}\ \Omega$m.

A correction factor is proposed by Dahneke [29] to take the deformation of a particle into account. This factor is discussed in detail in Ch. 6.

5.3.3 Van der Waals Energy with Deformation

If the change in contact area due to deformation during impact is considered, the contact area in Eq. (5.32) becomes [14]:

$$\pi r_0^2 = \pi d_{\mathrm{P}} \cdot h, \tag{5.35}$$

where the depth of penetration, h, is assumed to be much smaller than the particle diameter. The energy needed for the deformation is found by integrating the product of the yield stress and area between 0 and the plastic deformed height, h_{pl}

$$\begin{aligned} E_{\mathrm{pl}} &= \int_0^{h_{\mathrm{pl}}} p_{\mathrm{pl}} \pi d_{\mathrm{P}} \cdot h \mathrm{d}h \\ &= \frac{1}{2} p_{\mathrm{pl}} \pi d_{\mathrm{P}} h_{\mathrm{pl}}^2. \end{aligned} \tag{5.36}$$

If the deformation is only plastic and no other forces but van der Waals play a role, the depth of penetration is equated from the equilibrium between the plastic van der Waals energy and the kinetic energy excluding the energy loss of the elastic deformation:

$$h_{\mathrm{pl}} = \sqrt{1 - e_{\mathrm{pl}}^2}\, w_{\mathrm{P},1} d_{\mathrm{P}} \sqrt{\frac{\rho_{\mathrm{P}}}{6 p_{\mathrm{pl}}}} \tag{5.37}$$

Here, e_{pl} is the coefficient of restitution, which is discussed in Sec. 5.5. From Eq. (5.37) it

is obvious that the van der Waals energy becomes a function of the impact velocity:

$$E_{\mathrm{vdW}} = \frac{\hbar\varpi}{16\pi z_0^2} d_{\mathrm{P}}^2 \sqrt{\frac{\rho_{\mathrm{P}}}{6p_{\mathrm{pl}}}} w_{\mathrm{P},1} \left(1 - e_{\mathrm{pl}}^2\right)^{1/2}. \tag{5.38}$$

5.4 Electrostatic Energy

The electrostatic energy before and after collision can be expressed according to Israelachvilli [74] as

$$E_{\mathrm{el\,st},1} = \frac{q_{\mathrm{P},1}^2}{16\pi\epsilon_0 l_0} \tag{5.39}$$

and

$$E_{\mathrm{el\,st},2} = \frac{q_{\mathrm{P},2}^2}{16\pi\epsilon_0 \left(z_0 + \frac{d_{\mathrm{P}}}{2}\right)}, \tag{5.40}$$

respectively, in which $q_{\mathrm{P,i}}$ are the particle charges, ϵ_0 is the relative permittivity and l_0 the distance between the particle's centre and the wall before collision. It may be obvious, that the distance of a particle sticking on the wall ($\frac{d_{\mathrm{P}}}{2} + z_0$) will be much smaller than l_0 and only the particle charge after impact is needed for the calculation of the netto change in the electrostatic energy. By stating this, $E_{\mathrm{el\,st},1} << E_{\mathrm{el\,st},2}$ in Eq. (5.1). Several models to calculate the particle charge *before* and *after* collision are given in Tab. 4.2.

5.5 Energy Loss after Collision

The energy loss in Eq. (5.1) can be eliminated after introduction of the plastic coefficient of restitution, e_{pl}, which is defined as:

$$e_{\mathrm{pl}}^2 = \frac{E_{\mathrm{kin},1} - E_{\mathrm{l}}}{E_{\mathrm{kin},1}}, \tag{5.41}$$

where, E_{l}, is the energy loss due to plastic deformation and friction. Since a particle in contact with a wall also contains a certain amount of stored elastic, adhesion energy, E_{ad} , the elastic coefficient of restitution, e_{a}, which is a function of e_{pl}, is introduced:

$$e_{\mathrm{a}}^2 = \frac{E_{\mathrm{ad}}}{E_{\mathrm{kin}}} = f(e_{\mathrm{pl}}). \tag{5.42}$$

Then, the total coefficient of restitution, e, follows from combination of Eq. (5.41) and (5.42) [60]:

$$\begin{aligned} e^2 &= e_{\mathrm{pl}}^2 - e_{\mathrm{a}}^2(e_{\mathrm{pl}}) \\ &= e_{\mathrm{pl}}^2 - \frac{E_{\mathrm{a}}}{E_{\mathrm{kin},1}}. \end{aligned} \tag{5.43}$$

From Eq. (5.43), it is clear that the total coefficient of restitution is always smaller than the plastic coefficient of restitution.

Heinl and Bohnet use a value of $e = 0.9$, which is in same order of magnitude as the measurements of Imre et al. [73], who performed experiments with steel balls dropped at limestone plates. Furthermore, sometimes the normal differs from the tangential coefficient of restitution.

Löffler [89] gives values for e_{pl} for particles between 1.0 and 15 μm in diameter. The values are based on measurements of quartz particles impacting at a plain surface respectively made off steel, Polyvinylchlorid and Polyamid. Also measurements of limestone particles impacting at Polyamid are available. All values for e_{pl} are in the range of 0.37-0.61, where a negative correlation between e_{pl} and d_{P} seems to exist. The material of the plain surface does not have a significant contribution to the value of the plastic coefficient of restitution, hence the values for the contact between limestone and Polyamid will not differ from those between limestone and steel. Significant quantities influencing e_{pl} are within the microstructure of the particle and surface, such as a dirty surface, the surface roughness, or existing layers of deposits.

In this thesis the value of 0.5 for e_{pl} will be further used, which is the mean value of the range mentioned by Löffler [88].

5.6 Comparison of Energies

The van der Waals and surface energies are compared with the kinetic energy for impact velocities of 0.1, 1 and 10 m/s in Fig. 5.1(a). The contact radius used for the determination of E_{s} in Eq. (5.7) is calculated from the adhesion map, which is introduced in Ch. 6. The adhesion energies are scaled to the kinetic energy.

The dependency of this dimensionless adhesion energy on the particle diameter is smallest for E_{vdW}, for which it is proportional to d_{P}^{-1}. For E_{s} and $E_{\mathrm{vdW,0}}$, it decreases faster for increasing particle diameter. For three typical particle impact velocities, the following behaviour for the adhering energies is observed:

- For a small impact velocity of 0.1 m/s, the adhering energy of E_{vdW} and $E_{\mathrm{vdW,0}}$ are in the range of E_{kin} but only for small particle diameters; for the last one, it drops fast for particles larger than 1 μm.
- For a medium impact velocity of 1 m/s, only E_{s} becomes larger than E_{kin}, but only for submicron particles.
- For a high impact velocity of 10 m/s, all adhering energies are significantly smaller than the kinetic energy.

Summarised, only small particles with low impact velocities tend to deposit as a consequence of the adhering energy.

When the differences in the electrostatic energy before and after collision are compared with the kinetic energy of the impacting particle in Fig. 5.1(b), it appears that the prediction according Matsuyama and Yamamoto [97] is only little dependent on the particle diameter. The relative electrostatic energy in the model of Derjaguin [34] increases for an increasing particle size, in contrast to the model of Lianze et al. [91], which furthermore predicts much smaller values. Summarising:

a. Only large particles, that impact with a low velocity, have a ratio of electrostatic to kinetic energy close to unity. Knowing this and the fact, that the test cyclone was earthed during experiments, the influence of electrostatics will be further neglected.

b. Since the electrostatic energy will be further neglected and for particles larger than 1 μm the adhesive energy is smaller than the kinetic energy for the whole range of impact velocities, it has to be compensated by a relative low coefficient of restitution to give a physical realistic view of particle deposition as observed in the experiments.

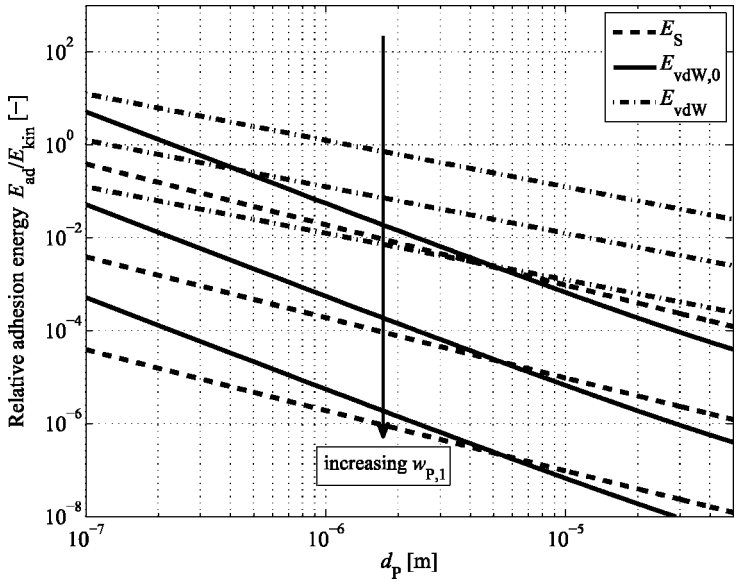

(a) Surface energy according to Eq. (5.34) ($E_{\mathrm{VdW},0}$), Eq. (5.38) (E_{vdW}) and Eq. (5.7) (E_{S}) for impact velocities $w_{\mathrm{P},1} = 0.1; 1; 10$ m/s.

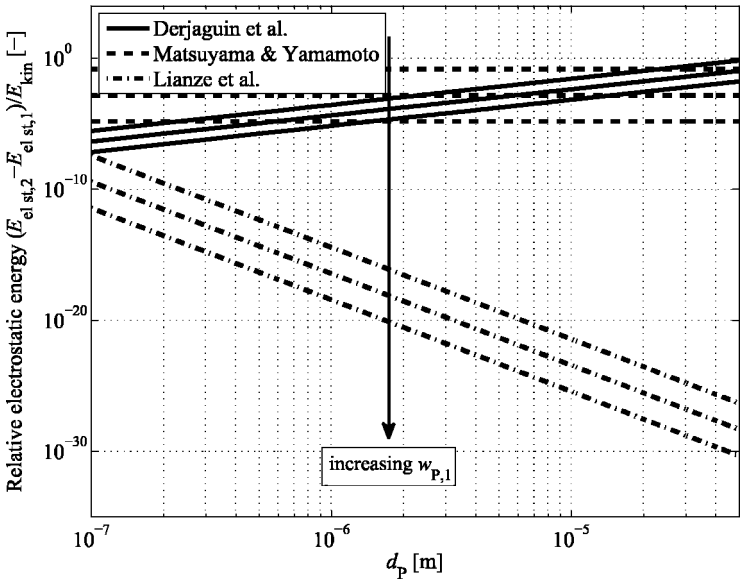

(b) Relative differences in electrostatic energy according to the models of Derjaguin [34], Matsuyama and Yamamoto [97] and Lianze et al. [91] in respect to the kinetic energy for the impact velocities $w_{\mathrm{P},1} = 0.1; 1; 10$ m/s. The models are presented in Tab. 4.2

Figure 5.1: *Comparison of adhesion and electrostatic energy calculation models. The material properties are the mean values of the ranges mentioned in Tab. 5.2.*

6 Adhesion Map

In Fig. 4.1 five ways are visualised for modelling the particle-wall interactions. These models, which are described in detail by Schwarz [129], are:

a. the Hertz model;

b. the Johnson, Kendall and Roberts model (JKR);

c. the Derjaguin, Muller and Toporov model (DMT);

d. the Maugis-Dugdale model (MD);

e. and the new model introduced by Schwarz [129].

The models are compared with a realistic interaction. Besides these models, for stiff, rigid particles the Bradley model is valid [75]. The grey shaded area in Fig. 4.1 includes the distance dependent adhesion pressures, whereas the arrows describe the point forces. The models and their restrictions are discussed below.

Between two spherical particles of radius r_1 and r_2 the reduced radius is given by:

$$r^* = \left(\frac{1}{r_1} + \frac{1}{r_2}\right)^{-1}. \tag{6.1}$$

From Eq. (6.1), it is clear that for the contact between a sphere with radius r_1 and a flat surface, r_2 goes to infinity and r^* becomes half the particle's diameter

$$\lim_{r_2 \to \infty} r^* = \left(\frac{1}{r_1} + \frac{1}{r_2}\right)^{-1} \approx r_1 = \frac{d_P}{2}. \tag{6.2}$$

However, it should be noticed that, because of symmetry, the work of adhesion, γ, between a particle and a plain has half the value of that between two particles. Eq. (6.2) describes the situation where a particle sticks on a clean, plain wall and Eq. (6.1) if a layer of deposited spherical particles already exists.

6.1 Hertz Theory

The Hertz theory neglects any attractive forces [129]. Therefore, an external force, F_1, is needed to achieve deformation of the particle. The contact radius becomes a function of the reduced radius

$$r_0 = \left(\frac{r^* F_1}{K}\right)^{1/3}. \tag{6.3}$$

Here, K represents the effective elastic modulus, which differs a factor 4/3 from the reduced Young's modulus, Y^*

$$\begin{aligned} K &= \frac{4}{3\left(\frac{1-\nu_1^2}{Y_1}+\frac{1-\nu_2^2}{Y_2}\right)}. \\ &= \frac{4}{3}Y^* \end{aligned} \tag{6.4}$$

The vertical displacement of the bodies in contact is given by [129]

$$\delta = \frac{r_0}{r^*}, \tag{6.5}$$

and the pressure distribution within the contact area by

$$p(r) = \frac{3Kr_0}{2\pi r^*}\sqrt{1-\left(\frac{r}{r_0}\right)^2}. \tag{6.6}$$

6.2 Bradley Rigid Theory

The Bradley model describes the contact for stiff particles. It was adapted by Dahneke [29] to apply for a larger range including soft contacts.

6.2.1 Classical Bradley Rigid Theory

For stiff materials and low external loads, the elastic deformation becomes small [75]. For this situation, the contact force is best described by the Bradley model. The van der Waals' attractive potential between two molecules separated at a distance r_{sep} reads [29]

$$\phi_{\text{L}} = -\frac{\lambda}{r_{\text{sep}}^6} \tag{6.7}$$

where, λ denotes the London dispersion force coefficient. Integrated over two spherical molecules with volumes, V_1 and V_2 and molecule densities, n_1 and n_2, the van der Waals interaction energy becomes

$$\begin{aligned} E_{\text{vdW}} &= -\int_{V_1}\int_{V_2}\frac{\lambda}{r^6}n_1\mathrm{d}V_1 n_2\mathrm{d}V_2 \\ &= \frac{-A_{12}d^*}{12z_0}, \end{aligned} \tag{6.8}$$

where

$$d^* = 2r^*. \tag{6.9}$$

The van der Waals force is found after differentiating E_{vdW} to z_0 and is given by

$$F_{\text{vdW}} = -\frac{\mathrm{d}E_{\text{vdW}}}{\mathrm{d}z_0} = -\frac{A_{12}d^*}{12z_0^2}. \tag{6.10}$$

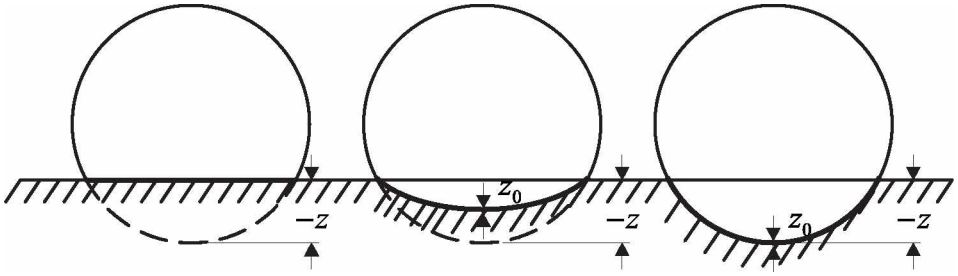

Figure 6.1: *A soft sphere in contact with a hard surface (left), a sphere in contact with a surface of the same hardness (middle) and a hard sphere in contact with a soft surface (right) [29, 121].*

6.2.2 Correction for Soft Contact by Dahneke

Dahneke [29] describes three types of contact between a flattened sphere and a surface (see Fig. 6.1). Limestone is much softer than steel, so the first graph shows the situation of a particle on a clean wall. For a wall that is already covered with deposits, the particle has approximately the same hardness as the surface such as in the second graph. The contact between a hard particle and a soft surface, shown in the third graph, is further not considered in this thesis.

Dahneke [29] gives a dimensionless diameter, d_{D}^*, to describe the influence of deformation on the ratios between the true van der Waals energy and -force on the one side and those for undeformed particles on the other side. The dimensionless particle diameter is given by the following expression:

$$d_{\mathrm{D}}^* = \frac{A^2 k_{\mathrm{e}}^2 d_{\mathrm{P}}}{108 z_0^7}. \tag{6.11}$$

In Eq. (6.11), $k_{\mathrm{e}} = \pi\,(k_1 + k_2)$, with

$$k_{\mathrm{i}} = \frac{1 - \nu_{\mathrm{i}}^2}{\pi Y_{\mathrm{i}}}. \tag{6.12}$$

The ratio between F_{vdW} and $F_{\mathrm{vdW,0}}$ (where the subscript 0 denotes the undeformed state) reads then

$$\frac{F_{\mathrm{vdW}}}{F_{\mathrm{vdW,0}}} = 1 + d_{\mathrm{D}}^*. \tag{6.13}$$

This means, that for values of d_{D}^* smaller than 0.1, the influence of deformation on the van der Waals force is smaller than 10%. The quantity h_{e} denotes the penetration depth of two spheres at which E_{vdW} obtains its minimum. h_{e} is made dimensionless with z_0 in the following equation:

$$\frac{h_{\mathrm{e}}}{z_0} = \frac{3}{8}\sqrt[3]{q} + \frac{24 d_{\mathrm{D}}^* + 27 {d_{\mathrm{D}}^*}^2}{8\sqrt[3]{q}} + \frac{9}{8} d_{\mathrm{D}}^*. \tag{6.14}$$

In Eq. (6.14), q is only a function of d_{D}^*:

$$q = 36 {d_{\mathrm{D}}^*}^2 + 8 d_{\mathrm{D}}^* + 27 {d_{\mathrm{D}}^*}^3 + 8\sqrt{{d_{\mathrm{D}}^*}^3 + {d_{\mathrm{D}}^*}^2}. \tag{6.15}$$

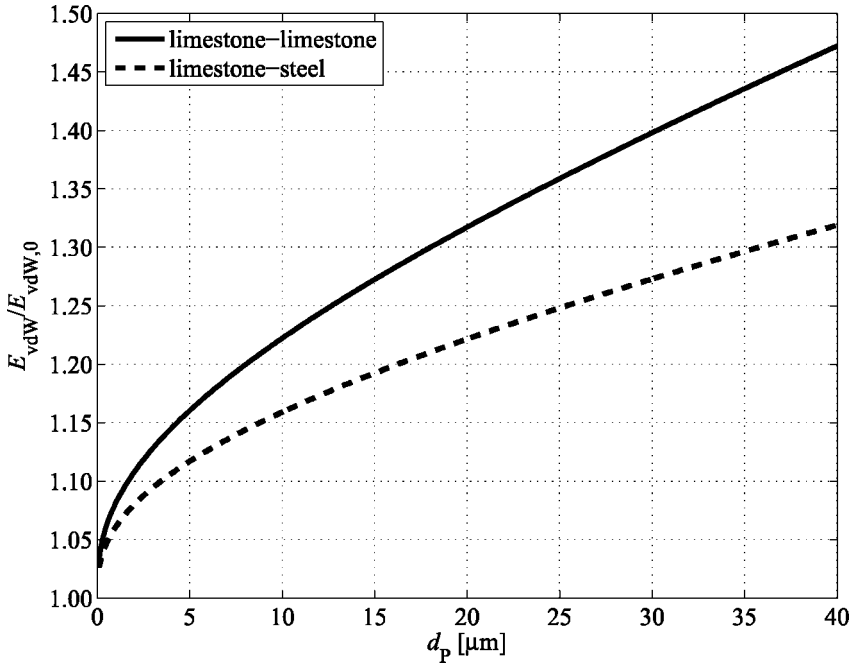

Figure 6.2: *Ratio of the van der Waals energy on a deformed particle (E_{vdW}) to that of an undeformed particle ($E_{\mathrm{vdW},0}$) according to Dahneke [29] for the systems limestone-steel and limestone-limestone.*

Dahneke calculates the van der Waals energy of a deformed particle with

$$E_{\mathrm{vdW}} = -\left(\frac{Ad_{\mathrm{p}}}{12z_0}\right)\left(1+\frac{h_{\mathrm{e}}}{z_0}+\frac{h_{\mathrm{e}}^2}{z_0^2}\right)+\left(\frac{4\sqrt{2d_{\mathrm{P}}}}{15k}\right)h_{\mathrm{e}}^{5/2} \tag{6.16}$$

and that of undeformed particle with

$$E_{\mathrm{vdW},0} = -\frac{Ad_{\mathrm{P}}}{12z_0}. \tag{6.17}$$

The minus sign in Eq. (6.16) and (6.17) indicate the attractive energy. Thus, the influence of deformation on the van der Waals energy is found by the ratio of Eq. (6.16) and (6.17) and will be larger than that of the van der Waals force. For the systems limestone-steel and limestone-limestone the ratios of $E_{\mathrm{vdW}}/E_{\mathrm{vdW},0}$ are drawn in Fig. 6.2. In the particle range considered, an up to 50% higher van der Waals energy is possible if deformation is taken into account.

6.3 JKR Theory

Johnson, Kendall and Roberts [76] developed the JKR model to describe the surface energy between two elastic solids as an extension of the Hertz theory with an additional adhesion force [129]. The interaction is described by a point force (i.e. a dirac delta function) around the distance at zero contact z_0. The total force is given by [129]

$$\begin{aligned} F_{\mathrm{H}}^{\mathrm{JKR}} &= F_1 + 3\pi r^*\gamma + \sqrt{6\pi r^*\gamma F_1 + (3\pi r^*\gamma)^2} \\ &= \left(\sqrt{-F_{\mathrm{c}}^{\mathrm{JKR}}} + \sqrt{F_1 - F_{\mathrm{c}}^{\mathrm{JKR}}}\right)^2. \end{aligned} \tag{6.18}$$

In Eq. (6.18), $F_{\mathrm{c}}^{\mathrm{JKR}} = -1.5\pi r^*\gamma$, is the critical force , i.e. the pull-off force to separate a sphere from a plate. The contact radius after deformation then reads

$$\begin{aligned} r_0 &= \left(\frac{r^* F_{\mathrm{H}}^{\mathrm{JKR}}}{K}\right)^{1/3} \\ &= \left(\frac{r^*}{K}\right)^{1/3} \left(\sqrt{-F_{\mathrm{c}}^{\mathrm{JKR}}} + \sqrt{F_1 - F_{\mathrm{c}}^{\mathrm{JKR}}}\right)^{2/3} \end{aligned} \tag{6.19}$$

and the vertical displacement becomes [129]

$$\delta = \frac{r_0^2}{r^*} - \sqrt{\frac{8\pi\gamma r_0}{3K}}. \tag{6.20}$$

The pressure distribution is given by

$$p(r) = \frac{3Kr_0}{2\pi r^*}\sqrt{1 - \left(\frac{r}{r_0}\right)^2} - \sqrt{\frac{3\gamma K}{2\pi r_0}}\left[1 - \left(\frac{r}{r_0}\right)^2\right]^{-1/2}, \tag{6.21}$$

where, the 2nd term between the brackets describes the pressure due to the surface energy. If no external forces are applied on the particle, Eq. (6.18) and (6.19) respectively become

$$F_{0,0}^{\mathrm{JKR}} = 6\pi\gamma r^*, \tag{6.22}$$

$$r_{0,0}^{\mathrm{JKR}} = \left(\frac{6\pi\gamma r^{*2}}{K}\right)^{1/3}. \tag{6.23}$$

6.4 DMT Theory

In the DMT model from Derjaguin, Muller and Toporov [51], the particle-wall interaction is modelled with a long range force of the van der Waals type [129]. Because the original model did not take any deformation into account, Maugis [98] superposed an additional Hertzian force as a correction:

$$F_{\mathrm{H}}^{\mathrm{DMT\text{-}M}} = F_1 - F_{\mathrm{c}}^{\mathrm{DMT}}, \tag{6.24}$$

where, in contradiction to the JKR model, the pull-off force is given by $F_{\mathrm{c}}^{\mathrm{DMT}} = -2\pi r^*\gamma$ and thus differs by a factor 4/3. The contact radius is

$$r_0^{\mathrm{DMT}} = \left(\frac{r^* \left(F_1 - F_c^{\mathrm{DMT}} \right)}{K}, \right)^{1/3} \tag{6.25}$$

which becomes

$$r_{0,0}^{\mathrm{DMT}} = \left(\frac{2\pi\gamma r^{*2}}{K} \right)^{1/3}, \tag{6.26}$$

for zero applied external load. This value differs by a factor of $3^{1/3}$ with the contact radius predicted by the JKR-model (Eq. (6.23)). The deformation and pressure distribution are equal to the Hertz model (Eq. (6.5) and (6.6)).

6.5 M-D Theory

In the Maugis-Dugdale theory, the long range forces are modelled by a block pressure between z_0 and $z_0 + h_{\mathrm{D}}$ [129]. From the (arbitraire) choice to match the maximum pressure σ_{D} to that of the Lennart-Jones potential, it follows that [75, 129]

$$h_{\mathrm{D}} = 0.971 z_0. \tag{6.27}$$

A set of two equations with two unknowns are simultaniously solved (usually) using numerical methods [129]. The set of equations is:

$$\hat{F} = \hat{a}^3 - \lambda\hat{a}^2 \left[\sqrt{m^2 - 1} + m^2 \arccos\left(\frac{1}{m} \right) \right], \tag{6.28a}$$

$$1 = \frac{\lambda\hat{a}^2}{2} \left[\sqrt{m^2 - 1} + (m^2 - 2) \arccos\left(\frac{1}{m} \right) \right] + \frac{4\lambda^2\hat{a}}{3} \left[\sqrt{m^2 - 1} \arccos\left(\frac{1}{m} \right) - m + 1 \right], \tag{6.28b}$$

where, $\hat{F}$ is the reduced force in which the first term is due to the Hertz pressure and the second denotes the adhesive force. $\hat{F}$ is defined by

$$\hat{F} = \frac{F_c}{\pi\gamma r^*}, \tag{6.29}$$

and $\hat{a}$, the reduced contact radius, by

$$\hat{a} = r_0 \left(\frac{K}{\pi\gamma r^{*2}} \right)^{1/3}. \tag{6.30}$$

The dimensionless parameter, m, is defined as the ratio between the distance at which the surface in contact have been separated, c, and the contact radius:

$$m = c/r_0. \tag{6.31}$$

The elastic parameter, λ, is calculated from [75]

$$\lambda = 1.16\mu. \tag{6.32}$$

Here, the Tabor parameter, μ, is defined as [138]:

$$\mu = \left(\frac{16r^*\gamma^2}{9K^2z_0^3}\right)^{1/3}. \tag{6.33}$$

After the calculation of m and $\hat{a}$ the dimensionless deformation is calculated

$$\hat{\delta} = \hat{a}^2 - \frac{4\lambda\hat{a}}{3}\sqrt{m^2-1}, \tag{6.34}$$

from which the real deformation follows in dimensional units:

$$\delta = \hat{\delta}\left(\frac{K^2}{\pi^2\gamma^2 r^*}\right)^{-1/3}. \tag{6.35}$$

6.6 Model of Schwarz

Schwarz [129] introduced a new model for the transition region, since in the Maugis-Dugdale theory no explicit solution for the contact radius, the deformation depth and the pressure distribution is given. By superposition of the critical loads of the JKR and DMT model the new critical force becomes

$$F_c^S = -\frac{3}{2}\pi r^* w_1 - 2\pi r^* w_2. \tag{6.36}$$

In this model, the work of adhesion by the short range forces, w_1, are separated from that of the long ranges forces, w_2. The surface energy follows from the sum of both components:

$$\gamma = w_1 + w_2. \tag{6.37}$$

The effective Hertzian load reads

$$F_H^S = \left(\sqrt{3F_c + 6\pi r^*\gamma} + \sqrt{F_1 - F_c}\right)^2, \tag{6.38}$$

from which the contact radius, deformation and pressure distribution follow:

$$r_0 = \left(\frac{r^*}{K}\right)^{1/3}\left(\sqrt{3F_c + 6\pi r^*\gamma} + \sqrt{F_1 - F_c}\right)^{2/3}, \tag{6.39}$$

$$\delta = \frac{r_0^2}{r^*} - 4\sqrt{\frac{\pi r_0}{3K}\left(\frac{F_c}{\pi r^*} + 2\gamma\right)}, \tag{6.40}$$

$$p(r) = \frac{3Kr_0}{2\pi r^*}\sqrt{1-\left(\frac{r}{r_0}\right)^2} - \sqrt{\frac{3K}{\pi r_0}\left(\frac{F_c}{\pi r^*} + 2\gamma\right)}\left[1-\left(\frac{r}{a}\right)^2\right]^{-1/2}. \tag{6.41}$$

Eq. (6.36)-(6.41) correspond to the DMT-M model if $w_1 = 0$ and to the JKR model if $w_2 = 0$. However, if the single contributions of w_1 and w_2 to γ are unknown, the equations are not usable.

To scale the way of contact between 0 (full DMT character) and 1 (full JKR character), Schwarz [129] introduced the following parameter

$$\tau_2 = -\frac{3F_c + 6\pi r^*\gamma}{F_c}, \tag{6.42}$$

where the critical force F_c can still vary between $-1.5\pi r^*\gamma$ and $-2\pi r^*\gamma$. Furthermore, Schwarz introduced the parameter

$$\alpha = \sqrt{\tau_2}, \tag{6.43}$$

by which the contact radius becomes

$$r_0 = r_{0,0}\left(\frac{\alpha + \sqrt{1 - \frac{F_1}{F_c}}}{1+\alpha}\right)^{2/3}. \tag{6.44}$$

Here, the contact radius at zero external load is given by

$$r_{0,0} = \left(\frac{r^*}{K}\right)^{1/3}\left[(1+\alpha)\sqrt{-F_c}\right]. \tag{6.45}$$

In Eq. (6.44) and (6.45), F_c and α are still unknown. These unknowns can be calculated by numerically solving the set of equations in the M-D theory (Eq. (6.28)) but this is not always desired. To avoid an iterative calculation, a proposal of Carpick et al., which fits the values of $\hat{F}$ (Eq. (6.29)) and $\hat{a}$ (Eq. (6.30)) within an accuracy of $\sim 1\%$, is useful [19]. These fits read

$$\hat{F}(\lambda) = -\frac{4}{7} + \frac{1}{4}\left(\frac{4.04\lambda^{1.4} - 1}{4.04\lambda^{1.4} + 1}\right), \tag{6.46}$$

$$\hat{a}(\lambda) = 1.54 + 0.279\left(\frac{2.28\lambda^{1.3} - 1}{2.28\lambda^{1.3} + 1}\right). \tag{6.47}$$

Furthermore Carpick et al. give an empirical equation for λ as function of α:

$$\lambda = -0.924\ln(1 - 1.02\alpha). \tag{6.48}$$

Or, mutatis mutandis, for $\lambda \geq 0$:

$$\alpha = \frac{1 - \exp\left(-\frac{\lambda}{0.924}\right)}{1.02}. \tag{6.49}$$

6.7 Comparison of Adhesion Models

A map with the different models introduced in Sec. 6.1-6.5 is given in Fig. 6.3.

The boundary of the Hertz zone is given by the ratio of the adhesion force, F_{ad}, to the total force, F

$$\left|\frac{F_{ad}}{F}\right| = \left|1 - \frac{F_1}{F}\right| < \xi \tag{6.50}$$

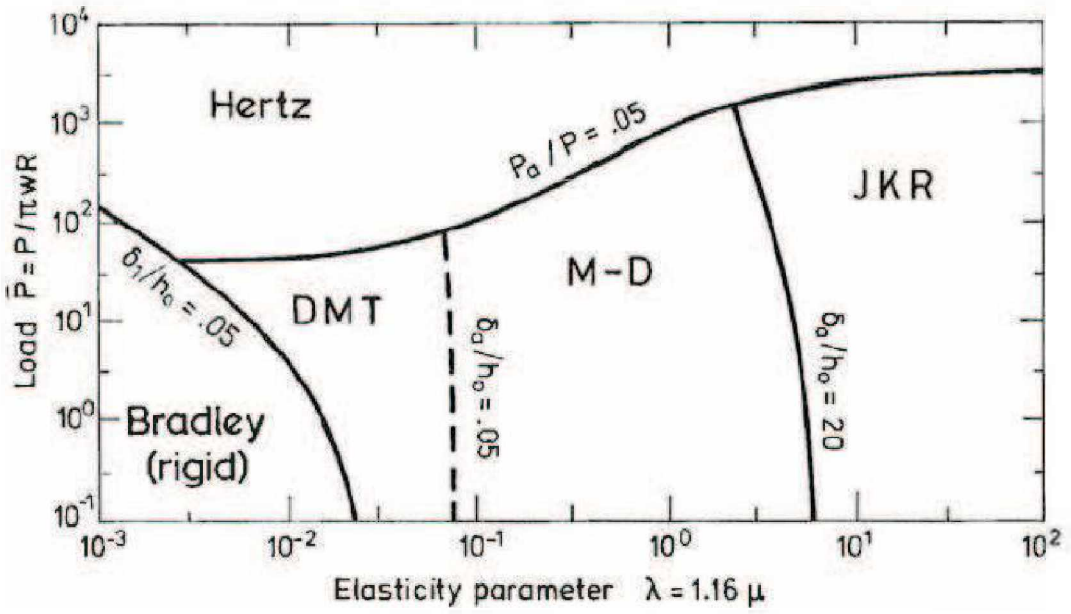

Figure 6.3: *Vadility of several adhesion models as function of λ and pull-off force $\bar{P}$ (copied from [75]).*

where, ξ has the somehow arbitrair value of 0.05 [75]. The borders between the Bradley, DMT, M-D and JKR zones are given by values of

$$\left|\frac{\delta_a}{h_0}\right| = \eta, \tag{6.51}$$

where, $h_0 = 0.97 z_0$ [75]. The elastic displacement is calculated from

$$\delta_a = -\frac{2\sigma_D}{E^*}\sqrt{m^2 - 1}, \tag{6.52}$$

where the adhesive force intensity is calculated from

$$\sigma_D = \frac{\gamma}{h_0}. \tag{6.53}$$

For small loads $\bar{P}$, the limits between the M-D model and the DMT and JKR correspond to values of $\lambda \approx \mu = 0.1$ and $\lambda \approx \mu = 5$, respectively.

For limestone-steel contact $K = 8.0 \times 10^{10}$ and when $\gamma = 90\ \mathrm{mJ \cdot m^{-2}}$, the lower and upper limits for the M-D regime equal $d_P = 0.06\ \mu\mathrm{m}$ and $d_P = 7$ mm, respectively. Therefore, the whole range of particle diameters of interest will be covered by the M-D model.

7 Particle Sticking Criterions

Two major sticking criterions are compared. The first one is based on energy conservation of the impacting particle and the second one on a equilibrium of force and moment of force on a particle in contact with a wall.

7.1 Sticking Criterions Based on Energy Conservation

The critical sticking velocity follows by stating that the coefficient of restitution in Eq. (5.43) becomes 0:

$$e_{\mathrm{crit}}^2 = 0 = e_{\mathrm{pl}}^2 - \frac{E_{\mathrm{ad}}}{E_{\mathrm{kin,1,crit}}}. \tag{7.1}$$

Thus, the critical sticking velocity for a spherical particle reads:

$$w_{\mathrm{P,1,crit}} = \frac{1}{e_{\mathrm{pl}}}\sqrt{\frac{12E_{\mathrm{ad}}}{\pi\rho_{\mathrm{P}}d_{\mathrm{P}}^3}}. \tag{7.2}$$

Impacting particles with a velocity $w_{\mathrm{P,1}} \leq w_{\mathrm{P,1,crit}}$ will stick to the wall, whereas particles with $w_{\mathrm{P,1}} > w_{\mathrm{P,1,crit}}$ will regain their elastic energy and rebound with their original velocity multiplied with the plastic coefficient of restitution

$$w_{\mathrm{P,2}} = e_{\mathrm{pl}} \cdot w_{\mathrm{P,1}}. \tag{7.3}$$

In terms of the wall normal and tangential components, Eq. (7.3) becomes

$$w_{\mathrm{P,2,n}} = -e_{\mathrm{pl}} \cdot w_{\mathrm{P,1,n}}, \tag{7.4a}$$

$$w_{\mathrm{P,2,t}} = e_{\mathrm{pl}} \cdot w_{\mathrm{P,1,t}}. \tag{7.4b}$$

The energy based sticking criterion has been implemented by Houben [68] for the simulations of wall depositions in gas cyclones. However, he found that only submicron particles were able to meet the sticking criterion. A possible explanation for this is that the model was developed for the sticking of particles at fibre filters by [60]. However, since the particles and the diameter of the cylinder are in the same order in magnitude for fibre filters, the models might not be valid anymore for larger cylinders, such as in a cyclone separator. Therefore, Wang [150] advises only to compare the radial velocity with the critical velocity under assumption that the tangential velocity is totally dissipated by friction.

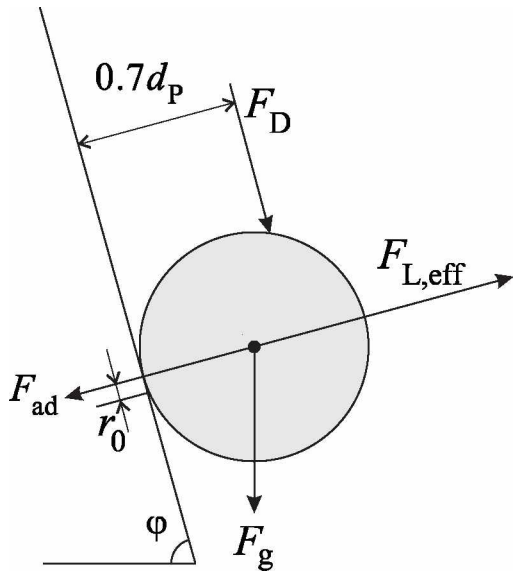

Figure 7.1: *Forces on a particle in contact with the wall under an angle, ϕ, with the horizontal and contact radius r_0, with: F_D drag force, $F_{L,eff}$ effective lift force (as sum of the lift force in a shear flow, Saffman force, pressure gradient force, turbophoresis force etc.), F_{ad} adhesion force, F_g gravitational force.*

7.2 Force and Moment Based Sticking Criterions

When a particle bounds with a wall, a force and a moment of forces balance is made as criterion whether a particle sticks or is re-entrained back into the flow. The relevant forces working on a particle in contact with the wall with an angle ϕ in respect with the horizontal are shown in Fig. 7.1. Three ratios for vertical lift off, sliding or tangential rolling respectively are computed for each collision with the wall [132]:

$$R_v = \frac{F_{L,eff}}{F_{ad} + F_g \cos\phi} \tag{7.5a}$$

$$R_s = \frac{F_D + F_g \sin\phi}{k_s \left[F_{ad} + F_g \cos\phi - F_{L,eff}\right]} \tag{7.5b}$$

$$R_t = \mathrm{abs}\left\{\frac{(0.7d_P)\, F_D + r_0 \left(F_{L,eff}\right) + 0.5 d_P F_g \sin\phi}{r_0 \left(F_{ad} + F_g \cos\phi\right)}\right\}. \tag{7.5c}$$

The effective lift force, $F_{L,eff}$, is the sum of all relevant wall normal flow forces as introduced in Sec. 4.2. This is thus the sum of the lift force in a shear flow, the Saffmann lift force, turbophoresis, the pressure gradient force etc.:

$$F_{L,eff} = F_{L,LA} + F_{Saff} + F_{Tu} + F_{PG} + \ldots. \tag{7.6}$$

Also the adhesive force is the sum of the Lifshitz-van der Waals, capillary, electrical and Coulomb forces

$$F_{\mathrm{ad}} = F_{\mathrm{vdW}} + F_{\mathrm{C}} + F_{\mathrm{el}} + F_{\mathrm{ES}}. \tag{7.7}$$

The contact radius r_0 in Eq. (7.5), as shown in Fig. 7.1, is calculated as described in Ch. 6. The sliding ratio, k_{s}, in Eq. (7.5b) has the value 0.3 [132]. If one or more of the ratios in Eq. (7.5) is larger than unity, the particle will rebound with velocity

$$w_{\mathrm{P},2} = e_{\mathrm{pl}} \cdot w_{\mathrm{P},1}, \tag{7.8}$$

where the plastic coefficient of restitution is calculated as in Eq. (5.41). Otherwise, it will stick at the wall.

8 Computational Fluid Dynamics

Computational Fluids Dynamics (abbreviated as CFD) is a method of calculating fluid flows, heat and mass transfer, chemical reactions and similar phenomena by numerical solving mathematical expression [95]. The accuracy of the solutions is dependent on the following properties [22]:

- *Consistency:* The discretisation error should approach zero for infinite small grid sizes or time steps. For this case, the algebraic finite difference equations become equal to the original partial differential equations.
- *Stability:* Numerical errors (truncation errors for example) should be bounded for each iteration step and not explode the solution.
- *Convergence:* A numerical method is convergent if its solution approaches that of the partial differential equation for decreasing grid sizes and time steps and if numerical errors are bounded. This means that both consistency and stability are required to achieve convergence.

The CFD simulations were performed with the commercial software program ANSYS Fluent 13.0 [39]. For the calculation of the particle trajectories, the discrete phase model (DPM) was applied. This model is based on the Euler-Lagrange method and uses the following steps [39]:

1. Solve the continuous-phase flow.
2. Create the discrete-phase injections.
3. Solve the coupled flow, if desired.
4. Track the discrete-phase injections, using plots or reports.

The DPM model has the following two restrictions:

1. The volume fraction flow of the discrete phase is not allowed to exceed a critical value of 10-12%. For the experiments described in Ch. 9, the maximal volume fraction equals 3.6 ppm (i.e. at a solid loading of 7.9 g limestone per kg of air). This value is assumed to be low enough, although it is known from Pirker and Kahrimanovic [120] that in cyclone separators strands near the wall might be formed at higher solid loadings for which they developed the Euler-Euler-Lagrange (EuEuLa) model .
2. Well defined entrance and exit conditions are needed. These conditions are the inlet and vortex finder outlet for a cyclone separator, respectively. To avoid back-flow through the vortex finder, it is possible to model a flat round surface, positioned at a certain distance above the vortex finder. This surface should have the same diameter as the vortex finder and the distance from the upper side of the vortex finder should be chosen in such a way that the ring-shaped gap has the same surface as the cross sectional area of the vortex finder [53, 62].

Table 8.1: Differences between laminar and turbulent flows [111].

laminar	turbulent
stratified, uniform	disorderly
smooth	fluctuating
regulated	chaotic

8.1 Calculation of the Flow Field of the Continuous Phase

The flow in most industrial applications is turbulent. The main differences between laminar and turbulent flows are summarised in Tab. 8.1. It may be obvious that turbulence is a time dependent phenomenon, which makes it difficult to model and almost impossible to solve it analytically. Therefore, CFD is offen used, which is either based on a continuous approach modelling macroscopic continua (such as the finite volume method used in ANSYS Fluent 13.0 [39]) or on microscopic models and mesoscopic kinetic equations in the lattice Boltzmann method (LBM, described by Chen and Doolen [20] for example, and implemented for cyclone separators by Gronald and Derksen [54]). In this thesis, only the continuous approached is considered furthermore.

8.1.1 Transport Equations

The behaviour of (turbulent) flows is described by the equation of conservation of mass (continuity equation), the equation of motion (Navier-Stokes for Newtonian fluids) and the conservation of energy:

Conservation of mass: The continuity equation describes the change of mass in a control volume by means of the transport of mass through the faces of the volume. Its general equation in cartesian coordinates reads [111]:

$$\frac{\partial \rho_g}{\partial t} + u_j \frac{\partial \rho_g}{\partial x_j} + \rho_g \frac{\partial u_i}{\partial x_i} = 0. \tag{8.1}$$

For low Mach numbers the fluid velocity is much smaller than the speed of sound of the fluid under the same conditions. Therefore, the flow becomes incompressible and the first term in Eq. (8.1) vanishes. Eq. (8.1) then reduces to [111]

$$\frac{\partial u_i}{\partial x_i} = 0. \tag{8.2}$$

Conservation of momentum: The conservation of momentum in cartesian coordinates is given by the following equation:

$$\rho_g \frac{\partial u_i}{\partial t} + \rho_g u_j \frac{\partial u_i}{\partial x_j} = \rho_g g_i + \frac{\partial \sigma_{ij}}{\partial x_j}, \tag{8.3}$$

where, g_i, is the gravitational constant and σ_{ij} the stress tensor. For a Newtonian fluid, the stress tensor is given by

$$\sigma_{ij} = -p\delta_{ij} + 2\mu_g s_{ij}, \tag{8.4}$$

in which p is the pressure and δ_{ij} the Kronecker Delta function, which equals 1 for $i = j$ and 0 for $i \neq j$. The rate of strain tensor is calculated with

$$s_{ij} = \frac{1}{2}\left(\frac{\partial u_i}{\partial x_j} + \frac{\partial u_j}{\partial x_i}\right). \tag{8.5}$$

After combining Eq. (8.2)-(8.5), the Navier-Stokes equation follows:

$$\rho_g \frac{\partial u_i}{\partial t} + \rho_g u_j \frac{\partial u_i}{\partial x_j} = \rho_g g_i - \frac{\partial p}{\partial x_i} + \mu_g \frac{\partial^2 u_i}{\partial {x_j}^2}. \tag{8.6}$$

The Navier-Stokes equations apply for incompressible Newtonian fluids.

Conservation of energy: The general equation of conservation of energy is given by [111]

$$\frac{\partial T}{\partial t} + u_j \frac{\partial T}{\partial x_j} = k_T \frac{\partial^2 T}{\partial {x_j}^2}, \tag{8.7}$$

where, the first term on the left hand side is the instationary term and the second the convective term. Conduction is described by the right hand side, where k_T denotes the thermal conductivity. Since only isothermal flows are treated in this thesis, Eq. (8.7) is further not taken into account anymore.

8.1.2 Turbulence

The velocities in the equations in Sec. 8.1.1 will not be constant in time but fluctuate in most applications. This turbulence can be described by one of the three following methods [111]:

a. *Direct numerical simulation* (DNS): The Navier-Stokes equations are direct modelled on a three dimensional grid with the central difference method, for example. For each step in time, the velocity in each grid point is calculated. For high Reynolds numbers, this solution will be unsteady in position and time. Although DNS is the most precise and physically correct method to describe turbulence, it is very expensive in computational time. The reason for this is that the grid needs a very fine spatial resolution to describe all length scales in turbulence. These scales are the macro scale, $\mathscr{L}$, and the micro scale (the so called Kolmogorov scale), η_K. The number of nodes needed to describe the turbulence then becomes in the order of

$$N_t \sim \left(\frac{\mathscr{L}}{\eta_K}\right)^3. \tag{8.8}$$

Since $\eta_K/\mathscr{L} \sim \mathrm{Re}^{-3/4}$, where $\mathrm{Re} = \frac{w\mathscr{L}}{\nu_g}$, the number of nodes needed to describe all turbulent phenomena scales with $N_t \sim \mathrm{Re}^{9/4}$. This means, that only flows with relative low Reynolds numbers can be simulated using DNS within a reasonable time.

b. *Large eddy simulation (*LES*)*: In LES the grid is so coarse that only the macro structure of the turbulence is solved, i.e. only the movement of the *large eddies* is described. This is achieved by filtering the smaller eddies out of the equations. Subgrid scales are modelled afterwards with additional equations (closure problem). Since the closing equations in LES only describe the subgrid scales, which are easier to model, LES gives better results

than RANS turbulence models. The computational effort is not as large as in DNS thus the simulation of larger Reynolds numbers is possible.

c. *Reynolds averaged Navier-Stokes (RANS)*: The turbulence is not solved directly in RANS models but modelled with additional equations. A closer look on two widely used RANS models is taken below.

In RANS models, the velocities, pressure and temperature of the fluid are divided into a part that is constant in time (denoted with a bar) and a fluctuating part with zero time average (denoted with an accent):

$$u_\mathrm{i} = \overline{u}_\mathrm{i} + u'_\mathrm{i} \tag{8.9a}$$
$$p = \overline{p} + p' \tag{8.9b}$$
$$T = \overline{T} + T'. \tag{8.9c}$$

This method is called Reynolds decomposition. Applied on Eq. (8.1), (8.3) and (8.7) these equations become for continuity

$$\frac{\partial \overline{u}_\mathrm{i}}{\partial x_\mathrm{i}} = 0, \tag{8.10a}$$
$$\frac{\partial u'_\mathrm{i}}{\partial x_\mathrm{i}} = 0, \tag{8.10b}$$

for momentum, using the Boussinesq approximation,

$$\frac{\partial \overline{u}_\mathrm{i}}{\partial t} + \frac{\partial \overline{u}_\mathrm{i}\overline{u}_\mathrm{j}}{\partial x_\mathrm{j}} = -\frac{1}{\rho_0}\frac{\partial \overline{p}}{\partial x_\mathrm{i}} + \frac{g}{T_0}\overline{T}\delta_{\mathrm{i}3} + \nu_\mathrm{g}\frac{\partial^2 \overline{u}_\mathrm{i}}{\partial {x_\mathrm{j}}^2} - \frac{\partial \overline{u'_\mathrm{i}u'_\mathrm{j}}}{\partial x_\mathrm{j}}, \tag{8.11a}$$
$$\frac{\partial u'_\mathrm{i}}{\partial t} + \overline{u}_\mathrm{j}\frac{\partial u'_\mathrm{i}}{\partial x_\mathrm{j}} + u'_\mathrm{j}\frac{\partial \overline{u}_\mathrm{i}}{\partial x_\mathrm{j}} + \frac{\partial u'_\mathrm{i}u'_\mathrm{j}}{\partial x_\mathrm{j}} - \frac{\partial \overline{u'_\mathrm{i}u'_\mathrm{j}}}{\partial x_\mathrm{j}} = -\frac{1}{\rho_0}\frac{\partial p'}{\partial x_\mathrm{i}} + \frac{g}{T_0}T'\delta_{\mathrm{i}3} + \nu_\mathrm{g}\frac{\partial^2 u'_\mathrm{i}}{\partial {x_\mathrm{j}}^2}, \tag{8.11b}$$

and for energy

$$\frac{\partial \overline{T}}{\partial t} + \overline{u}_\mathrm{j}\frac{\partial \overline{T}}{\partial x_\mathrm{j}} = k_\mathrm{T}\frac{\partial^2 T}{\partial {x_\mathrm{j}}^2} - \frac{\partial \overline{u'_\mathrm{j}T'}}{\partial x_\mathrm{j}}, \tag{8.12a}$$
$$\frac{\partial T'}{\partial t} + \overline{u}_\mathrm{j}\frac{\partial T'}{\partial x_\mathrm{j}} + u'_\mathrm{j}\frac{\partial \overline{T}}{\partial x_\mathrm{j}} + \frac{\partial u'_\mathrm{j}T'}{\partial x_\mathrm{j}} - \frac{\partial \overline{u'_\mathrm{j}T'}}{\partial x_\mathrm{j}} = k_\mathrm{T}\frac{\partial^2 T'}{\partial {x_\mathrm{j}}^2}, \tag{8.12b}$$

respectively. In Eq. (8.11b) and (8.12b), the new terms $\overline{u'_\mathrm{i}u'_\mathrm{j}}$ and $\overline{u'_\mathrm{j}T'}$ are introduced, from which the latter one vanishes for isothermal flows. The terms $\rho_0\overline{u'_\mathrm{i}u'_\mathrm{j}}$, where ρ_0 is the reference density, are called the Reynolds stress terms and are elements of the turbulent stress tensor

$$\Sigma_\mathrm{ij} = -\frac{1}{3}\rho_0\overline{{u'_\mathrm{k}}^2}\delta_\mathrm{ij} + \rho_0\left(-\overline{u'_\mathrm{i}u'_\mathrm{j}} + \frac{1}{3}\rho_0\overline{{u'_\mathrm{k}}^2}\delta_\mathrm{ij}\right). \tag{8.13}$$

The turbulent stress tensor is per definition symmetric. Therefore, maximal 6 additional differential equations are needed to model the transport of the Reynolds stresses. The models common used are divided into zero, one, two and more-equation models.

8.1.2.1 $k-\epsilon$ model

One of the most used turbulence models is the $k-\epsilon$ model. It is defined by one equation for the turbulent kinetic energy, k, and by one for the turbulent dissipation rate, ϵ [39]. These quantities are defined by [111]

$$k = \frac{1}{2}\overline{u_{\mathrm{i}}'^2}, \tag{8.14}$$

$$\epsilon = \nu_{\mathrm{g}}\frac{\mathcal{V}^2}{\overline{\eta_{\mathrm{K}}^2}}, \tag{8.15}$$

where, η_{K} and $\mathcal{V}$ are the Kolmogorov length- and velocity scale respectively. The turbulent kinetic energy is made dimensionless by relating it to the time mean velocity, $\overline{u}$, in the turbulent intensity [111]:

$$I_{\mathrm{turb}} = \frac{k}{\overline{u}^2}. \tag{8.16}$$

The $k-\epsilon$ model is relative stable and since there are only two additional equations to be solved, the extra computational effort is not too high.

A disadvantage is that the model is not able to describe anisotropic turbulence, which is a problem for strongly swirling flows. For cyclone separators Hoffmann and Stein [66], Hoekstra [62], Gorton-Hülgerth and Staudinger [47] and Brunnmair and Houben [16, 67] noticed that the solid body rotation (forced) vortex ranges from the cyclone's centre line up to a radial position not far away from the wall, where the tangential velocity suddenly drops to zero to meet the no-slip boundary condition, when using the $k-\epsilon$-model. In reality, a free vortex exists in the outer region, where the tangential velocity smoothly decreases to zero.

The standard $k-\epsilon$ model has been modified in the RNG model, for rotating flows, and the realizable $k-\epsilon$ model. The realizable $k-\epsilon$ model is assumed to achieve more precise results and to convergate faster than the RNG model [95]. However, none of the $k-\epsilon$ models has been optimised for strongly swirling flow in cyclone separators [21].

In the standard $k-\epsilon$ model, the following two equations for the transport of k and ϵ are used [39]:

$$\frac{\partial}{\partial t}\left(\rho_{\mathrm{g}}k\right) + \frac{\partial}{\partial x_{\mathrm{i}}}\left(\rho_{\mathrm{g}}k u_{\mathrm{i}}\right) = \frac{\partial}{\partial x_{\mathrm{j}}}\left[\left(\mu_{\mathrm{g}} + \frac{\mu_{\mathrm{t}}}{\sigma_{\mathrm{k}}}\right)\frac{\partial k}{\partial x_{\mathrm{j}}}\right] + G_{\mathrm{k}} + G_{\mathrm{b}} - \rho_{\mathrm{g}}\epsilon - Y_{\mathrm{M}} + S_{\mathrm{k}}, \tag{8.17}$$

$$\frac{\partial}{\partial t}\left(\rho_{\mathrm{g}}\epsilon\right) + \frac{\partial}{\partial x_{\mathrm{i}}}\left(\rho_{\mathrm{g}}\epsilon u_{\mathrm{i}}\right) = \frac{\partial}{\partial x_{\mathrm{j}}}\left[\left(\mu_{\mathrm{g}} + \frac{\mu_{\mathrm{t}}}{\sigma_{\epsilon}}\right)\frac{\partial \epsilon}{\partial x_{\mathrm{j}}}\right] + C_{1\epsilon}\frac{\epsilon}{k}\left(G_{\mathrm{k}} + C_{3\epsilon}G_{\mathrm{b}}\right) - C_2\rho_{\mathrm{g}}\frac{\epsilon^2}{k} + S_{\epsilon}, \tag{8.18}$$

where, $G_{\mathrm{k}} = -\rho_{\mathrm{g}}\overline{u_{\mathrm{i}}'u_{\mathrm{j}}'}\frac{\partial u_{\mathrm{j}}}{\partial x_{\mathrm{i}}}$, is the generation of turbulent energy due to velocity gradients and G_{b} that due to buoyancy, which is not present in isothermal flows. The dilatation dissipation,

Table 8.2: Default values for constants in the standard $k-\epsilon$ model [39].

contant	default value	name
$C_{1\epsilon}$	1.44	
$C_{2\epsilon}$	1.92	
C_μ	0.09	
σ_k	1.0	turbulent Prandtl number for k
σ_ϵ	1.3	turbulent Prandtl number for ϵ

Y_M, is only important in compressible flows and is defined in Eq. (8.24). σ_k and σ_ϵ are the turbulent Prandtl numbers for the kinetic turbulent energy and dissipation rate respectively. The eddy, or turbulent, viscosity is calculated with:

$$\mu_\mathrm{t} = \rho_\mathrm{g} C_\mu \frac{k^2}{\epsilon}. \tag{8.19}$$

$C_{1\epsilon}$, $C_{2\epsilon}$, C_μ, σ_k and σ_ϵ are constants, whose default values in ANSYS Fluent 13.0 are given in Tab. 8.2.

8.1.2.2 Reynolds Stress Model

In the Reynolds stress model (RSM), beside one equation for the turbulent dissipation rate, one equation for each independent element in the turbulent stress tensor is solved. This means that five additional equations are needed for the closure problem in 2D- and seven additional equations in 3D-problems. The RSM model allows anisotropic turbulence and is known to give good results for the simulation of cyclone separators [39]. The elements of the turbulent stress tensor are described by the following equation [39]

$$\frac{\partial}{\partial t}\left(\rho_\mathrm{g}\overline{u_\mathrm{i}'u_\mathrm{j}'}\right) + \frac{\partial}{\partial x_\mathrm{k}}\left(\rho_\mathrm{g}u_\mathrm{k}\overline{u_\mathrm{i}'u_\mathrm{j}'}\right) = D_{\mathrm{T,ij}} + D_{\mathrm{L,ij}} + P_\mathrm{ij} + G_\mathrm{ij} + \phi_\mathrm{ij} - \epsilon_\mathrm{ij} + F_\mathrm{ij} + S_\mathrm{user}, \tag{8.20}$$

where, the first term on the left hand side is the local time derivative and the second the convective term. The terms on the right hand side are:

$$D_{\mathrm{T,ij}} = -\frac{\partial}{\partial x_\mathrm{k}}\left[\rho_\mathrm{g}\overline{u_\mathrm{i}'u_\mathrm{j}'u_\mathrm{k}'} + \overline{p\left(\delta_\mathrm{kj}u_\mathrm{i}' + \delta_\mathrm{ik}u_\mathrm{j}'\right)}\right] \quad \text{turbulent diffusion;} \tag{8.21a}$$

$$D_{\mathrm{L,ij}} = \frac{\partial}{\partial x_\mathrm{k}}\left[\mu_\mathrm{g}\frac{\partial}{\partial x_\mathrm{k}}\left(\overline{u_\mathrm{i}'u_\mathrm{j}'}\right)\right] \quad \text{molecular diffusion;} \tag{8.21b}$$

$$P_\mathrm{ij} = -\rho_\mathrm{g}\left(\overline{u_\mathrm{i}'u_\mathrm{k}'}\frac{\partial u_\mathrm{j}}{\partial x_\mathrm{k}} + \overline{u_\mathrm{j}'u_\mathrm{k}'}\frac{\partial u_\mathrm{i}}{\partial x_\mathrm{k}}\right) \quad \text{stress production;} \tag{8.21c}$$

$$G_\mathrm{ij} = -\rho_\mathrm{g}\beta\left(g_\mathrm{i}\overline{u_\mathrm{j}'T} + g_\mathrm{j}\overline{u_\mathrm{i}'T}\right) \quad \text{buoyancy production;} \tag{8.21d}$$

$$\phi_\mathrm{ij} = \overline{p\left(\frac{\partial u_\mathrm{i}'}{\partial x_\mathrm{j}} + \frac{\partial u_\mathrm{j}'}{\partial x_\mathrm{i}}\right)} \quad \text{pressure strain;} \tag{8.21e}$$

$$\epsilon_{ij} = 2\mu_g \overline{\frac{\partial u_i'}{\partial x_k} \frac{\partial u_j'}{\partial x_k}} \qquad \text{dissipation;} \tag{8.21f}$$

$$F_{ij} = -2\rho_g \Omega_k \left(\overline{u_j' u_m'} \epsilon_{ikm} + \overline{u_i' u_m'} \epsilon_{jkm} \right) \qquad \text{production by system rotation;} \tag{8.21g}$$

$$S_{user} \qquad \text{user - defined source term.} \tag{8.21h}$$

No additional equations for the closing are needed for the terms for convection, molecular diffusion, stress production and production by system rotation. This in contrast to the turbulent diffusion, buoyancy production (for non isothermal flows), pressure strain and dissipation that need to be modelled.

In ANSYS Fluent 13.0, the turbulent diffusive transport is modelled by an adapted model of Daly and Harlow [30, 39]. Their equation reads:

$$D_{T,ij} = \frac{\partial}{\partial x_k} \left(\frac{\mu_t}{\sigma_k} \frac{\partial \overline{u_i' u_j'}}{\partial x_k} \right), \tag{8.22}$$

where, the turbulent viscosity is calculated as in Eq. (8.19). The constant σ_k, however, can differ from the default value in the $k - \epsilon$-model [39, 92].

The pressure strain term, ϕ_{ij}, is the sum of the slow, the rapid and the wall reflection terms. The wall reflection term damps the wall normal stress component near the wall and enhances the parallel component.

The dissipation tensor is defined in ANSYS Fluent 13.0 as:

$$\epsilon_{ij} = \frac{2}{3} \delta_{ij} \left(\rho_g \epsilon + Y_M \right). \tag{8.23}$$

The second term between the brackets is the additional "dilatation dissipation" and is calculated from the turbulent Mach number, Ma_t

$$Y_M = 2\rho_g \epsilon Ma_t^2, \tag{8.24}$$

$$Ma_t = \sqrt{\frac{k}{a_s^2}}, \tag{8.25}$$

where, $a_s \equiv \sqrt{\gamma_a R_u T}$ is the speed of sound. The transport equation for the scalar dissipation rate, ϵ, then reads:

$$\frac{\partial}{\partial t} (\rho_g \epsilon) + \frac{\partial}{\partial x_i} (\rho_g \epsilon u_i) = \frac{\partial}{\partial x_j} \left[\left(\mu_g + \frac{\mu_t}{\sigma_\epsilon} \right) \frac{\partial \epsilon}{\partial x_j} \right] C_{\epsilon 1} \frac{1}{2} \left[P_{ii} + C_{\epsilon 3} G_{ii} \right] \frac{\epsilon}{k} - C_{\epsilon 2} \rho_g \frac{\epsilon^2}{k} + S_\epsilon. \tag{8.26}$$

The RSM model is the most advanced RANS turbulence model and therefore needs the highest computational time. Because of the high coupling between the equations, convergence is harder to achieve than with the use of the $k - \epsilon$ model. However, the $k - \epsilon$ is suitable for the first iteration steps in a simulation before changing to RSM [95].

8.1.3 Discretisation and Solving of the PDEs

The goal of discretisation is to convert the set of partial differential equations into an algebraic set of (matrix) equations which has the following form:

$$\mathbf{A} \cdot \boldsymbol{x} = \boldsymbol{b}. \tag{8.27}$$

In Eq. (8.27), $\mathbf{A}$ is a matrix connecting the vector with unknown quantities $\boldsymbol{x}$ (e.g. velocities, pressure, temperature) with the vector with known elements $\boldsymbol{b}$ (e.g. from boundary or initial conditions).

Since for almost all problems it is not possible to calculate the inverse of the matrix $\mathbf{A}$, numerical methods are required. For this purpose, in ANSYS Fluent 13.0 the two following solvers are provided [39]:

a. *Pressure based*: developed for low speed incompressible flows,

b. *Density based*: for high speed compressible flows.

The difference between both models is within the method of solving the pressure and density field. In the density based solver, the density field is equated directly from the continuity equation from which the pressure field follows from the equation of state. In the pressure based solver, the continuity and momentum equations are manipulated in such a way that the pressure (or pressure correction) is solved. From this pressure, the pressure fields follows. Three steps are needed to write the set of partial differential equations in the form of a set of algebraic equations:

a. Creating a mesh, which divides the domain into discrete elements;

b. Integration of the governing equations over each volume element in the mesh;

c. Linearisation in order to write the algebraic equations in algebraic (matrix) form.

In ANSYS Fluent 13.0, the second step is accomplished by the finite volume method (FVM). The equations are obtained in integral form. Each volume is considered to be fixed in space to apply the Eulerian approach (i.e. the physical quantities are only a function of the position and time) and to be large enough to treat the fluid as continuum [61]. For each control volume with volume V, the following equation is set up for any physical quantity ϕ [53]

$$\frac{\partial}{\partial x_\mathrm{i}} \left(\rho_\mathrm{g} u_\mathrm{i} \phi\right) = \frac{\partial}{\partial x_\mathrm{i}} \left(\Gamma_\phi \frac{\partial \phi}{\partial x_\mathrm{i}}\right) + S_\phi, \tag{8.28}$$

where, Γ_ϕ, is the diffusion coefficient and S_ϕ, a source term. Eq. (8.28) is now integrated over the control volume resulting in

$$\iiint\limits_V \frac{\partial}{\partial x_\mathrm{i}} \left(\rho_\mathrm{g} u_\mathrm{i} \phi\right) \mathrm{d}V = \iiint\limits_V \frac{\partial}{\partial x_\mathrm{i}} \left(\Gamma_\phi \frac{\partial \phi}{\partial x_\mathrm{i}}\right) \mathrm{d}V + \iiint\limits_V S_\phi \mathrm{d}V. \tag{8.29}$$

With the Gauss-theorem

$$\iiint\limits_V \frac{\partial}{\partial x_\mathrm{i}} \mathrm{d}V = \iint\limits_A \phi \mathrm{d}A, \tag{8.30}$$

Eq. (8.29) becomes

$$\iint_A \rho_g u_i \phi dA = \iint_A \Gamma_\phi \frac{\partial \phi}{\partial x_i} dA + \iiint_V S_\phi dV. \tag{8.31}$$

The area-integrals over the volume, V in Eq. (8.31), are written as the sum over all faces of the volume. Furthermore, the source term is treated as a constant, whose value is determined in the volume's midpoint ($S_{\phi,MP}$). In consequence, Eq. (8.32) is found:

$$\sum_f^{N_f} \rho_g u_{i,f} \phi_f A_f = \sum_f^{N_f} \Gamma_{\phi,f} \left(\frac{\partial \phi}{\partial x_i}\right)_f A_f + S_{\phi,MP} V. \tag{8.32}$$

8.1.3.1 Spatial Discretisation

As is seen from Eq. (8.32), derivatives of scalars evaluated on the faces of each control volume are required. However, ANSYS Fluent 13.0 only stores the values in the centres of the control volumes. Therefore, an interpolation scheme in space is needed. ANSYS Fluent 13.0 provides the following schemes:

a. *First Order Upwind*: the values at the cell's faces are assumed to have the same value as in the cell's centre. For first order upwind, the values of the cell located upstream are taken;

b. *Power Law*: in the Power Law scheme the value of the quantity at any position in the cell is calculated with

$$\frac{\phi(x) - \phi_0}{\phi_L - \phi_0} = \frac{\exp\left(Pe\frac{x}{L}\right) - 1}{\exp(Pe) - 1} \tag{8.33}$$

where,

$$\phi_0 = \phi|_{x=0}, \tag{8.34a}$$
$$\phi_L = \phi|_{x=L}. \tag{8.34b}$$

The Peclet number is defined as

$$Pe = \frac{\rho_g \mu_g L}{\Gamma}, \tag{8.35}$$

in which, Γ is a constant in the differential equation describing the transport of ϕ.

c. *Second Order Upwind*: higher accuracy is achieved by calculating a Taylor series expansion around the value in the cell's centre. The value of the quantity $\phi_{f,SOU}$, for *second order upwind*, at the face is calculated as a function of the value in the cell located upstream, ϕ, its gradient, $\nabla\phi$, and the vector between the centroid of this cell and the face considered, $\vec{r}$

$$\phi_{f,SOU} = \phi + \nabla\phi \cdot \vec{r}. \tag{8.36}$$

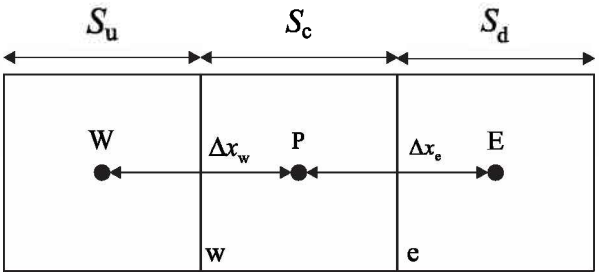

Figure 8.1: *One dimensional visualisation of the* QUICK *scheme for a flow with direction from the left to the right [39].*

d. The *Central-Differencing Scheme* is only available in LES. The face value is calculated as follows:

$$\phi_{f,CD} = \frac{1}{2}(\phi_0 + \phi_1) + \frac{1}{2}(\nabla\phi_0 \cdot \vec{r}_0 + \nabla\phi_1 \cdot \vec{r}_1). \tag{8.37}$$

To avoid instability problems, it is useful to add an additional, implicit, convective upwind term:

$$\phi_f = \underbrace{\phi_{f,UP}}_{\text{implicit part}} + \underbrace{(\phi_{f,CD} - \phi_{f,UP})}_{\text{explicit part}}. \tag{8.38}$$

e. For hexaeder cells with a clear flow direction the *Quadratic Upwind for Interpolation for Convective Kinematics* (QUICK) scheme is provided. The QUICK scheme is third order in accuracy [87]. If the flow is from left to right in Fig. 8.1, the scheme is given by the following equation

$$\phi_e = \theta\left[\frac{S_d}{S_c + S_d}\phi_P + \frac{S_c}{S_c + S_d}\phi_E\right] + (1-\theta)\left[\frac{S_u + 2S_c}{S_u + S_c}\phi_P\phi_P - \frac{S_c}{S_u + S_c}\phi_W\right]. \tag{8.39}$$

The value of θ can be varied between 0 (to achieve the central differencing scheme) and 1 (for second order upwind). In ANSYS Fluent 13.0 the default value is $\theta = 1/8$. ANSYS Fluent 13.0 allows to implement the QUICK scheme for unstructured grids as well. In this case the second order upwind discretisation scheme is applied (i.e. $\theta = 1$).

f. The *Monotone Upstream-Centered Schemes for Conservation Laws*, MUSCL, combines a central differencing- with a second order upwind-scheme:

$$\phi_f = \theta\phi_{f,CD} + (1-\theta)\,\phi_{f,SOU}. \tag{8.40}$$

The scheme is third order in accuracy and is applicable to arbitrary meshes.

8.1.3.2 Time Discretisation

For unsteady flows, the time derivatives in the transport equations in Sec. 8.1.1 do not vanish. Therefore, beside a spatial, also a time discretisation is needed. This time discretisation can whether be explicit or implicit. In the first case, the scalars are evaluated at time $t = \Delta t n$ before moving to the next time step $t = \Delta t\,(n+1)$. The first and second order explicit methods are defined as in Eq. (8.41a) and (8.41b), respectively

$$\frac{\phi^{n+1} - \phi^{n}}{\Delta t} = F\left(\phi^{n}\right), \tag{8.41a}$$

$$\frac{3\phi^{n+1} - 4\phi^{n} + \phi^{n-1}}{2\Delta t} = F\left(\phi^{n}\right). \tag{8.41b}$$

Explicit methods are not unconditionally stable and are not provided by ANSYS Fluent 13.0 in the pressure based solver for incompressible flows.

Alternatively, implicit methods are used, for which the solution is unconditionally stable for any time step Δt. Its first order scheme reads

$$\frac{\phi^{n+1} - \phi^{n}}{\Delta t} = F\left(\phi^{n+1}\right), \tag{8.42}$$

in which $F\left(\phi^{n+1}\right)$ is unknown yet, and has to be calculated iteratively.

8.1.4 Mesh Quality

It is important for the accuracy and stability of the numerical computation to use a grid with a good quality [39]. Two important dimensionless numbers to qualify the mesh quality are the aspect ratio (Q_{AR}) and the equi-angle-skewness (Q_{EAS}).

In 3D, the aspect ratio is distinguished for tetrahedral (Eq. (8.43a)) and hexahedral elements (Eq. (8.43b)) and respectively reads

$$Q_{\mathrm{AR}} = f\left(\frac{r_{\mathrm{o}}}{r_{\mathrm{i}}}\right), \tag{8.43a}$$

$$Q_{\mathrm{AR}} = \frac{\max\left[e_1, e_2, \ldots, e_{\mathrm{n}}\right]}{\min\left[e_1, e_2, \ldots, e_{\mathrm{n}}\right]}, \tag{8.43b}$$

where, $f = 1/3$ and r_{o} and r_{i} are the radii of the outer and inner sphere respectively in- and describing the tetrahedral element. In 3D, the index n equals 3, and e_{i} describes the average length of the element in the coordinate direction i. By definition the value of Q_{AR} is larger than unity, where the lowest values describes an equilateral element (a cube for hexahedral cells and a tetrahedron with all faces equal in shape and size).

The equi-skewness ratio describes the skewness of a cell, whose value is always between 0 (for a perfect cell) and 1 (for a completely degenerated cell). It is equated from the following expression

$$Q_{\mathrm{EAS}} = \max\left[\frac{q_{\max} - q_{\mathrm{eq}}}{180^{\circ} - q_{\mathrm{eq}}}, \frac{q_{\mathrm{eq}} - q_{\min}}{q_{\mathrm{eq}}}\right], \tag{8.44}$$

Table 8.3: *Mesh quality for several ranges of the equi-angle-skewness (Q_{EAS}) [40].*

EAS Range	Quality
$Q_{\text{EAS}} = 0$	Equilateral (perfect)
$0 < Q_{\text{EAS}} < 0.25$	Excellent
$0.25 < Q_{\text{EAS}} < 0.5$	Good
$0.5 < Q_{\text{EAS}} < 0.75$	Fair
$0.75 < Q_{\text{EAS}} < 0.9$	Poor
$0.9 < Q_{\text{EAS}} < 1$	Very poor (sliver)
$Q_{\text{EAS}} = 1$	Degenerate

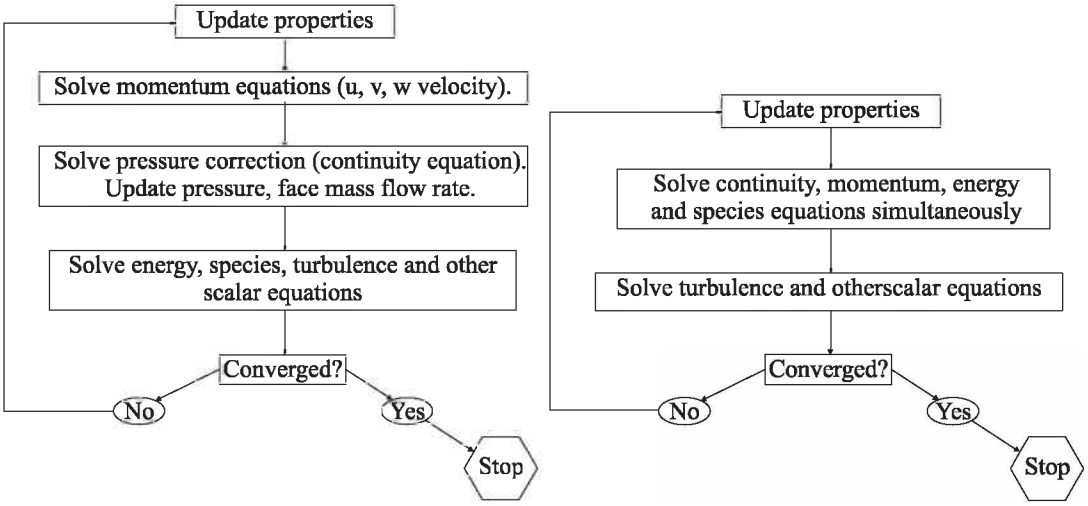

(a) Segregated solver. (b) Coupled solver.

Figure 8.2: *Overview of solvers (redrawn from [39]).*

where, $q_{\max}$ is the maximal angle between the edges of the cell, $q_{\min}$, the minimum angle and q_{eq}, the value for equilateral cells (i.e. $q_{\text{eq}} = 60°$ for tetrahedral cells and $q_{\text{eq}} = 90°$ for hexahedral cells). Other values of Q_{EAS} and their corresponding mesh quality are presented in Tab. 8.3.

8.1.5 Solvers

For solving the sets of equations with the unknowns (e.g. p, u, v, w, T), two methods are available (Fig. 8.2). In the segregated (or decoupled) solver all transport equations are treated independently, i.e. the unknowns in the equations only depend on themselves. Eq. (8.32) is linearised resulting in

$$a_{\text{p}}\phi_{\text{p}} = \sum_{\text{nb}} a_{\text{nb}}\phi_{\text{nb}} + b, \tag{8.45}$$

where, ϕ, is the quantity in the cell, ϕ_{nb}, the quantity in the neighbouring cell and a_{p} and a_{nb} are the linearised coefficients for these quantities respectively. After Eq. (8.45) is setup for each cell in the domain, the result is a set of algebraic equations, that is written in matrix form. ANSYS Fluent 13.0 solves this set of equations using the Gauss-Seidl algorithm.

The coupled solver simultaneously solves the equations for continuity, momentum, pressure, energy and species, which is important for compressible flows with high Mach numbers. Compared with the segregated solver, the rate of solution convergence is improved, however the computational effort increases by a factor of 1.5-2.0 [39].

Eq. (8.45) is rewritten in such a way that the left hand side gives zero if the set of equations is solved exactly. This exact solution will not be achievable and some residual will remain. For the segregated pressure based solver, the unscaled residual of quantity ϕ is defined as

$$R^{\phi} = \sum_{\text{cells } p} \left| \sum_{\text{nb}} a_{\text{nb}} \phi_{\text{nb}} + b - a_{\text{p}} \phi_{\text{p}} \right|, \tag{8.46}$$

and the scaled residual as

$$R^{\phi} = \frac{\sum_{\text{cells } p} \left| \sum_{\text{nb}} a_{\text{nb}} \phi_{\text{nb}} + b - a_{\text{p}} \phi_{\text{p}} \right|}{\sum_{\text{cells } p} \left| a_{\text{p}} \phi_{\text{p}} \right|}. \tag{8.47}$$

For a convergating iterative calculation R^{ϕ} should asymptotically approach a value close to zero. The default value for cutting off the calculation is 1.0×10^{-3} for the continuity, momentum and turbulence equations and 1.0×10^{-6} for the energy equations.

In practice, it is important to check convergence with relevant surface and volume monitors. Examples for these monitors are the pressure drop *of* and typical (turbulent) velocities *in* cyclone separators.

8.1.6 Calculation of the Boundary Layer

At the wall the tangential component of the mean and fluctuating velocity equals zero because of the no-slip condition and viscous damping. The normal velocities are zero because of the impenetrable wall. However, even at small distances from the wall, the turbulent kinetic energy increases rapidly due to the large gradients in the mean velocity.

As shown in Fig. 8.3, the near wall region can be divided into three regions of the dimensionless wall distance, which is defined as

$$\begin{aligned} y^{+} &= \frac{\rho_{\text{g}} u_{*} y}{\mu_{\text{g}}} \\ &= \frac{u_{*} y}{\nu_{\text{g}}}. \end{aligned} \tag{8.48}$$

The velocity is made dimensionless with the following equation [111]:

$$u^{+} = \frac{\overline{u}}{u_{*}}. \tag{8.49}$$

Directly at the wall, a viscous sublayer exists, where the transport of momentum and heat is dominated by viscous effects. Here, the velocity profile is described by

$$u^{+} = y^{+} \qquad 0 < y^{+} < 5. \tag{8.50}$$

In the outer layer, turbulent transport dominates. In literature different fits are found for the dimensionless velocity as well as different ranges of its validity

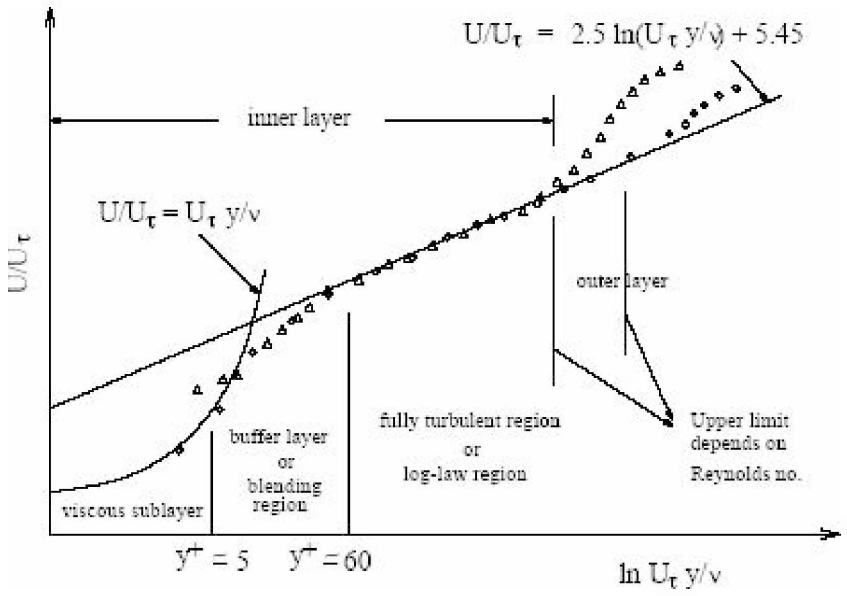

Figure 8.3: *Near wall treatment of turbulent flows with $U_\tau = u_*$ the friction velocity (copied from [39]).*

$$u^+ = 2.5 \ln\left(y^+\right) + 5.45 \qquad 60<y^+ \text{ [39]}, \tag{8.51a}$$

$$u^+ = 2.5 \ln\left(y^+\right) + 5 \qquad 30<y^+ \text{ [111]}. \tag{8.51b}$$

In the region in between, both effects play a role. Two approaches are available in ANSYS Fluent 13.0 to describe this intermediate region, which is known as the buffer layer:

a. *Standard Wall functions* are used to bridge the laminar sublayer and the fully turbulent layer in the core. The (high Reynolds) turbulence models are adapted to account for the presence of the wall. The wall function approach is popular in industrial applications for high Reynolds flows because of its economical cheap calculation times, robustness and acceptable accuracy. Good results were also achieved for the simulation of cyclone separators [35, 47, 53]. The default standard wall function used in ANSYS Fluent 13.0 reads:

$$U^* = \frac{1}{\kappa} \ln\left(E y^*\right) \qquad \text{for } y^* > 11.225, \tag{8.52}$$

where,

$$U^* \equiv \frac{U_\mathrm{p} C_\mu^{1/4} k_\mathrm{p}^{1/2}}{\tau_\mathrm{w}/\rho_\mathrm{g}}, \tag{8.53}$$

$$y^* \equiv \frac{\rho_\mathrm{g} C_\mu^{1/4} k_\mathrm{p}^{1/2} y_\mathrm{p}}{\mu_\mathrm{g}}. \tag{8.54}$$

The subscript p indicates the values evaluated in the midpoint of the wall neighbouring cell for respectively the mean velocity (U_p) the turbulent kinetic energy (k_p) and the wall normal local coordinate (y_p). The von Kármán constant has a numerical value of $\kappa = 0.4187$ and $E = 9.793$, is an empirical constant. Although the logarithmic mean velocity is valid for values of the dimensionless wall distance $30 < y^* < 300$, ANSYS Fluent 13.0 applies Eq. (8.52) when $y^* > 11.225$. For smaller values the following equation is used

$$U^* = Ey^* \qquad \text{for } y^* < 11.225. \tag{8.55}$$

For turbulent boundary layers the quantities y^+ and y^* have approximately the same value [39].

Explicit functions for the wall shear stress, τ_w, are found by manipulation of Eq. (8.52)-(8.55):

$$\tau_\mathrm{w} = \frac{\rho_\mathrm{g} U_\mathrm{p} \kappa C_\mu^{1/4} k_\mathrm{p}^{1/2}}{\ln(Ey^*)} \qquad \text{for } y^* > 11.225 \tag{8.56a}$$

$$\tau_\mathrm{w} = \frac{\mu_\mathrm{g}}{y_\mathrm{p}} U_\mathrm{p} \qquad \text{for } y^* < 11.225, \tag{8.56b}$$

and for the velocity at a certain position y_p from the wall, e.g. one particle radius

$$U_\mathrm{p} = \frac{\tau_\mathrm{w} \ln(Ey^*)}{\rho_\mathrm{g} \kappa C_\mu^{1/4} k_\mathrm{p}^{1/2}} = \tau_\mathrm{w} \frac{y_\mathrm{p}}{\mu_\mathrm{g}} \frac{\ln(Ey^*)}{y^* \kappa} \qquad \text{for } y^* > 11.225 \tag{8.57a}$$

$$U_\mathrm{p} = \tau_\mathrm{w} \frac{y_\mathrm{p}}{\mu_\mathrm{g}} \qquad \text{for } y^* < 11.225, \tag{8.57b}$$

where, only an interpolation of k_p between the cell's midpoints value and the value at the wall is needed.

When making the grid, the first cell's centroid should be placed within the range of $30 < y^* < 300$. The first cell of a too fine mesh would fall within the buffer layer. In a too coarse mesh, the first cell would fall outside the log-layer, where the wake component becomes substantially large. Lower values than $y^* = 11.225$ should be avoided because the wall function cease to be valid in the viscous sublayer. As a rule of thumb, the first cell should be at a distance of [95]

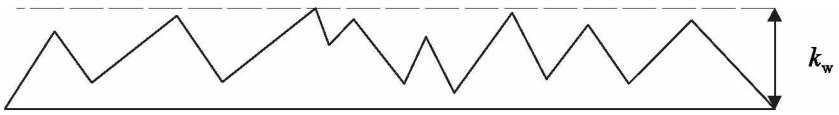

Figure 8.4: *Definition of the wall roughness [111].*

$$y_1 = \frac{50\nu_g}{u_*}, \tag{8.58}$$

where, the friction velocity is calculated from

$$u_* \equiv \sqrt{\frac{\tau_w}{\rho_g}} = U_{in}\sqrt{\bar{c}_f/2}. \tag{8.59}$$

The friction coefficient, $\bar{c}_f$, should be estimated from a turbulent flow over a flat plate

$$\bar{c}_f/2 \approx 0.0359 \mathrm{Re_L}^{-0.2}, \tag{8.60}$$

or from a pipe flow

$$\bar{c}_f/2 \approx 0.039 \mathrm{Re_D}^{-0.2}, \tag{8.61}$$

with $\mathrm{Re_L}$ and $\mathrm{Re_D}$ defined from the plate's length, L, and the pipe's diameter, D, respectively:

$$\mathrm{Re_L} = \frac{u_\infty L}{\nu_g}, \tag{8.62a}$$

$$\mathrm{Re_D} = \frac{u_\infty D}{\nu_g}. \tag{8.62b}$$

Other wall functions that can be used are *Non-Equilibrium Wall Functions*, where pressure gradients are taken into account and *Enhanced Wall Functions*, where the boundary layer is discretised and is suitable for low Reynolds flows [95].

b. In the *Near Wall Approach*, the mesh in the near wall region is resolved fine enough to describe the physics in both the laminar sublayer and the buffer layer correctly. Turbulence models that are valid in these near wall regions are the Spalart-Allmaras and the $k-\omega$ model for example. The enhanced wall approach is usable for low Reynolds flows or flows with complex boundary layer effects, which have to be resolved very fine.

Wall Roughness: The velocity profiles in Eq. (8.50) and (8.51) are valid for smooth walls [111]. The smoothness of the wall is determined from the Reynolds number for the wall roughness, k_w, as shown in Fig. 8.4 [39, 111]

Table 8.4: *Regimes of the wall roughness, their domains and their roughness functions ΔB [39, 78].*

name	domain	function for ΔB
hydrodynamically smooth	$K_s^+ < 2.25$	$\Delta B = 0$
transitional regime	$2.25 \leqq K_s^+ \leqq 90$	$\Delta B = \frac{1}{\kappa} \ln\left(1 + C_s K_s^+\right)$
fully rough	$K_s^+ > 90$	$\Delta B = \frac{1}{\kappa} \ln\left(\frac{K_s^+ - 2.25}{87.75} + C_s K_s^+\right) \times \sin\left[0.4258\left(K_s^+ - 0.811\right)\right]$

$$\mathrm{Re_k} = K_s^+ = \frac{k_w u_*}{\nu_g}. \tag{8.63}$$

$\mathrm{Re_k}$ is the ratio of the wall roughness and the thickness of the viscous sublayer ($y^+ \sim \frac{\nu_g}{u_*}$). For $\mathrm{Re_k} > 1$, the equations for hydrodynamically smooth walls cannot be used anymore. The velocity profile has the same value of the gradient ($1/\kappa$) but a different intercept (additive constant $B = 5.56$ for hydrodynamically smooth walls [39, 78]). The mean velocity is scaled to the friction velocity by the following general equation [78]:

$$\frac{u}{u_*} = \frac{1}{\kappa} \ln\left(\frac{y u_*}{\nu_g}\right) + B - \Delta B\left(K_s^+\right). \tag{8.64}$$

ANSYS Fluent 13.0 treats walls with $K_s^+ < 2.25$ as hydrodynamically smooth, and those with $K_s^+ > 90$ as fully rough. The roughness functions for the regimes are summarised in Tab. 8.4. Kaya et al. [78] used in their simulations the following values for the roughness constants

$$B = 5.56, \tag{8.65a}$$
$$C_s = 0.5. \tag{8.65b}$$

They further found the following four effects for increasing wall roughness:

1. the tangential velocity in the cyclone separator is reduced;
2. the upward axial velocity in the core region increases;
3. the separation efficiency decreases;
4. and the pressure drop decreased as well.

Kaya et al. [78] use relative wall roughnesses in the range of $0 < \epsilon_k < 0.028$ which is defined as

$$\epsilon_k = \frac{k_s}{D_{cb}}. \tag{8.66}$$

Since they used a cyclone with 31 mm in diameter, the resulting maximal wall roughness is 0.9 mm. Muschelknautz [104] gives values in the range of $1.3 \times 10^{-5} < \epsilon_k < 3 \times 10^{-3}$ m.

8.2 Calculation of the Path Lines of the Dispersed Phase

Gas solid flows are divided into three regimes of increasing solid fraction [39]:

a. particle laden flows,

b. pneumatic conveying: the flow pattern is dependent on the solid loading, Reynolds numbers and particle properties,

c. fluidised beds.

In cyclone separators, the first or second case will be valid. To describe their interactions, the following coupling methods between the two phases are available [95]:

a. *one way coupling*: the continuous (fluid) phase influences the dispersed (particle) phase by fluid-dynamic forces from the time mean and time fluctuating fluid velocities and pressures. The dispersed phase does not influence the continuous phase, i.e. at the places where discrete particles are found in reality the fluid phase should be modified, since no eddies can exist here [49];

b. *two way coupling*: the fluid phase influences the dispersed phase by fluid-dynamic forces. The dispersed phase influences the continuous phase by source terms describing the change of mass, momentum and energy.

c. *four way coupling*: dispersed particles influence the turbulence and particle-particle collisions create particle pressures and viscous stresses.

Furthermore, Eulerian and Lagrangian descriptions are sophisticated to describe the dispersed phase:

- In Eulerian models, each phase is modelled with an own set of continuum equations for their conservation laws. This means that twice the number of equations has to be solved. Eulerian codes are efficient in computational time, but are based on the assumption of the dispersion tensor, which makes them less general [49].

- In Lagrangian methods, first the equations of the continuous (fluid) phase are solved. After that, the trajectories of single particles are calculated in a local frame. The Lagrangian DPM model is only valid for volume fractions lower than 10% [39]. For dispersed particles, with a density much larger than that of the continuous phase, also higher mass fractions are allowed. The exchange of momentum, energy and mass between the dispersed and continuous phase is modelled, whereas particle-particle interactions as well as the effects of the particle volume fraction on the gas phase are neglected [39, 95]. Lagrangian methods are based on the statistical analysis of many particle trajectories, which make them expensive in terms of computational effort [49].

Since the mass fraction of limestone in the experiments is maximal 1%, the Lagrangian way is chosen to calculate the particle trajectories. This is done in a frozen flow field without the two way coupling from the dispersed to the continuous phase.

8.2.1 Equation of Motion

After solving the flow field of the continuous phase as described in Sec. 8.1, Newtons 2nd law of motion is applied on each single particle

$$\frac{\mathrm{d}w_\mathrm{P}}{\mathrm{d}t} = F_\mathrm{D}\left(u - w_\mathrm{P}\right) + \frac{g_\mathrm{x}\left(\rho_\mathrm{P} - \rho_\mathrm{g}\right)}{\rho_\mathrm{P}} + F_\mathrm{x}. \tag{8.67}$$

Here, the first term on the right hand side represents the drag force scaled to the particle mass, the second gravity and the third any flow force as described in Sec. 4. The particle's velocity equals the time derivative of its position

$$w_\mathrm{P} = \frac{\mathrm{d}x}{\mathrm{d}t}. \tag{8.68}$$

For a small time step and under assumption that all body forces stay constant, Eq. (8.67) is written as

$$\frac{\mathrm{d}w_\mathrm{P}}{\mathrm{d}t} = \frac{1}{\tau_\mathrm{P}}\left(u - w_\mathrm{P}\right) + a, \tag{8.69}$$

where in the term a all forces with the exception of drag are included. ANSYS Fluent 13.0 solves Eq. (8.68) and (8.69) to calculated the particle's position and velocity components at any time.

8.2.2 Turbulent Dispersion

The turbulent dispersion of dispersed particles is important to model because it gives more realistic results. Furthermore, it stabilises the result because it spreads local maxima caused by source terms. The largest disadvantage is the higher computational effort [95]. From CFD software, only the mean velocity components as well as the variances of the fluctuating parts are known [49]. Therefore, for each integration step Gouesbet and Berlemont [49] give four degrees of taking into account the turbulent dispersion with increasing sophistication:

a. *degree 0.* The continuous phase is considered as a laminar flow. In this situation, turbulence is not taken into account at all. For this reason, it is called degree 0. The model may give realistic results for some few cases, such as dense particles in a turbulent flow, which act like steel bullets in air.

b. *degree 1.* In this model, called *eddy lifetime approach*, the fluctuating part in the fluid velocity is kept constant during the Lagrangian time macro scale, T_L. Although, the Langrangian velocity correlation coefficient, R_fL, is not considered at itself, some linear decreasing memory effect exists between the integration starting time (t_0) and $t_0 + 2T_\mathrm{L}$ which can be analytically demonstrated:

$$R_\mathrm{fL}\left(\tau\right) = 1 - \frac{\tau}{2T_\mathrm{L}}. \tag{8.70}$$

c. *degree 2.* The difference with *degree 1.* is that the time, in which turbulent fluctuations are kept constant, is varied by sampling a random number. It is called the *random*

eddy lifetime approach and is included in ANSYS Fluent 13.0. Also here, the correlation coefficient follows from statistics:

$$R_{\mathrm{fL}}(\tau) = \exp\left(-\tau/T_{\mathrm{L}}\right). \tag{8.71}$$

Compared to degree 2, this method is more attractive since the exponential decrease is more realistic than a linear.

d. *degree 3.* The method of *degree 3.* is called the *correlation slave approach.* Where, the methods of *degree 1.* and *2.* use a priori stochastic processes, resulting in uncontrolled Langrangian correlation coefficients, the turbulence history of a particle is saved in a correlation matrix. In 1D the vector for the fluctuating velocity $u(n\delta t)$ for the time after each time step $n\delta t$ reads

$$U = [u(0),\ u(\delta t),\ u(2\delta t)\ldots,\ u(i\delta t),\ \ldots]. \tag{8.72}$$

The matrix for the correlation between the fluctuating velocities is defined as

$$A_{\mathrm{cor}} = \begin{bmatrix} \overline{u(0)^2} & \cdot & \cdot \\ \overline{u(0)\,u(\delta t)} & \overline{u(\delta t)^2} & \cdot \\ \overline{u(0)\,u(2\delta t)} & \overline{u(\delta t)\,u(2\delta t)} & \overline{u(2\delta t)^2} \end{bmatrix}. \tag{8.73}$$

The matrix R_{cor} is the reduced form of A_{cor}, whose elements read

$$r_{\mathrm{ij}} = \overline{u^*(i\delta t)\,u^*(j\delta t)} = \frac{\overline{u(i\delta t)\,u(j\delta t)}}{\sqrt{\overline{u(i\delta t)}}\sqrt{\overline{u(j\delta t)}}}. \tag{8.74}$$

For a Frenkiel shape these elements become

$$r_{\mathrm{ij}} = \exp\left[\frac{-|j-i|\,\delta t}{\left(m_{\mathrm{Fr}}^2+1\right)T_{\mathrm{L}}}\right]\cos\left[\frac{m_{\mathrm{Fr}}\,|j-i|\,\delta t}{\left(m_{\mathrm{Fr}}^2+1\right)T_{\mathrm{L}}}\right], \tag{8.75}$$

where, the Frenkiel parameter, m_{Fr}, has the favoured value of 1. A too large correlation matrix is avoided by assuming that the correlations are zero, after a time has elapsed, which equals more than five times the Lagrangian time macroscale, T_{L}. Although more information is stored in the correlation matrices, the runs are not more time-consuming since the time steps can generally be chosen larger than for using the methods of *degree 1.* and *2.* The correlation matrix for 2D flows is described in the literature [9].

8.2.2.1 Discrete Random Walk Model

The velocity of the continuous phase in the equation of motion (Eq. (8.68)) is divided into a time mean and a fluctuating part

$$u = \overline{u} + u'. \tag{8.76}$$

In the discrete random walk model, the value of u' is determined from a random number, ζ, generated from a Gaussian probability function with zero mean. In isotropic turbulence models, such as $k-\epsilon$, the fluctuations in all coordinate directions have the same value ($u' = v' = w'$), and are calculated from the turbulent kinetic energy

$$u' = v' = w' = \zeta\sqrt{\frac{2k}{3}}. \tag{8.77}$$

For the RSM model, the turbulent fluctuations are not isotropic anymore. Therefore, three random numbers are generated independently

$$u' = \zeta_{\mathrm{x}}\sqrt{\overline{u'^2}}, \tag{8.78a}$$

$$v' = \zeta_{\mathrm{y}}\sqrt{\overline{v'^2}}, \tag{8.78b}$$

$$w' = \zeta_{\mathrm{z}}\sqrt{\overline{w'^2}}, \tag{8.78c}$$

where $\overline{u'^2}$, $\overline{v'^2}$ and $\overline{w'^2}$ are known from the diagonal of the Reynolds stress tensor. The eddy lifetime, τ_{e}, is most realistic calculated from a random number, r_{rand}, whose value is between 0 and 1 and reads

$$\tau_{\mathrm{e}} = -T_{\mathrm{L}}\log\left(r_{\mathrm{rand}}\right), \tag{8.79}$$

where,

$$T_{\mathrm{L}} \approx 0.30\frac{k}{\epsilon} \tag{8.80}$$

for the RSM model. Another important time scale is the particle eddy crossing time which is defined as

$$t_{\mathrm{cross}} = -\tau_{\mathrm{P}}\ln\left[1-\left(\frac{L_{\mathrm{e}}}{\tau_{\mathrm{P}}\left|u-u_{\mathrm{P}}\right|}\right)\right], \tag{8.81}$$

where, L_{e}, is the turbulent length scale, i.e. the Kolmogorov scale which is defined as

$$\eta_{\mathrm{K}} = \left(\frac{\nu_{\mathrm{g}}^3}{\epsilon}\right)^{1/4}. \tag{8.82}$$

After the minimum time of Eq. (8.79) and (8.81) has elapsed, new random numbers are generated to calculate the current fluid velocity.

8.2.2.2 Continuous Random Walk Model

Continuous random walk (CRW) models are based on the Langevin equation. The general Langevin equation reads [32, 139]

$$\mathrm{d}u_{\mathrm{i}} = -u_{\mathrm{i}}\left(t\right)\frac{\mathrm{d}t}{\tau_{\mathrm{i}}} + \sigma_{\mathrm{i}}\sqrt{\frac{2}{\tau_{\mathrm{i}}}}\mathrm{d}\xi_{\mathrm{i}}, \tag{8.83}$$

where, τ_i, is a time scale (the Lagrangian time scale, T_L, for example [139]), σ_i, is the rms value of the fluctuating velocity and $\mathrm{d}\xi_\mathrm{i}$, is a succession of uncorrelated numbers with zero mean and variance $\mathrm{d}t$ [32].

The approach by Ahn Ho and Sommerfeld [2] uses the correlation between the fluid at its old and new position, which is described by the following function

$$u'_{\mathrm{n+1}} = R_{\mathrm{P,i}}\left(\Delta t, \Delta r\right) u'_{\mathrm{i,n}} + \sigma_{\mathrm{F,i}} \sqrt{1 - R^2_{\mathrm{P,i}}\left(\Delta t, \Delta r\right)} \xi_\mathrm{i}. \tag{8.84}$$

The first term on the right-hand side is the correlated and the second, the uncorrelated part. The correlation function, $R_{\mathrm{P,i}}\left(\Delta t, \Delta r\right)$, is the product of a Lagrangian and an Eulerian factor:

$$R_{\mathrm{P,i}}\left(\Delta t, \Delta r\right) = R_\mathrm{L}\left(\Delta t\right) R_{\mathrm{E,i}}\left(\Delta r\right). \tag{8.85}$$

The index i denotes the direction in x, y or z. The Lagrangian component is often written as an exponential function, such as by Ahn Ho and Sommerfeld [2]:

$$R_\mathrm{L}\left(\Delta t\right) = \exp\left(-\frac{\Delta t}{T_\mathrm{L}}\right). \tag{8.86}$$

The Eulerian components give the correlation between two arbitrary points, a distance Δr separated from each other, and are written in a correlation tensor with the following components

$$R_{\mathrm{E,ij}}\left(\Delta r\right) = \left\{f\left(\Delta r\right) - g\left(\Delta r\right)\right\} \frac{r_\mathrm{i} r_\mathrm{j}}{r^2} + g\left(\Delta r\right) \delta_\mathrm{ij}. \tag{8.87}$$

Furthermore, Sommerfeld and Ho only take the diagonal terms into account, for which the longitudinal and transverse correlations are respectively given by

$$f\left(\Delta r\right)_\mathrm{i} = \exp\left(-\frac{\Delta r}{L_{\mathrm{E,i}}}\right), \tag{8.88a}$$

$$g\left(\Delta r\right)_\mathrm{i} = \left(1 - \frac{\Delta r}{L_{\mathrm{E,i}}}\right) \exp\left(-\frac{\Delta r}{L_{\mathrm{E,i}}}\right). \tag{8.88b}$$

In Eq. (8.88a) and (8.88b), the integral length scales for stream-wise and lateral components are given by

$$L_{\mathrm{E,x}} = 1.1 T_\mathrm{L} \sigma_\mathrm{F}, \tag{8.89a}$$

$$L_{\mathrm{E,y}} = L_{\mathrm{E,z}} = 0.5 T_\mathrm{L} \sigma_\mathrm{F}, \tag{8.89b}$$

where, the (turbulent) fluctuating velocity is taken from

$$\sigma_\mathrm{F} = \sqrt{\frac{2}{3} k}, \tag{8.90}$$

and thus treads turbulence homogeneous. However, since in regions near the wall, turbulence is not homogenous anymore and rms values and Lagrangian time scales are not position

independent anymore, Dehbi [32] adapted the general Langevin equation. His model is based on a drift correction by adding an extra term to the general Langevin equation (Eq. (8.83)), to ensure that tracer particles follow the streamlines. For example Legg and Raupach [85] modified the Langevin equation in wall normal direction

$$\mathrm{d}u_2 = -\frac{u_2\,(t)}{\tau_2}\mathrm{d}t + \sigma_2\sqrt{\frac{2}{\tau_2}}\mathrm{d}\xi_2 + \frac{\partial\sigma_2^2}{\partial x_2}\mathrm{d}t. \tag{8.91}$$

Dehbi [32] gives the following equations for the normalised Langevin equations near the wall for the streamwise, wall normal and spanwise direction, with index 1, 2 and 3 respectively

$$\mathrm{d}\left(\frac{u_1}{\sigma_1}\right) = -\left(\frac{u_1}{\sigma_1}\right)\frac{\mathrm{d}t}{\tau_1} + \sqrt{\frac{2}{\tau_1}}\mathrm{d}\xi_1 + \frac{\partial\left(\frac{\overline{u_1u_2}}{\sigma_1}\right)}{\partial x_2}\cdot\frac{\mathrm{d}t}{1+\mathrm{Stk}}, \tag{8.92a}$$

$$\mathrm{d}\left(\frac{u_2}{\sigma_2}\right) = -\left(\frac{u_2}{\sigma_2}\right)\frac{\mathrm{d}t}{\tau_2} + \sqrt{\frac{2}{\tau_2}}\mathrm{d}\xi_2 + \frac{\partial\sigma_2}{\partial x_2}\cdot\frac{\mathrm{d}t}{1+\mathrm{Stk}}, \tag{8.92b}$$

$$\mathrm{d}\left(\frac{u_3}{\sigma_3}\right) = -\left(\frac{u_3}{\sigma_3}\right)\frac{\mathrm{d}t}{\tau_3} + \sqrt{\frac{2}{\tau_3}}\mathrm{d}\xi_3. \tag{8.92c}$$

The factor $1/(1+\mathrm{Stk})$ in the last term in Eq. (8.92a)-(8.92b) scales the drift correction between zero for large particles, with large Stk numbers, and unity for tracer particles. In the bulk region, where turbulence is assumed to be isotropic, Eqs. (8.92a)-(8.92c) become

$$\mathrm{d}\left(\frac{u_1}{\sigma}\right) = -\left(\frac{u_1}{\sigma}\right)\frac{\mathrm{d}t}{T_\mathrm{L}} + \sqrt{\frac{2}{T_\mathrm{L}}}\mathrm{d}\xi_1 + \frac{1}{3\sigma}\frac{\partial k}{\partial x_1}\frac{\mathrm{d}t}{1+\mathrm{Stk}}, \tag{8.93a}$$

$$\mathrm{d}\left(\frac{u_2}{\sigma}\right) = -\left(\frac{u_2}{\sigma}\right)\frac{\mathrm{d}t}{T_\mathrm{L}} + \sqrt{\frac{2}{T_\mathrm{L}}}\mathrm{d}\xi_2 + \frac{1}{3\sigma}\frac{\partial k}{\partial x_2}\frac{\mathrm{d}t}{1+\mathrm{Stk}}, \tag{8.93b}$$

$$\mathrm{d}\left(\frac{u_3}{\sigma}\right) = -\left(\frac{u_3}{\sigma}\right)\frac{\mathrm{d}t}{T_\mathrm{L}} + \sqrt{\frac{2}{T_\mathrm{L}}}\mathrm{d}\xi_3 + \frac{1}{3\sigma}\frac{\partial k}{\partial x_3}\frac{\mathrm{d}t}{1+\mathrm{Stk}}. \tag{8.93c}$$

Dehbi [32] advises to take the Lagrangian time scales near the wall in Eq. (8.92) from fits of Kallio and Reeks [77] for the dimensionless Lagrangian time scale, T_L^+, as function of the dimensionless wall distance, y^+, as introduced in Eq. (8.48)

$$T_\mathrm{L}^+ = 10, \text{ for: } y^+ \leq 5 \tag{8.94}$$

$$T_\mathrm{L}^+ = 7.122 + 0.5731y^+ - 0.00129y^{+2}, \text{ for: } 5 \leq y^+ \leq 100. \tag{8.95}$$

In the bulk region he takes an ordinary calculation method

$$T_\mathrm{L} = \frac{2}{C_0}\frac{k}{\epsilon}, \tag{8.96}$$

with $C_0 = 14$. The values for the three dimensionless, fluctuating velocity components are

from Dreeben and Pope [37]

$$\sigma_1^+ = \frac{\sigma_1}{u^*} = \frac{0.40y^+}{1 + 0.0239\,(y^+)^{1.496}}, \tag{8.97a}$$

$$\sigma_2^+ = \frac{\sigma_2}{u^*} = \frac{0.0116y^{+2}}{1 + 0.203y^+ + 0.00140\,(y^+)^{2.421}}, \tag{8.97b}$$

$$\sigma_3^+ = \frac{\sigma_3}{u^*} = \frac{0.19y^+}{1 + 0.0361\,(y^+)^{1.322}}. \tag{8.97c}$$

8.2.2.3 Cloud Model

The cloud model calculates the particle tracks for each diameter from statistical fluid and particle properties [39, 95]. Starting from single injection points, a steady increasing area around a mean particle trajectory arises. The largest disadvantage is that for each particle diameter an own cloud has to be modelled, which makes the cloud model expensive in terms of computational effort.

8.2.2.4 Statistical Demands

Many particle trajectories must be calculated for a good statistical accuracy, mostly in the order of 10 000-100 000 [95]. Other authors use different numbers: Pascal and Oesterlé showed in their simulations of a simple shear flow with 10 000, 20 000 and 40 000 particles that the number of 20 000 particle was "sufficient" large for a "fair statistical" convergence [117]. However, Graham and Moyeed [50] state that the product of the number of particles, n_P, with the number of repetitions, n_r, determines the variability, but only if both numbers are sufficiently large by the following proportionality

$$\mathrm{var} \propto \sqrt{n_\mathrm{P} \cdot n_\mathrm{r}}. \tag{8.98}$$

50 to 100 repetitions appear to give reasonable results. Using smaller numbers risks the lack of smoothness in the results.

However, if particles are not released from a single point but from a surface, the number of repetitions might not be chosen too large to avoid the calculation of too many trajectories. Since the scatter of data measured in the experiments is relatively high, n_r is limited to 10 when using surface injections from 208 single points in the simulations of Ch. 11.

8.2.3 Boundary Conditions

The following boundary conditions are available in ANSYS Fluent 13.0 for the discrete phase for describing the particle behaviour when colliding with a wall, in- or outlet:

1. *escape*: particles leave the flow domain with the continuous phase. At this moment the particle trajectory is not calculated anymore. The vortex finder's exit has the escape boundary condition for a cyclone separator;

2. *trap*: each particle colliding with the wall is removed from the flow;

3. *reflect*: particles are bounced back after impacting with the wall. It is possible to give the coefficients of restitution in wall normal and tangential direction independent values as defined in Eq. (7.4). For a fully elastic impact, both equal unity;

4. *user defined.*

8.2.3.1 Particle-Wall Contact: Translational Velocity

Sommerfeld [133] distinguishes particle-wall collision with and without sliding. For a collision without sliding, Eq. (8.99) should be met

$$\left| w_{\mathrm{P},1} - \frac{d_\mathrm{P}}{2}\omega_{\mathrm{P},1} \right| < \frac{7}{2} k_\mathrm{s} \left(1 + e_\mathrm{n}\right) w_{\mathrm{P},1}. \tag{8.99}$$

Without sliding, the wall normal, tangential particle velocities after collision become

$$w_{\mathrm{P,n},2} = -e_\mathrm{n} w_{\mathrm{P,n},1}, \tag{8.100a}$$

$$w_{\mathrm{P,t},2} = \frac{1}{7}\left(5 w_{\mathrm{P,n},1} + d_\mathrm{P}\omega_{\mathrm{P},1}\right). \tag{8.100b}$$

and for a sliding collision:

$$w_{\mathrm{P,n},2} = -e_\mathrm{n} w_{\mathrm{P,n},1}, \tag{8.101a}$$

$$w_{\mathrm{P,t},2} = w_{\mathrm{P,t},1} - k_\mathrm{d}\left(1 + e_\mathrm{n}\right) w_{\mathrm{P,t},1}\epsilon_{0,\mathrm{r}}, \tag{8.101b}$$

The dynamic friction coefficient is denoted by k_d and the symbol $\epsilon_{0,\mathrm{r}}$, denotes the direction of the relative velocity between the particle's surface and the wall and is calculated with

$$\epsilon_{0,\mathrm{r}} = \mathrm{sgn}\left(w_{\mathrm{P},1,\mathrm{n}} - \frac{d_\mathrm{P}}{2}\omega_{\mathrm{P},1} \right). \tag{8.102}$$

8.2.3.2 Particle-Wall Contact: Rotational Velocity

For a collision without sliding, the particle rotational velocity after collision becomes

$$\omega_{\mathrm{P},2} = 2\frac{w_{\mathrm{P,n},2}}{d_\mathrm{P}}, \tag{8.103}$$

and for a sliding collision

$$\omega_{\mathrm{P},2} = \omega_{\mathrm{P},1} + 5k_\mathrm{d}\left(1 + e_\mathrm{n}\right)\frac{w_{\mathrm{P,t},1}}{d_\mathrm{P}}\epsilon_0. \tag{8.104}$$

8.2.4 Time Step

After a maximum number of time steps, over which the particle's trajectory has been calculated, the further calculation of the trajectory is aborted. There are two ways to define the time step:

1. From a length scale, L_s (which must be defined), the current particle velocity, w_P, and fluid velocity of the cell in which the particle is currently in, u_c

$$\Delta t = \frac{L_s}{w_P + u_c}. \tag{8.105}$$

The length scale has to be smaller than the dimensions of the cell.

2. From a factor, which predicts in how many steps the particle will travel through the cell. The default value in ANSYS Fluent 13.0 equals 5.

The time step can also be controlled by an user defined function. Sommerfeld [134] takes the time step equal to 20% of the smallest of the relevant time scales in the cell, in which the particle is currently in:

$$\Delta t = \min\left(\tau_P, T_L, \tau_{C,i}\right), \tag{8.106}$$

where, the particle relaxation time and Lagrangian time scale are defined as in Eq. (3.5) and (8.80), respectively. The inter-particle collision time is defined by Eq. (8.107) [134]:

$$\tau_{c,i} = \frac{1}{\frac{\pi}{4}\left(d_{P,min} + d_{P,max}\right)^2 \Delta w_{P,max} N_P}. \tag{8.107}$$

The collision diameter is defined by the minimal, $d_{P,min}$ and maximal, $d_{P,max}$, particle diameter in the particle size distribution function. $\Delta w_{P,max}$ is the maximal relative velocity between colliding particles. The particle concentration (N_P in $\frac{\#particles}{m^3}$) is dilute in the experiments described in Ch. 9. This means that $\tau_{c,i}$ becomes large for one way particle coupling and the time step becomes the minimum value of two other relevant time scales:

$$\Delta t = \min\left(\tau_P, T_L\right). \tag{8.108}$$

8.2.5 Separation Criteria

Several criteria, which are used by other authors to calculate the grade and total separation efficiency, are summarised in Tab.8.5. Some of the models are based on the event of particles to reach the cyclone's wall ([52, 93, 153]) or the bottom of the dustbin [46, 62]. Other authors consider particles as separated if they were not able to leave the computational domain through the vortex finder [3, 53]. Shi and Bayless [132] use a separation condition based on balances of force and moment of particles in contact with the wall.

In this thesis, the separation criterion of Gronald [53] is used, with the exception that the maximal number of time steps of 4×10^6 is not taken to cut off the calculation, which resulted in mean residence times of 26 s and 31 s for particles of 3 μm and 8 μm in diameter respectively. In stead of this, particles that are longer than 10 times the cyclone's volume refreshment time are assumed to be separated. This results in simulation times between 4.1 s and 8.2 s for volume flow rates of 600 m^3/h and 1 200 m^3/h respectively. This simulation time is shorter than the times used by Gronald [53], but assumed to be large enough for accurate results.

Table 8.5: *Particle separation criteria used in literature.*

Author	criterium
Ahn Ho and Sommerfeld [3]	Particles that do not leave the computational domain are considered to be separated.
Gorton-Hülgerth [46]	Particles that reach the bottom of the dustbin are separated.
Griffiths and Boysan [52]	Particles that touch the cylindrical wall are separated.
Gronald [53]	Particles that do not leave the computational domain are separated. The maximal number of time steps for calculating the trajectories is 4×10^6.
Hoekstra [62]	Particles that reach the dustbin are considered to be separated. Particles that reach to vortex finder are treated as overflow. Particles neither reaching the dustbin nor the vortex finder are not taken into the calculation of the separation efficiency.
Ma et al. [93]	Particles that hit the cyclone's wall are assumed to be washed down to the dustbin and are considered to be separated.
Shi and Bayless [132]	Particles that reach the wall and fulfil the separation condition of the force and moment balance are separated.
Yoshida [153]	Particles are assumed to be collected when they touch the cyclone's wall.

9 Experimental Investigations

Experiments were performed with the test cyclone shown in Fig. A.1 in App. A. The solid loading and volume flow rate were varied. The relative mass and kind of deposition appeared to be strongly dependent on these operating conditions.

9.1 Experimental Setup

The experiments were performed with the setup shown in Fig. 9.1. The material of the dispersed phase (A) is dosed into the experimental setup with a differential weighing scale (1) and transported through a vibrating chute (2) to the atomiser (3), where agglomerates of particles are disturbed. The volume flow rate of the continuous phase is controlled by an orifice (7), a throttle flap (9), a pressure regulator (10) and a blower (8). The created mixture is led into the cyclone (4), from which the separated dust (called the underflow) is collected in the dustbin (G). The slipped dust (F) leaves the cyclone through the vortex finder with the overflow and is separated in a bag filter (5).

9.2 Particle Size Distributions

The experiments were performed with approximately 7 kg limestone as feed, whose material properties are given in Tab. 9.1. After each experiment, the mass of the over-, underflow and depositions as well as the particle size distribution functions (PDF) were determined. The PDF's were measured with the SediGraph 5100, which is a laser analyser based on sedimentation. During the experiments the PDF's can *decrease* since the atomiser works as a mill or *increase* due to particle agglomeration inside the cyclone. Therefore, the PDF of the feed was compared with the mass weighted sum of the particular particle size distributions after the experiments. The cumulative particle volume/mass distribution function (CPDF) was fitted to a Rosin-Rammler-Sperling-Bennett (RRSB) function by Gebhard [42, 142]. The general equation of this function reads:

Table 9.1: *Material parameters of the feed (limestone) [42].*

Trading name	OMYACARB 5-GU	Chemical composition	
Mass density ρ_P	2770 kg/m^3	94%	$CaCO_3$
Median diameter $d_{P,50}$	5 μm	4-4.5%	$MgCO_3$
Parameters in the RRSB equation (Eq. 9.1) after atomiser			
$d_{P,50}$	4.5 μm	calculated from over- and underflow	
d'_P	6.06 μm	calculated from median diameter	
n_{RRSB}	1.2		

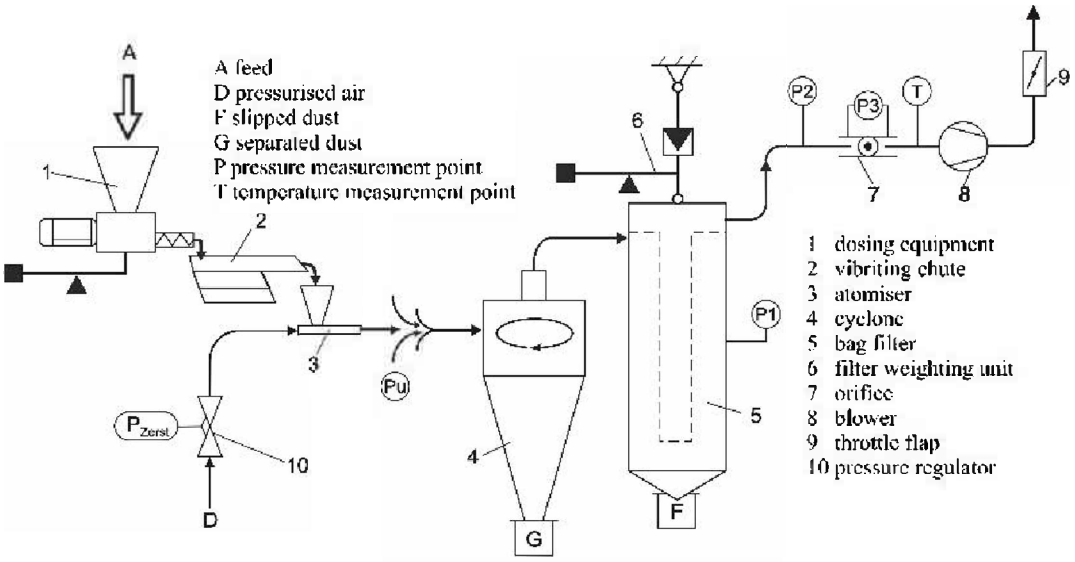

Figure 9.1: *Experimental setup.*

$$Q_3 = 1 - \exp\left[-\left(\frac{d_P}{d'_P}\right)^{n_{RRSB}}\right], \tag{9.1}$$

in which the median particle diameter, d'_P, was found to be 4.5 μm and the parameter n_{RRSB}, which is a measure for the width of the distribution, 1.2. In the CFD study, the Q_3 distribution was converted to a Q_0 distribution, as described by Hoffmann and Stein [66], and explained in App. D. As a consequence, the amount of small particles in the CFD study is relatively large, if the ratios between the particle diameters in the q_0 distribution function are remained. Alternatively a correction factor for each particle diameter can be used in such a way that each simulated particle represents a certain amount of real particles.

9.3 Experimental Results

With the setup as described in Ch. 9.1, several experiments were performed with volume flow rates of 600, 800, 1 000 and 1 200 m^3/h and with solid loadings of 0.66, 1.0, 2.0, 3.0, 5.31, 6.9 and 7.9 g/kg [69]. The ambient pressure, temperature and relative humidity of the air were determined at the beginning of the experiments. However, no significant correlations between the relative depositions in the cyclone and these weather conditions were found. Full details of the experimental results, as well as a statistical analysis can be found in App. B.

9.3.1 Structure and Location of the Depositions

The different parts of the cyclone showed the following kind of depositions [69] as illustrated with photographs in Fig. 9.2 and particle distribution functions in Fig. 9.5:

vortex finder inside: In all experiments a closed, thick, hard ring of depositions is visible on the lowest 5 to 10 mm of the tube. In the upper area, the depositions vary from pattern. They can exist of thin unpredictable lines, which reminds on the wet sand on the coast

after the waves have redrawn. Sometime, free spots with thicker depositions between them are seen. A closed helix with three or four windings is build in the extreme case. The median particle diameter is smaller than that of the depositions on the cyclone body and vertical tube section but slightly larger than that of the vortex finder outside. Furthermore, the particle size distribution function is relatively steep;

vortex finder outside: The character of the depositions is independent on the volume flow rate or solid loading and is similar to those on the vortex finder inside. The upper 5 to 10 mm, where the boundary flow of the roof is located, stay clean. This boundary flow has been observed in experiments performed from Gorton-Hülgerth et al. [48], who noticed high tangential velocities just on the edge between the vortex finder and the roof. Also the mean particle diameter in this region appeared to be higher than elsewhere. An up to 50 mm high deposition with a thickness between 0.2 and 1.0 mm is formed under this clean ring. The rest of the area is covered with a thin film. All depositions can be removed with a brush without any effort worth mentioning. The depositions on the vortex finder outside have the smallest median particle diameter. Similar depositions have been noticed by Brunnmair as shown in Fig. 9.3 [15];

roof: Depositions were only notices for experiments with a volume flow rate of 600 m^3/h at all solid loadings and of 800 m^3/h for low solid loadings. They are ring-shaped and seem to start from the top of the inlet for the experiments with a volume flow rate of 600 m^3/h. The depositions on the roof are stained for a volume flow rate of 800 m^3/h. The total mass of the deposition was, without any exception, too small for a particle size analysis;

cyclone body: A small stripe of deposits arises on the right hand side of the inlet during all experiments. From the inlets left hand side, a helix was formed. First, several spots of chevron-shaped depositions are visible, which grow together from the top to the bottom in a wider and thicker line. Thin depositions are hard to remove with a brush;

vertical tube section: In the upper part depositions are formed, whose structure is comparable with those formed on the vortex finder inside. The lower 10 cm are covered with up to 2.5 mm thick depositions whose structure varies from smooth to stained. These depositions continue around the corner on the back of the flange between the vertical tube section and the dustbin. The particle size distribution is the largest one of all depositions distinguished.

9.3.2 Relative Masses of the Depositions

The total sums of masses of the depositions on the parts distinguished, as a function of the volume flow rate and solid loading, are presented in Fig. 9.4(a). The total relative deposition, defined as the quotient of the deposited mass and the (total) feed mass, decreases for an increasing volume flow rate. In all experiments a maximum of the relative depositions arises around a solid loading of $\mu_e = 2$ g/kg. This maximum is best recognisable for the experiments with a volume flow rate of $\dot{V} = 600 m^3/h$, where the relative deposition is up to 5%wt of the feed mass.

The cyclone body and the vertical tube section have the largest contribution to the total depositions; those on in- and outside of the vortex finder are much less than 1 wt% of the feed. The depositions on the roof only arise at a volume flow rate of 600 m^3/h and low solid loadings.

(a) Vortex finder inside with a helix of thick depositions on an underlay with a pattern of thin lines ($V600\_\mu_e1.0$).

(b) Vortex finder outside with the three regions of depositions: a clean ring, thick depositions, thin depositions ($V600\_\mu_e3.0$).

(c) The cyclone's roof covered with a closed ring of depositions ($V600\_\mu_e2.0$).

(d) Vertical tube section and flange with thick, stained depositions ($V600\_\mu_e3.0$).

(e) Almost clean cyclone body at ($V1200\_\mu_e3.0$).

(f) Almost full covered cyclone body with "chevron shaped" depositions ($V600\_\mu_e2.0$).

Figure 9.2: *Typical depositions on the distinguished cyclone parts during experiments with volume flow rate* V [m^3/h] *and solid loading* μ_e [g/kg].

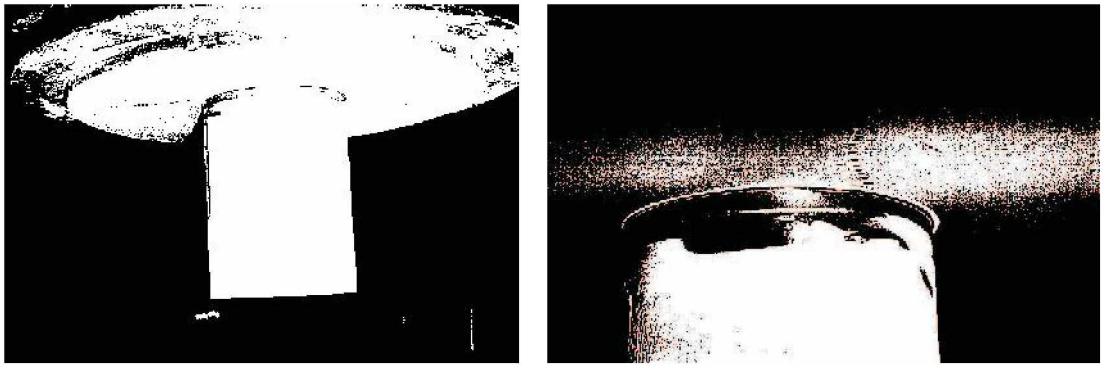

(a) Depositions on the vortex finder and roof during the experiments of Brunnmair.

(b) Detail of the depositions with the ring of clean area visible.

Figure 9.3: *Depositions during the experiments of Brunnmair [15] .*

9.3.3 Statistical Analysis of the Maximal Relative Deposition

To proof that the total sum of the depositions have a maximum around a solid loading of $\mu_e = 2.0$ g/kg at a volume flow rate of $\dot{V} = 600$ m^3/h, a hypothesis test is made. The null- and alternative hypothesis are respectively defined as

- H_0: $\bar{x}_2 = \bar{x}_i$ and
- H_1: $\bar{x}_2 \neq \bar{x}_i$.

Here, $\bar{x}_2$ is the mean relative deposited mass during the experiments at a solid loading of $\mu_e = 2.0$ g/kg and $\bar{x}_i$ that at $\mu_e = 1.0$ g/kg or $\mu_e = 3.0$ g/kg, respectively. In Tab. 9.2 it is demonstrated that the total depositions at $\mu_e = 2.0$ g/kg differ from those at $\mu_e = 1.0$ g/kg and $\mu_e = 3.0$ g/kg with a probability between 99.0% and 98.6%. Therefore, a local maximum can be assumed. At a volume flow rate of 800 m^3/h these values are less pronounced but still 80.6% and 77.0%. For a volume flow rate of 1 000 m^3/h these values become 70.7% and 80.4% and for 1 200 m^3/h 87.1% and 62.8%. Full tables with the statistical analyses of for the volume flow rates of 800, 1 000 and 1 200 m^3/h can be found in App. B.

9.3.4 Particle Size Distributions of the Depositions

The particle size distributions of the depositions are in between those of the under- and overflow as seen in Fig. 9.5(a) and 9.5(b). The depositions on the vortex finder, both inside and outside, are finer than the feed. Those on the cyclone body and vertical tube are coarser.

The particle size distribution curve for the vortex finder inside is steeper than that for the outside, which indicates a narrower particle size distribution function. A possible explanation is that all particle sizes of the feed reach the vortex outside from which the smallest ones tend to deposit on this part. Alternatively they may form agglomerates elsewhere in the cyclone. In the vortex finder inside only small particles deposit, which are hardly larger than those in the overflow.

The depositions on the body and the vertical tube section are larger in diameter. The particle size distribution curve of the latter one is almost equal to that of the underflow for particles smaller than 4 μm, although particles larger than 20 μm do not appear.

Table 9.2: *Calculation procedure for the student t-test, that the total relative mass depositions during the experiments V600_μ_e2.0 (index 2) are always larger than those during the experiments V600_μ1.0 (index 1) and V600_μ_e3.0 (index 3) respectively, with a significance level of α ($\mu_{e,i}$, population mean value, $\bar{x}_i$, sample mean, n the sample size) More information about the hypothesis testing can be found in App. B.*

Part	H_0	H_1	n_1	n_2	n_3	$\bar{x}_1$ [%]	$\bar{x}_2$ [%]	$\bar{x}_3$ [%]	s_1	s_2	s_3	t_0	α	$(1-\alpha)$ [%]
all parts	$\mu_{e,1} = \mu_{e,2}$	$\mu_{e,1} < \mu_{e,2}$	5	3	-	1.9081	5.2547	-	1.5911	1.2337	-	3.3240	0.0095	99.0
	$\mu_{e,3} = \mu_{e,2}$	$\mu_{e,3} < \mu_{e,2}$	-	3	3	-	5.2547	2.0775	-	1.2337	1.0304	3.4235	0.0140	98.6
vortex finder outside	$\mu_{e,1} = \mu_{e,2}$	$\mu_{e,1} < \mu_{e,2}$	5	3	-	0.0862	0.1581	-	0.0559	0.0160	-	2.6978	0.0215	97.7
	$\mu_{e,3} = \mu_{e,2}$	$\mu_{e,3} < \mu_{e,2}$	-	3	3	-	0.1581	0.1267	-	0.0160	0.0796	0.6701	0.2836	71.6
vortex finder inside	$\mu_{e,1} = \mu_{e,2}$	$\mu_{e,1} < \mu_{e,2}$	5	3	-	0.1936	0.6971	-	0.2102	0.2387	-	3.0184	0.0204	98.0
	$\mu_{e,3} = \mu_{e,2}$	$\mu_{e,3} < \mu_{e,2}$	-	3	3	-	0.6971	0.6318	-	0.2387	0.1769	0.3811	0.3620	63.8
roof	$\mu_{e,1} = \mu_{e,2}$	$\mu_{e,1} < \mu_{e,2}$	5	3	-	0.0286	0.0248	-	0.0319	0.0429	-	0.1363	0.4497	55.0
	$\mu_{e,3} = \mu_{e,2}$	$\mu_{e,3} < \mu_{e,2}$	-	3	3	-	0.0248	0.0037	-	0.0429	0.0065	0.8400	0.2430	75.7
cyclone body	$\mu_{e,1} = \mu_{e,2}$	$\mu_{e,1} < \mu_{e,2}$	5	3	-	0.7663	3.7317	-	1.0128	0.9595	-	4.1441	0.0055	99.5
	$\mu_{e,3} = \mu_{e,2}$	$\mu_{e,3} < \mu_{e,2}$	-	3	3	-	3.7317	0.8158	-	0.9595	1.0947	3.4695	0.0132	98.7
vertical tube section	$\mu_{e,1} = \mu_{e,2}$	$\mu_{e,1} < \mu_{e,2}$	5	3	-	0.4532	0.6430	-	0.6378	0.2355	-	0.6008	0.2860	71.4
	$\mu_{e,3} = \mu_{e,2}$	$\mu_{e,3} < \mu_{e,2}$	-	3	3	-	0.6430	0.4996	-	0.2355	0.1546	0.8830	0.2174	78.3

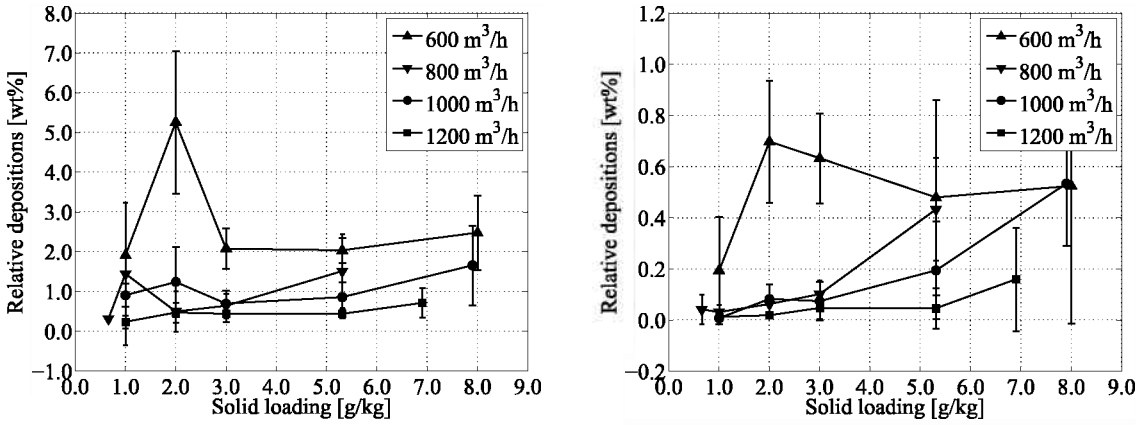

(a) Sum of all parts.

(b) Vortex finder outside.

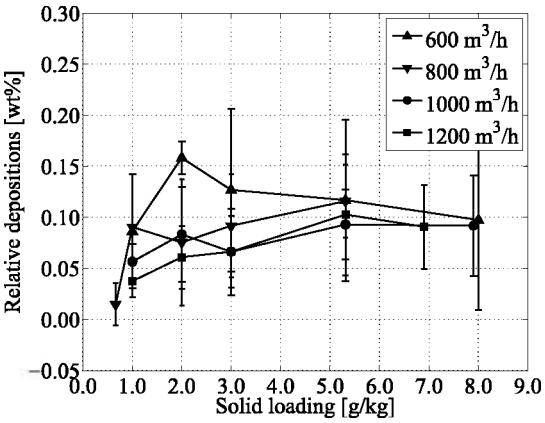

(c) Vortex finder inside.

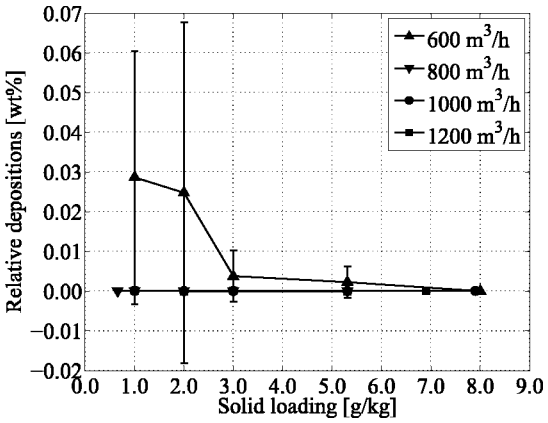

(d) Roof.

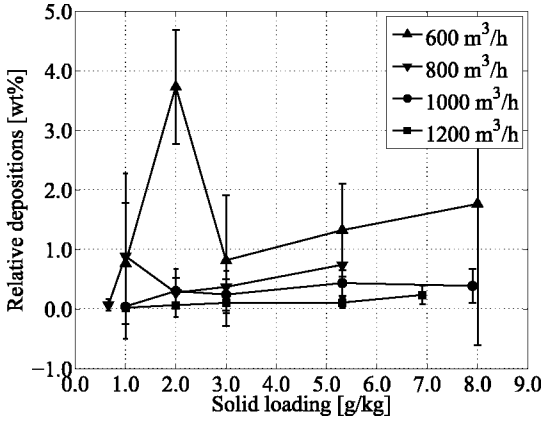

(e) Cyclone body.

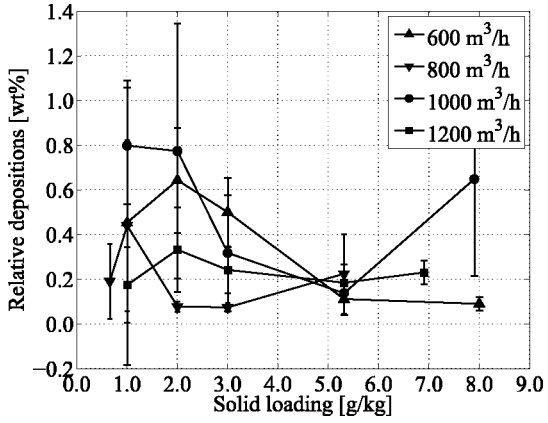

(f) Vertical tube section.

Figure 9.4: *Relative deposited masses and their standard deviations in %wt of the total solid feed mass for several air volume flow rates and solid loadings.*

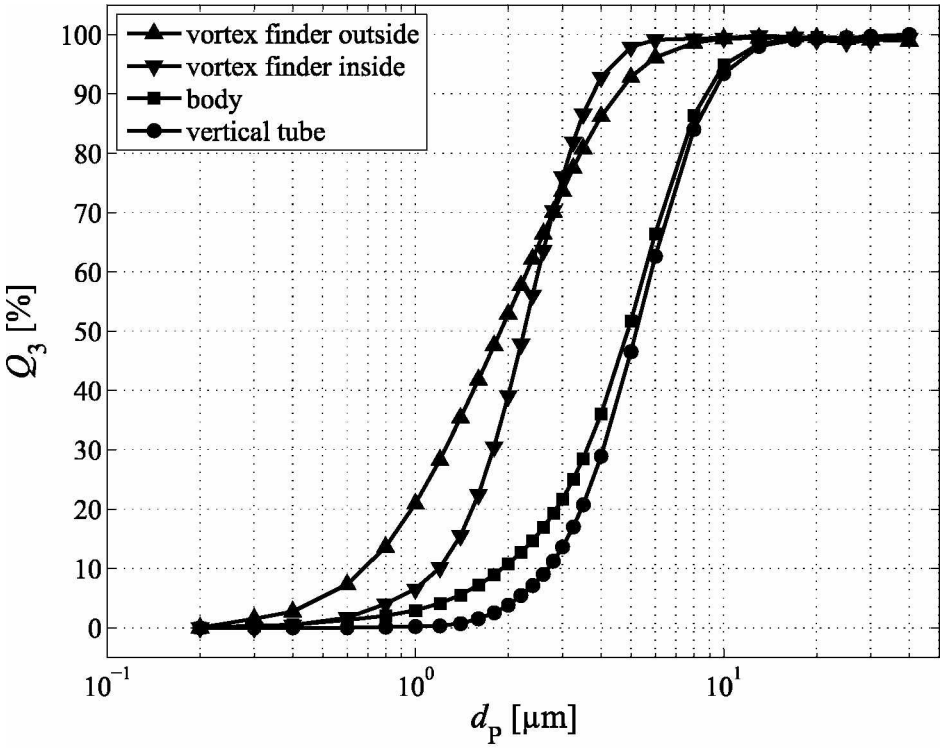

(a) Particle size distributions of the depositions.

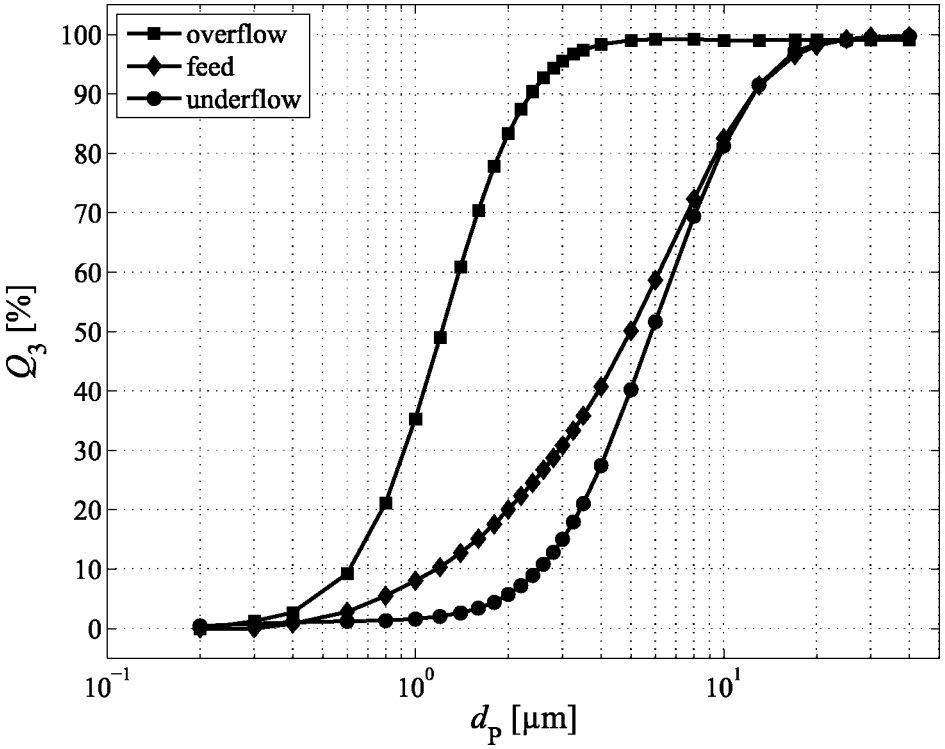

(b) Particle size distributions of the feed, over- and underflow.

Figure 9.5: *Particle size distributions of the feed, over- and underflow and depositions during the experiment with a volume flow rate of* $\dot{V} = 600\ \mathrm{m^3/h}$ *and solid loading of* $\mu_e = 2.0\ \mathrm{g/kg}$.

10 Introduction of a Particle Velocity Damping Factor

Usually, in computational fluid dynamics (CFD) simulations, the size of the mesh is smaller in the near wall regions. These boundary layers can be made by a commercial software package. Although, some three-dimensional geometries (e.g. a cyclone separator) are so complex, that it is nearly impossible to create a consistent boundary layer for all walls at the same time. Furthermore, the size of the cells in the boundary layer will be still approximately two orders of magnitude larger than the typical diameter of a particle in a multiphase flow (which is usually in the range of 0.1 to 100 μm). Therefore the wall near flow field is not well resolved and a simulation of that kind will be unable to describe the particle's trajectory near the wall correctly. The underresolved wall region leads to overpredicted impact velocities even for small tracer particles.

Therefore, it is useful to introduce a damping factor, which relates the particle's impact velocity, $\boldsymbol{w}_{\mathrm{P,e}}$, directly with its velocity at the time it has entered the wall neighbouring cell, $\boldsymbol{w}_{\mathrm{P,0}}$

$$\zeta_{\mathrm{tot}} = \frac{|\boldsymbol{w}_{\mathrm{P,e}}|}{|\boldsymbol{w}_{\mathrm{P,0}}|}, \tag{10.1}$$

such as drawn in Fig. 10.1. The indices 0 and e denote the time for a particle entering the cell and the time past until collision respectively. The total velocity damping factor is devided into a wall normal (index n) and a tangential (index t)[1] component, which are defined as:

$$\zeta_{\mathrm{n}} = \frac{w_{\mathrm{P,n,e}}}{w_{\mathrm{P,n,0}}}, \tag{10.2a}$$

$$\zeta_{\mathrm{t}} = \frac{w_{\mathrm{P,t,e}}}{w_{\mathrm{P,t,0}}}. \tag{10.2b}$$

The relation between ζ_{n} and ζ_{t} in respect with ζ_{tot} reads

[1] As simplification in this thesis, the vectors of the wall tangential fluid and particle cell entrance velocity are assumed to have the same direction but can differ in magnitude. In reality, two perpendicular tangential vectors exist, which have the independent tangential damping factors $\zeta_{\mathrm{t},1} = \frac{w_{\mathrm{P,t,e,1}}}{w_{\mathrm{P,t,0,1}}}$ and $\zeta_{\mathrm{t},2} = \frac{w_{\mathrm{P,t,e,2}}}{w_{\mathrm{P,t,0,2}}}$. From this, the total tangential damping factor follows analog to Eq. (10.3): $\zeta_{\mathrm{t}} = \sqrt{\zeta_{\mathrm{t},1}^2 \cos^2 \alpha_{\mathrm{t}} + \zeta_{\mathrm{t},2}^2 \sin^2 \alpha_{\mathrm{t}}}$ with $\alpha_{\mathrm{t}} = \arctan\left(\frac{w_{\mathrm{P,t,0,2}}}{w_{\mathrm{P,t,0,1}}}\right)$. The tangential vectors can be defined in such a way that the first one is parallel and the second one perpendicular to the tangential fluid velocity vector at the wall. Therefore, the assumption makes a quasi two dimensional analysis possible.

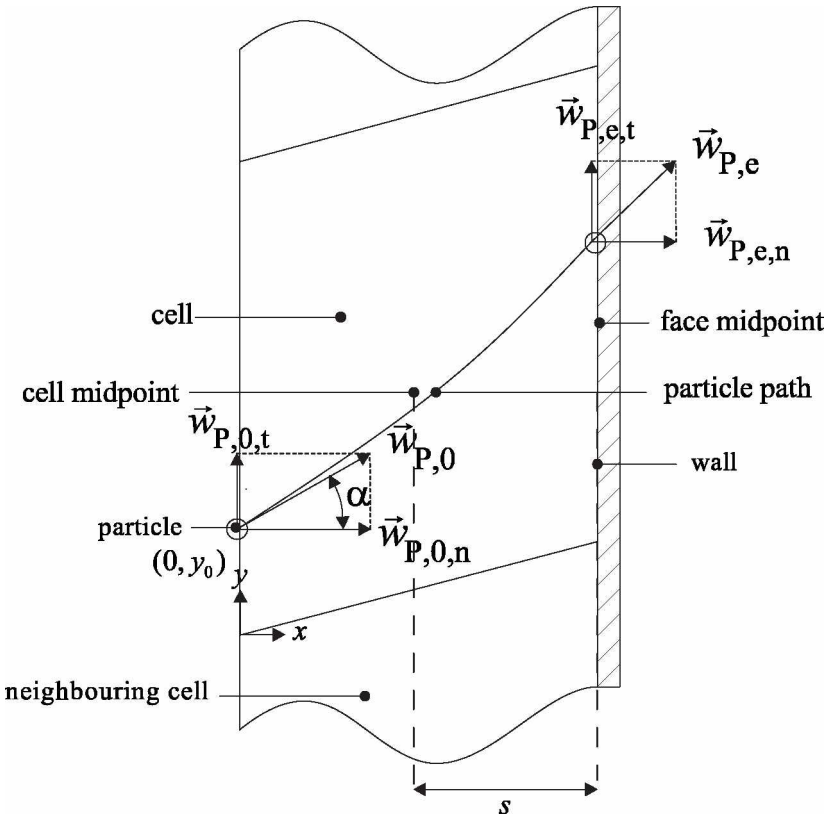

Figure 10.1: *Problem definition: a particle enters a hexaeder cell at the local coordinates* $(x, y) = (0, y_0)$ *through the face opposite of the wall boundary with velocity* $w_{P,0}$ *and angle* α *in respect with the wall normal vector at the fictive time* $t = 0$ *and moves along a, from the flow field prescribed, path until it colloids with the wall at time* $t = t_e$ *with end velocity* $w_{P,e}$*, covering twice the distance s in wall normal direction. The local coordinate system is defined by the vector x in wall normal negative direction and y in tangential direction with its origin in the cell's corner. Along this coordinate system, the particle's velocity is divided into a wall normal and tangential component with indices n and t respectively.*

$$\zeta_{\mathrm{tot}} = \sqrt{\zeta_{\mathrm{n}}^2 \cos^2\alpha + \zeta_{\mathrm{t}}^2 \sin^2\alpha} \tag{10.3a}$$

$$\alpha = \arctan\left(\frac{w_{\mathrm{P,t,0}}}{w_{\mathrm{P,n,0}}}\right), \tag{10.3b}$$

where, α is the angle between the particle velocity vector and the wall normal vector at time $t = 0$. Since,

$$\cos^2\left\{\arctan\left(\frac{w_{\mathrm{P,t,0}}}{w_{\mathrm{P,n,0}}}\right)\right\} = \frac{1}{1+\left(\frac{w_{\mathrm{P,t,0}}}{w_{\mathrm{P,n,0}}}\right)^2} \tag{10.4a}$$

$$\sin^2\left\{\arctan\left(\frac{w_{\mathrm{P,t,0}}}{w_{\mathrm{P,n,0}}}\right)\right\} = \frac{\left(\frac{w_{\mathrm{P,t,0}}}{w_{\mathrm{P,n,0}}}\right)^2}{1+\left(\frac{w_{\mathrm{P,t,0}}}{w_{\mathrm{P,n,0}}}\right)^2}, \tag{10.4b}$$

Eq. (10.3a) and (10.3b) can be written together as

$$\zeta_{\mathrm{tot}} = \sqrt{\frac{1}{1+\left(\frac{w_{\mathrm{P,t,0}}}{w_{\mathrm{P,n,0}}}\right)^2}\left(\zeta_{\mathrm{n}}^2 + \zeta_{\mathrm{t}}^2\left(\frac{w_{\mathrm{P,t,0}}}{w_{\mathrm{P,n,0}}}\right)^2\right)}. \tag{10.5}$$

From Eq. (10.5) it is obvious that ζ_{tot} is only a function of the velocity components at $t = 0$, which will be known from the macros in commercial CFD software programs, ζ_{n} and ζ_{t}. For the calculation of the latter two quantities as function of other flow macros, in this thesis a proposal is made, which follows from the equation of motion for the following restriction for the dimensionless particle relaxation time as introduced in Eq. (3.4):

> Since Brownian motion is not taken into account in this thesis for the calculation of the particle's trajectory in the wall neighbouring cell and turbulent fluid motion is only calculated once from the Reynolds stress values and a random generated number, the results in diffusional-deposition and in the diffusion-impaction regime should be treated with caution. Turbulence is not important in case that the wall neighbouring cell is in the viscous sublayer with thickness
>
> $$1 \times \nu_{\mathrm{g}}/u_* < \delta_{\mathrm{v}} < 10 \times \nu_{\mathrm{g}}/u_*, \tag{10.6}$$
>
> where, the rms value of the fluctuating velocity components is much smaller than u_* [154]. It should be avoided to place the first cell in the buffer layer. However, for a wide range of volume flow rates this could be the problem if no (local) adaptation of the grid is desired or possible. In this thesis, a method is presented to predict the particle impact velocity more accurate in case of $5 < y^+ < 60$.

10.1 Equation of Motion

Given a particle diameter much smaller than the dimensions of a cell in the grid, the cell's midpoint velocity is not a good measure for its final impact velocity, because of the no-slip

condition of the fluid at the wall. Three types of flow profiles in the boundary layer (see Fig. 10.2), which meet the no-slip criterion, are proposed and finally compared for several typical impact situations. Therefore, the differential equation describing the particle's movement is set up using Newtons second law of motion

$$\boldsymbol{F}_{\mathrm{res}} = m_{\mathrm{P}} \cdot \frac{\mathrm{d}\boldsymbol{w}_{\mathrm{P}}}{\mathrm{d}t}, \tag{10.7}$$

where, $\boldsymbol{F}_{\mathrm{res}}$ denotes the resultant force working on the particle with current velocity, $\boldsymbol{w}_{\mathrm{P}}$, along the position vector, $\boldsymbol{x}$, and t, the time calculated from the moment a particle enters the cell.

For a spherical particle in a laminar flow, the mass is given by $m_{\mathrm{P}} = \frac{\pi}{6}\rho_{\mathrm{P}} d_{\mathrm{P}}^3$ and the drag force in the Stokes regime according to Bird, Stewart and Lightfoot [10] as

$$\boldsymbol{F}_{\mathrm{D}} = \frac{-3\pi\mu_{\mathrm{g}}\left(\boldsymbol{w}_{\mathrm{P}} - \boldsymbol{w}_{\mathrm{g}}\right) d_{\mathrm{P}}}{C_c}, \tag{10.8}$$

with the minus sign denoting, that $\boldsymbol{F}_{\mathrm{D}}$ is in opposite direction of the difference between particle and gas velocity, $\boldsymbol{w}_{\mathrm{g}}$. According to Bird et al. [10], Eq. (10.8) is valid for particle Reynolds numbers $\mathrm{Re}_{\mathrm{P}} = \frac{d_{\mathrm{P}} v_\infty \rho_{\mathrm{g}}}{\mu_{\mathrm{g}}}$ of about 0.1. For $\mathrm{Re}_{\mathrm{P}} = 1$, Eq. (10.8) overestimates the drag force by approximately 10%.

The Cunningham slip correction factor, C_{c}, is used for particle diameters around the mean free path of the carrier gas molecules, λ_{g}, and is calculated as in Eq. (3.6).

McLaughlin [99] states that furthermore only the Saffman lift force plays a role in the equation of motion and neglects gravity, the virtual mass effect, and Basset history terms. The Saffman lift force has already been introduced in Eq. (4.65).

Although the Saffman lift force is known to play an important role in the deposition of particles [99], it is not taken into account within the current derivation because of the nonlinearity of Eq. (4.65) in respect with $\boldsymbol{w}_{\mathrm{P,t}}$ and because it is small compared to the wall normal drag, especially in the viscous sublayer close to the wall [99]. This means, its ratio to the drag force must be much smaller than unity:

$$\begin{aligned}\left|\frac{\boldsymbol{F}_{\mathrm{L,Saff}}}{\boldsymbol{F}_{\mathrm{D,n}}}\right| &= \frac{1.615}{3\pi}\frac{C_{\mathrm{c}} d_{\mathrm{P}}}{\nu_{\mathrm{g}}}\sqrt{\frac{\tau_{\mathrm{w}}}{\rho_{\mathrm{g}}}}\left|\frac{w_{\mathrm{g,t}} - w_{\mathrm{P,t}}}{w_{\mathrm{g,n}} - w_{\mathrm{P,n}}}\right| \\ &= \frac{1.615}{3\pi} C_{\mathrm{c}} \frac{d_{\mathrm{P}}}{s} y^+ \left|\frac{w_{\mathrm{g,t}} - w_{\mathrm{P,t}}}{w_{\mathrm{g,n}} - w_{\mathrm{P,n}}}\right|\end{aligned} \tag{10.9}$$

For a grid with good quality the value of y^+ should be in the range of 30-300. If furthermore $C_{\mathrm{c}} \approx 1$ and $\left|\frac{w_{\mathrm{g,t}} - w_{\mathrm{P,t}}}{w_{\mathrm{g,n}} - w_{\mathrm{P,n}}}\right| \approx 1$, the wall normal drag will be one order of magnitude larger than the Saffman lift force for a particle of 20 μm in diameter for a cell with dimensions of 1 cm and for a particle of 2 μm in a cell with dimensions of 1 mm.

Also the ratio of the turbophoresis force, which is defined in Eq. (4.70), to the wall normal drag force must be much smaller than unity:

$$\begin{aligned}\left|\frac{\boldsymbol{F}_{\mathrm{Tu}}}{\boldsymbol{F}_{\mathrm{D}}}\right| &= \frac{\tau_{\mathrm{P}}}{2\left(w_{\mathrm{P,n}} - w_{\mathrm{g,n}}\right)}\frac{\mathrm{d}\overline{u_{\mathrm{n}}'}^2}{\mathrm{d}\boldsymbol{n}} \\ &\approx \frac{1}{2}\frac{\tau_{\mathrm{P}} w_{\mathrm{P,n}}}{s}\frac{u_{\mathrm{n}}'^2}{{w_{\mathrm{P,n}}}^2} = \frac{1}{2}\mathrm{Stk}_{\mathrm{n}}\frac{u_{\mathrm{n}}'^2}{{w_{\mathrm{P,n}}}^2}.\end{aligned} \tag{10.10}$$

The second factor is the current wall normal Stokes number, i.e. calculated from the instant wall normal particle velocity (which has value between that at the moment of entering the wall neighbouring cell and that at the time of colliding with the wall), and will be approximately unity. Therefore, the fluctuating velocity component should much smaller than the particle-wall normal velocity ($u'_{\mathrm{n}} << w_{\mathrm{P,n}}$).

After substitution of Eq. (10.8) into Eq. (10.7), under assumption of Eq. (10.9) and (10.10) the following equation is found

$$\frac{\mathrm{d}\boldsymbol{w}_{\mathrm{P}}}{\mathrm{d}t} = \frac{-1}{\tau_{\mathrm{P}}}\left(\boldsymbol{w}_{\mathrm{P}} - \boldsymbol{w}_{\mathrm{g}}\right), \tag{10.11}$$

where, the particle relaxation time, τ_{P}, has been introduced in Eq. (3.5).

10.2 Dimensionless Quantities

Eq. (10.11) is made dimensionless by the use of the the following scaling parameters

$$t' = \frac{t}{\tau_{\mathrm{P}}}, \tag{10.12a}$$

$$\boldsymbol{w}'_{\mathrm{P}} = \frac{\boldsymbol{w}_{\mathrm{P}}}{\boldsymbol{w}_{\mathrm{P,0}}}, \tag{10.12b}$$

$$\boldsymbol{w}'_{\mathrm{g}} = \frac{\boldsymbol{w}_{\mathrm{g}}}{2\boldsymbol{w}_{\mathrm{cell}}}, \tag{10.12c}$$

where, $\boldsymbol{w}_{\mathrm{cell}}$, is the cell's fluid velocity calculated at the point $(x, y) = (s, y_0)$ by linear extrapolation from the closest cell's midpoint (index MP):

$$w_{\mathrm{cell}} \approx w_{\mathrm{g}}|_{\mathrm{MP}} + \left.\frac{\partial w_{\mathrm{g}}}{\partial X}\right|_{\mathrm{MP}} \Delta X + \left.\frac{\partial w_{\mathrm{g}}}{\partial Y}\right|_{\mathrm{MP}} \Delta Y + \left.\frac{\partial w_{\mathrm{g}}}{\partial Z}\right|_{\mathrm{MP}} \Delta Z \tag{10.13}$$

X, Y and Z are the components of the global cartesian coordinate system and ΔX, ΔY and ΔZ those of the distance vector between the point (s, y_0) and the nearest cell's midpoint.

The following dimensionless differential equation is found:

$$\frac{\mathrm{d}\boldsymbol{w}'_{\mathrm{P}}}{\mathrm{d}t'} = -\left(\boldsymbol{w}'_{\mathrm{P}} - \frac{2\boldsymbol{w}_{\mathrm{cell}}}{\boldsymbol{w}_{\mathrm{P,0}}}\boldsymbol{w}'_{\mathrm{g}}\right), \tag{10.14}$$

in which the velocities can be split into a normal and tangential component in respect of the wall

$$\frac{\mathrm{d}w'_{\mathrm{P,n}}}{\mathrm{d}t'} = -\left(w'_{\mathrm{P,n}} - \frac{2w_{\mathrm{cell,n}}}{w_{\mathrm{P,0,n}}}w'_{\mathrm{g,n}}\right), \tag{10.15a}$$

$$\frac{\mathrm{d}w'_{\mathrm{P,t}}}{\mathrm{d}t'} = -\left(w'_{\mathrm{P,t}} - \frac{2w_{\mathrm{cell,t}}}{w_{\mathrm{P,0,t}}}w'_{\mathrm{g,t}}\right). \tag{10.15b}$$

Table 10.1: *Variables used for the dimensionless numbers in the Buckingham-pi theorem ([18]).*

quantity	unit	dimension
$w_{\mathrm{P,0,n}}$	$\mathrm{m\,s^{-1}}$	$l\,t^{-1}$
$w_{\mathrm{P,0,t}}$	$\mathrm{m\,s^{-1}}$	$l\,t^{-1}$
w_{cell}	$\mathrm{m\,s^{-1}}$	$l\,t^{-1}$
ρ_{P}	$\mathrm{kg\,m^{-3}}$	$m\,l^{-3}$
ρ_{g}	$\mathrm{kg\,m^{-3}}$	$m\,l^{-3}$
d_{P}	m	l
s	m	l
x	m	l
λ_{g}	m	l
t_{end}	s	t
μ_{g}	$\mathrm{kg\,m^{-1}\,s^{-1}}$	$m\,l^{-1}\,t^{-1}$

The particle velocity components are

$$w_{\mathrm{P,0,n}} = \boldsymbol{w}_{\mathrm{P},0} \cdot \boldsymbol{n} \tag{10.16a}$$

$$w_{\mathrm{P,0,t}} = \left|\boldsymbol{w}_{\mathrm{P},0} - \boldsymbol{w}_{\mathrm{P,0,n}}\right|. \tag{10.16b}$$

The quantities listed in Tab. 10.1 are used in the differential equation or are relevant for the system. There are $n = 11$ variables and $k = 3$ basic units, so according the Buckingham-pi theorem [18] $n - k = 11 - 3 = 8$ independent dimensionless numbers describe the system. If the particle variables ($w_{\mathrm{P,0,n}}$, d_{P} and ρ_{P}) are (arbitrarily) chosen as fundamental, these dimensionless numbers become:

$$\pi_1 = \frac{w_{\mathrm{cell}}}{w_{\mathrm{P,0,n}}}, \tag{10.17a}$$

$$\pi_2 = \frac{w_{\mathrm{cell}}}{w_{\mathrm{P,0,t}}}, \tag{10.17b}$$

$$\pi_3 = \frac{\mu_{\mathrm{g}}}{w_{\mathrm{P,0,n}}\rho_{\mathrm{P}}d_{\mathrm{P}}} = \frac{1}{\mathrm{Re}_{\mathrm{P,n}}}, \tag{10.17c}$$

$$\pi_4 = \frac{\rho_{\mathrm{g}}}{\rho_{\mathrm{P}}}, \tag{10.17d}$$

$$\pi_5 = \frac{s}{d_{\mathrm{P}}}, \tag{10.17d}$$

$$\pi_6 = \frac{\lambda_{\mathrm{g}}}{d_{\mathrm{P}}} = \mathrm{Kn}, \tag{10.17e}$$

$$\pi_7 = \frac{x}{s}, \tag{10.17f}$$

$$\pi_8 = \frac{w_{\mathrm{P,0,n}}\tau_{\mathrm{P}}}{d_{\mathrm{P}}}. \tag{10.17g}$$

It will follow from section 10.3 that only the following three dimensionless numbers are relevant for the calculation of ζ_{tot}

$$\Pi_1 = \frac{w_{\mathrm{P,0,n}}\tau_{\mathrm{P}}}{s} = \mathrm{Stk}_{\mathrm{0,n}} = \frac{\pi_8}{\pi_5}, \tag{10.18a}$$

$$\Pi_2 = \frac{w_{\mathrm{cell}}}{w_{\mathrm{P,0,t}}} = \pi_2, \tag{10.18b}$$

$$\Pi_3 = \frac{w_{\mathrm{P,0,n}}}{w_{\mathrm{P,0,t}}} = \cot(\alpha) = \frac{\pi_1}{\pi_2}. \tag{10.18c}$$

The dimensionless particle relaxation time follows from the following combination of the

dimensionless numbers

$$\tau_{P+} = \frac{\Pi_1 \cdot \Pi_2}{\Pi_3}. \tag{10.19}$$

10.3 Velocity Damping Factor

It may be clear that for small values of $\frac{2w_{\text{cell,i}}}{w_{\text{P,0,i}}}$ in Eq. (10.15), the gas velocity, which can be approximated by a function of the wall distance, is negligible. This will be the case for the wall normal velocity; streamlines approaching the wall will bend into tangential direction since the wall is impermeable. For particle deposition this is described by Cleaver and Yates [24]. Hence, Eq. (10.15a), without the 2nd term between the brackets, is solved for the particle velocity

$$w_{\text{P,n}} = w_{\text{P,0,n}} e^{-t/\tau_{\text{P}}} \tag{10.20a}$$

$$x = \tau_{\text{P}} w_{\text{P,0,n}} \left(1 - e^{-t/\tau_{\text{P}}}\right). \tag{10.20b}$$

The cell has a width of twice the to the wall normal projected vector between the cell's and face's midpoint, $\boldsymbol{r}$, which is calculated from

$$s = |\boldsymbol{r} \cdot \boldsymbol{n}|. \tag{10.21}$$

Thus, the distance travelled in wall normal direction, x, in Eq. (10.20b) is put equal to $2s$ to calculate the end time for the particle between entering the cell and colliding at the wall:

$$\begin{aligned} t_{\text{end}} &= -\tau_{\text{P}} \ln\left(1 - \frac{2s}{\tau_{\text{P}} w_{\text{P,0,n}}}\right) \\ &= -\tau_{\text{P}} \ln\left(1 - \frac{2}{\text{Stk}_{\text{0,n}}}\right). \end{aligned} \tag{10.22}$$

This end time should have a positive, real value in case of a collision, so only particles with

$$\text{Stk}_{\text{0,n}} > \text{Stk}_{\text{0,n,crit}} = 2 \tag{10.23}$$

will be able to reach the wall. After substitution into Eq. (10.20a) and division by $w_{\text{P,0,n}}$ the damping term for the wall normal velocity is found

$$\begin{aligned} \zeta_{\text{n}} &= 1 - \frac{2s}{\tau_{\text{P}} w_{\text{P,0,n}}} \\ &= 1 - \frac{2}{\text{Stk}_{\text{0,n}}}, \end{aligned} \tag{10.24}$$

whose value has to be between 0 and 1 by definition.

If the assumption that $w_{\text{cell,n}} = 0$ cannot be made but $w_{\text{cell,n}}$ is assumed to be constant in space and time (it should be noticed that in this case the wall is not impermeable anymore for

the continuous phase), Eq. (10.20) would become

$$w_{\mathrm{P,n}} = (w_{\mathrm{P,n,0}} - w_{\mathrm{cell,n}})\, e^{-t/\tau_{\mathrm{P}}} + w_{\mathrm{cell,n}}, \tag{10.25a}$$

$$x = \tau_{\mathrm{P}} \left(1 - e^{-t/\tau_{\mathrm{P}}}\right) (w_{\mathrm{P,n,0}} - w_{\mathrm{cell,n}}) + w_{\mathrm{cell,n}} t, \tag{10.25b}$$

and Eq. (10.22)

$$t_{\mathrm{end}} = \tau_{\mathrm{P}} \left(1 + \mathrm{W}\left[\left(\frac{w_{\mathrm{P,n,0}}}{w_{\mathrm{cell,n}}} - 1\right) \exp\left(\frac{w_{\mathrm{P,n,0}}}{w_{\mathrm{cell,n}}} - \frac{2s}{\tau_{\mathrm{P}} w_{\mathrm{cell,n}}} - 1\right)\right] - \frac{w_{\mathrm{P,n,0}}}{w_{\mathrm{cell,n}}} + \frac{2s}{\tau_{\mathrm{P}} w_{\mathrm{cell,n}}}\right). \tag{10.26}$$

W is the LambertW function, i.e. $\mathrm{W}(x)$ is the solution of the equation $w \exp w = x$, which has a real value if the argument is larger than $-1/e$ [27].

It can further be shown that Eq. (10.24) would become

$$\zeta_{\mathrm{n}} = \frac{w_{\mathrm{cell,n}}}{w_{\mathrm{P,n,0}}} + \left(1 - \frac{w_{\mathrm{cell,n}}}{w_{\mathrm{P,n,0}}}\right) \exp(f), \tag{10.27}$$

where, f is the following function of known quantities

$$f = \frac{w_{\mathrm{P,n,0}}}{w_{\mathrm{cell,n}}} - \frac{2s}{\tau_{\mathrm{P}} w_{\mathrm{cell,n}}} - 1 - \mathrm{W}\left(\left[\frac{w_{\mathrm{P,n,0}}}{w_{\mathrm{cell,n}}} - 1\right] \exp\left[\frac{w_{\mathrm{P,n,0}}}{w_{\mathrm{cell,n}}} - \frac{2s}{\tau_{\mathrm{P}} w_{\mathrm{cell,n}}} - 1\right]\right). \tag{10.28}$$

It may be clear that the particle-wall distance as function of time is more complicated for Eq. (10.25b) than for Eq. (10.20b). Since in Sec. 10.3.1-10.3.5 the fluids tangential velocity is calculated from the wall normal position x, its analytical solution must be included into the tangential equation of motion. Because an analytical solution for the damping factors in Eq. (10.3) is desired, without the use of an iterative algorithm, the simpler solution of Eq. (10.20b) will be further used.

10.3.1 Negligible Fluid Velocity:

When $|\boldsymbol{w}_{\mathrm{g}}| << |w_{\mathrm{P,0,t}}|$, the differential equation for the wall parallel particle velocity is solved similar as for the normal component resulting in

$$\zeta_{\mathrm{no,t}} = 1 - \frac{2}{\mathrm{Stk}_{\mathrm{0,n}}}, \tag{10.29}$$

and thus

$$\zeta_{\mathrm{no,tot}} = \zeta_{\mathrm{no,t}} = \zeta_{\mathrm{n}}. \tag{10.30}$$

The particle's angle to the wall normal will not change during its stay in the cell.

10.3.2 Constant Velocity Profile

If the tangential fluid velocity is assumed to be constant over whole the wall neighbouring cell, the tangential component of the drag force is given by

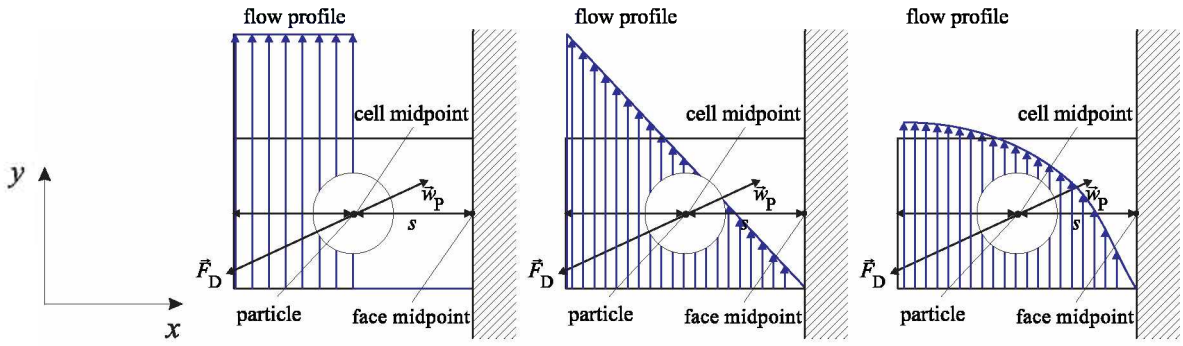

(a) Step function in flow profile.

(b) Linear flow profile.

(c) Logarithmic flow profile.

Figure 10.2: *Flow profiles for the boundary layer with: x and y, the local coordinate system, $\vec{w}_P$ the particle velocity vector, $\vec{F}_D$ the drag force vector and s the perpendicular distance between the cell's centroid and the wall.*

$$F_{D,t} = \frac{-3\pi\mu_g \left(w_{P,t} - w_{cell}\right) d_P}{C_c}. \tag{10.31}$$

Thus, the differential equation in tangential direction becomes

$$\frac{-\tau_P}{w_{P,t} - w_{cell}} \frac{\mathrm{d}w_{P,t}}{\mathrm{d}t} = 1, \tag{10.32}$$

with as solution

$$w_{P,t} = w_{cell} + \exp\left(-\frac{t}{\tau_P}\right)\left(w_{P,t} - w_{cell}\right). \tag{10.33}$$

After substitution of the end time, as defined in Eq. (10.22) and division by $w_{P,t,0}$, the damping factor in tangential direction becomes:

$$\zeta_{t,c} = \Pi_2 + \left(1 - \frac{2}{\mathrm{Stk}_{0,n}}\right)\left(1 - \Pi_2\right). \tag{10.34}$$

10.3.3 Step Function in the Velocity Profile:

Considering the situation in Fig. 10.2(a), in which the fluid velocity is approached with the Heaviside step function around the cell's midpoint, the components of velocity vector are given by:

$$w_{g,n} = 0 \tag{10.35a}$$

$$w_{g,t} = 2w_{cell}\mathrm{H}(x - s). \tag{10.35b}$$

The tangential fluid velocity component, $w_{g,t}$, is substituted into the tangential component of the drag force

$$F_{D,t} = \frac{-3\pi\mu_g \left(w_{P,t} - w_{g,t}\right) d_P}{C_c}. \tag{10.36}$$

Newton's 2nd law of motion is applied, which gives the following differential equation:

$$\frac{-\tau_\mathrm{P}}{w_\mathrm{P,t} - w_\mathrm{g,t}} \frac{\mathrm{d}w_\mathrm{P,t}}{\mathrm{d}t} = 1. \tag{10.37}$$

Eq. (10.37) is integrated for the first half of the cell with the initial condition $w_\mathrm{P,t}(t = 0) = w_\mathrm{P,0,t}$ and over the second half with initial condition $w_\mathrm{P,t}(t = t_\mathrm{s}) = w_\mathrm{P,s,t}$.

$$w_\mathrm{P,s,t} = (w_\mathrm{P,0,t} - 2w_\mathrm{cell})\, e^{-t_\mathrm{s}/\tau_\mathrm{P}} + 2w_\mathrm{cell}, \tag{10.38a}$$

$$w_\mathrm{P,2s,t} = w_\mathrm{P,s,t} e^{-(t_\mathrm{2s} - t_\mathrm{s})/\tau_\mathrm{P}}, \tag{10.38b}$$

where $t_\mathrm{s} = -\tau_\mathrm{P} \ln\left(1 - \frac{s}{\tau_\mathrm{P} w_\mathrm{P,0,n}}\right)$, the time needed for the particle to travel through the first half of the cell and $t_\mathrm{2s} = -\tau_\mathrm{P} \ln\left(1 - \frac{s}{\tau_\mathrm{P} w_\mathrm{P,s,n}}\right)$, the time needed for the particle to travel through the second half of the cell. Dividing Eq. (10.38) through $w_\mathrm{P,0,t}$ gives the normal and parallel damping factors for the first half

$$\zeta_\mathrm{s,n} = 1 - \frac{s}{\tau_\mathrm{P} w_\mathrm{P,0,n}} = 1 - \frac{1}{\mathrm{Stk}_\mathrm{0,n}}, \tag{10.39a}$$

$$\zeta_\mathrm{s,t} = \left(1 - 2\frac{w_\mathrm{cell}}{w_\mathrm{P,t,0}}\right)\left(1 - \frac{s}{\tau_\mathrm{P} w_\mathrm{P,0,n}}\right) + 2\frac{w_\mathrm{cell}}{w_\mathrm{P,t,0}}. \tag{10.39b}$$

The time needed for a particle to travel from the cell's midpoint to the wall is

$$\begin{aligned} \Delta t_\mathrm{s\to 2s} &= t_\mathrm{2s} - t_\mathrm{s} \\ &= -\tau_\mathrm{P} \ln\left(1 - \frac{2}{\mathrm{Stk}_\mathrm{0,n}}\right) + \tau_\mathrm{P} \ln\left(1 - \frac{1}{\mathrm{Stk}_\mathrm{0,n}}\right) \\ &= -\tau_\mathrm{P} \ln\left(\frac{\mathrm{Stk}_\mathrm{0,n} - 2}{\mathrm{Stk}_\mathrm{0,n} - 1}\right). \end{aligned} \tag{10.40}$$

After substitution in Eq. (10.38b) and division by $w_\mathrm{P,s,t}$, the damping factors for the second half of the cell follow

$$\zeta_\mathrm{2s,n} = \frac{w_\mathrm{P,2s,n}}{w_\mathrm{P,s,n}} = \frac{\mathrm{Stk}_\mathrm{0,n} - 2}{\mathrm{Stk}_\mathrm{0,n} - 1}, \tag{10.41a}$$

$$\zeta_\mathrm{2s,t} = \frac{w_\mathrm{P,2s,t}}{w_\mathrm{P,s,t}} = \frac{\mathrm{Stk}_\mathrm{0,n} - 2}{\mathrm{Stk}_\mathrm{0,n} - 1}. \tag{10.41b}$$

Combining Eq. (10.39) and (10.41) leads to:

$$\zeta_\mathrm{step,n} = 1 - \frac{2}{\mathrm{Stk}_\mathrm{0,n}}, \tag{10.42a}$$

$$\zeta_\mathrm{step,t} = \frac{(\mathrm{Stk}_\mathrm{0,n} - 1 + 2\Pi_2)\,(\mathrm{Stk}_\mathrm{0,n} - 2)}{\mathrm{Stk}_\mathrm{0,n}\,(\mathrm{Stk}_\mathrm{0,n} - 1)}. \tag{10.42b}$$

10.3.4 Linear Flow Profile:

The linear flow profiles are divided into the one with zero intercept at the wall, which therefore meets the no-slip boundary condition at the wall and the ones which are linearised from a first order Taylor series expansion around the wall neighbouring cell's midpoint.

10.3.4.1 Linear Flow Profile with Zero Intercept

In Fig. 10.2(b) a linear boundary flow is presented. If the mean fluid velocity in the cell is remained, the velocity function is given by

$$w_{\mathrm{g,t}} = w_{\mathrm{cell}} \frac{2s - x}{s}, \tag{10.43}$$

i.e. the drag force in Eq. (10.36) becomes a function of the x-coordinate. The tangential component of the differential equation then reads

$$-\tau_{\mathrm{P}} \frac{\mathrm{d}^2 y}{\mathrm{d}t^2} - \frac{\mathrm{d}y}{\mathrm{d}t} - \frac{w_{\mathrm{cell}}}{s} x(t) + 2w_{\mathrm{cell}} = 0. \tag{10.44}$$

With $x(t)$ known from Eq. (10.20b) and the initial conditions $\frac{\mathrm{d}y}{\mathrm{d}t}(t=0) = w_{\mathrm{P,t}}(0) = w_{\mathrm{P,0,t}}$ and $y(t=0) = 0$, the following function for the tangential particle velocity is found

$$w_{\mathrm{P,t}}(t) = w_{\mathrm{cell}} \left(2 - \mathrm{Stk}_{0,\mathrm{n}}\right) + w_{\mathrm{cell}} \mathrm{Stk}_{0,\mathrm{n}} \frac{t}{\tau_{\mathrm{P}}} e^{-t/\tau_{\mathrm{P}}} + \left\{w_{\mathrm{P,0,t}} + w_{\mathrm{cell}} \left(\mathrm{Stk}_{0,\mathrm{n}} - 2\right)\right\} e^{-t/\tau_{\mathrm{P}}}. \tag{10.45}$$

After substitution of the end time, $t_{\mathrm{end}} = -\tau_{\mathrm{P}} \ln\left(1 - \frac{2}{\mathrm{Stk}_{0,\mathrm{n}}}\right)$, in Eq. (10.45) and division through $w_{\mathrm{P,0,t}}$, the parallel damping factor becomes

$$\zeta_{\mathrm{lin,t}} = \Pi_2 \left(2 - \mathrm{Stk}_{0,\mathrm{n}}\right) - \Pi_2 \left(\mathrm{Stk}_{0,\mathrm{n}} - 2\right) \ln\left(1 - \frac{2}{\mathrm{Stk}_{0,\mathrm{n}}}\right) + \left(1 - \frac{2}{\mathrm{Stk}_{0,\mathrm{n}}}\right) \left(1 - 2\Pi_2 + \Pi_2 \mathrm{Stk}_{0,\mathrm{n}}\right). \tag{10.46}$$

10.3.4.2 Linear Profile from the Velocity Gradient

The linear flow profile can also be defined from the value of the fluid velocity and that of the fluid velocity gradient, $\frac{\mathrm{d}w_{\mathrm{cell}}}{\mathrm{d}x}$, both determined in the cell's midpoint. The equation for describing the flow profile is in that case given by

$$w_{\mathrm{g,t}} = w_{\mathrm{cell}} + \frac{\mathrm{d}w_{\mathrm{cell}}}{\mathrm{d}x} \left(s - x\right). \tag{10.47}$$

It should be noticed that the no-slip boundary condition is not met anymore for all gradient values with

$$\frac{\mathrm{d}w_{\mathrm{cell}}}{\mathrm{d}x} \neq \frac{w_{\mathrm{cell}}}{s}, \tag{10.48}$$

otherwise, the flow profile is equals that of Eq. (10.43). From solving the equation of motion in tangential direction, the damping factor follows again:

$$\zeta_{\mathrm{t,gr}} = \left[\Pi_4\Pi_3 + 1 - \frac{\Pi_4\Pi_3}{\mathrm{Stk}_{0,\mathrm{n}}} - \Pi_2 - \Pi_4\Pi_3 \ln\left(1 - \frac{2}{\mathrm{Stk}_{0,\mathrm{n}}}\right)\right]\left(1 - \frac{2}{\mathrm{Stk}_{0,\mathrm{n}}}\right) + \frac{\Pi_4\Pi_3}{\mathrm{Stk}_{0,\mathrm{n}}} - \Pi_4\Pi_3 + \Pi_2. \tag{10.49}$$

where, the fourth dimensional number is introduced:

$$\Pi_4 = \frac{\mathrm{d}w_{\mathrm{cell}}}{\mathrm{d}x}\tau_{\mathrm{P}}. \tag{10.50}$$

If the velocity gradient equals zero, Π_4 also becomes zero and Eq. (10.49) becomes equal to Eq. (10.34).

10.3.5 Logarithmic Flow Profile:

The volume flow rate through a cell with uniform velocity, w_{cell}, and width, $2s$, is stated to be the same as one with a logarithmic velocity function with no slip condition on the wall, i.e.

$$w_{\mathrm{cell}} 2s = \int_{x=0}^{x=2s} c_{\log} \ln\left(2 - \frac{x}{2s}\right) \mathrm{d}x, \tag{10.51}$$

with $c_{\log}$ the weighted mean velocity. After solving Eq. (10.51), an expression for $c_{\log}$ as function of w_{cell} is found:

$$c_{\log} = \frac{w_{\mathrm{cell}}}{2\ln(2) - 1}. \tag{10.52}$$

Hence, the velocity function becomes

$$w_{\mathrm{g,t}} = \frac{w_{\mathrm{cell}}}{2\ln(2) - 1} \ln\left(2 - \frac{x(t)}{2s}\right) \tag{10.53}$$

and the equation of motion in tangential direction

$$-\tau_{\mathrm{P}}\frac{\mathrm{d}^2y}{\mathrm{d}t^2} - \frac{\mathrm{d}y}{\mathrm{d}t} + \frac{w_{\mathrm{cell}}}{2\ln(2) - 1} \ln\left(2 - \frac{x(t)}{2s}\right) = 0. \tag{10.54}$$

After substitution of the end time and dividing by $w_{\mathrm{P,0,t}}$, the damping factor for the parallel velocity is found again:

$$\zeta_{\log,\mathrm{t}} = \left\{\frac{\Pi_2}{2\ln(2) - 1}\left(\frac{\mathrm{Stk}_{0,\mathrm{n}}}{\mathrm{Stk}_{0,\mathrm{n}} - 4}\right) \ln\left(2 - \frac{4}{\mathrm{Stk}_{0,\mathrm{n}}}\right) + 1 - \frac{\ln(2)\Pi_2}{2\ln(2) - 1}\right\}\left(1 - \frac{2}{\mathrm{Stk}_{0,\mathrm{n}}}\right). \tag{10.55}$$

10.4 Comparison of the Damping Factors

In Fig. 10.3 the tangential velocity damping factors, as defined in Eq. (10.2b), are plotted for several impact angles, α, and dimensionless cell midpoint velocities, Π_2, as function of the

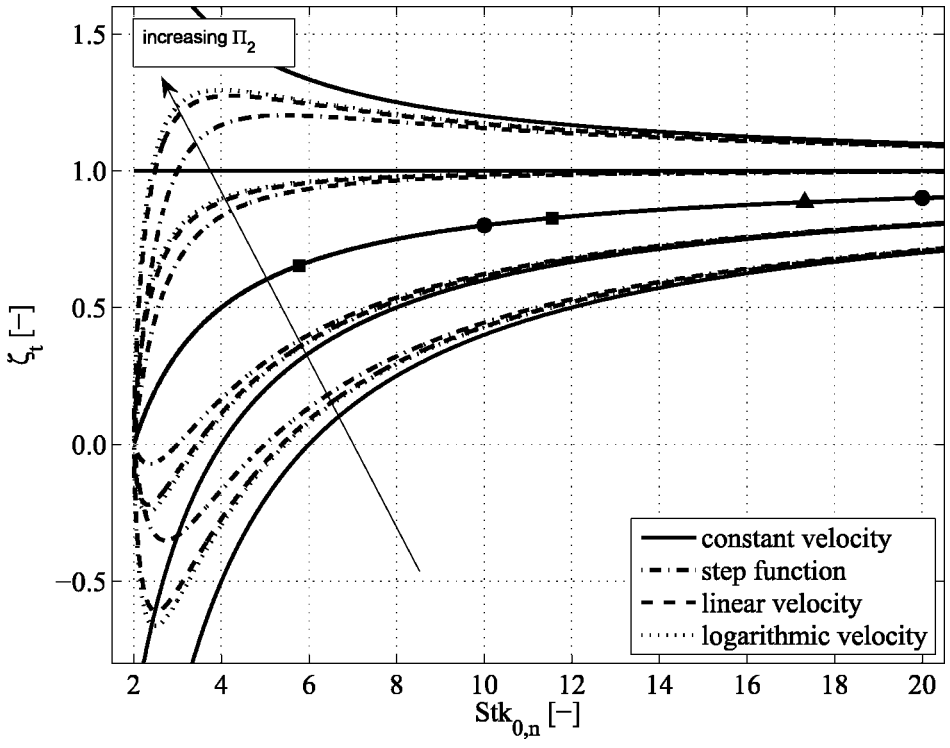

Figure 10.3: *Tangential velocity damping factor, ζ_t without fluid velocity (equals ζ_n), constant, step, linear, and logarithmic velocity profile as function of the wall normal Stokes number ($Stk_{0,n}$), the impact angle in respect to the wall normal vector α and the dimensionless fluid cell midpoint velocity Π_2 (values $\Pi_2 = -2; -1; 0; 1; 2$) for the assumption that no other forces than drag are acting on the particle. The critical $Stk_{0,n}$ number for which $\tau_+ = 0.2$ and $\tau_+ = 20$ are denoted by the square, circle and triangle symbol for impact angles of $\alpha = \pi/6$, $\alpha = \pi/4$ and $\alpha = \pi/3$, respectively, where the value for $Stk_{0,n}$ for $\tau_{P+} = 20$ and $\alpha = \pi/3$ is larger than the visible range in the plot.*

Stokes number of a particle entering the wall neighbouring cell, $Stk_{0,n}$. Some characteristics are:

- As predicted by Eq. (10.22) and (10.23), the critical value of $Stk_{0,n}$ is equal to 2. Particles with $Stk_{0,n} < 2$ will not be able to reach the wall. All profiles, with exception of the one without velocity, show an asymptotic behaviour when approaching this critical Stokes number from above. This means that there is a large variation of the damping factor for a relative small increase of the Stk number above 2;

- The logarithmic flow profile predicts the largest velocity damping factor (i.e. the smallest ratio between the particle's cell entering and wall collision speed) slightly followed by the linear. The differences with the Heaviside profile are larger;

- The total damping factor has a maximum (in certain cases the particle is even accelerated instead of decelerated). This maximum is more pronounced for large impact angles and negative values of Π_2;

Table 10.2: *Pressure velocity coupling and spatial discretisation schemes used in the simulations.*

Pressure velocity coupling:	scheme	SIMPLE
Spatial discretisations:	gradient	least squares cell based
	pressure	1^{st} order upwind
	momentum	1^{st} order upwind
	turbulent kinetic energy	1^{st} order upwind
	turbulent dissipation rate	1^{st} order upwind
	Reynolds stresses	1^{st} order upwind

- For a perpendicular impact, ζ_{tot} is only a function of $Stk_{0,n}$. This because $w_{P,0,t} = 0$ and Π_2 will become infinite. There exists no difference between the velocity profiles for this case;
- The total damping factor is independent of the impact angle, if the fluid velocity vanishes.

10.5 Simulation Setup

The relevance of the model is demonstrated with two case studies. The first case describes a fine grid with a resolution of 1 mm. The second one is typical for industrial applications where the resolution is 1 cm. With industrial dimensions in the order 1 m in 3D, this resolution results in a number of cells of $\mathcal{O}(10^6)$, which is close to the maximal number of cells for a simulation on a desktop computer. A finer resolution of 1 mm would result in a number of cells of $\mathcal{O}(10^9)$, which is hard to realise.

10.5.1 Grid

Two different cases (denoted by the indices 1 and 2) were used in the 2D simulations, with two rectangular grids for each case. The first grid uses a boundary layer of ten cells thickness, whereas the other one has only one single layer of cells on the same position. The grids represent a cylindrical pipe, with diameter $D_1 = 0.1$ m and $D_2 = 1.0$ m and length $L_1 = 10.0$ m and $L_2 = 100.0$ m, respectively. For both cases the resolutions are 50 (i.e. 59 with boundary layer) in radial and 10 000 cells in axial direction.

On the position $(r; z) = (49D_i/100; L_i/2)$, where the flow is assumed to be fully developed and no effects of the in- and outlet are present, particles with properties with $\tau_{P+} = 0.2$ and $\tau_{P+} = 20$ under angles of $\pi/6$, $\pi/4$ and $\pi/3$ are released in a such a way that Π_2 equals 0.5, 1.0 or 2.0. The impact velocity of the particles on the wall is statistically evaluated.

10.5.2 Continuous Phase

The velocity-pressure coupling and the discretisation schemes used in the simulations are summarised in Tab. 10.2 and are standard provided by the CFD-code ANSYS Fluent 13.0 [39].

The inlet velocity equals 5 m/s, resulting in Reynolds number of $Re_{D,1} = 2.8 \times 10^4$ and $Re_{D,2} = 2.8 \times 10^5$ and therefore in a turbulent flow. Turbulence was calculated with the Reynolds stress model which is the most sophisticated RANS model and is able to describe inhomogeneous turbulence.

Table 10.3: *Values for the dimensionless wall distance y^+ at the injection point for case 1 and 2 and the velocity at the wall from the Taylor expansion $w_{g,w} = \left(w_{cell} - \frac{dw_{g,t}}{dn}\Big|_{cell} s\right)$ with and without boundary layer (indicated as bl).*

			without bl	with bl
case 1	y^+	[-]	8.4	1.1
	$w_{g,w}$	[m/s]	0.72	0.08
	$\sqrt{\tau_{nn}/\rho_g}$	[m/s]	0.26	0.21
case 2	y^+	[-]	65.3	6.8
	$w_{g,w}$	[m/s]	2.55	0.45
	$\sqrt{\tau_{nn}/\rho_g}$	[m/s]	0.17	0.17

The dimensionless wall distances for the wall neighbouring cell, with the axial coordinate of the particle's injection points, are summarised in Tab. 10.3. For case 1, the coarse grid is within the buffer layer, whereas the finer one describes the viscous sublayer. For case 2, both grids are within the fully turbulent and buffer layer, respectively. Also the remaining tangential fluid velocity at the wall, $w_{g,w}$, calculated from a first order Taylor series expansion around the cell's midpoint is given. This velocity is defined as

$$w_{g,w} = \left(w_{cell} - \frac{dw_{g,t}}{dn}\Big|_{cell} s\right) \tag{10.56}$$

and is a factor 9.0 smaller when using a boundary layer for case 1 and a factor 5.7 for case 2 compared to the velocities without boundary layer.

10.5.3 Dispersed Phase

The calculation of the particle trajectories is performed by integrating Eq. (10.11) in a Lagrangian reference frame, using the one-way coupling in a frozen flow field. The step length factor was left on the default value of 5 in ANSYS Fluent 13.0 [39], which means that a particle will travel through a cell in approximately 5 time steps. Alternatively, it is possible to adapt the integration time step. Sommerfeld [134] recommends to set the time step to a value of 20% of the minimum of the relevant time scales (particle relaxation time, time scale of turbulence and inter-particle collision time, see Eq. (8.106)). However, because of simplicity, the default value of step length factor was further used.

Turbulent motion is created with the Discrete Random Walk Model with a random eddy life time, which is calculated from Eq. (8.79) and (8.80). The DRW model is standard provided by ANSYS Fluent 13.0, but considers turbulence rather in a statistical than in a physical correct way.

A more realistic particle dispersion is generated with the Continuous Random Walk Model (CRW), which is mostly based on the Langevin equation. The implementation of the CRW model in wall-bounded geometries is described by Dehbi [32] for example and discussed in detail in Sec. 8.2.2.2.

10.5.3.1 Wall Impact Frequency Correction

If the impact speed and angle are known from software macros and assuming a linear tangential flow profile, the wall normal Stokes number of the particle entering the wall neighbouring cell follows from the Stokes number at impact by solving Eq. (10.2a) and (10.24)

$$\begin{aligned} \mathrm{Stk}_{0,\mathrm{n}} &= \frac{w_{\mathrm{P,e,n}}\tau_{\mathrm{P}}}{s} + 2 \\ &= \mathrm{Stk}_{\mathrm{e,n}} + 2. \end{aligned} \tag{10.57}$$

10.5.3.2 Wall Impact Velocity Correction

From $\mathrm{Stk}_{0,\mathrm{n}}$ the instant particle normal velocity is calculated, which is corrected with a fluctuating normal fluid velocity

$$w_{\mathrm{P,0,n}} = \frac{\mathrm{Stk}_{0,\mathrm{n}}\tau_{\mathrm{P}}}{s} + \chi_{\mathrm{n}}\sqrt{\frac{\tau_{\mathrm{nn}}}{\rho_{\mathrm{g}}}}. \tag{10.58}$$

where, χ_{n}, is a random Gaussian number with zero mean and τ_{nn}, the Reynolds stress in wall normal direction. This correction means that the condition for impact is not automatically met anymore since the corrected Stk number may have a value smaller than 2.

Since the dimensionless numbers are evaluated at $x = 0$, the tangential particle velocity at this position has to be determined, which follows from putting $\zeta_{\mathrm{gr,t}} = \frac{w_{\mathrm{P,e,t}}}{w_{\mathrm{P,0,t}}}$ in Eq. (10.49) and solving it to $w_{\mathrm{P,0,t}}$. The result then reads:

$$w_{\mathrm{P,0,t}} = \frac{1}{\mathrm{Stk}_{0,\mathrm{n}} - 2}\left(\Pi_4 w_{\mathrm{P,0,n}}\left[2 - \frac{2}{\mathrm{Stk}_{0,\mathrm{n}}} + \ln\left(\frac{\mathrm{Stk}_{0,\mathrm{n}} - 2}{\mathrm{Stk}_{0,\mathrm{n}}}\right)(\mathrm{Stk}_{0,\mathrm{n}} - 2)\right] - 2w_{\mathrm{cell}} + w_{\mathrm{P,e,t}}\mathrm{Stk}_{0,\mathrm{n}}\right), \tag{10.59}$$

where, the value for $w_{\mathrm{P,0,n}}$ follows from Eq. (10.49) and the dimensionless number Π_4 is independent of the particle velocity. Alternatively the velocity at entering the wall neighbouring cell is calculated from the linear profile with the no slip wall condition as in Eq. (10.46):

$$w_{\mathrm{P,0,t}} = \frac{w_{\mathrm{P,t,e}}\mathrm{Stk}_{0,\mathrm{n}}}{\mathrm{Stk}_{0,\mathrm{n}} - 2}\left(1 + \Pi_{2,\mathrm{e}}\left[2 + (\mathrm{Stk}_{0,\mathrm{n}} - 2)\ln\left(\frac{\mathrm{Stk}_{0,\mathrm{n}} - 2}{\mathrm{Stk}_{0,\mathrm{n}}}\right) - \frac{4}{\mathrm{Stk}_{0,\mathrm{n}}}\right]\right), \tag{10.60}$$

where,

$$\Pi_{2,\mathrm{e}} = \frac{w_{\mathrm{cell}}}{w_{\mathrm{P,e,t}}}. \tag{10.61}$$

The turbulence is introduced with from the anisotropic Reynolds stress model (RSM), in which the cell midpoint tangential velocity is calculated from the time mean and fluctuating part by

$$w_{\mathrm{cell}} = \bar{u}_{\mathrm{t}} + \chi_{\mathrm{t}}\sqrt{\frac{\tau_{\mathrm{tt}}}{\rho_{\mathrm{g}}}}, \tag{10.62}$$

where, τ_{tt}, is the Reynolds stress in tangential direction and χ_{t}, is a random generated Gaussian number with zero mean, which is fully independent of χ_{n}.

Finally, the tangential impact velocity is multiplied with the following correction factor

$$f_{\mathrm{corr}} = \frac{\zeta_{\mathrm{lin,t}}}{\zeta_{\mathrm{gr,t}}}, \tag{10.63}$$

where, $\zeta_{\mathrm{lin,t}}$ and $\zeta_{\mathrm{gr,t}}$ are as defined in Eq. (10.46) and (10.49) respectively and have to be evaluated at the time a particle enters the cell. For the simulations the tangential velocity of a particle entering the cell is calculated with Eq. (10.60).

10.6 Results and Discussion

The wall impact velocity and fraction of particles reaching the wall are compared using one of the following three methods:

a. the fine grid with boundary layer (BL) as benchmark;

b. the course grid (NOBL) as common method used in industrial applications;

c. the course grid with the correction of this proposal (UDF).

In the following sections the results for case 1 and case 2 are presented.

10.6.1 Case 1

In Fig. 10.4, the statistical analysis from 100 000 particles per class and three repetitions is shown. The class size is five times as big as the critical number of particles at which a fair convergence was reached in the simulation of a simple shear flow [117] and should be therefore large enough.

For a limestone particle with density 2 770 kg/m^3 in air, the dimensionless particle relaxation times of 0.2 and 20 correspond with diameters of 1.6 μm and 16 μm, respectively. The wall tangential start velocities are 2.5, 5.0 and 10 m/s, resulting in starting angles with the wall normal of $\pi/6$, $\pi/4$ and $\pi/3$ rad, respectively.

A clear difference in the damping factors is noticed between the case with and without boundary layer. The main reason lies within the overpredicted tangential impact velocity for the mesh without boundary layer. This is especially true for the smaller particles, where a difference over 100% is noticed, whereas the difference in the normal impact velocity is lower than 10%. For the larger particles, these values become of the order of 0.1 and 1% respectively. Therefore, it seems reasonable to adapt the tangential velocity by means of Eq. (10.63) and the wall normal velocity by Eq. (10.58).

The results of the correction are shown by the black lines. The adapted damping factors give values closer to that of the grid with the boundary layer but underpredict their values without exception. Furthermore, it should be said, that the uncertainty still remains relatively large due to the turbulent motion.

For the fraction of particles able to reach the wall, the following is observed. Maximal 76% of the $\tau_{\mathrm{P}+} = 0.2$ particles reach the wall in the coarse grid. In the fine grid this fraction is with 53% significant smaller. The new predicted wall normal velocity of a particle entering the wall neighbouring cell results in a new predicted Stokes number and therefore the criterion for the particle to reach the wall (Eq. (10.23)) is not automatically met anymore. As a consequence, the fraction of particles able to reach the wall is adjusted to a lower value, which is shown in Fig. 10.6(a), 10.6(c) and 10.6(e) for the diameter with $\tau_{\mathrm{P}+} = 0.2$. The model reduces the error between the grid *with* and *without* a boundary layer within a range of 33-43%.

The $\tau_{\mathrm{P}+} = 20$ particles always reach the wall using both the coarse and the fine grid. In some exceptions, the correction predicts that these particles are not able to reach the wall but the probability for this events is smaller than 0.1%.

10.6.2 Case 2

For case 2, the particle diameters are 5.2 μm and 53 μm for dimensionless particle relaxation times of $\tau_{P+} = 0.2$ and $\tau_{P+} = 20$ respectively. The results of the three boundary conditions are shown in Fig. 10.5. For the smaller particles, the results look pretty similar to those shown in Fig. 10.4. Also here, the damping function is rated too low. However, since the difference between the grid *without* and *with* a boundary layer is even larger than for case 1 (in Fig. 10.4), the improvement satisfies. The fraction of the $\tau_{P+} = 0.2$ particles that is able to reach the wall is within the range of 53-57% when a boundary layer is used and albeit 67-74% without a boundary layer. Using the correction factor, this range becomes 59-66% which means an improvement of 44-54% (Fig. 10.6(b), 10.6(d) and 10.6(f)).

The results of the $\tau_{P+} = 20$ particles, however, look different. For tangential particle starting velocities smaller or equal to the mean fluid velocity, the mean impact speed with boundary layer is larger than without one. Therefore, the user defined boundary condition sometimes predicts a correction in the wrong direction.

10.7 Conclusions and Recommendations

With an example, it is shown that the particle impact velocity at the wall is dependent on the resolution of the grid near the wall. The impact velocity is overpredicted in a coarse grid in comparison with a grid that has a finer resolution near the wall, i.e. a boundary layer. The wall tangential particle velocity has the largest contribution to this difference. Also the fraction of particles, that is able to reach the wall is rated too high.

Therefore, a correction factor is introduced, which recalculates the tangential impact velocity. The correction factor is based on the assumption that the drag force is dominant and the wall normal component of the fluid velocity is negligible small. In this way, the equation of motion for a particle travelling in a boundary layer is solved analytically. The influence of the Saffman lift force is difficult to estimate because of the wall tangential fluid velocity component entering the wall normal equation of motion. Therefore, it is not possible to decouple both directions and calculate the velocity damping factors.

Four types of velocity flow profiles (which are: zero velocity, step function, linear and logarithmic) are compared for the tangential fluid velocity. It is shown that the normal, tangential and total velocity damping factors (defined as the ratio between cell entering and collision velocity of the particle) are only dependent on three dimensionless numbers, which are the wall normal Stokes number, the angle of impact and the ratio of the fluid cell velocity and particle tangential velocity. The results of the last two flow profiles only differ a little. The correction factor, used for the wall tangential impact velocity, equals the ratio of the damping factors for step function and the linear flow profile. The wall normal particle velocity is re-estimated by the use of the Reynolds stress component in this direction and a random generated number. The fraction of particles able to reach the wall is adapted as well with this method.

Knowing the damping factors, the particle's tangential impact velocity is computed from explicit equations, which only contain variables, that can be called up from standard flow macros in commercial CFD software programs, and the particles velocity at the moment it collides with the wall. Turbulence is taken into account by the components of the Reynolds stress tensor and a random calculated Gaussian number with zero mean.

The tangential impact velocity, which is overpredicted for a coarse grid, is recalculated. The results give overall better values for the particle impact velocity in the coarse mesh, where the

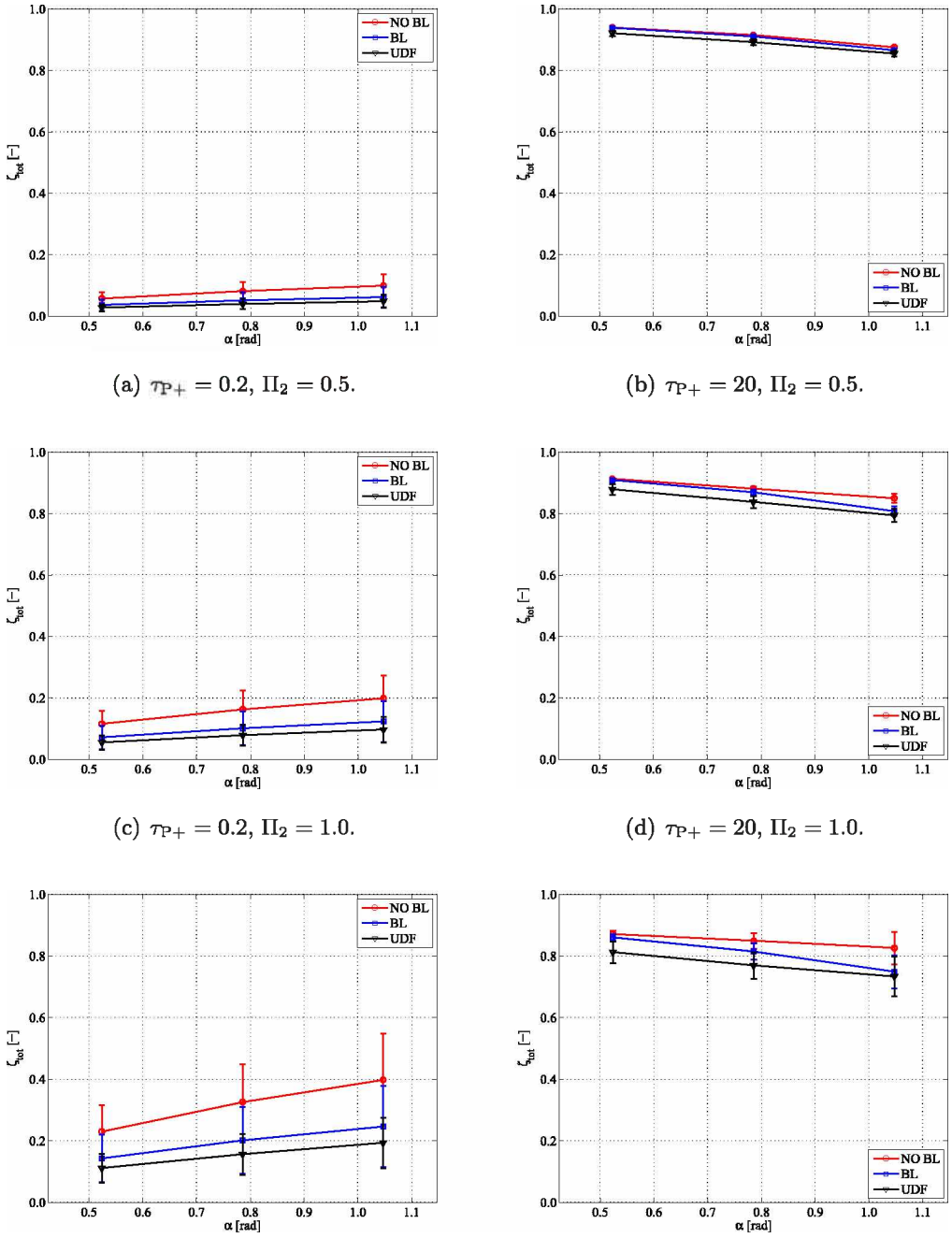

(a) $\tau_{P+} = 0.2$, $\Pi_2 = 0.5$.

(b) $\tau_{P+} = 20$, $\Pi_2 = 0.5$.

(c) $\tau_{P+} = 0.2$, $\Pi_2 = 1.0$.

(d) $\tau_{P+} = 20$, $\Pi_2 = 1.0$.

(e) $\tau_{P+} = 0.2$, $\Pi_2 = 2.0$.

(f) $\tau_{P+} = 20$, $\Pi_2 = 2.0$.

Figure 10.4: *Total velocity damping factors as function of angle, α, dimensionless particle relaxation time, τ_{P+}, and velocity ratio, Π_2, for the fine mesh (BL), for the coarse mesh (NO BL) and for the coarse mesh with adapted wall function (UDF). The mesh equals a pipe of 0.1 m in diameter and 10 m in length (case 1).*

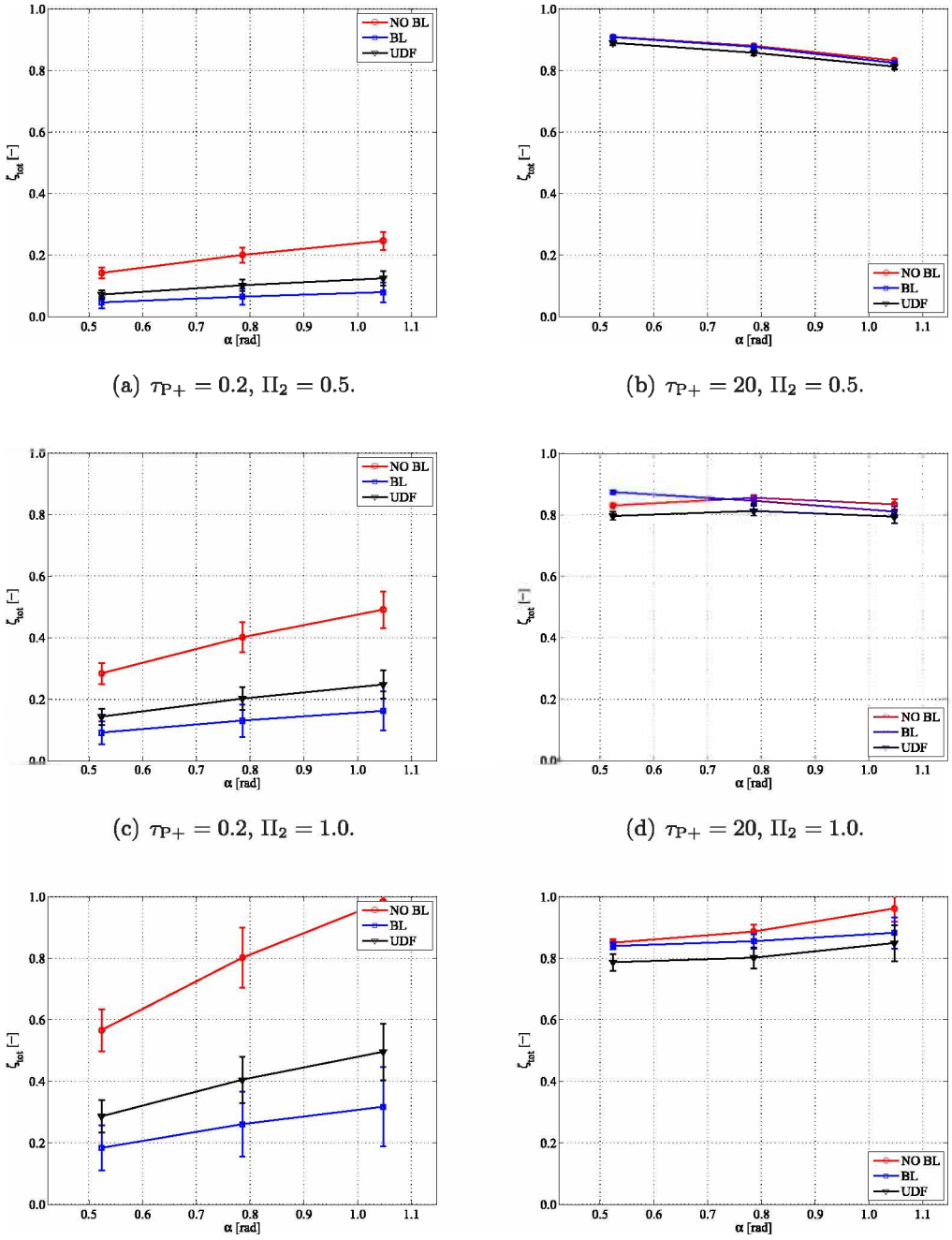

(a) $\tau_{P+} = 0.2$, $\Pi_2 = 0.5$.

(b) $\tau_{P+} = 20$, $\Pi_2 = 0.5$.

(c) $\tau_{P+} = 0.2$, $\Pi_2 = 1.0$.

(d) $\tau_{P+} = 20$, $\Pi_2 = 1.0$.

(e) $\tau_{P+} = 0.2$, $\Pi_2 = 2.0$.

(f) $\tau_{P+} = 20$, $\Pi_2 = 2.0$.

Figure 10.5: *Total velocity damping factors as function of angle, α, dimensionless particle relaxation time, τ_{P+}, and velocity ratio, Π_2, for the fine mesh (BL), for the coarse mesh (NO BL) and for the coarse mesh with adapted wall function (UDF). The mesh equals a pipe of 1 m in diameter and 100 m in length (case 2).*

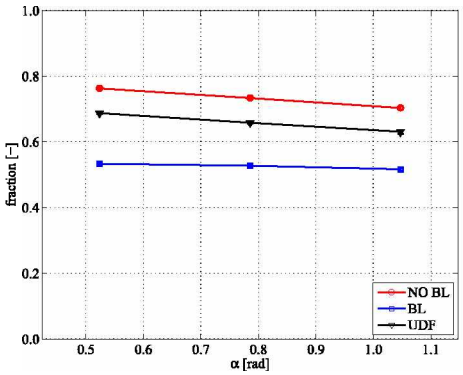

(a) $\tau_{P+} = 0.2$, $\Pi_2 = 0.5$ for case 1.

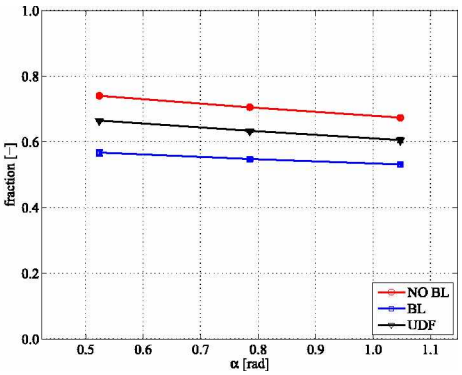

(b) $\tau_{P+} = 0.2$, $\Pi_2 = 0.5$ for case 2.

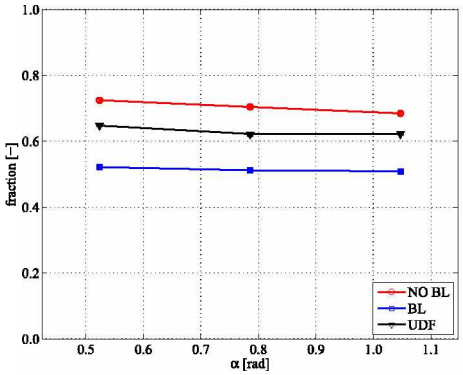

(c) $\tau_{P+} = 0.2$, $\Pi_2 = 1.0$ for case 1.

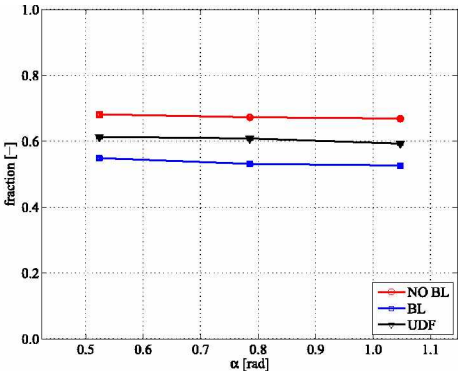

(d) $\tau_{P+} = 0.2$, $\Pi_2 = 1.0$ for case 2.

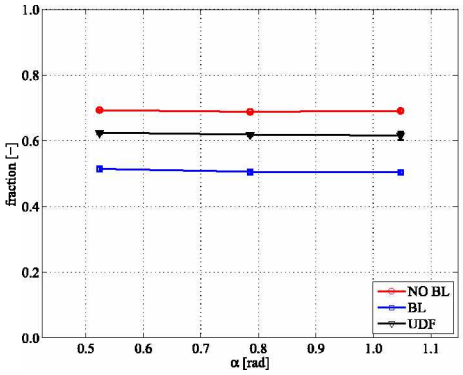

(e) $\tau_{P+} = 0.2$, $\Pi_2 = 2.0$ for case 1.

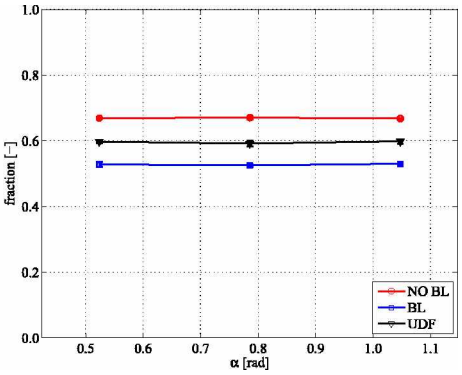

(f) $\tau_{P+} = 0.2$, $\Pi_2 = 2.0$ for case 2.

Figure 10.6: *Fraction of particles entering the wall neighbouring cell able to reach the wall.*

error with the results with fine mesh is reduced by a factor of 2. The error of the fraction of particles able to reach the wall is lowered within a range of 33-54% for small particles and (almost) left unchanged for large particles.

Some further improvements are desirable since the recalculated velocity damping factor is rated too low for most situations.

11 CFD-Calculation

In this chapter are described the mesh and boundary conditions, used for the flow field of the continuous phase in the cyclone separator, as well as the way how convergence was achieved. The results are discussed in respect of their importance for the deposition models introduced in Ch. 7.

Also the computation of the particle trajectories is discussed as well as their relevant statistics considering wall depositions. The deposition models of Ch. 7 are built in the simulations by user defined functions (UDF), using the forces and energies working on a particle near the wall, which have been introduced in Ch. 4 and 5 respectively. Also the influence of the damping factor of Ch. 10 is treated.

Finally, the simulated depositions are compared to each other and to experimental data in respect of the deposited masses and particle size distributions on the parts that are distinguished.

11.1 Mesh and Boundary Conditions

The mesh used for the simulation of the wall deposition was taken from Gronald [53] and is shown in Fig. 11.1. It consist out of 435 504 hexaeder cells from which 0.52% have an equiskew angle larger than 0.5, as defined in Eq. (8.44). The maximal aspect ratio is 16.4 (Eq. (8.43b)). The area around the cyclone's centre axis is meshed with cubical cells to prevent that all cells come together in the cyclone's centre axis, which would cause highly deformed cells.

The cyclone's inlet was put on a *velocity inlet* boundary condition with an uniform block profile, calculated from the inlet's area, A_{in} and the volume flow rate, Q, with velocity

$$v_{\text{in}} = \frac{Q}{A_{\text{in}}}. \tag{11.1}$$

The inlet velocity is assumed to become fully developed over the length of the inlet.

The turbulence boundary conditions are the hydraulic diameter and the turbulent intensity, which are calculated with [39]

$$D_{\text{H}} = \frac{4A_{\text{in}}}{U}, \tag{11.2a}$$

$$I_{\text{turb}} = 0.16\left(\text{Re}_{D_{\text{H}}}\right)^{-1/8}, \tag{11.2b}$$

where, the perimeter is calculated from the inlet's width b_{in} and height a_{in}

$$U = 2\left(a_{\text{in}} + b_{\text{in}}\right). \tag{11.3}$$

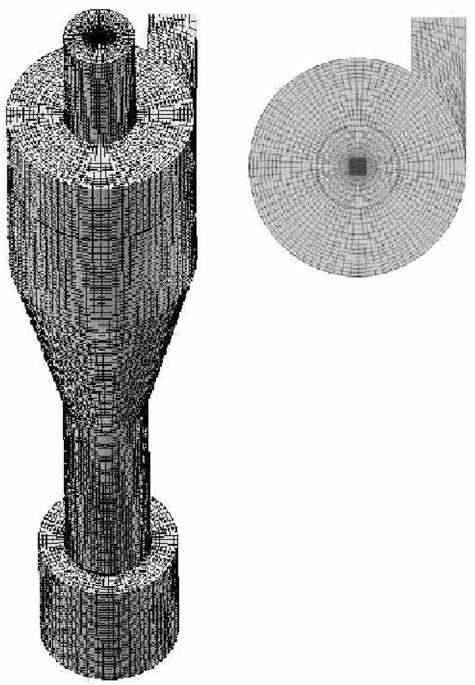

Figure 11.1: *The mesh used in the simulations [53].*

Reversed flow at the outlet is avoided by placing a circular plate above the vortex finder at such a distance that the area of the fictive cylinder equals that of the original outflow. This method has been successfully used by several other authors before [35, 46, 53]. A constant pressure of 1.013 bar is set as Dirichlet (*pressure outlet*) boundary condition for the continuous phase at the ring-shaped area. The plate above is impermeable for the fluid. For the discrete particles, the ring is a wall with the same boundary condition as all other walls and the plate is an *escape* boundary condition. The vortex finder is thus quasi prolonged with a height of $h = 0.25 D_{\mathrm{vf}}$.

All walls were modelled as hydrodynamically smooth and for the sticking and reflecting boundary conditions, the user defined functions of App. E were used.

11.2 Continuous Phase

The flow fields, corresponding to the volume flow rates of 600, 800, 1 000, 1 200 $\mathrm{m^3/h}$, were obtained with the following steps as described by Gronald [53] and Zagorski [155]

a. Starting with the inlet velocity, corresponding to the lowest volume flow rate, assuming a laminar flow. The used discratisation scheme used is first order upwind;

b. Changing to $k - \epsilon$;

c. Applying the RSM turbulence model with QUICK discretisation;

d. Higher inlet velocities for the corresponding volume flow rates;

e. Unsteady simulation with a step size of 0.001 s and 500 time steps, which results in a total simulation time of 0.5 s. The maximal number of iterations per time steps was 20.

In experiments, the proceeding vortex core was found to have a frequency between 13 Hz and 66 Hz [115]. The step size in the unsteady simulation is thus smaller than 10% of the typical period, which was used as step size by Derksen [35].

11.2.1 Convergence

Convergence was followed with monitors for pressure the pressure at the inlet and lower side of the vortex finder. Also the three velocity components in three points were monitored.

11.2.2 Flow Field

In this thesis, the flow field calculated in the CFD simulations is discussed in respect to the consequences for the particle deposition models. For details and comparisons between the simulation and experimental data, the reader is referred to former work ([53, 115, 155]).

From the adhesion criterion based on energy conversion, it follows that the impact of particles with low velocity increases the deposition. In Fig. 11.2(a), 11.2(d) and 11.2(g) the velocity magnitude in the centroids of the wall adjacent cells is shown for a volume flow rate of 600 m^3/h. At the wall itself, the value equals zero because of the no-slip boundary condition. The turbulent kinetic energy, k, is shown in Fig. 11.2(b), 11.2(e) and 11.2(h).

In the vortex finder, the velocity is in the range of 20-28 m/s and therefore it is the region with the highest kinetic energy of the flow. The vortex is visible in Fig. 11.2(d) in the regions where the gas velocity is locally higher. This vortex could explain the helix shaped deposition observed in experiments (Fig. 9.2(a) and 9.2(b)), although also for this region the kinetic energy of the flow still seems to be relatively high. Also the turbulent kinetic energy is high. The highest values are at the lower and higher edge of the vortex finder. The last phenomenon is physically not correct but a consequence of the radial pressure outlet boundary condition.

Less kinetic energy is present in the vertical tube section, where the velocity magnitude is between 10 and 20 m/s. No clear vortex is seen anymore in this region. The turbulent kinetic energy is relatively high. At the edge between the vertical tube and the bunker, the kinetic energy increases. This is in contradiction to the experiments, where thick, stained depositions where observed (Fig. 9.2(d)).

In the cyclone body, the velocity magnitude is relatively low and only reaches values higher than 10 m/s in the conical part. No clear helical vortex is visible. Also the turbulent kinetic energy is low.

The velocity magnitude in the bunker is low and relatively stable. At the same time, the turbulent kinetic energy is higher than in the vertical tube section and cyclone body.

At the roof, the kinetic energy and turbulent kinetic energy become higher close to the vortex finder. This agrees with the experiments, where the clean ring between the vortex finder and roof is visible (Fig. 9.2(c)).

11.2.3 Wall Shear Stress

The shear stress at the cyclone's outer wall and a detail of the vortex finder and roof is shown in Fig. 11.2(c), 11.2(f) and 11.2(i).

The lowest wall shear stress is at the wall of the cylindrical part, where its value is lower than 1.0 Pa. Also at the roof, the wall shear stress is relatively low, although it increases near to the

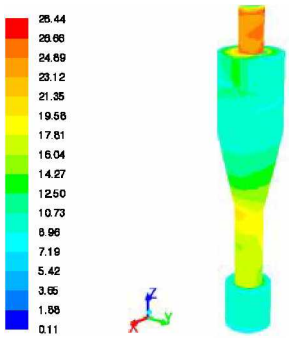

(a) Front view of the velocity magnitude in the wall adjacent cells.

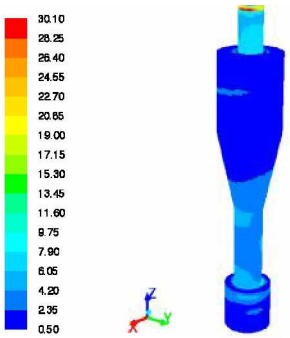

(b) Front view of the turbulent kinetic energy, k, in the wall adjacent cells.

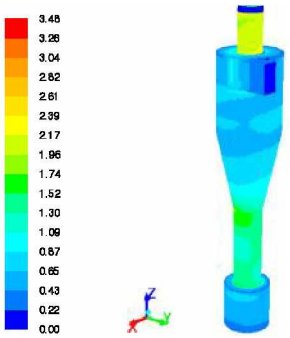

(c) Front view of the wall shear stress.

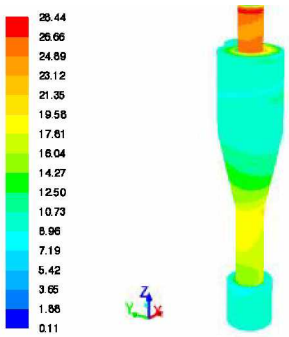

(d) Rear view of the velocity magnitude in the wall adjacent cells.

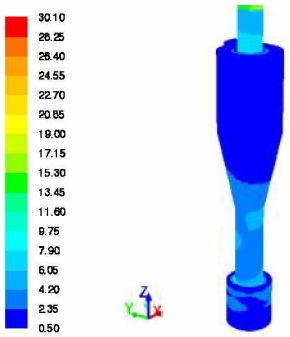

(e) Rear view of the turbulent kinetic energy, k, in the wall adjacent cells.

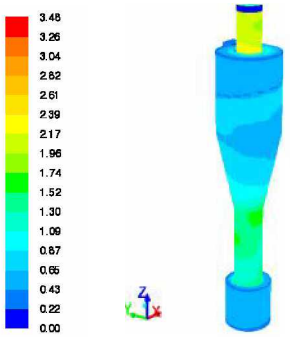

(f) Rear view of the wall shear stress.

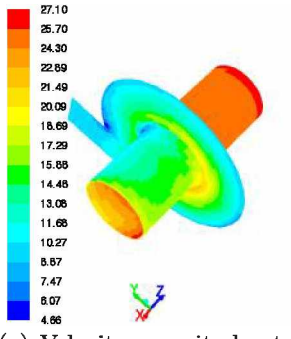

(g) Velocity magnitude at the roof and vortex finder.

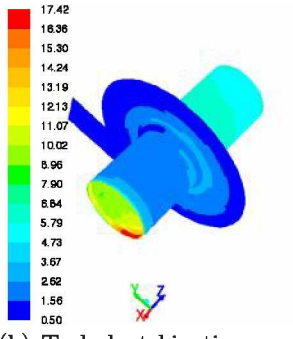

(h) Turbulent kinetic energy, k, at the roof and vortex finder.

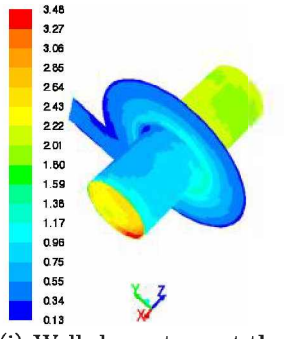

(i) Wall shear stress at the roof and vortex finder.

Figure 11.2: *Velocity magnitude* $[\mathrm{m\,s^{-1}}]$*, turbulent kinetic energy* $[\mathrm{m^2\,s^{-2}}]$ *and wall shear stress* [Pa] *at a volume flow rate of 600* $\mathrm{m^3/h}$.

vortex finder. In the conical part the wall shear stress increases from the top to the bottom to finally reach values up to 2.0 Pa in the vertical tube section. The values in the bunker are low. The highest wall shear stress is found at the vortex finders inside, especially at the lower edge, where its value becomes more than 3.0 Pa.

The wall shear stress is known to be proportional to the wall normal velocity gradient. This velocity gradient is found in the equations for drag, as in Eq. (4.55) and lift on a particle, as in Eq. (4.66) and Eq. (4.69), in contact with the wall. These forces increase the values for the ratios used for the forces based particle sticking criterion in Eq. (7.5a)-(7.5c), which, as a consequence, becomes harder to meet. This means that particles tend to stick in regions with a low wall shear stress. However, this is not in agreement with the experimental observations, where for example thick depositions at the vortex finders inside where noticed. As mentioned before, the wall shear stress in this region is the highest all over the computational domain.

11.3 Dispersed Phase

Firstly, some analyses are treated about the particle-wall collision statistics and forces acting on a particle in contact with a wall. From these statistical data, conclusions are drawn about which forces are important in the adhesion models introduced in Ch. 7.

Secondly, the particle residence time and the grade and total separation efficiency are discussed.

Both analysis are performed at a volume flow rate of 600 m^3/h because for this volume flow rate the depositions noticed in the experiments are most distinguished.

11.3.1 Particle-Wall Collision Statistics

Statistics were made to determine which of the adhesion and fluid-dynamic forces are dominant for particle wall-sticking. A number of 208 particles per diameter was released uniform from the inlet and tracked until they left the computational domain or exceeded the residence time limit. To avoid too large data-amounts, only 0.1% of the collisions were taken for the statistics. This was achieved by generating a random number for each particle-wall collision. Collisions in the dustbin are excluded from the statistics. The results are presented in Fig. 11.3 and 11.4.

11.3.1.1 Collision Frequency

The number of collisions between a particle and the wall shows a typical S-shape (Fig. 11.4(a)). Particles smaller than 5 μm have an average number of collisions lower than 50, with an absolute minimum at a particle diameter of 0.7 μm. For particles larger than 10 μm this number becomes close to 1×10^4. The number of collisions per particle increases continuously in between.

11.3.1.2 Impact Angle

The impact angle in respect to the wall normal is shown in Fig. 11.4(b). The root mean square value is situated between 80° and 90°. There is no clear correlation between particle diameter and impact angle. The standard deviation is approximately 5°. The high impact angles are easily explained because of the high tangential velocities in a cyclone.

11.3.1.3 Dimensionless Numbers

The particle-wall normal Reynolds and Stokes numbers are shown in Fig. 11.4(c). The wall normal Reynolds number, Re_n, is over whole the particle range smaller than unity, which is the condition for the drag force equation (Eq. (10.8)) used in the velocity damping factor calculation (Ch. 10).

11.3.1.4 Adhesion Forces

The van der Waals force, capillary force, electrostatic force and electrical force are shown in Fig. 11.4(d) for the moment that a particle collides with the wall. The van der Waals force is dominant over the whole range of particle diameters: for a particle of 40 μm in diameter it is two orders of magnitude larger than the capillary force. Capillary forces and electrical forces become of interest for particles smaller than 1 μm, although they are both still significant smaller than the van der Waals force. Electrostatic forces are negligible for all particles sizes considered.

11.3.1.5 Flow and Field Forces

The drag forces according to O'Neill, $F_{D,ON}$, and according to Al-Hayes and Winterton, $F_{D,AW}$, are compared in Fig. 11.3(a). Interesting is the fact that $F_{D,ON}$ shows a continuously increasing value for increasing particle size, whereas $F_{D,AW}$ fluctuates with a range of one order of magnitude around a mean value. However, the drag force of O'Neill predicts values which are two to four orders of magnitude larger than the one of Al-Hayes and Winterton. The tangential gravity force, shown in Fig. 11.3(d), is one to ten orders of magnitude smaller than the drag force. Therefore, it is reasonable to neglect gravity.

The lift force models are compared in Fig. 11.3(b). The Saffman lift force predicts values, which are two orders of magnitude larger for small particles in comparison with the lift force by Leighton and Acrivos. All other wall normal forces are in the same order of magnitude as $F_{L,LA}$: the turbophoresis force, the pressure gradient (both shown in Fig. 11.3(c)) and the wall normal gravity (Fig. 11.3(c)) are all in the range of $\left[10^{-18} : 10^{-9}\right]$ N.

11.3.2 Particle Residence Time

The particle residence time and the calculation cut-off time are shown in Fig. 11.5(a). The cut-off time is based on the time that is needed for 10 refreshment times and is slightly larger than 8 s. Only particles that leave through the vortex finder with the overflow are taken into the statistics. The residence time generally increases for increasing particle diameters. Some smaller drops in the trend might be caused by the decreasing number of particles in the overflow for increasing particle diameter which might mislead the statistics. Therefore, also the standard deviation increases.

The time at which 95% of the particles in the overflow of a certain diameter has left the computational domain, t_{95}, is calculated from the Weibull distribution function (App. B.3). No single particle larger than 11.5 μm was able to leave the domain within the cut-off time. As is seen from Fig. 11.5(a), the ratio between t_{cut} and t_{95} is between 1.5 and 7.4 and decreases for larger particles. Therefore, it seems to be reasonable to assume the cut-off time to be chosen large enough.

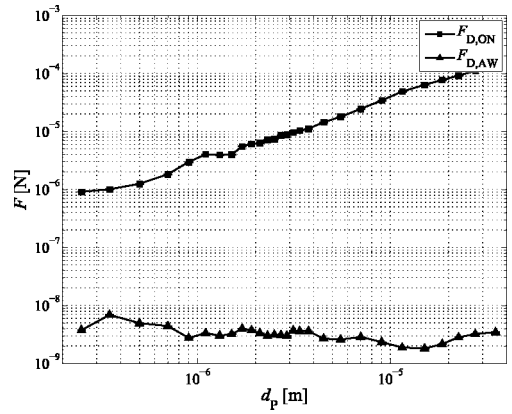

(a) Drag forces according to O'Neill ($F_{\mathrm{D,ON}}$ as in Eq. (4.55)) and according to Al-Hayes and Winterton ($F_{\mathrm{D,AW}}$ as in Eq. (4.53)).

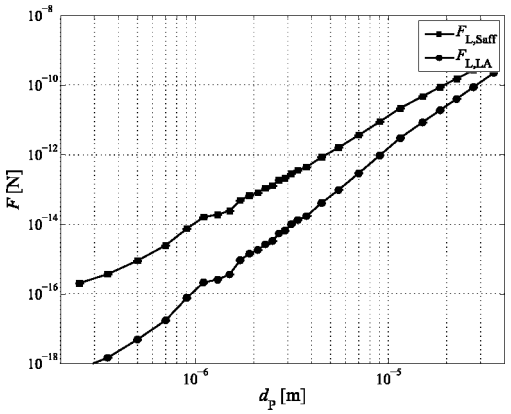

(b) Saffmann lift force ($F_{\mathrm{L,Saff}}$) and the lift force according to Leighton and Acrivos ($F_{\mathrm{L,LA}}$).

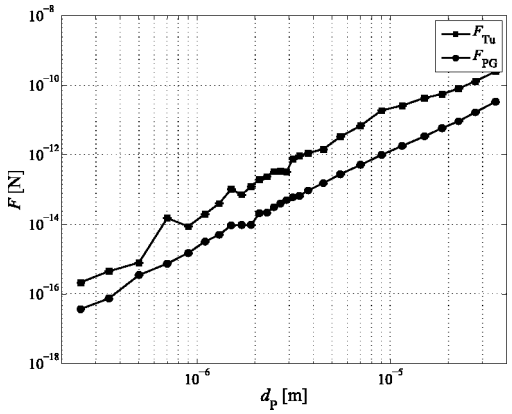

(c) Turbophoresis (F_{Tu}) and pressure gradient (F_{PG}) force.

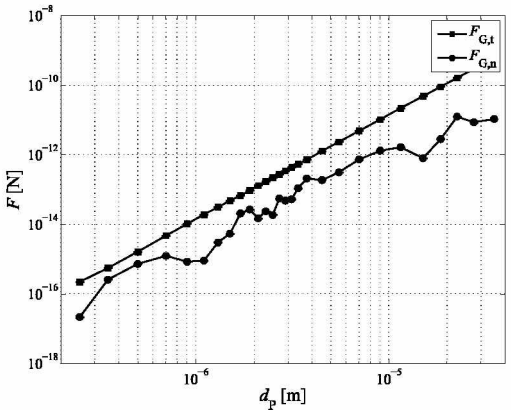

(d) Wall normal ($F_{\mathrm{G,n}}$) and tangential ($F_{\mathrm{G,t}}$) gravity force.

Figure 11.3: *Root mean square values and (negligible small) standard deviations of fluid-dynamic forces and gravity of particles colliding with a wall.*

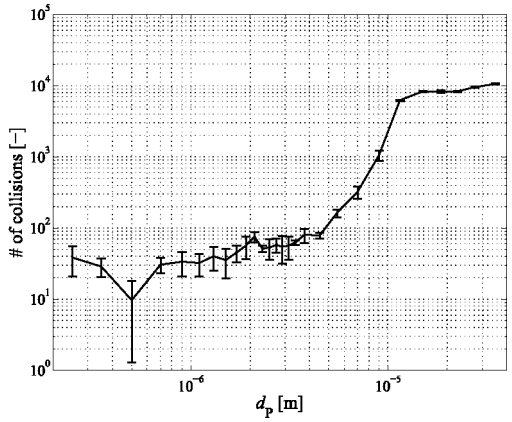

(a) Number of particle-wall collisions per particle.

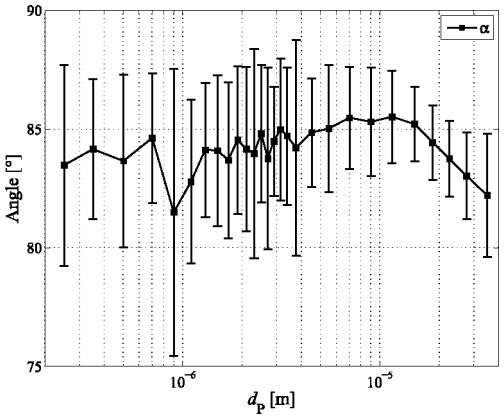

(b) Impact angle in respect to the wall normal.

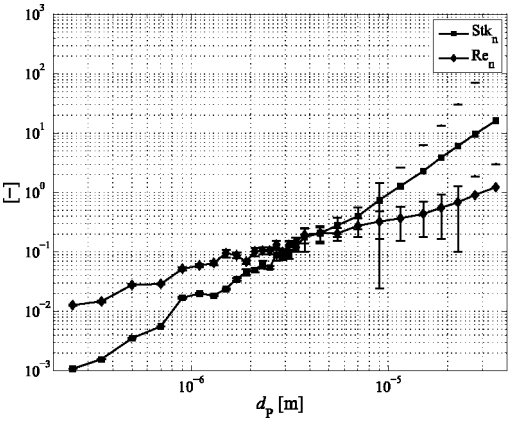

(c) Wall normal Stokes ($\mathrm{Stk_n}$) and Reynolds ($\mathrm{Re_n}$) numbers.

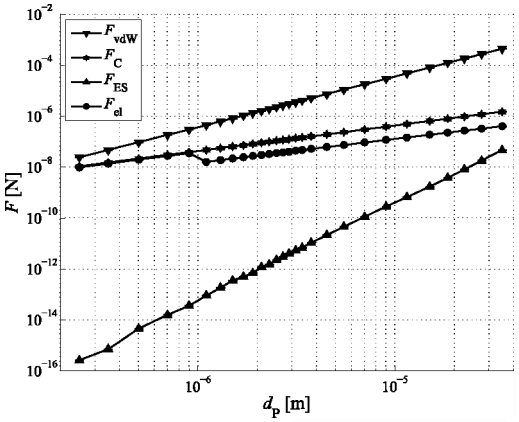

(d) Adhesion forces: van der Waals force (F_{vdW}), capillary force (F_{C}), electrostatic force (F_{ES}) and electrical force (F_{el}).

Figure 11.4: *Particle-wall collision statistics (rms values and rms standard deviations).*

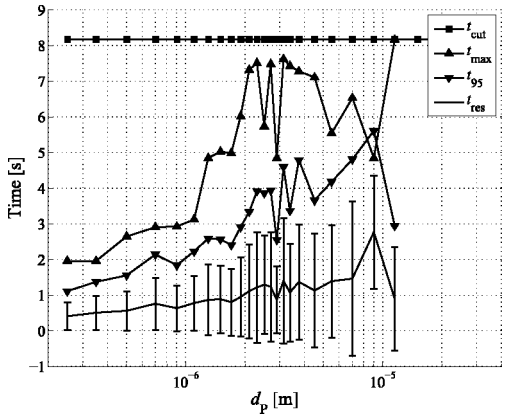

(a) Mean particle residence time of particles leaving through the vortex finder (t_{res}) with its standard deviation as well as the calculation cut-off time (t_{cut}), the critical time in the Weibull distribution for a 95% confidence, t_{95} and the residence time of the slowest particle in the overflow in its class (t_{max}).

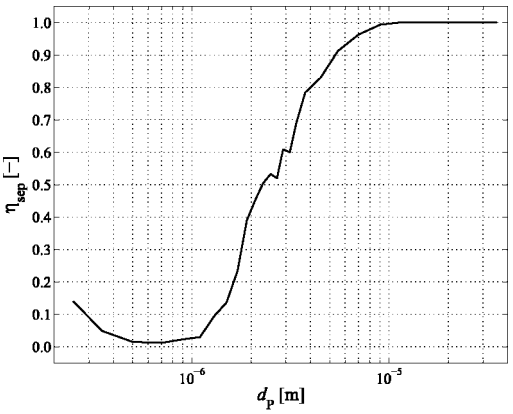

(b) Grade efficiency, η_{sep}, with its standard deviation: a fishhook is visible around $d_P = 0.7$ μm.

Figure 11.5: *Particle separation at a volume flow rate of 600* m^3/h.

11.3.3 Total and Grade Separation Efficiency

In Fig. 11.5(b), the grade efficiency is shown for a simulation with a volume flow rate of 600 m^3/h. A small fishhook is visible around a particle diameter of 0.7 μm. Since neither wall depositions nor agglomeration, as investigated by Gronald [53], are taken into account in the simulation, this fishhook is caused by the separation criterion only.

This means that some small particles (with $d_P = 0.25$ μm, for example) are not able to leave the computational domain within the cut-off time. However, the small particles that *are* able to leave the cyclone do this in a much smaller time than the cut-off time. For all submicron particles, the slowest particle in the overflow leaves the computational domain in a time, t_{max}, that is smaller than half the cut-off time, as demonstrated in Fig. 11.5(a). The simulation predicts a total separation efficiency of 62.9%, which is significant smaller than the separation efficiency during the experiments with the lowest solid loading of 1.0 g/kg, which was 72.4±5.5%.

12 Implementation of the Deposition Models into CFD

The deposition found in the experiments is compared to those calculated in the simulations in respect to the relative deposited mass and their particle size distributions. The parts distinguished are in principle the same as in Ch. 9, with the only difference that this time the sum of whole the vortex finder, i.e. both in- and outside, is calculated, instead of evaluating the depositions on these parts separately.

Both the deposition models based on conservation of energy on the one side and on the balance of the (moments of) forces on the other side are discussed. For the latter model, the forces are only determined from the time averaged flow field since the particles will be in general smaller than the thickness of the laminar sublayer in the boundary layer, as described in Eq. (10.6). Furthermore, the influence of the method for interpolating this velocity is discussed, i.e. the difference between linear interpolation, calculation from the wall shear stress and interpolation from the wall function.

Finally, the influence of the damping factor introduced in Ch. 10 is discussed and the results obtained *with* the use of the damping factor are compared to those *without*.

12.1 Comparison of Energy Based Deposition Models

The particle deposition with the deposition criterion of Eq. (7.2) is simulated with the following adhesion energies:

1. The van der Waals energy for undeformed particle, $E_{\mathrm{vdW},0}$ in Eq. (5.34), with the correction of Dahneke, discussed in Sec. 6.2.2;

2. The van der Waals energy for deformed particles, E_{vdW}, calculated with Eq. (5.38);

Table 12.1: *Material properties used in the simulations with the energy based models.*

quantity	contact value		unit
A_{12}	15×10^{-20}		J
$\Delta G_{12}^{\mathrm{LW}}$	-90.5×10^{-3}		$\mathrm{J\,m^{-2}}$
z_0	0.4×10^{-9}		m
e_{pl}	0.5		-
quantity	value limestone	value steel	unit
ρ_{P}	2.770×10^{3}		$\mathrm{kg\,m^{-3}}$
p_{pl}	3.5×10^{8}		Pa
Y	9.0×10^{10}	1.5×10^{11}	Pa
ν	0.265	0.25	-

Table 12.2: *Relative depositions during experiments and simulations with energy based deposition models with original impact velocity (mean values ± 95% confidence interval, experimental values from the experiments with* $\dot{V} = 600$ m^3/h *and* $\mu_e = 2.0$ g/kg*).*

	total [%wt]	vortex finder [%wt]	cyclone body [%wt]	vertical tube [%wt]
experiment	5.25 ± 3.93	0.86 ± 0.81	3.73 ± 3.05	0.64 ± 0.75
$E_{\mathrm{vdW},0}$	0.00 ± 0.00	0.00 ± 0.00	0.00 ± 0.00	0.00 ± 0.00
E_{vdW}	0.02 ± 0.01	0.00 ± 0.00	0.02 ± 0.01	0.00 ± 0.00
E_{S}	0.00 ± 0.00	0.00 ± 0.00	0.00 ± 0.00	0.00 ± 0.00

3. The surface energy, E_{S}, from Eq. (5.7), where the contact radius is determined with the adhesion map in Ch. 6. The Maugis-Dugdale regime is covered with the fit of Eq. (6.46).

The material properties of the quantities used in these deposition criterions are listed in Tab. 12.1. It should be noticed that the free energy of adhesion, $\Delta G_{12} = -90.5$ mJ/m^2, calculated in Ch. 5 would provide a value of the Hamaker constant of $A_{12} = 54.6 \times 10^{-20}$ J, which is a factor 3.6 higher than the one used in the simulations.

12.1.1 Separation and Grade Efficiency

The grade efficiency curves and the probability for a particle to get deposited, separated or to leave with the overflow are shown in Fig. 12.1. As is noticed, only the model, where the van der Waals energy with deformation is used, is able to predict depositions. Both other models do not predict any depositions at all. Therefore, all grade efficiency curves look similar to the one without depositions in Fig. 11.5(b).

The relative deposited masses are presented in Tab. 12.2. As remarked before, only the model with $E_{\mathrm{ad}} = E_{\mathrm{EvdW}}$ is able to predict depositions, which are only found at the cyclone body. The relative mass of 0.02±0.01%wt is over two orders of magnitude smaller than found in the experiments.

12.1.2 Particle Size Distribution of the Depositions

The cumulative particle size distribution function of the depositions on the cyclone body is shown in Fig. 12.2. The largest particle that is able to deposit is 0.4 μm in diameter. Particles larger than 1 μm do not deposit at all, which was already observed in earlier work [68] and is in contradiction to the experimental data.

12.2 Comparison of Force Based Deposition Models

Since particle depositions are found in the boundary layer of the flow near the walls, the fluid-dynamic forces are assumed to be steady state. For the calculation of the ratios, introduced in Sec. 7.2, the drag force (and the resulting moment of this force) according to O'Neil (Eq. 4.55), the lift force according to Leighton and Acrivos (Eq. (4.66)), gravity and the adhesion force with a Hamaker constant of $A = 15 \times 10^{-20}$ J, are used. The contact radius is calculated with the adhesion map in Sec. 6. The contact radius of particle diameters that fall in the Maugis-Dugdale regime are calculated with the fit of Eq. (6.46). The shear rate is required

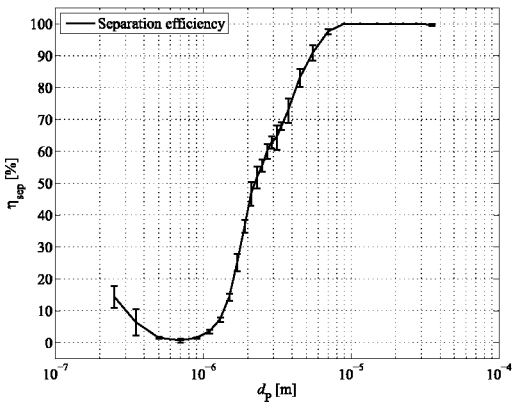

(a) Grade efficiency calculated with $E_{\mathrm{vdW},0}$ as defined in Eq. (5.34).

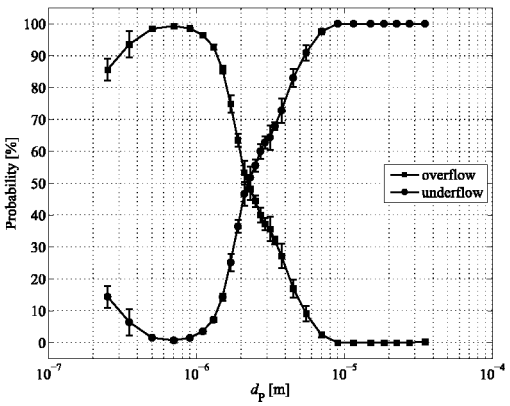

(b) Probability for a particle to get deposited, separated or to leave with the overflow with $E_{\mathrm{vdW},0}$ as defined in Eq. (5.34).

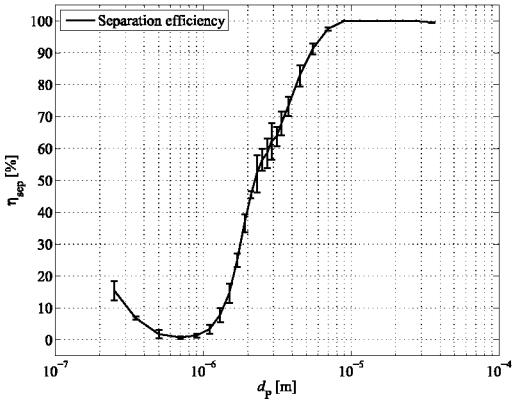

(c) Grade efficiency calculated with E_{vdW} as defined in Eq. (5.38).

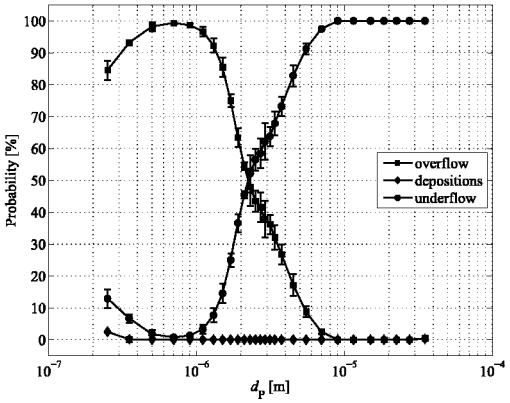

(d) Probability for a particle to get deposited, separated or to leave with the overflow with E_{vdW} as defined in Eq. (5.38).

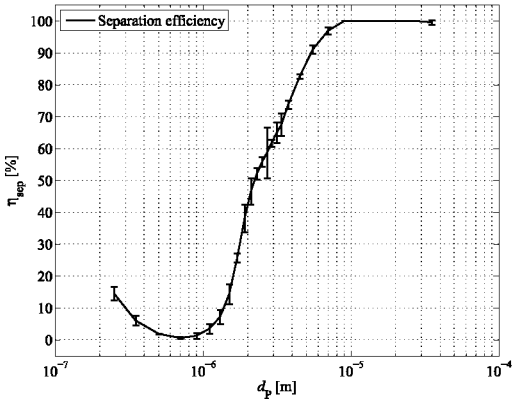

(e) Grade efficiency calculated with E_{S} as defined in Eq. (5.7).

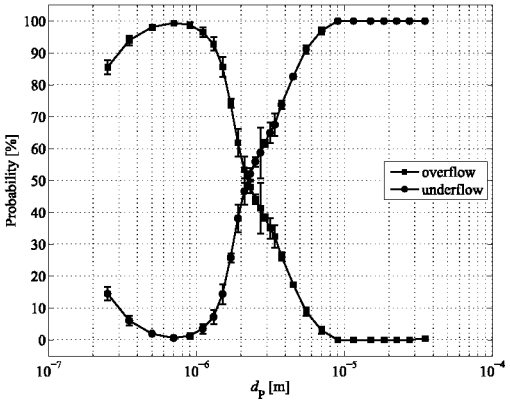

(f) Probability for a particle to get deposited, separated or to leave with the overflow with E_{S} as defined in Eq. (5.7).

Figure 12.1: *Separation efficiency and probability for under-, overflow and depositions for the deposition models based on energy conservation, with the original particle impact velocity.*

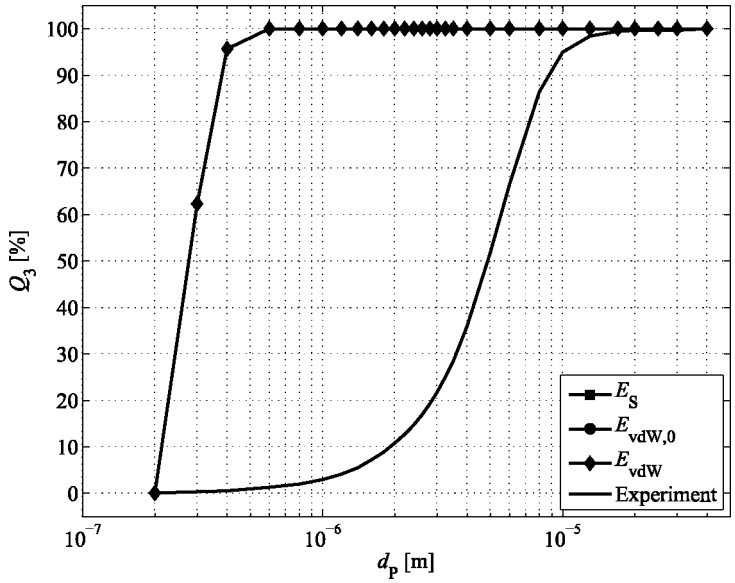

Figure 12.2: *Particle size distribution function of the depositions on the cyclone body for the energy based deposition models, without corrected velocity.*

for the calculation of the drag and lift force. In the boundary layer it is calculated with one of the following three methods:

1. from a linear profile between the tangential fluid velocity in the cell's midpoint, $u_{g,t}|_{cell}$, and the no-slip boundary condition at the wall:

$$\frac{du_t}{d\vec{n}} = \frac{u_{g,t}|_{cell}}{s}; \tag{12.1}$$

2. from the wall shear stress, τ_w, and the dynamic viscosity:

$$\frac{du_t}{d\vec{n}} = \frac{\tau_w}{\mu_g}; \tag{12.2}$$

3. from the flow profile of the turbulent boundary layer:

$$\frac{du_t}{d\vec{n}} = \frac{2\bar{u}}{d_P} = \frac{2u^+ u_*}{d_P}, \tag{12.3}$$

where, the value of u^+ has to be taken from the fits as function of y^+ in Eq. (8.50) or (8.51). Since the particles will be smaller than the thickness of the viscous sublayer for most cases, Eq. (8.50) will be valid and therefore Eq. (12.3) will equal Eq. (12.2).

12.2.1 Separation and Grade Efficiency

The results for the several methods of computing the fluid-dynamic forces are presented in Fig. 12.3. The shape of the grade efficiency curve using the linear interpolation equals that of

Table 12.3: *Relative depositions during experiments and simulations with force based deposition models with original impact frequency (mean values ± 95% confidence interval, experimental values from the experiments with $\dot{V} = 600$ m^3/h and $\mu_e = 2.0$ g/kg), where the shear rate is determined from Eq. (12.1) (linear), Eq. (12.2) (wall shear stress) and (Eq. 12.3) (boundary layer).*

	total [%wt]	vortex finder [%wt]	cyclone body [%wt]	vertical tube [%wt]
experiment	5.25 ± 3.93	0.86 ± 0.81	3.73 ± 3.05	0.64 ± 0.75
linear	1.54 ± 0.24	0.00 ± 0.00	1.54 ± 0.24	0.00 ± 0.00
wall shear stress	1.49 ± 0.04	0.00 ± 0.00	1.49 ± 0.04	0.00 ± 0.00
boundary layer	34.68 ± 0.51	0.71 ± 0.01	33.69 ± 0.46	0.28 ± 0.06

the curve using the wall shear stress. From this behaviour, it follows, that ANSYS Fluent 13.0 calculates the wall shear stress from the wall tangential value of the laminar velocity component in the cell's midpoint and that both models can be treated together. Depositions of particles takes place for particles smaller than 10 μm in diameter, with a maximum of approximately 4% for the smallest particles considered ($d_{P,min}$=0.25 μm). As a consequence, the fishhook is a little more pronounced than for the situation where depositions are neglected (Fig. 11.5(b)), where η_{sep} (0.25 μm) = 0.14 and the minimum of the grade efficiency 1%.

The total relative deposited mass is with a value around 1.5%wt lower than in the experiments (5.25%wt), but it should be remarked that the reproducibility in the simulations is significantly higher (Tab. 12.5). Furthermore, all depositions are found at the cyclone body, whereas in the experiments also depositions at the vortex finder and the vertical tube exist.

When calculating the fluid-dynamic forces from the boundary layer function, a completely different behaviour is observed, as in seen from Fig. 12.3(e) and 12.3(f). This behaviour is best explained by the probability of a particle to get deposited, demonstrated in Fig. 12.3(f): where of the smaller particles only 5% deposit, a suddenly increase of this value for the particle of 0.5 μm in diameter happens. Then, this value only drops down slowly to more or less zero for the maximal particle diameter in the feed. As a consequence, the grade efficiency curve does not show the typical S-shape anymore and has a local maximum around $d_P = 0.5$ μm.

A result of the grade efficiency curve, is the overpredicted separation efficiency of 34.5%. The lion's share of these depositions originate from the cyclone body, although also depositions at the vortex finder and the vertical tube section are found, which are in the same order of magnitude as in the experiments.

12.2.2 Particle Size Distribution of the Depositions

Since the largest contribution of the total depositions originates from the cyclone body, the Q_3-curves of all parts together and that of the body differ only very little (Fig. 12.4(a) and 12.4(b), respectively). All three interpolation methods predict smaller distributions than found in the experiments. Details on the $d_{P,25}$, $d_{P,50}$ and $d_{P,75}$ values are listed in App. C. The cut size of $d_{P,50} = 4.2$ μm is smaller in the simulations (3.8 μm when using the linear velocity interpolation and 2.7 μm when calculating the tangential velocity from the boundary layer function).

As mentioned before, only when using the boundary layer function, depositions at the vortex finder and the vertical tube are predicted, whose cut sizes respectively are 0.48 μm (experiment: 2.3 μm (inside) and 1.9 μm (outside)) and 0.93 μm (experiment: 5.22 μm). Especially the small depositions at the vertical tube are remarkable. A possible explanation is that most of

the larger particles are already deposited at the cyclone body, leaving only very small particles a possibility for depositing in the vertical tube.

12.3 Effect of the Damping Factor on Depositions

The velocity damping model as described in Ch. 10 was applied. The damping factor results in lower impact velocities, by which the energy sticking criterions are easier to meet, especially for small particles. Also the number of particle-wall impacts is reduced. Therefore, the sticking criterion based on forces is harder to meet. The results for both models is discussed below.

12.3.1 Energy Based Models

Whereas without the damping factor only depositions are found for $E_{\mathrm{ad}} = E_{\mathrm{vdW}}$, also the model with $E_{\mathrm{ad}} = E_{\mathrm{vdW,0}}$ predicts depositions with the use of the damping factor. From Tab. 12.4, the following remarks on the three adhesion energy calculation methods are made:

1. It is clear that if the adhesion energy calculated with E_{S}, no depositions are predicted at all. Even if the plastic coefficient of restitution is lowered to a value of 0.4, the relative depositions are still underpredicted by more than two orders of magnitude. Furthermore, depositions are then only found at the cyclone body;

2. The model with the van der Waals energy without deformation, $E_{\mathrm{vdW,0}}$, is able to predict depositions with the damping factor only at the cyclone body. The total sum of the relative depositions is much lower than the experimental values. However, the reproducibility during the simulations is much higher than during the experiments, resulting in a standard deviation which is one order of magnitude smaller.

3. When the adhesion energy is calculated from the van der Waals energy with deformation, E_{vdW}, the total relative depositions are only little underestimated. The depositions are mainly found in the cyclone body, where the simulated value of 3.08%wt is pretty close to the experimental one of 3.73%wt. Moreover, the standard deviation during the experiments is that large that the simulations agree with a probability of 79.5%. The relative depositions on the vortex finder and in the vertical tube section are nevertheless underestimated by more than one order of magnitude.

12.3.1.1 Separation and Grade Efficiency

The grade efficiency curves and the probability for a particle for getting deposited, separated or to leave with the overflow are shown in Fig. 12.5 for all three energy based models with the use of the damping factor. Since for the surface energy model (E_{S}) no depositions are found, the grade efficiency curve is very similar to that without depositions and thus a fishhook is visible. This fishhook is clearer seen for $E_{\mathrm{vdW,0}}$, where the grade efficiency, η_{sep}, becomes approximately 20% for a particle diameter of 0.9 μm, which is larger than the original diameter of 0.7 μm, i.e. without using the damping factor. This particle diameter is even larger for E_{vdW}, where its value is 1.7 μm. Furthermore, the smallest value of η_{sep} equals approximately 50%, here.

12.3.1.2 Particle Size Distributions

The particle size Q_3-distributions are given in Fig. 12.6. When the distribution of all depositions are summed, it is seen from Fig. 12.6(a) that the simulations predict finer distributions.

Table 12.4: *Relative depositions during experiments and simulations with energy based deposition models with corrected impact velocity, where the dimensionless numbers are evaluated by means of Eq. (10.60) (mean values ± 95% confidence interval, experimental values from the experiments with* $\dot{V} = 600\ \mathrm{m^3/h}$ *and* $\mu_e = 2.0\ \mathrm{g/kg}$*).*

	total [%wt]	vortex finder [%wt]	cyclone body [%wt]	vertical tube [%wt]
Experiment	5.25 ± 3.93	0.86 ± 0.81	3.73 ± 3.05	0.64 ± 0.75
$E_{\mathrm{vdW},0}$	0.01 ± 0.01	0.00 ± 0.00	0.01 ± 0.01	0.00 ± 0.00
E_{vdW}	3.12 ± 0.08	0.02 ± 0.01	3.08 ± 0.11	0.03 ± 0.02
E_{S}	0.00 ± 0.00	0.00 ± 0.00	0.00 ± 0.00	0.00 ± 0.00

Table 12.5: *Relative depositions during experiments and simulations with force based deposition models with the corrected impact frequency (mean values ± 95% confidence interval, experimental values from the experiments with* $\dot{V} = 600\ \mathrm{m^3/h}$ *and* $\mu_e = 2.0\ \mathrm{g/kg}$*), where the shear rate is determined from Eq. (12.1) (linear), Eq. (12.2) (wall shear stress) and (Eq. 12.3) (boundary layer).*

	total [%wt]	vortex finder [%wt]	cyclone body [%wt]	vertical tube [%wt]
Experiment	5.25 ± 3.93	0.86 ± 0.81	3.73 ± 3.05	0.64 ± 0.75
linear	1.49 ± 0.15	0.00 ± 0.00	1.49 ± 0.15	0.00 ± 0.00
wall shear stress	1.49 ± 0.13	0.00 ± 0.00	1.49 ± 0.13	0.00 ± 0.00
boundary layer	34.47 ± 0.31	0.72 ± 0.14	33.48 ± 0.35	0.26 ± 0.02

As is expected from the high contribution of the depositions on the cyclone body to the total depositions, the shape of this Q_3-distribution is almost equal (Fig. 12.6(b)). Only the models using $E_{\mathrm{vdW},0}$ and E_{vdW} are able to predict depositions, from which for the latter one also depositions at the vortex finder are noticed. The cut sizes are for all models still much lower than in the experiments and are, without exception, smaller than 1 μm. For details, the reader is again referred to App. C.

12.3.2 Force Based Models

The application of the correction factor to the models, which are based on the equilibrium of (moments of) forces, only influences the impact frequency, not the sticking probability. As consequence the positions, where the depositions principally can be found, are unchanged, however the model changes the number of impacts mostly in regions with high turbulent fluctuating velocities in wall normal direction.

12.3.2.1 Separation and Grade Efficiency

Only little difference is seen between the grade efficiency curve with and without the velocity damping model (Fig. 12.7 vs. Fig. 12.3, respectively). In general, the curves have moved to somewhat smaller particle diameters but the effect is only small. This is also clear from the total relative depositions, which decrease from 34.7%wt to 34.5%wt, when using the boundary layer function and remain approximately 1.5%wt for both other models.

12.3.2.2 Particle Size Distributions

Almost no changes for the particle size distribution functions of the depositions are noticed compared to those without using the damping model. The cut size of all depositions together decreases with circa 1.3% for the linear interpolation and wall shear stress models and remains unchanged when using the boundary layer function (details in App. C).

12.4 Conclusions and Recommendations

In general, the energy based sticking models predict too low values for the relative depositions. Also the implementation of the velocity damping factor does not change this behaviour, although it improves the results. The use of a higher Hamaker constant, calculated from the free energy of adhesion, would better the results. As alternative, a lower plastic constant of restitution of 0.4 instead of 0.5, will have a similar effect.

The use of the force and moment based sticking models, results in overrated and unrealistic depositions when the fluid-dynamic forces are calculated from the analytical function of the fluid velocity in the boundary layer. Better results are obtained from linear interpolating the tangential velocity between the value in the midpoint of the wall neighbouring cell and at the wall, where the no-slip boundary condition applies. Calculating the velocity gradient from the wall shear stress and dynamic viscosity gives exactly the same results.

The implementation of the damping factor does not change the results very much, since particles that are excluded from depositing, may deposit during the next wall collision. Furthermore, the damping model only has a significant influence on the behaviour of small particles. The use of the higher Hamaker constant will result in larger relative depositions and coarser particle size distributions of these depositions. Furthermore, also depositions at the vortex finder and the vertical tube section may be found with this higher Hamaker constant.

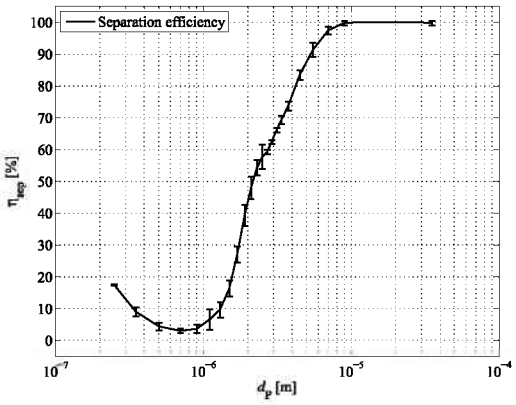

(a) Grade efficiency from linear interpolation of the fluid-dynamic forces.

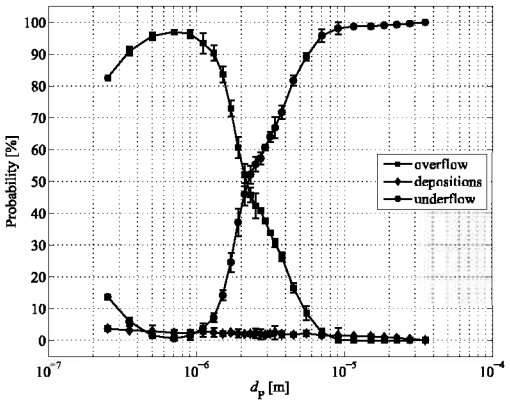

(b) Probability for a particle for getting deposited, separated or to leave with the overflow for linear interpolation of the fluid-dynamic forces.

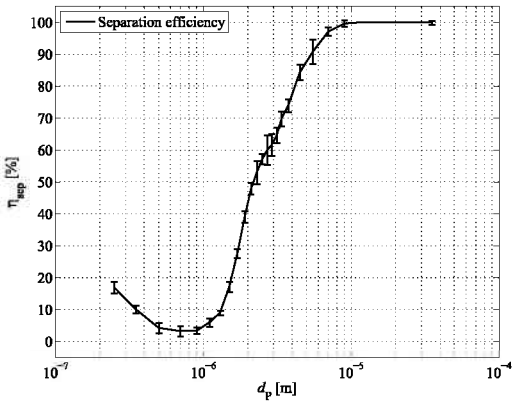

(c) Grade efficiency, where the fluid-dynamic forces are determined from the wall shear stress.

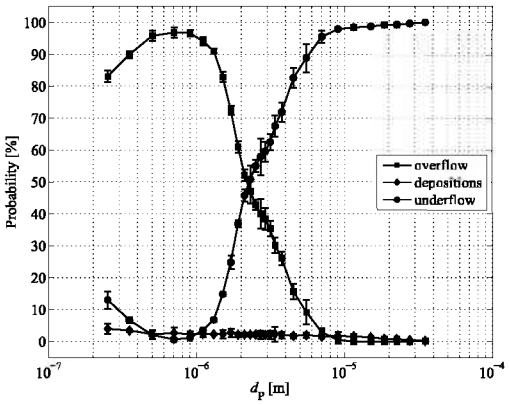

(d) Probability for a particle for getting deposited, separated or to leave with the overflow, where the fluid-dynamic forces are determined from the wall shear stress.

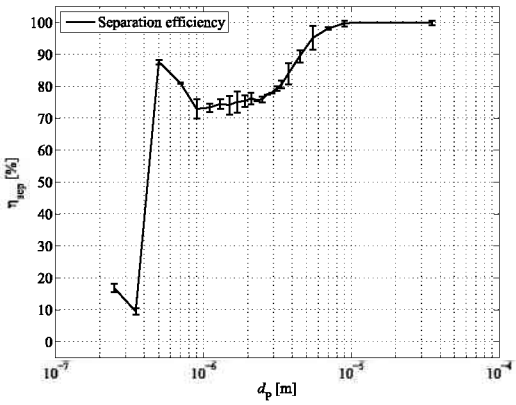

(e) Separation efficiency, where the fluid-dynamic forces are calculated from the boundary layer function.

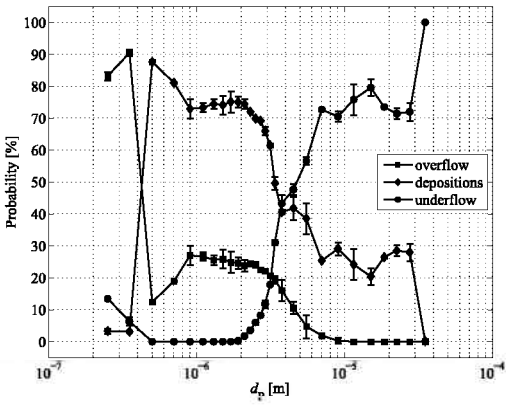

(f) Probability for a particle for getting deposited, separated or to leave with the overflow, where the fluid-dynamic forces are calculated from the boundary layer function.

Figure 12.3: *Separation efficiency and probability for under-, overflow and depositions for the deposition models based on a balance of forces and moments of forces, where the fluid-dynamic forces are linear interpolated from the cell's midpoint, or alternatively determined from the wall shear stress or from the boundary layer function.*

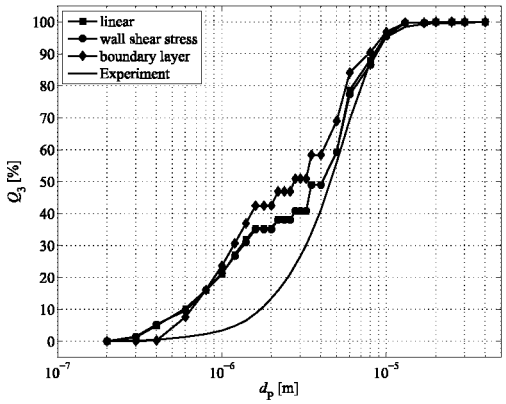

(a) Sum of all parts.

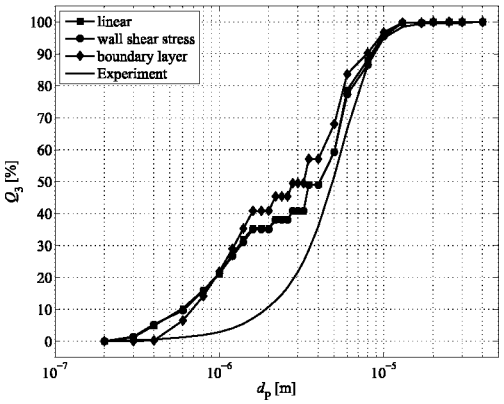

(b) Cyclone body.

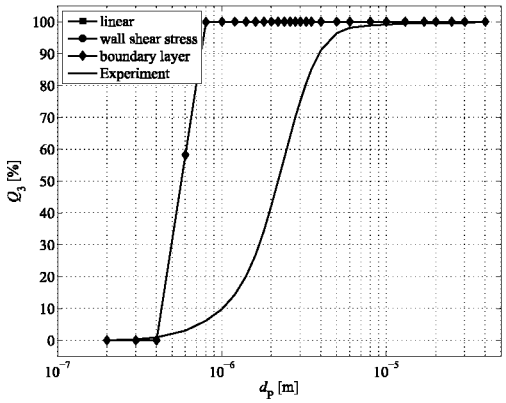

(c) Vortex finder, sum of in- and outside.

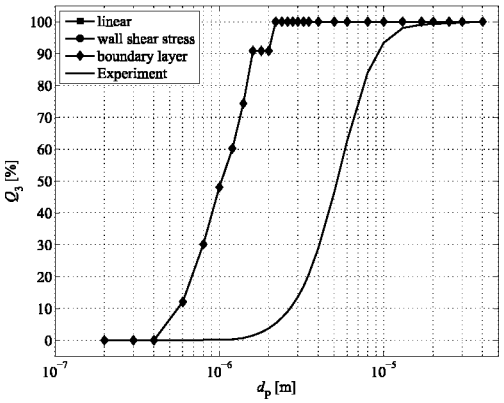

(d) Vertical tube.

Figure 12.4: *Cumulative particle size distributions, Q_3, calculated with force based deposition criterions without particle impact correction, where the fluid-dynamic forces are calculated from linear interpolation, or alternatively determined from the wall shear stress and from the boundary layer function.*

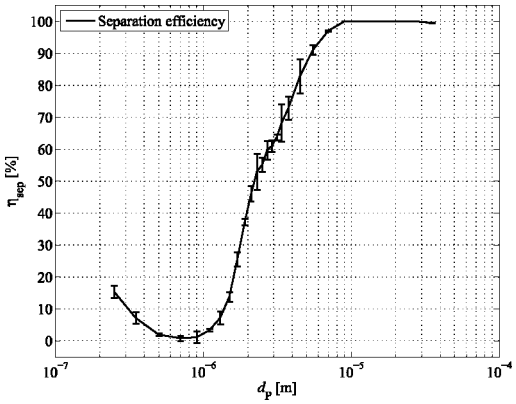

(a) Grade efficiency curve with $E_{\mathrm{vdW},0}$.

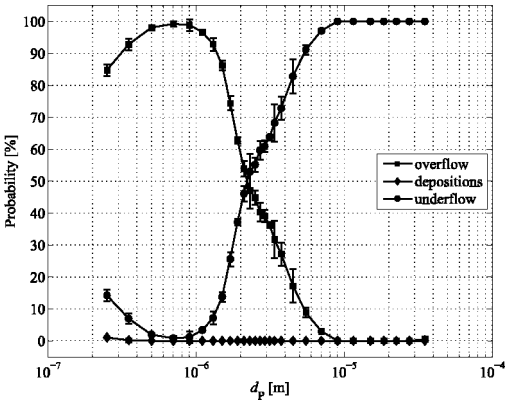

(b) Probability for a particle to get deposited, separated or to leave with the overflow with $E_{\mathrm{vdW},0}$ as defined in Eq. (5.34).

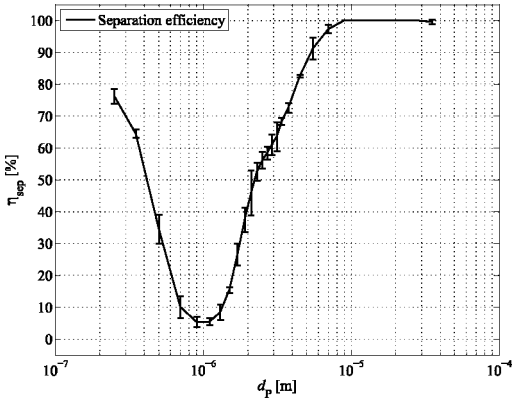

(c) Grade efficiency curve with E_{vdW}.

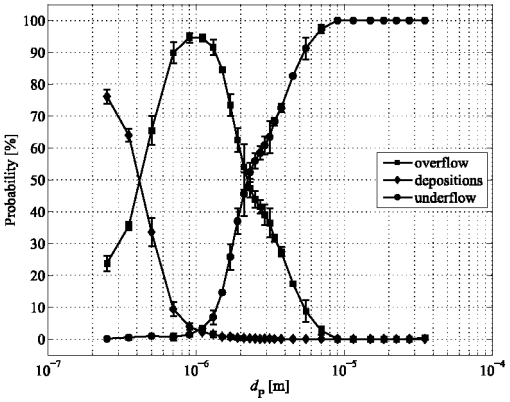

(d) Probability for a particle to get deposited, separated or to leave with the overflow with E_{vdW} as defined in Eq. (5.38).

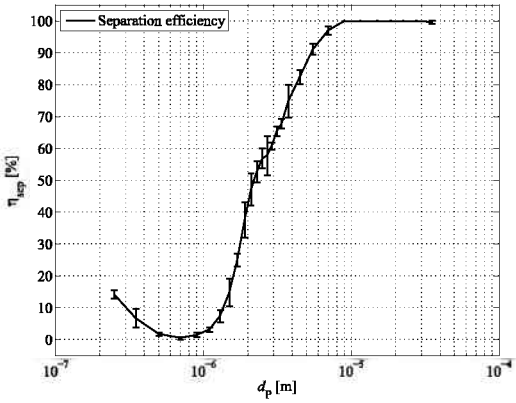

(e) Grade efficiency curve with E_{S}.

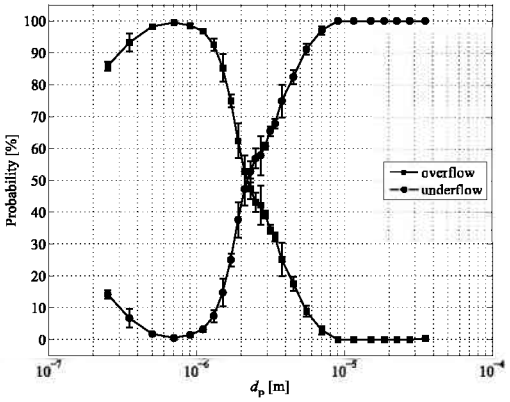

(f) Probability for a particle to get deposited, separated or to leave with the overflow with E_{S} as defined in Eq. (5.7).

Figure 12.5: *Separation efficiency and probability for under- overflow and depositions for the deposition models based on energy conservation, where the particle impact velocity has been corrected with the damping model as introduced in Ch. 10.*

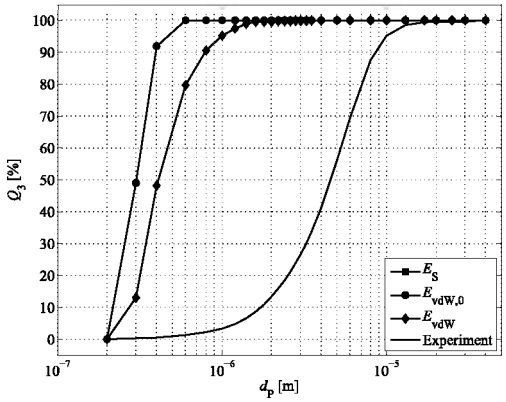

(a) Sum of all parts.

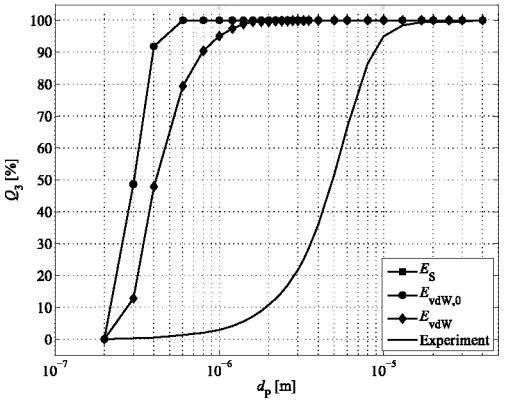

(b) Cyclone body.

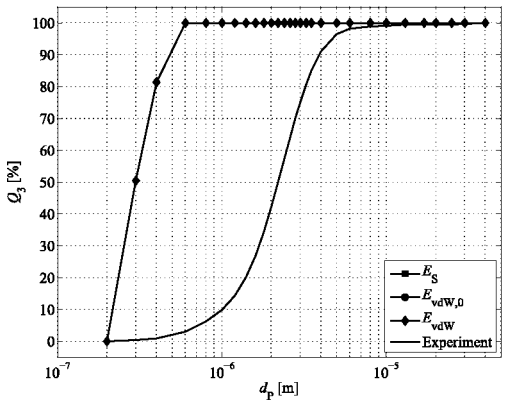

(c) Vortex finder, sum of in- and outside.

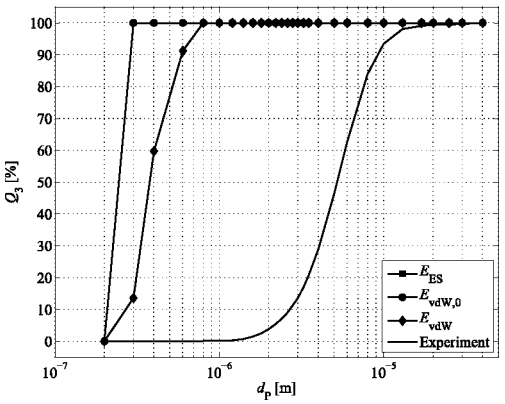

(d) Vertical tube.

Figure 12.6: *Cumulative particle size distributions, Q_3, calculated with the energy based deposition criterion and corrected particle impact velocity.*

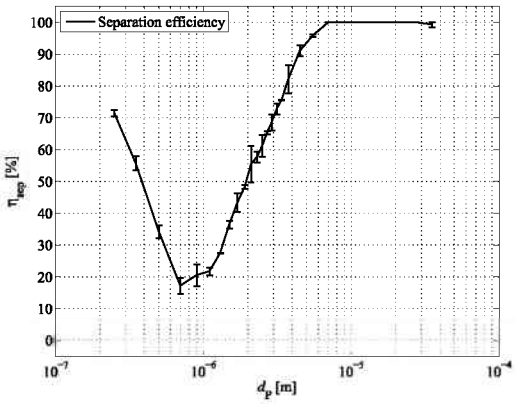

(a) Grade efficiency from linear interpolation of the fluid-dynamic forces.

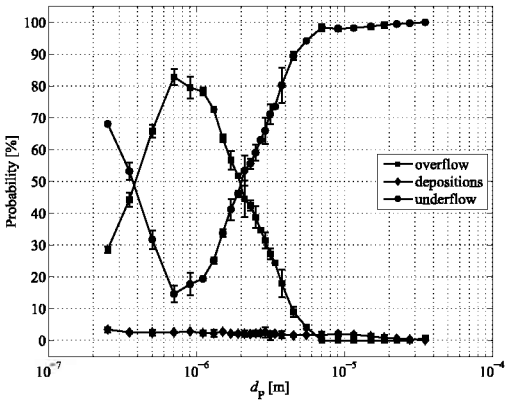

(b) Probability for a particle for getting deposited, separated or to leave with the overflow for linear interpolation of the fluid-dynamic forces.

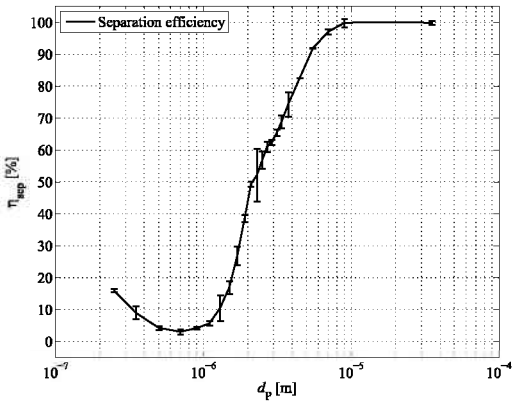

(c) Grade efficiency, where the fluid-dynamic forces are determined from the wall shear stress.

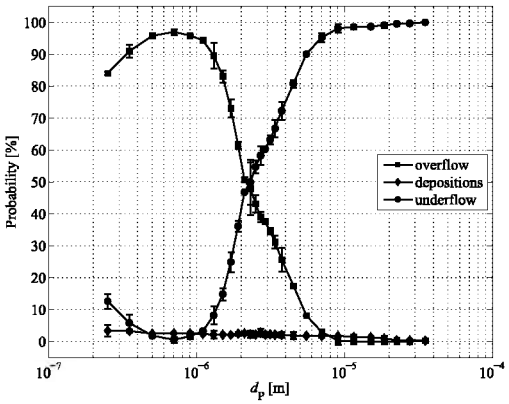

(d) Probability for a particle for getting deposited, separated or to leave with the overflow, where the fluid-dynamic forces are determined from the wall shear stress.

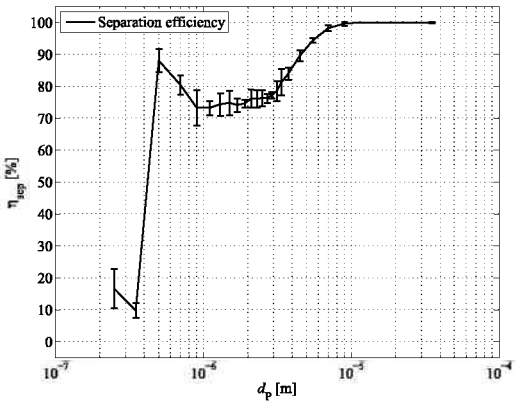

(e) Separation efficiency, where the fluid-dynamic forces are calculated from the boundary layer function.

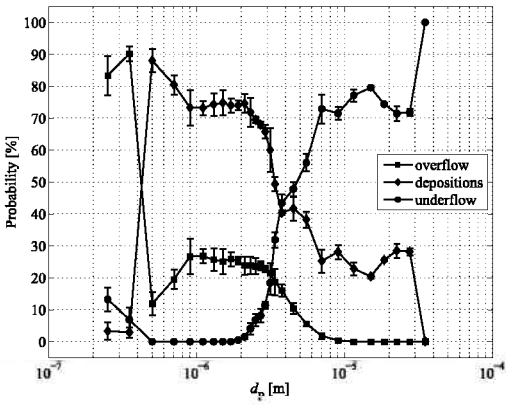

(f) Probability for a particle for getting deposited, separated or to leave with the overflow, where the fluid-dynamic forces are calculated from the boundary layer function.

Figure 12.7: *Separation efficiency and probability for under-, overflow and depositions for the deposition models based on a balance of forces and moments of forces, where the fluid-dynamic forces are linear interpolated from the cell's midpoint, or alternatively determined from the wall shear stress or from the boundary layer function.*

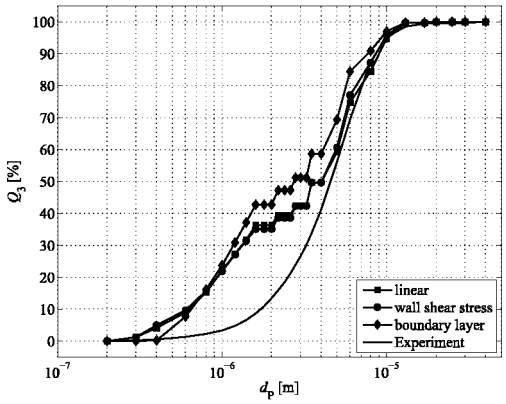

(a) Sum of all parts.

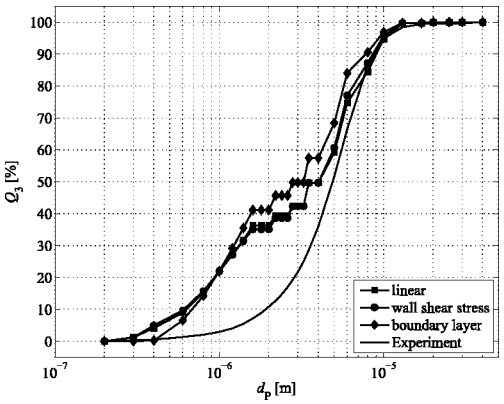

(b) Cyclone body.

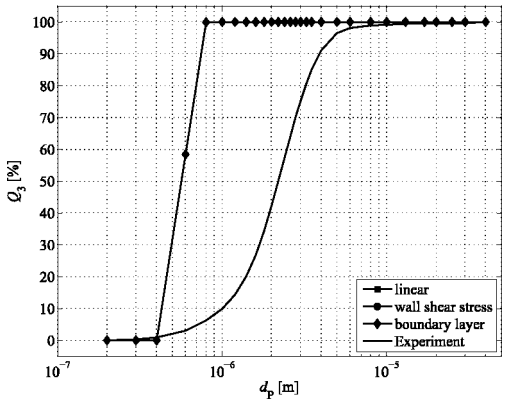

(c) Vortex finder, sum of in- and outside.

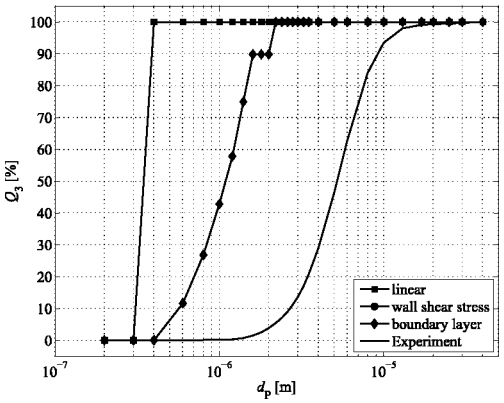

(d) Vertical tube.

Figure 12.8: *Cumulative particle size distributions, Q_3, calculated with force based deposition criterions with particle impact correction, where the fluid-dynamic forces are calculated from linear interpolation, or alternatively determined from the wall shear stress and from the boundary layer function.*

13 Conclusions and Recommendations

From the experimental investigations, it is known that the relative depositions in a cyclone separator are dependent on both the volume flow rate of air and the solid loading of the feed. The volume flow rate in the experiments was in the range of 600-1 200 m^3/h and the range of the solid loading was 0.66-7.9 g of limestone per kg of air. The relative depositions, defined as the fraction between the deposited mass and the total feed mass, always decrease for increasing volume flow rates, independently of the solid loading. However, a maximum in the depositions is found at a value of approximately 2.0 g/kg, although these solid loadings have such a low value that the assumption of one phase coupling in CFD simulations should be theoretically reasonable. This deposition behaviour has the following consequences for developing and dimensioning cyclone separators for a certain feed material:

- If no wall depositions are observed at a particular volume flow rate, also no wall depositions may be expected at higher volume flow rates. This provides a critical lower value for the volume flow rate;
- Since a local maximum in the relative deposited mass around a particular solid loading is found, it is important to know if the solid loading, for which test runs are performed, is lower or higher than this critical solid loading. If the latter is known, an upper or lower value for the solid loading can be given, respectively, to be sure wall depositions are avoided at a specific volume flow rate.

The sticking behaviour of particles during the experiments is described with physical models, based on the conservation of energy or on the balance of (moments of) forces, respectively. From an analysis of possible relevant forces and energies, it is shown that the van der Waals energy and -force are most important at ambient conditions for the deposition of limestone particles at a steel wall or at other limestone particles as well. The values of these quantities, calculated with several mathematical models, are compared with each other. Also the lift and drag force of a particle in a shear flow at the wall, as well as gravity are taken into account, as (flow) field forces.

The physical sticking criteria are implemented into computational fluid dynamics (CFD) simulations, using the commercial software package ANSYS Fluent 13.0. Besides realistic adhesion forces and -energies, also the impact velocities and frequencies in the CFD simulations should be true-to-nature. Generally, finer resolved grids give better results if consistency is given for the problem. However, this consistency is hard to achieve using a reasonable number of cells in a complex geometry like a cyclone separator. Also the creation of a so called boundary layer is not always possible, when using a commercial software package. Therefore, by means of two simple case studies, it is demonstrated that quantities like particle impact speed and frequency are highly dependent on the grid size near the wall. As a rule, the wall impact speed, as well as the impact frequency are overrated in the coarse grids, especially for small particles. With the use of a new proposal, the impact velocities in a coarse grid are recalculated in such

a way that the results are closer to those obtained when using a fine grid, which are taken as benchmark.

This could explain the behaviour of the depositions as observed in the simulations. In these simulations, Lagrangian particle trajectories have been calculated in an Eulerian flow field of the continuous phase. The turbulent motion of the particles has been created with the Discrete Random Walk model with a random eddy lifetime. Using the deposition models with the original, uncorrected impact velocities and frequencies, the following was noticed for the energy and (moments of) forces models, respectively:

- *Energy based models:* dependent on the method of calculating the van der Waals energy, some depositions of small particles are found *or* no depositions at all. When particles were noticed to deposit, their diameters were smaller than 0.5 μm and therefore even more tiny than the particles that deposited during the experimental investigations.
- *Force based models:* almost each particle-wall impact results in the deposition of the involved particle. Therefore, the relative depositions are much higher than those noticed in the experiments.

When using the damping factor these observations become:

- *Energy based models:* the damping factor results in lower particle-wall impact velocities that are closer to the critical values. Dependent on the model for calculating the van der Waals energy some depositions are predicted, which are coarser than without the use of the damping factor. The model based on the van der Waals energy and soft contact predicts a total relative deposition on all parts, which is relatively close to the experimental value. These depositions, however, are mainly found at the cyclone body and not in the vertical tube section and vortex finder, as noticed during experiments.
- *Force based models:* the corrected impact frequency provides only small changes of the deposition behaviour, since particles, that are excluded from colliding with the wall, may collide another time successfully. The last event is reasonable to happen, since the number of particle-wall collisions per single trajectory is significantly higher than unity.

Summarising the following recommendations are given for future work:

1. Theoretical modelling:
   - More reliable material properties are required to describe the adhesion energies and forces. Especially the Hamaker constant or the free energy of adhesion between steel and limestone should be known more exactly for the calculation of the van der Waals force and -energy. The Hamaker constant between limestone particles is better described in the literature and can be implemented to model the growth of a deposition layer.
   - In the particle damping model, the influence of the adapted wall normal Stokes number should be investigated in more detail. In the current model, this number is adapted (only) ones with a random number and by means of the wall normal component of the Reynolds stress tensor. This single number could be substituted by a series of independent numbers, depending on the size of the wall neighbouring cell and the number of eddies that is expected to interact with the particle in this cell.

2. Experimental investigations:

   - In several experiments with monodispersed particles, it could be investigated if a critical particle diameter exists, above which the test cyclone is not sensitive for depositions anymore. These experiments should be ideally performed at a volume flow rate of 600 m^3/h and a solid loading of 2.0 g/kg. At higher volume flow rates this critical particle diameter will probably increase as well.
   - The growth of the layer of depositions could be investigated in more detail to find out if the relative depositions are independent on the total mass feed or if an asymptotical behaviour may be expected. A series of experiments of increasing duration will provide this information.
   - Experiments performed at higher temperatures could give insight, if for these conditions other mechanisms than at ambient conditions influence the deposition behaviour. At such temperatures, thermophoresis could dominate the transport of particles to the wall. There, other forces than the van der Waals force could be dominant, for example capillary forces, if water from a hot flue gas condensates at the wall.

3. Numerical simulations:

   - The particle deposition models require exact particle impact velocities and probabilities in the CFD simulations. The use of the velocity damping factor gives better results for these quantities. However, the impact velocity and probability are in general *under-* and *over*estimated, respectively. A more sophisticated model, that is able to predict both quantities more correctly, will give more realistic results when still using the classical deposition models.
   - In the deposition model based on energy conservation, the influence of comparing the critical velocity to the wall *normal* impact velocity only, will result in a larger relative deposition because the wall normal impact velocity of a particle is per definition smaller than or as large as its impact speed. However, when using a model for the wall roughness, the wall normal vector is not clearly defined. This would (theoretically) give a particle the possibility to impact with the wall in a "pure tangential" manner.
   - The influence of the particle dispersion could be investigated in more detail. The direct random walk (DRW) model with a random eddy lifetime, that has been used in this thesis, treads turbulence in a rather statistical way. The continuous random walk (CRW) model is not standard provided by ANSYS Fluent 13.0 (yet) but may be implemented, for a physically more correct way of describing turbulence. The CRW model is also described for wall bounded flows in the literature, although, this implementation is neither open source yet nor self-evident in complex three-dimensional geometries.
   - Additional simulations at higher volume flow rates of 800, 1 000 and 1 200 m^3/h should be made to explain the dependency of the relative deposited mass on the volume rate. It may be expected that higher volume flow rates result in higher particle impact velocities and higher fluid-dynamic forces and therefore in decreasing depositions, which has also been observed in the experiments.
   - To explain the dependency on the solid loading, CFD models that are able to calculate strands, like the Euler-Euler-Lagrange model, could be useful. Small particles will be forced faster into the direction of the wall because their motion is influenced by that of larger ones, which experience higher centrifugal forces. This could make clear, how the

relative depositions can increase for increasing solid loadings up to the critical value of 2.0 g/kg. The decrease at higher solid loadings may be explained by an increase of fluid-dynamic forces near the wall because of increasing velocity gradients, since particles transport kinetic energy from the core region to the wall.

- For the compatibility with both deposition criteria, dispersed particles should be able to impact with the wall with a finite velocity and probability. If the strands of particles are modelled as a purely Eulerian phase, these conditions are not automatically given, because of the no-slip boundary condition at the wall. An option is to tread the particles within an Eulerian reference frame for all cells in the computational domain with exception of those neighbouring the wall. With the introduced particle damping model, it could be determined if a particle, that enters a wall neighbouring cell with known initial conditions, is able to reach the wall or if it will stay within the strand.
- The growth of a layer of depositions can be modelled by different van der Waals energies and -forces between limestone and steel on the one hand and between limestone with itself on the other hand. The fraction of the area of a wall neighbouring cell that is already covered with depositions can be saved in the user defined memory which is standard provided by ANSYS Fluent 13.0. Also the information of deposition in surrounding cells will be available. A particle impacting with the wall will experience these existing depositions if this fraction is larger than a random number, generated from an uniform distribution between zero and unity.
- Besides the contact forces and -energies, also the fluid-dynamic forces could be modelled dependent on already existing depositions. This means that impacting particles will experience the wake of other particles already sticking at the wall in the same or in neighbouring cells.
- The coupling between polydispersed particles is not automatically given in ANSYS Fluent 13.0, because particles are always injected in the same order. Therefore, such a distribution has to be provided from a single injection containing a collection of randomly ordered particles, which can be made in advance with a statistical software package for example.

Bibliography

[1] M. Abd-Elhady. *Gas-side particulate fouling in biomass gasifiers.* PhD thesis, Eindhoven University of Technology, 2005.

[2] C. Ahn Ho and M. Sommerfeld. Modelling of micro-particle agglomeration in turbulent flows. *Chemical Engineering Science*, 57(15):3073–3084, 2002.

[3] C. Ahn Ho and M. Sommerfeld. Numerische Berechnung der Staubabscheidung im Gaszyklon unter Berücksichtigung der Partikelagglomeration. *Chemie Ingenieur Technik*, 77(3):282–290, 2005.

[4] R. Al-Hayes and R. Winterton. Bubble diameter on detachment in flowing liquids. *International Journal of Heat and Mass Transfer*, 24(2):223–230, 1981.

[5] F. Barreiros, P. Ferreira, and M. Figueiredo. Calculating shape factors from particle sizing data. *Particle & Particle Systems Characterization*, 13(6):368–373, 1996.

[6] M. Barth. Mechanische Staubabscheider. *Starch - Stärke*, 28(9):315–322, 1976.

[7] W. Barth. Berechnung und Auslegung von Zyklonabscheidern auf Grund neuerer Untersuchungen. *Brennstoff Wärme Kraft, 8 (1)*, pages 1–9, 1956.

[8] W. Barth and L. Leineweber. Beurteilung und Auslegung von Zyklonabscheidern. *Staub und Reinhaltung der Luft*, 24(2):41–55, 1964.

[9] A. Berlemont, P. Desjonquères, and G. Gouesbet. Particle lagrangian simulation in turbulent flows. *International Journal of Multiphase Flow*, 16(1):19–34, 1990.

[10] R. Bird, E. Stewart, and E. Lightfoot. *Transport Phenomena.* John Wiley & Sons, Inc. New York, 2nd edition, 2006.

[11] M. Bohnet. Zyklonabscheider zum Trennen von Gas/Feststoff-Strömungen. *Chemie Ingenieur Technik*, 54(7):621–630, 1982.

[12] L. Botto, C. Narayanan, M. Fulgosi, and D. Lakehal. Effect of near-wall turbulence enhancement on the mechanisms of particle deposition. *International Journal of Multiphase Flow*, 31(8):940–956, 2005.

[13] G. Brenn, H. Braeske, G. Zivkivic, and F. Durst. Experimental and numerical investigation of liquid channel flows with dispersed gas and solid particles. *International Journal of Multiphase Flow*, 29(2):219–247, 2003.

[14] R. Bruchsal. *Der Einfluß von Partikelstoß und Partikelhaftung auf die Abscheidung in Faserfiltern.* PhD thesis, Technische Universität Karlsruhe, 1981.

[15] E. Brunnmair. Own photographs. unpublished.

[16] E. Brunnmair. *Entwicklung und Modellierung eines neuen Hochleistungszyklons zur Trennung von Feststoff / Gas-Gemischen.* PhD thesis, Montanuniversitaet Leoben, 2010.

[17] A. Bucchianico. *Statistisch Compendium.* Faculteit Wiskunde en Informatica, Technische Universiteit Eindhoven, 1996.

[18] E. Buckingham. On physically similar systems; illustrations of the use of dimensional equations. *Physical Review*, 4(4):345–376, 1914.

[19] R. Carpick, D. Ogletree, and M. Salmeron. A general equation for fitting contact area and friction vs load measurements. *Journal of Colloid and Interface Science*, 211(2):395–400, 1999.

[20] S. Chen and G. Doolen. Lattice Boltzmann method for fluid flows. *Annual Review of Fluid Mechanics*, 30(1):329–364, 1998.

[21] T. Chuah, J. Gimbun, and T. Choong. A CFD study of the effect of cone dimensions on sampling aerocyclones performance and hydrodynamics. *Powder Technology*, 162(2):126–132, 2006.

[22] T. Chung. *Computational Fluid Dynamics*. Cambridge University Press, 2002.

[23] J. Cleaver and B. Yates. Mechanism of detachment of colloidal particles from a flat substrate in a turbulent flow. *Journal of Colloid and Interface Science*, 44(3):464–474, 1973.

[24] J. Cleaver and B. Yates. A sub layer model for the deposition of particles from a turbulent flow. *Chemical Engineering Science*, 30(8):983–992, 1975.

[25] R. Clift, J. Grace, and M. Weber. *Bubbles, drops, and particles*. Academic press New York, 1978.

[26] R. Cordes. Cyclones to lessen Fouling, 1972. US Patent 3,675,401.

[27] R. Corless, G. Gonnet, D. Hare, D. Jeffrey, and D. Knuth. On the LambertW function. *Advances in Computational Mathematics*, 5(1):329–359, 1996.

[28] C. Cortés and A. Gil. Modeling the gas and particle flow inside cyclone separators. *Progress in Energy and Combustion Science*, 33(5):409–452, 2007.

[29] B. Dahneke. The influence of flattening on the adhesion of particles. *Journal of Colloid and Interface Science*, 40(1):1–13, 1972.

[30] B. Daly and F. Harlow. Transport equations in turbulence. *Physics of Fluids*, 13:2634–2649, 1970.

[31] A. De Lazzer, M. Dreyer, and H. Rath. Particle-surface capillary forces. *Langmuir*, 15(13):4551–4559, 1999.

[32] A. Dehbi. Turbulent particle dispersion in arbitrary wall-bounded geometries: A coupled CFD-Langevin-equation based approach. *International Journal of Multiphase Flow*, 34(9):819–828, 2008.

[33] B. Derjaguin, I. Aleinikova, and Y. Toporov. On the role of electrostatic forces in the adhesion of polymer particles to solid surfaces. *Powder Technology*, 2(3):154–158, 1969.

[34] B. Derjaguin, V. Muller, N. Mikhovich, and Y. Toporov. Influence of contact electrification on the collision of elastic particles with a rigid surface. *Journal of Colloid and Interface Science*, 118:553–563, 1987.

[35] J. Derksen. Separation performance predictions of a Stairmand high-efficiency cyclone. *AIChE Journal*, 49(6):1359–1371, 2003.

[36] J. Derksen, H. van den Akker, and S. Sundaresan. Two-way coupled large-eddy simulations of the gas-solid flow in cyclone separators. *AIChE Journal*, 54(4):872–885, 2008.

[37] T. Dreeben and S. Pope. Probability density function and reynolds-stress modeling of near-wall turbulent flows. *Physics of Fluids*, 9(1):154–163, 1997.

[38] F. Errington and E. Powell. A cyclone separator for aerosol sampling in the field. *The Journal of Hygiene*, 67(3):387–399, 1969.

[39] I. Fluent. FLUENT 6.0 User's Guide. *Lebanon, NH*, 2001.

[40] G. Gambit. 2.1 User Guide. *Fluent Inc.*

[41] C. Gao, G. Sun, R. Dong, and S. Fu. Characterizing the dynamic property of the vortex tail in a gas cyclone by wall pressure measurements. *Fuel Processing Technology*, 91(8):921–926, 2010.

[42] J. Gebhard. Einfluss der Beladung und des Gasdurchsatzes auf den Gesamtabscheidegrad und den Druckverlust eines Gaszyklons mit Fallrohr. Master's thesis, Graz University of Technology, 2004.

[43] A. Gil, C. Cortes, L. Romeo, and J. Velilla. Gas-particle flow inside cyclone diplegs with pneumatic extraction. *Powder Technology*, 128(1):78–91, 2002.

[44] R. Glass. A letter from the frustrated author of a journal paper. *Journal of Systems and Software*, 54(1):1–2, 2001.

[45] A. Goldman, R. Cox, and H. Brenner. Slow viscous motion of a sphere parallel to a plane wall–II couette flow. *Chemical Engineering Science*, 22(4):653–660, 1967.

[46] A. Gorton-Hülgerth. *Messung und Berechnung der Geschwindigkeitsfelder und Partikelbahnen im Gaszyklon.* PhD thesis, Graz University of Technology, 1998.

[47] A. Gorton-Hülgerth and G. Staudinger. Dreidimensionale Strömungssimulation in einem Gaszyklon mit "Reynolds-Stress-Modell". *Chemie Ingenieur Technik*, 71(4):354–356, 1999.

[48] A. Gorton-Hülgerth, J. Woisetschläger, G. Wigley, and G. Staudinger. Investigation of the flow field in the upper part of a cyclone with laser and phase Doppler anemometry. *Particle & Particle Systems Characterization*, 17(1):21–27, 2000.

[49] G. Gouesbet and A. Berlemont. Eulerian and Lagrangian approaches for predicting the behaviour of discrete particles in turbulent flows. *Progress in Energy and Combustion Science*, 25(2):133–159, 1998.

[50] D. Graham and R. Moyeed. How many particles for my Lagrangian simulations? *Powder Technology*, 125(2-3):179–186, 2002.

[51] J. Greenwood. Adhesion of elastic spheres. *Proceedings of the Royal Society of London. Series A: Mathematical, Physical and Engineering Sciences*, 453(1961):1277–1297, 1997.

[52] W. Griffiths and F. Boysan. Computational fluid dynamics (CFD) and empirical modelling of the performance of a number of cyclone samplers. *Journal of Aerosol Science*, 27(2):281–304, 1996.

[53] G. Gronald. *Experimentelle und numerische Untersuchungen zur Partikelagglomeration im Gaszyklon.* PhD thesis, Graz University of Technology, 2005.

[54] G. Gronald and J. Derksen. Simulating turbulent swirling flow in a gas cyclone: A comparison of various modelling approaches. *Powder Technology*, (205):160–171, 2010.

[55] A. Haider and O. Levenspiel. Drag coefficient and terminal velocity of spherical and nonspherical particles. *Powder Technology*, 58(1):63–70, 1989.

[56] H. Hamaker. The London-van der Waals attraction between spherical particles. *Physica*, 4(10):1058–1072, 1937.

[57] E. Heinl and M. Bohnet. Calculation of particle-wall adhesion in horizontal gas-solids flow using CFD. *Powder Technology*, 159(2):95–104, 2005.

[58] R. Herman. An introduction to electrical resistivity in geophysics. *American Journal of Physics*, 69:943–952, 2001.

[59] W. Hermans. *Onder Professoren.* De Bezige Bij, 1975.

[60] R. Hiller and F. Löffler. Einfluß von Auftreffgrad und Haftanteil auf die Partikelabscheidung in Faserfiltern. *Staub und Reinhaltung der Luft*, 40(9):405–411, 1980.

[61] H. Hoeijmakers. *Numerieke Stromingsleer.* Eindhoven University of Technology, lecture notes, 2004.

[62] A. Hoekstra. *Gas flow field and collection efficiency of cyclone separators.* PhD thesis, Delft University of Technology, 2000.

[63] A. Hoffmann, M. De Groot, W. Peng, H. Dries, and J. Kater. Advantages and risks in increasing cyclone separator length. *AIChE Journal*, 47(11):2452–2460, 2001.

[64] A. Hoffmann, R. de Jonge, H. Arends, and C. Hanrats. Evidence of the 'natural vortex length' and its effects on the separation efficiency of gas cyclones. *Filtration & Separation*, 32(8):799–804, 1995.

[65] A. Hoffmann and L. Stein. *Gas Cyclones and Swirl Tubes - Principles, Desing and Operation.* Springer-Verlag, Berlin, Germany, 1st edition, 2002.

[66] A. Hoffmann and L. Stein. *Gas Cyclones and Swirl Tubes - Principles, Design and Operation.* Springer-Verlag, Berlin, Germany, 2nd edition, 2007.

[67] J. Houben. CFD-Simulationen in einem Zyklon mit zentralem Leitkörper und logarithmischen Einlauf. Mentioned in Brunnmair 2010.

[68] J. Houben. Wall depositions in gas cyclones. Master's thesis, Eindhoven University of Technology, 2006.

[69] J. Houben and G. Staudinger. Wandablagerungen im Gas/Feststoff beladenen Zyklon. *Chemie Ingenieur Technik*, 80(5):615–619, 2008.

[70] S. Hu and A. McFarland. Wetted wall cyclone system and methods, June 27 2008. US Patent App. 12/163,265.

[71] M. Hubbe. Theory of detachment of colloidal particles from flat surfaces exposed to flow. *Colloids and Surfaces*, 12:151–178, 1984.

[72] J. Hughes. *Electrostatic Particle Charging-Industrial & Health Care Applications.* Research Studies Press, 1997.

[73] B. Imre, S. Räbsamen, and S. Springman. A coefficient of restitution of rock elements. *Computers & Geosciences*, 34:339–350, 2008.

[74] J. Israelachvili. *Intermolecular and Surface Forces.* Academic Press, 2nd edition, 1992.

[75] K. Johnson and J. Greenwood. An adhesion map for the contact of elastic spheres. *Journal of Colloid and Interface Science*, 192(2):326–333, 1997.

[76] K. Johnson, K. Kendall, and A. Roberts. Surface energy and the contact of elastic solids. *Proceedings of the Royal Society of London. A. Mathematical and Physical Sciences*, 324(1558):301–313, 1971.

[77] G. Kallio and M. Reeks. A numerical simulation of particle deposition in turbulent boundary layers. *International Journal of Multiphase Flow*, 15(3):433–446, 1989.

[78] F. Kaya, I. Karagoz, and A. Avci. Effects of surface roughness on the performance of tangential inlet cyclone separators. *Aerosol Science and Technology*, 45(8):978–985, 2011.

[79] W. Kraipech, A. Nowakowski, T. Dyakowski, and A. Suksangpanomrung. An investigation of the effect of the particle–fluid and particle–particle interactions on the flow within a hydrocyclone. *Chemical Engineering Journal*, 111(2-3):189–197, 2005.

[80] W. Krambrock. Die Berechnung des Zyklonabscheiders und praktische Gesichtspunkte zur Auslegung , Teil 1. *Aufbereitungstechnik*, 7:391–401, 1971.

[81] H. Krupp, W. Schnabel, and G. Walter. The Lifshitz-Van der Waals constant: Computation of the Lifshitz-Van der Waals constant on the basis of optical data. *Journal of Colloid and Interface Science*, 39(2):421–423, 1972.

[82] H. Krupp and G. Sperling. Theory of adhesion of small particles. *Journal of Applied Physics*, 37(11):4176–4180, 1966.

[83] J. Kuerten and A. Vreman. Can turbophoresis be predicted by large-eddy simulation? *Physics of Fluids*, 17:011701–4, 2005.

[84] D. Kwok. The usefulness of the Lifshitz–van der Waals/acid–base approach for surface tension components and interfacial tensions. *Colloids and Surfaces A: Physicochemical and Engineering Aspects*, 156(1-3):191–200, 1999.

[85] B. Legg and M. Raupach. Markov-chain simulation of particle dispersion in inhomogeneous flows: the mean drift velocity induced by a gradient in Eulerian velocity variance. *Boundary-Layer Meteorology*, 24(1):3–13, 1982.

[86] D. Leighton and A. Acrivos. The shear-induced migration of particles in concentrated suspensions. *Journal of Fluid Mechanics*, 181:415–439, 1987.

[87] B. Leonard. Order of accuracy of QUICK and related convection-diffusion schemes. *Applied Mathematical Modelling*, 19(11):640–653, 1995.

[88] F. Löffler. Partikelabscheidung an Tropfen und Fasern Vortrag auf der GVC-Tagung, Technik der Gas/Feststoff-Strömung, 7./8. Dez. 1981 in Düsseldorf. *Chemie Ingenieur Technik*, 55(3), 1983.

[89] F. Löffler. *Staubabscheiden.* Thieme, 1988.

[90] F. Löffler and W. Muhr. Die Abscheidung von Feststoffteilchen und Tropfen an Kreiszylindern infolge von Trägheitskräften. *Chemie Ingenieur Technik*, 44(8):510–514, 1972.

[91] W. Lianze, Z. Xiangrong, and Z. Keqin. An analytical expression for the coagulation coefficient of bipolary charged particles by an external field with the effect of Coulomb force. *Journal of Aerosol Science*, 36:1050–1055, 2005.

[92] F. Lien and M. Leschziner. Assessment of turbulence-transport models including non-linear RNG eddy-viscosity formulation and second-moment closure for flow over a backward-facing step. *Computers & Fluids*, 23(8):983–1004, 1994.

[93] L. Ma, D. Ingham, and X. Wen. Numerical modelling of the fluid and particle penetration through small sampling cyclones. *Journal of Aerosol Science*, 31(9):1097–1119, 2000.

[94] J. Mahrenholtz, J. Schmitz, K. Zeyen, and O. Fleschentrager. Self-cleaning separator for cohesive or adhesive products, Dec. 20 1999. US Patent App. 09/467,702.

[95] S. Martens. *Strömungsmechanik und Stoffaustausch.* Institut für Thermische Verfahrenstechnik und Umwelttechnik, Graz University of Technology, script, 2004.

[96] H. Masuda, K. Higashitani, and H. Yoshida. *Powder technology handbook.* CRC Press, 2006.

[97] J. Matsuyama and H. Yamamoto. Electrification of single polymer particles by successive impacts with metal targets. *IEEE Transactions on Industry Applications*, 31:1441–1445, 1995.

[98] D. Maugis. Adhesion of spheres: the JKR-DMT transition using a Dugdale model. *Journal of Colloid and Interface Science*, 150(1):243–269, 1992.

[99] J. McLaughlin. Aerosol particle deposition in numerically simulated channel flow. *Physics of Fluids A: Fluid Dynamics*, 1:1211–1224, 1989.

[100] A. Mizuno. Electrostatic precipitation. *IEEE Transactions on Dielectrics and Electrical Insulation*, 7(5):615–624, 2000.

[101] O. Molerus. Effect of interparticle cohesive forces on the flow behaviour of powders. *Powder Technology*, 20(2):161–175, 1978.

[102] O. Molerus. The role of science in particle technology. *Powder Technology*, 122(2-3):156–167, 2002.

[103] S. Morsi and A. Alexander. An investigation of particle trajectories in two-phase flow systems. *Journal of Fluid Mechanics*, 55:193–208, 1972.

[104] E. Muschelknautz. Auslegung von Zyklonabscheidern in der technischen Praxis. *Staub und Reinhaltung der Luft*, 30(5):187–195, 1970.

[105] E. Muschelknautz. Die Berechnung von Zyklonabscheidern für Gase. *Chemie Ingenieur Technik*, 44(1-2):63–71, 1972.

[106] E. Muschelknautz and K. Brunner. Untersuchungen an Zyklonen. *Chemie Ingenieur Technik*, 39(9-10):531–538, 1967.

[107] E. Muschelknautz, V. Greif, and M. Trefz. *VDI-Wärmeatlas*, chapter Zyklone zur Abscheidung von Feststoffen aus Gasen, pages Lja 1–11. VDI-Wärmeatlas Düsseldorf, 1997.

[108] E. Muschelknautz and W. Krambrock. Aerodynamische Beiwerte des Zyklonabscheiders aufgrund neuer und verbesserter Messungen. *Chemie Ingenieur Technik*, 42(5):247–255, 1970.

[109] E. Muschelknautz and M. Trefz. *VDI-Wärmeatlas, Auflage*, volume 6, chapter Druckverlust und Abscheidegrad von Zyklonen, pages Lja 9–9. VDI-Wärmeatlas Düsseldorf, 1991.

[110] S. Nelson and P. Bartley, Jr. Open-ended coaxial-line permittivity measurements on pulverized materials. *IEEE Transactions on Instrumentation and Measurement*, 47:133–137, 1998.

[111] F. Nieuwstadt. *Turbulentie: theorie en toepassingen van turbulente stromingen.* Epsilon Uitgaven Utrecht, 1998.

[112] S. Obermair, M. Bohnet, and G. Staudinger. Einfluss der Feststoffaustragsgeometrie auf die Abscheidung in einem Gaszyklon bei hoher Temperatur. *Chemie Ingenieur Technik*, 76(1-2):76–80, 2003.

[113] S. Obermair and G. Staudinger. The dust outlet of a gas cyclone and its effects on separation efficiency. *Chemical Engineering Technology*, 24(12):1259–1263, 2001.

[114] S. Obermair and G. Staudinger. Einfluss der Feststoffaustragsgeometrie auf die Abscheidung im Gaszyklon. *Chemie Ingenieur Technik*, 73:203–207, 2003.

[115] S. Obermair, J. Woisetschläger, and G. Staudinger. Investigation of the flow pattern in different dust outlet geometries of a gas cyclone by laser doppler anemometry. *Powder Technology*, (138):239–251, 2003.

[116] M. O'Neill. A sphere in contact with a plane wall in a slow linear shear flow. *Chemical Engineering Science*, 23(11):1293–1298, 1968.

[117] P. Pascal and B. Oesterlé. On the dispersion of discrete particles moving in a turbulent shear flow. *International Journal of Multiphase Flow*, 26(2):293–325, 2000.

[118] W. Peng, A. Hoffmann, H. Dries, M. Regelink, and L. Stein. Experimental study of the vortex end in centrifugal separators: the nature of the vortex end. *Chemical Engineering Science*, 60(24):6919–6928, 2005.

[119] W. Pietsch and H. Rumpf. Haftkraft, Kapillardruck, Flüssigkeitsvolumen und Grenzwinkel einer Flüssigkeitsbrücke zwischen zwei Kugeln. *Chemie Ingenieur Technik*, 39(15):885–893, 1967.

[120] S. Pirker and D. Kahrimanovic. A combined method for simulating gas-particle flows in highly laden cyclones. In *5th Int. Conf. on CFD in Process Industries, Melbourne, Australia, CD-ROM Proc*, page 6, 2006.

[121] F. Podczeck. *Particle-particle adhesion in pharmaceutical powder handling.* Imperial College Press London, 1998.

[122] F. Podczeck. Investigations into the reduction of powder adhesion to stainless steel surfaces by surface modification to aid capsule filling. *International Journal of Pharmaceutics*, 178(1):93–100, 1999.

[123] F. Qian and M. Zhang. Study of the natural vortex length of a cyclone with response surface methodology. *Computers and Chemical Engineering*, 29(10):2155–2162, 2005.

[124] H. Rumpf. Über das Ansetzen fein verteilter Stoffe an den Wänden von Strömungskanälen. *Chemie Ingenieur Technik*, 25(6):317–327, 1953.

[125] P. Saffman. The lift on a small sphere in a slow shear flow. *Journal of Fluid Mechanics*, 22(02):385–400, 1965.

[126] E. Schmidt, C. Wadenpohl, and F. Löffler. Mathematische Beschreibung von Agglomerationsvorgängen im Zykloneinlauf. *Chemie Ingenieur Technik*, 64(1):76–78, 1992.

[127] A. Schütz. Über die elektrische Aufladung von Aerosolen. *Staub-Reinhaltung der Luft*, 27(12):534–540, 1967.

[128] H. Schubert. Grundlagen des Agglomerierens. *Chemie Ingenieur Technik*, 51(4):266–277, 1979.

[129] U. Schwarz. A generalized analytical model for the elastic deformation of an adhesive contact between a sphere and a flat surface. *Journal of Colloid and Interface Science*, 261(1):99–106, 2003.

[130] M. Sharma, H. Chamoun, D. Sarma, and R. Schechter. Factors controlling the hydrodynamic detachment of particles from surfaces. *Journal of Colloid and Interface Science*, 149(1):121–134, 1992.

[131] C. Shephered and C. Lapple. Flow pattern and pressure drop in cyclone dust collectors. *Industrial & Engineering Chemistry*, 31(8):972–984, 1939.

[132] L. Shi and D. Bayless. Comparison of boundary conditions for predicting the collection efficiency of cyclones. *Powder Technology*, (173):29–37, 2007.

[133] M. Sommerfeld. Modelling of particle-wall collisions in confined gas-particle flows. *International Journal of Multiphase Flow*, 18(6):905–926, 1992.

[134] M. Sommerfeld. Analysis of collision effects for turbulent gas-particle flow in a horizontal channel: Part I. particle transport. *International Journal of Multiphase Flow*, 29(4):675–699, 2003.

[135] W. G. Spitzer and D. A. Kleinman. Infrared lattice bands of quartz. *Physical Review*, 121(5):1324–1335, 1961.

[136] G. Staudinger. *Mechanische Verfahrenstechnik 1.* Institut für Apparatebau, Mechanische Verfahrenstechnik und Feuerungstechnik, Graz University of Technology, script, 2004.

[137] T. Stifter, O. Marti, and B. Bhushan. Theoretical investigation of the distance dependence of capillary and van der Waals forces in scanning force microscopy. *Physical Review B*, 62(20):13667–13673, 2000.

[138] D. Tabor. Surface forces and surface interactions. *Journal of Colloid and Interface Science*, 58(1):2–13, 1977.

[139] D. Thomson. Criteria for the selection of stochastic models of particle trajectories in turbulent flows. *Journal of Fluid Mechanics*, 180:529–556, 1987.

[140] J. Tomas. Fundamentals of cohesive powder consolidation and flow. *Granular Matter*, 6(2):75–86, 2004.

[141] M. Trefz and E. Muschelknautz. Extended cyclone theory for gas flows with high solids concentrations. *Chemical Engineering & Technology*, 16(3):153–160, 1993.

[142] O. Triesch and M. Bohnet. Measurement and CFD prediction of velocity and concentration profiles in a decelerated gas-solids flow. *Powder Technology*, 115(2):101–113, 2001.

[143] C. van Oss. Use of the combined Lifshitz-van der Waals and Lewis acid-base approaches in determining the apolar and polar contributions to surface and interfacial tensions and free energies. *Journal of Adhesion Science and Technology*, 16(6):669–677, 2002.

[144] C. Van Oss, M. Chaudhury, and R. Good. Interfacial Lifshitz-van der Waals and polar interactions in macroscopic systems. *Chemical Reviews*, 88(6):927–941, 1988.

[145] C. van Oss, R. Good, and M. Chaudhury. The role of Van der Waals forces and hydrogen bonds in hydrophobic interactions between biopolymers and low energy surfaces. *Journal of Colloid and Interface Science*, 111(2):378–390, 1986.

[146] C. van Oss, R. Good, and M. Chaudhury. Additive and nonadditive surface tension components and the interpretation of contact angles. *Langmuir*, 4(4):884–891, 1988.

[147] A. Varaksin. *Turbulent particle-laden gas flows.* Springer Verlag, 2007.

[148] J. Visser. On Hamaker constants: A comparison between Hamaker constants and Lifshitz-van der Waals constants. *Advances in Colloid and Interface Science*, 3(4):331–363, 1972.

[149] J. Visser. Van der Waals and other cohesive forces affecting powder fluidization. *Powder Technology*, 58(1):1–10, 1989.

[150] H. Wang. Theoretical adhesion efficiency for particles impacting a cylinder at high reynolds number. *Journal of Aerosol Science*, 17(5):827–837, 1986.

[151] Z. Xiangrong, W. Lianze, and Z. Keqin. A simple criterion for particle-wall adhesion in a wire-plate electrostatic precipitator. *Journal of Aerosol Science*, 36(3):411–417, 2005.

[152] K. Yang and H. Yoshida. Effect of mist injection position on particle separation performance of cyclone scrubber. *Separation and Purification Technology*, 37(3):221–230, 2004.

[153] H. Yoshida. Three-dimensional simulation of air cyclone and particle separation by a revised-type cyclone. *Colloids and Surfaces A: Physicochemical and Engineering Aspects*, 109:1–12, 1996.

[154] J. Young and A. Leeming. A theory of particle deposition in turbulent pipe flow. *Journal of Fluid Mechanics*, 340:129–159, 1997.

[155] C. Zagorski. Numerische Berechnung von Strömung und Partikelbahnen im Gaszyklon. Master's thesis, Graz University of Technology, 2004.

[156] F. Zhang, A. Busnaina, M. Fury, and S. Wang. The removal of deformed submicron particles from silicon wafers by spin rinse and megasonics. *Journal of Electronic Materials*, 29(2):199–204, 2000.

Nomenclature

Latin

A	m^2	contact area
a	$\mathrm{m\,s}^{-2}$	acceleration term
A_{cor}	$\mathrm{m}^2\,\mathrm{s}^{-2}$	correlation matrix between fluctuating velocities
A_{ijk}	J	Hamaker constant
a_{in}	m	inlet width
A_{S}	m^2	real particle surface
A_{s}	m^2	particle surface of a sphere with the same surface
a_{s}	$\mathrm{m\,s}^{-1}$	speed of sound
b_{in}	m	inlet height
c	m	distance at which the surface in contact have been separated
C_0	-	constant for the calculation of the Lagrangian time scale
C_{E}	$\mathrm{m}^{-1}\,\mathrm{s}^{-1}$	constant
C_{i}	$\mathrm{m\,s}^{-1}$	thermal velocity of ion
c_{log}	$\mathrm{m\,s}^{-1}$	constant in logarithmic flow profile
d	m	diameter
d'_{P}	m	particle diameter in RRSB equation
D_{cb}	m	cyclone body diameter
D_{H}	m	hydraulic diameter
$D_{\mathrm{L,ij}}$	$\mathrm{kg\,m}^{-1}\,\mathrm{s}^{-3}$	molecular diffusion
$d_{\mathrm{P,50}}$	m	cut size / median particle diameter
D_{P}	$\mathrm{m}^2\,\mathrm{s}^{-1}$	Brownian diffusion coefficient
$D_{\mathrm{T,ij}}$	$\mathrm{kg\,m}^{-1}\,\mathrm{s}^{-3}$	turbulent diffusion
D_{vf}	m	diameter vortex finder

D_{vf}	m	vortex finder inner diameter
E	J	energy
e	C	elementary charge
e_a	-	elastic coefficient of restitution
e_i	m	average length of element in direction i
e_{pl}	-	plastic coefficient of restitution
F	N	force
$f(\Delta r)_i$	-	correlation function
F_l	N	external Hertzian force
f_{corr}	-	tangential velocity correction factor
F_c	N	critical pull-off force
F_D	$m^4\,s^{-2}$	scaled drag force
F_{ij}	$kg\,m^{-1}\,s^{-3}$	production by system rotation
F_x	$m^4\,s^{-2}$	scaled non-drag forces
g	$m\,s^{-2}$	gravitational constant
$g(\Delta r)_i$	-	correlation function
G_b	$kg\,m^{-1}\,s^{-3}$	generation of turbulent energy due to buoyancy
G_{ij}	$kg\,m^{-1}\,s^{-3}$	buoyancy production
G_k	$kg\,m^{-1}\,s^{-3}$	generation of turbulent energy due to velocity gradients
h	m	depth of penetration
h	m	wall distance
h_D	m	distance over which the Maugis-Dugdale pressure exists
h_e	m	depth of penetration
h_{pl}	m	plastic deformed height
h_P	J s	Planck's constant
i	-	time step index
I_P	$kg\,m^2$	particle's moment of inertia
I_{turb}	-	turbulent intensity
j	-	time step index

J_w	$kg\,m^{-2}\,s^{-1}$	mass flux of particles per unit area
K	Pa	effective elastic modulus
k	$m^2\,s^2$	turbulent kinetic energy
k_b	$J\,K^{-1}$	Boltzmann constant
k_d	$s\,m^{-1}$	dynamic friction coefficient
k_e	$m^2\,N^{-1}$	elastic parameter
k_s	-	sliding ratio
k_T	$W\,m^{-1}\,K^{-1}$	thermal conductivity
k_w	m	wall roughness
L	m	length
l_0	m	distance from the wall
L_c	m	natural vortex length
$L_{E,i}$	m	integral length scale
L_e	m	turbulent length scale
L_s	m	length scale
m	kg	mass
m_{Fr}	-	Frenkiel parameter
m_i	kg	ion mass
m_P	kg	particle mass
n	m^{-3}	molecule density
n_{RRSB}	-	parameter in RRSB equation
N_f	number of faces	
n_i	m^{-3}	number density of ions in space
N_P	m^{-3}	particle concentration
n_P	-	number of particles
n_r	-	number of repetitions
N_t	-	number of nodes required in a DNS grid
p	Pa	pressure
p''_{vdW}	Pa	van der Waals pressure

P_{ij}	$kg\,m^{-1}\,s^{-3}$	stress production
p_{pl}	Pa	yield stress of the softer material
p_s	Pa	saturation pressure
Q	$m^3\,s^{-1}$	volume flow rate
q	°	angle
q	C	charge
Q_0	-	cumulative number distribution function
q_0	m^{-1}	number distribution function
q_0	C	particle charge of a neutral particle
Q_3	-	cumulative mass/volume distribution function
q_3	m^{-1}	mass/volume distribution function
q_e	C	equilibrium charge
r	m	radius
r	m	smaller meniscus curvature
r_0	m	contact radius
R_{cor}	-	reduced correlation matrix
$R_{E,i}$	-	Eulerian part of the correlation function
R_{fL}	-	Lagrangian velocity correlation coefficient
r_{ij}	-	reduced element of the correlation matrix between fluctuating velocities
r_i	m	radius of the inner circle
r_K	m	Kelvin radius
R_L	-	Lagrangian part of the correlation function
r_o	m	radius of the outer circle
$R_{P,i}$	-	correlation function
R_P	$m^2\,s^{-2}\,K^{-1}$	quotient of the Boltzmann constant and particle mass
r_{rand}	-	random number
r_{sep}	m	separation distance
R_u	$J\,mol^{-1}\,K^{-1}$	universal gas constant
R^ϕ	-	(scaled) residual

S	m	cell dimension
s	m	wall normal distance from cell's midpoint
S_ϵ	$\mathrm{kg\,m^{-1}\,s^{-3}}$	user defined source term
S_ϕ	source term	
s_{ij}	$\mathrm{s^{-1}}$	rate of strain tensor
S_{k}	$\mathrm{kg\,m^{-1}\,s^{-3}}$	user defined source term
S_{user}	$\mathrm{kg\,m^{-1}\,s^{-3}}$	user defined source term
T	K	absolute Temperature
t	s	time
t'	s	integration time
t_0	s	integration starting time
t_{95}	s	critical of for a 95% confidence in the Weibull distribution function
t_{cross}	s	particle eddy crossing time
t_{cut}	s	cut-off time
T_{e}	s	characteristic time for field charging
T_{L}	s	Lagrangian time scale
t_{max}	s	residence time of the slowest particle in the overflow of its diameter
U	m	perimeter
u	m s−1	fluid velocity
u_*	$\mathrm{m\,s^{-1}}$	friction velocity
u_{c}	$\mathrm{m\,s^{-1}}$	velocity of the cell the particle is currently in
u_{in}	$\mathrm{m\,s^{-1}}$	inlet velocity
U_{P}	$\mathrm{m\,s^{-1}}$	fluid velocity
V	$\mathrm{m^3}$	volume
V_{e}	V	contact electrical potential
V_{m}	$\mathrm{m^3\,mol^{-1}}$	molar volume
V_{P}	$\mathrm{m^3}$	particle volume
w	$\mathrm{m\,s^{-1}}$	velocity
w_1	$\mathrm{N\,m^{-1}}$	work of adhesion performed by short range forces

w_2	$\mathrm{N\,m^{-1}}$	work of adhesion performed by long range forces
W_{ad}	J	work of adhesion
w_{cell}	$\mathrm{m\,s^{-1}}$	cell's fluid velocity
$w_{\mathrm{g,w}}$	$\mathrm{m\,s^{-1}}$	remaining velocity at the wall
w_{P}	$\mathrm{m\,s^{-1}}$	particle velocity
X	m	global coordinate
x	m	position
x_{P}	m	coordinate of the contact point
Y	Pa	Young's modulus
Y	m	global coordinate
y	m	wall distance
y_1	m	distance between wall and first cell centroid
Y_{M}	$\mathrm{kg\,m^{-1}\,s^{-3}}$	the contribution of the fluctuating dilatation in compressible turbulence to the overall dissipation rate
y_{P}	m	coordinate of the contact point
Z	m	global coordinate
z	m	vertical coordinate
$\mathrm{d}\xi_{\mathrm{i}}$	$\mathrm{s^{1/2}}$	series of uncorrelated numbers with variance $\mathrm{d}t$
$\boldsymbol{n}$	m	wall normal vector
$\boldsymbol{r}$	m	vector between centroid and face's midpoint

Greek

α	-	bipolar coordinate
α	rad	angle between particle velocity vector and wall normal
β	$\mathrm{K^{-1}}$	volumetric thermal expansivity
χ	-	random number
δ	m	vertical displacement of the bodies in contact
δ_{ij}	-	Kronecker Delta function
ΔG	$\mathrm{J\,m^{-2}}$	free energy of adhesion
Δp	Pa	pressure difference
Δr	m	distance in space

Δt	s	time step
δt	s	time step
$\Delta w_{P,max}$	$m\,s^{-1}$	maximal relative velocity between colliding particles
ΔX	m	distance vector element
ΔY	m	distance vector element
ΔZ	m	distance vector element
ϵ	$m^2\,s^{-3}$	turbulent dissipation rate
$\epsilon_{0,r}$	$m\,s^{-1}$	direction of the relative velocity
ϵ_0	$A\,s\,V^{-1}\,m^{-1}$	vacuum permittivity
ϵ_{ij}	$kg\,m^{-1}\,s^{-3}$	dissipation term
ϵ_i	-	imaginary part of the complex dielectric constant
ϵ_k	-	relative wall roughness
ϵ_r	-	relative permittivity
η	-	separation efficiency
η_K	m	Kolmogorov length scale
Γ	$m^3\,s\,kg^{-2}$	constant
γ	$N\,m^{-1}$	work of adhesion
Γ_ϕ	-	diffusion coefficient
γ_a	-	adiabatic index
γ_L	$N\,m^{-1}$	surface tension
κ	-	sharpness of cut
λ_0	-	friction coefficient for a clean gas
λ_g	m	mean free path
λ_L	$J\,m^6$	London dispersion force coefficient
λ_s	-	friction coefficient
μ_e	kg kg−1	solid loading
μ_g	Pa s	dynamic viscosity
μ_t	Pa s	turbulent viscosity
ν	-	Poisson ratio

ν_g	$m^2\,s^{-1}$	kinematic viscosity
ω	$rad\,s^{-1}$	angular frequency
Ω_k	$rad\,s^{-1}$	system rotation
ω_P	$rad\,s^{-1}$	particle angular velocity
ϕ	-	particle sphericity
ϕ	-	physical quantity
ϕ	rad	angle to the horizontal
ϕ_e	$C\,m^{-2}$	surface charge
ϕ_{ij}	$kg\,m^{-1}\,s^{-3}$	pressure strain
ϕ_L	J	van der Waals attractive potential
ρ	$kg\,m^{-3}$	density
ρ_0	$kg\,m^{-3}$	reference density
ρ_{Pm}	$kg\,m^{-3}$	particle mass concentration
ρ_q	$\Omega\,m$	particle resistivity
σ	$N\,m^{-2}$	interaction pressure
σ_A	$N^{1/2}\,m^{-1}$	surface density of charge
σ_D	$N\,m^{-2}$	maximal Maugis-Dugdale pressure
σ_e	$C\,m^{-2}$	charge density at equilibrium
σ_F	$m\,s^{-1}$	turbulent fluctuating velocity
Σ_{ij}	Pa	turbulent stress tensor
σ_{ij}	Pa	stress tensor
σ_i	$m\,s^{-1}$	rms-value of fluctuating velocity
τ	Pa	stress
τ	s	relative time
$\tau_{C,i}$	s	inter-particle collision time scale
τ_c	s	collision time
τ_d	s	time constant for diffusion charging
τ_e	s	eddy life time
τ_i	s	time scale

τ_P	s	particle relaxation time
τ_q	s	charge relaxation time
τ_w	Pa	wall shear stress
θ	-	scaling parameter
θ_P	°	contact angle between particle and fluid
θ_s	°	wetting angle
θ_w	°	contact angle between particle and wall
ζ	-	damping factor
ζ	-	random number from Gaussian probability function

Supersripts

*	reduced
j	force index
n	time step index
+	electron acceptor
-	electron donator
AB	polar acid-base component
LW	apolar Lifshitz van der Waals component
DMT	Derjaguin, Muller and Toporov
JKR	Johnson, Kendall and Roberts
S	Model of Schwarz
tot	total

Subsripts

0	initial
0	zero external force
1	before collision
1	grid 1 resolved in mm
1	index material 1
1	normal direction
2	after collision

2	grid 2 resolved in cm
2	index material 2
2	spanwise direction
2s	value at the wall
3	spanwise direction
CD	central differencing
SOU	second order upwind
UP	upwind
A	due to capillary pressure difference
A	feed
ad	adhesion
Add	added mass
AW	Al-Hayes and Winterton
b	buoyancy
Bass	Basset history term
C	capillary
c	central
c	constant
crit	critical
CY	Cleaver and Yates
D	drag
d	downstream
E	cell downstream
e	end
e	face common with cell downstream
eff	effective
el	electrical
el st	electrostatic
eq	equilateral

F	overflow
f	face
G	underflow
g	gas
g	gravity
H	Hertz
i	coordinate index
i	material index
j	coordinate index
j	material index
k	coordinate index
kin	kinetic
L	liquid
l	limestone
l	loss
LA	Leighton and Acrivos
log	logarithmic
M	Magnus
max	maximal
min	minimal
MP	midpoint
n	normal
nb	neighbouring cell
nn	normal-normal element in Reynolds stress tensor
no	negligible fluid velocity
ON	O'Neill
P	particle
p	value in cell
p	wall neighbouring cell

PG	pressure gradient
pl	plastic
res	resultant
rot	rotational
S	due to surface tension
S	solid
s	steel
s	value at a distance s from the wall
Saff	Saffman
step	Heaviside step function
T	torque
T	Thermophoretic
t	tangential
tot	total
tt	tangential,tangential component in Reynolds stress tensor
Tu	turbophoresis
u	upstream
vdW	van der Waals
W	cell upstream
w	face common with cell upstream
w	water
z	centrifugal

Special symbols

$\hbar$	J s	Planck's constant divided by 2π
$\hbar\varpi$	J	Lifshitz van der Waals constant
$\mathscr{L}$	m	macro length scale
$\mathscr{U}$	$\mathrm{m\,s^{-1}}$	macro velocity scale
$\dot{m}$	$\mathrm{kg\,s^{-1}}$	mass flow rate
$\dot{V}$	$\mathrm{m^3\,s^{-1}}$	volume flow rate

$\mathcal{V}$	$\mathrm{m\,s^{-1}}$	Kolmogorov velocity scale

Dimensionless numbers

α	scaling parameter to Schwarz
η	dimensionless displacement
κ	value of gradient
κ	von Kármán constant
λ	elastic parameter
μ	Tabor parameter
Π_i	relevant dimensionless number in the Buckingham-pi theorem
π_i	dimensionless number in the Buckingham-pi theorem
σ_ϵ	turbulent Prandtl number
σ_k	turbulent Prandtl number
σ^+	dimensionless fluctuating velocity
τ_2	scaling parameter acc. to Schwarz
$\tau_{\mathrm{P}+}$	dimensionless particle relaxation time
ξ	dimensionless force
B	additive contant
$C_{1\epsilon}$	model constant
$C_{2\epsilon}$	model constant
$C_{3\epsilon}$	model constant
C_μ	model constant
C_s	wall roughness constant
d_D^*	dimensionless particle diameter by Danhneke
E	emperical constant
f	dimensionless coefficient of force
g	dimensionless coefficient of couple
h	sticking fraction
k	number of basic units in the Buckingham-pi theorem
k_M	dimensionless number in the Magnus force

K_s^+	dimensionless wall roughness
m	dimensionless ratio
n	number of dimensionless numbers according to the Buckingham-pi theorem
Q_{AR}	aspect ratio
Q_{EAS}	equi-skewness ratio
R	residual
T_L^+	dimensionless Lagrangian time scale
u^+	dimensionless wall velocity
U^*	dimensionless velocity
V_{dep+}	dimensionless deposition velocity
y^+	dimensionless wall distance
y^*	dimensionless wall distance
$\hat{a}$	reduced contact radius
ΔB	roughness function
$\bar{c}_f$	friction coefficient
C_c	Cunningham correction factor
$\hat{F}$	dimensionless force
Fr_P	Froude number
H	ratio of the van der Waals pressure and the yield stress of the softer material
Kn	Knudsen number
Ma	Mach number
Ma_t	turbulent Mach number
$\bar{P}$	dimensionless pull-off force
Pe	Peclet number
q	dimensionless function of dimensionless particle diameter
Re_D	cyclone Reynolds number
Re_{D_H}	Reynolds number based on hydraulic diameter
Re_k	roughness Reynolds number
RH	relative humidity

S	density ratio
Sc	Schmidt number
Stk	Stokes number
$\hat{\delta}$	dimensionless deformation

List of Figures

List of Tables

Summary

Depositions in cyclones separators should be avoided because they sometimes lead to congestions and to varying product quantities and qualities. Also, too large residence times are problematic when dealing with perishable products. Therefore, extra (periodical), cleaning efforts are needed, during which whole processes cannot be run. The results are decreasing efficiencies in time and financial efforts. Continuous or periodical removal of depositions can be achieved by the use of flexible walls or parts that scrap them off, for example. The disadvantage of the application of these parts is the limited range of operating temperatures and pressures, which are the traditional advantages of classical cyclones. Until now, no precise research has been performed to find out under which conditions depositions in cyclones are formed and how they can be avoided.

In regards to cyclone separators, in literature only depositions in the region around the natural length of the vortex are mentioned. Also some rules of thumbs are proposed about minimal velocities and shear rates, that are needed for the prevention of depositions. Depositions in other industrial applications, such as in (vertical) tubes, heat exchangers and fibre filters are discussed in more detail. In vertical tubes, mostly particles are assumed to stick at a wall when they have been able to reach it. These experimental data are made dimensionless in the dimensionless deposition velocity, by dividing the particle-wall flux through the product of the particle concentration in the core flow and the friction velocity at the wall.

From experimental investigations with a cyclone, the to the feed scaled deposited mass appeared to be dependent on both the volume flow rate of air and the solid loading of limestone particles. Where for an increasing volume flow rate, the relative deposited mass always decreases, for the dependency on the solid loading a maximum was found around a value of 2.0 g/kg; both a higher and a lower solid loading results in lower relative depositions. The depositions at the vortex finders in- and outside have particle size distribution functions, which are finer than that of the feed, those on the wall of the cyclone body and the vertical tube section are coarser. The depositions at the roof are below the minimal mass for a particle size distribution analysis.

If the wall is not assumed to absorb all impacting particles, the sticking fraction is described by the product of collision frequency and sticking probability. For the sticking probability, criterions based on the conservation of energy or on the equilibrium of forces and moments of forces are compared. The energy based models result in a critical sticking velocity; each particle, whose impact velocity is lower than the critical one, is assumed to deposit. The (moments of) forces models are based on ratios for vertical lift-off, sliding and rolling for a particle in contact with a wall.

For the criterions, the relevant particle-wall-energies and -forces, as well as fluid-dynamic forces are required. The fluid-dynamic forces are a function of the wall shear velocity, which

can be calculated from the tangential velocity in the cell's midpoint and the distance to the wall, from the wall shear stress, or from the function for the flow profile in the boundary layer. An overview and a comparison of the relevant fluid-dynamic forces is discussed. For the equilibrium of forces, the drag and lift forces for a particle in a shear flow at the wall, gravity and the van der Waals force, as adhesion force, are taken into account.

By means of mathematical models, it is shown that the van der Waals energy and -force are dominant for particle-wall adhesion. For the first one, three physical models are compared, which are based on stiff contact with a correction factor, on soft contact and on the Lewis acid-base approach. The latter one is calculated with an adhesion map, that describes the way of contact, for this particular case between a limestone particle and a wall made of steel. The reason for using the contact map is that the contact radius may differ from one of the classical models known from literature for some specific particle diameters of the feed used in the experiments. The transition region between the extreme models is described with another model and fits from literature.

The deposition models are implemented into computational fluid dynamics (CFD) simulations using the commercial software package ANSYS Fluent 13.0. The continuous flow field is calculated with the Reynolds stress turbulence model (RSM), because this model is the only Reynolds Averaged Navier-Stokes (RANS) model known from literature, that is able to predict the inner solid body rotation and outer free vortex in a cyclone correctly. Particle trajectories are calculated in a frozen flow field, using the one way coupling in the discrete phase model (DPM). The low particle loadings make the assumption of this one way coupling possible, which excludes the influence of the dispersed phase on the continuous phase and neglects particle-particle collisions and other interactions. The turbulent dispersion of the particles is created with the Direct Random Walk (DRW) model with a random eddy lifetime.

With the original deposition models, only submicron particles are observed to deposit when using any of the energy based criterions. For the (moments of) forces criterions the depositions are rated too high, because of overpredicted particle-wall collision frequencies. One of the reasons is the fact that the use of a boundary layer in a complex three dimensional geometry, such as a cyclone separator, is problematic and therefore the grid near the walls is still relatively coarse. The dispersed particle therefore may experience a tangential drag force near the wall, calculated from the fluid velocity and velocity gradient in the cell's midpoint, which does not physically exist. The no slip boundary condition is thus not automatically met anymore for the discrete particles.

Therefore, a velocity damping factor is introduced, which is based on the equation of motion of a particle in a linear shear flow in the very last wall adjacent cell. With two case studies it is demonstrated that both the wall impact velocity and probability are dependent on the resolution of the mesh in the boundary layer. The simulations with the coarse grid with the damping factor provide results, that are closer to those using a grid with a boundary layer, which is used as benchmark case.

The implementation of the damping factor in the cyclone simulations results in deposition rates which are closer to the experimental observations.

Summarising, the particle-wall sticking behaviour in cyclones is known from experiments to be both dependent on the volume flow rate and the solid loading. Exact material properties of the feed and wall are needed to describe the adhesion forces and energies. For industrial applications, it is difficult to predict particle-wall impact velocities and probabilities correctly in CFD simulations. These quantities, however, are essential when using the deposition models. With the use of an own made proposal these quantities are adapted, resulting in more realistic particle deposition properties.

Zusammenfassung

Ablagerungen in Zyklonabscheidern sollten vermieden werden weil sie zu Verstopfungen und zu variierenden Produktqualitäten und -quantitäten führen können. Auch zu lange Verweilzeiten im Zyklon sind problematisch falls es sich um verderbliche Produkte handelt. Darum müssen Zyklone regelmäßig gereinigt werden, währenddessen ganze Produktionsprozesse still liegen. Die Folgen hiervon sind abnehmende Effizienz in Zeit und Geld. Ablagerungen können von Zyklonwänden durch ein von außen eingebrachtes Schabeisen entfernt werden. Eine weitere Möglichkeit ergibt sich aus der doppelwändigen Ausführung von Zyklonen, wobei die innere Wand aus einem flexiblen Material besteht. Ablagerungen werden von der Wand entfernt, wenn der Druck an dieser flexiblen Wand mittels einem pulsierenden Volumenstrom oder externen Druckluft im Zwischenraum variiert wird. Die Vorteile von klassischen Zyklonen, wie hohe Temperatur- und Druckbelastbarkeit, werden mit solchen Maßnahmen zum Großteil aufgehoben. Bisher ist nicht genau untersucht worden, unter welchen Bedingungen Wandablagerungen in Zyklonen entstehen und wie sie vermieden werden können.

Für Zyklonabscheider werden in der Literatur nur Ablagerungen rund um das natürliche Wirbelende beschrieben. Für die Bestimmung der Mindestgeschwindigkeiten und -geschwindigkeitsgradienten um Ablagerungen zu vermeiden, sind bisher lediglich Faustformeln veröffentlicht worden. Ablagerungen in anderen industriellen Anwendungen, wie in (vertikalen) Rohren, Wärmeüberträgern oder Faserfiltern, sind genauer untersucht und beschrieben worden. In vertikalen Rohren wird meistens angenommen, dass Partikel, die die Wand erreicht haben, automatisch haften bleiben. Diese experimentellen Daten werden in der dimensionlosen Depositionsgeschwindigkeit dargestellt, die aus dem Quotient von dem Partikelwandflux einerseits und dem Produkt der Partikelkonzentration und Schubspannungsgeschwindigkeit an der Wand anderseits, berechnet wird.

Messungen mit einem Versuchszyklon haben ergeben, dass die relative Wandablagerung, bezogen auf die Gesamtmasse des Aufgabegutes, sowohl vom Volumenstrom der Luft, als auch von der Beladung abhängig ist. Während für einen zunehmenden Volumenstrom die Ablagerungen immer abnehmen, wurde für die Abhängigkeit der Beladung ein Maximum rund um den Wert von 2,0 g Staub pro kg Luft beobachtet; sowohl eine niedrigere als auch eine höhere Beladung führen zu geringeren Ablagerungen. Die Ablagerungen an der Innen- und Außenseite des Tauchrohrs haben eine feinere Korngrößenverteilung als das Aufgabegut, die Ablagerungen im Zyklonmantel und Fallrohr eine gröbere. Die Massen der Ablagerungen am Zyklondeckel sind zu gering für eine Korngrößenanalyse.

Mit der Annahme, dass nicht alle Partikel automatisch an der Wand haften bleiben, wird die Haftzahl aus dem Produkt von Auftreffgrad und Haftwahrscheinlichkeit bestimmt. Für die Haftwahrscheinlichkeit werden Modelle, basierend auf Energieerhaltung bzw. auf dem Kräfte- und Momentengleichgewicht, verglichen. Die Energieerhaltungsmodelle ergeben eine kritische Haftgeschwindigkeit. Von Partikeln, die mit einer Geschwindigkeit die kleiner ist als

die kritische Geschwindigkeit, auf die Wand auftreffen, wird angenommen, dass sie haften. Bei den Modellen, die auf Kräfte- und Momentengleichgewicht basieren, werden Verhältniszahlen berechnet, die ausdrücken, ob ein Partikel vertikal von der Wand abhebt, tangential von der Wand rutscht oder von der Wand rollt.

Zur Berechnung der Ablagerungskriterien sind die signifikanten Partikel-Wand-Energien und -Kräfte sowie die fluiddynamischen Kräfte erforderlich. Die fluiddynamischen Kräfte sind eine Funktion des Geschwindigkeitsgradienten an der Wand, der entweder aus der Tangentialgeschwindigkeit im Mittelpunkt einer an die Wand angrenzenden Zelle und der Wanddistanz, aus der Wandschubspannung oder aus der logarithmischen Geschwindigkeitsfunktion der Grenzschichtströmung berechnet werden kann. Eine Übersicht der signifikanten Kräfte wird präsentiert und diskutiert. In dem auf Kräften basierenden Modell werden die Widerstands- und Auftriebskraft für einen Partikel in einer Scherströmung, sowie die Schwerkraft und die Haftkraft berücksichtigt.

Mit mathematischen Modellen wird gezeigt, dass die "van der Waals"-Energien und Kräfte für die Partikelwandhaftung dominant sind. Zur Berechnung der "van der Waals"-Energien werden drei physikalische Modelle verglichen. Diese beruhen auf steifem Kontakt mit einem Korrekturfaktor, auf weichem Kontakt, sowie auf der "Lewis acid-base" -Interaktion. Im "Lewis acid-base"-Modell erfolgt die Berechnung der "van der Waals"-Energie mit einer Übersicht der Haftungsart, die für die Betrachtung in dieser Arbeit die Kontaktart zwischen Kalksteinpartikeln und einer ebenen Stahlwand beschreibt. Dies wird deshalb gemacht, weil sich der Kontaktradius, in den hier untersuchten Anwendungen, nicht in die in der Literatur beschriebenen klassischen Modelle einordnen lässt. Bei bestimmten Partikeldurchmessern des Aufgabegutes wird jedoch die Kontaktart mit keinem der klassischen Modelle richtig dargestellt. Der Übergangsbereich wird mit einem dritten Modell, sowie mit Fits aus der Literatur abgedeckt.

Die Ablagerungsmodelle werden implementiert in "Computational Fluid Dynamics" (CFD) Simulationen im kommerziellen Software Packet ANSYS Fluent 13.0. Die kontinuierliche Phase wird mit dem "Reynolds Spannungs-Turbulenzmodell" (RSM) berechnet, weil es das einzige Reynolds-gemittelte Navier-Stokes Modell (RANS) ist, das in der Lage ist, gleichzeitig sowohl den inneren Starrkörperwirbel, als auch den äußeren Potentialwirbel in einem Zyklon zu berechnen. Partikelbahnen werden in einem gefrorenen Strömungsfeld mit der Einwegkupplung im "Discrete Phase" Modell (DPM) berechnet. Die niedrige Partikelbeladung erlaubt die Verwendung des Konzepts der Einwegkupplung, welche die Einflüsse der dispersen Phase auf die kontinuierliche Phase, sowie Partikelkollisionen nicht berücksichtigt.

Mit dem ursprünglichen Energieerhaltungsmodell können sich nur Partikel mit einem Durchmesser kleiner als ein Mikrometer ablagern. Bei Verwendung der Kräftegleichgewichtsmodelle werden die Ablagerungen wegen zu hoher Partikelaufprallwahrscheinlichkeiten überschätzt. Einer der Gründe hierfür ist die Tatsache, dass die Verwendung von Grenzschichten in komplexen dreidimensionalen Geometrien, wie z.B. in einem Zyklonabscheider, nicht immer möglich ist. Deswegen wird in Wandnähe ein relativ grobes Rechennetz verwendet, mit der Folge, dass ein Partikel eine Widerstandskraft spüren kann, die unrealistisch groß ist. Der Grund hierfür ist, dass die Fluidgeschwindigkeit, die für die Berechnung verwendet wird, mithilfe der Werte der Fluidgeschwindigkeit und -gradienten im Zellmittelpunkt extrapoliert wird und dass hierdurch die Haftbedingung an der Wand nicht unbedingt mehr korrekt gegeben ist.

Deswegen wird ein Geschwindigkeitsdämpungsfaktor eingeführt, der aus der Bewegungsgleichung eines Partikels berechnet wird, welches sich in einer Scherströmung in der letzten Zelle vor der Wand befindet. Anhand zweier Beispiele wird gezeigt, dass sowohl die Aufprallgeschwindigkeit als auch die -wahrscheinlichkeit von der Gitterauflösung im wandnahen Bereich abhängen. Zur Beurteilung der Ergebnisse werden Simulationen mit einem feinen Gitter als Maßstab verwendet. Es zeigt sich, dass bei Verwendung des Dämpfungsfaktors die Ergebnisse im groben Gitter weniger vom Maßstab abweichen.

Die Einführung des Dämpfungsfaktors in den Simulationen mit dem Zyklonabscheider bewirkt, dass die berechneten Haftzahlen besser den aus Versuchen erhaltenen Messwerten entsprechen.

Zusammenfassend kann gesagt werden: aus experimentellen Untersuchungen geht hervor, dass das Wandablagerungsverhalten in Zyklonen sowohl vom Volumenstrom als von der Beladung abhängig ist. Genaue Materialeigenschaften werden benötigt, um die Haftkräfte und -energien zu beschreiben. Es ist weiters schwierig in Anwendungen im industriellen Maßstab die Auftreffwahrscheinlichkeiten und -geschwindigkeiten genau vorherzusagen. Jedoch sind diese physikalischen Größen für die Ablagerungsmodelle essentiell. Mit der Einführung eines Dämpfungsfaktors in die Berechnungsmodelle werden diese Größen so adaptiert, dass realistischere Partikelablagerungen berechnet werden können.

Samenvatting

Het is belangrijk deposities in cycloonafscheiders te vermijden omdat deze soms leiden tot verstoppingen of wisselende productqualiteiten en -quantiteiten. Ook leveren te hoge verblijftijden problemen op in het geval dat bederfbare waren geproduceerd worden. Daarom is de periodieke reiniging van cyclonen noodzakelijk, gedurende welke hele productieprocessen stil liggen. De gevolgen hiervan zijn afnemende rendementen, zowel uit financieel alsook uit tijdstandpunt gezien. Verwijderd worden kunnen deposities bijvoorbeeld met flexibele wanden uit rubber of met schraapijzers. Het nadeel van het gebruik van deze toepassingen is dat de grote voordelen van klassieke cyclonen, namelijk het gebruik in grote druk- en temperatuurbereiken, gedeeltelijk teniet worden gedaan. Tot nu toe is nog geen nauwkeurig onderzoek verricht over het ontstaan van deposities in cyclonen en over hoe deze vermeden kunnen worden.

Met betrekking tot cyclonen wordt in de literatuur alleen melding gemaakt van deposities rond het natuurlijke einde van de wervel. Ook wordt een aantal vuistregels genoemd over de minimale snelheden en snelheidsgradiënten, die nodig zijn om deposities te vermijden. Deposities in andere industriële toepassingen, zoals (verticale) pijpen, warmtewisselaars en vezelfilters, zijn gedetailleerder onderzocht. In verticale pijpen wordt meestal aangenomen dat deeltjes, die in staat zijn geweest de wand te bereiken, automatisch blijven plakken. Deze experimentele data worden normaliter in de vorm van de dimensieloze depositiesnelheid gepresenteerd, die het quotient is van de deeltjesflux richting de wand en van het product van de deeltjesconcentratie in het midden van de pijp en de wandschuifsspanningsnelheid aan de wand.

Uit experimenten met een testcycloon blijkt dat de relatief afgezette massa, gerelateerd aan de doorzet, afhankelijk is van zowel het debiet door de cycloon alsook van de stofconcentratie in de inloopstroming. Terwijl voor een toenemend debiet zonder uitzondering geringere afzettingen gevonden worden, werd voor de afhankelijkheid van de concentratie een maximum waargenomen rond een waarde van 2,0 g kalksteen per kg lucht: zowel een hogere als een lagere concentratie hadden geringere deposities ten gevolge. De deposities aan de binnen- en buitenkant van de wervelvormer hebben een deeltjesgrootteverdeling die fijner is dan die van het uitgangsmengsel, die op het cilindrische en conische gedeelte van de cycloon en op de verticale pijp hebben een grovere verdeling. De massa's van de deposities aan het deksel zijn te gering voor een deeltjesgrootteanalyse.

Indien aangenomen wordt dat niet alle botsende deeltjes automatisch aan de wand blijven kleven, wordt de adsorbtiefractie berekend uit het product van de bots- en adsorbtiewaarschijnlijkheid. Voor deze absorbtiewaarschijnlijkheid worden criteria, die gebaseerd zijn op het behoud van energie en op het evenwicht van krachten en momenten, met elkaar vergeleken. De energie-modellen resulteren in kritieke botssnelheden; een deeltje, diens botssnelheid kleiner is dan de kritieke, wordt geacht aan de wand te hechten. De modellen, die de krachten- en momentenevenwichten beschrijven, zijn gebaseerd op dimensieloze kentallen, die het verticaal

optillen, het tangentiaal schuiven en het om een punt rollen van een deeltje, dat zich aan de wand bevindt, omschrijven.

Voor deze criteria worden de energieën en krachten die optreden tussen een deeltje en de wand en de fluiddynamische krachten, die op een deeltje aan de wand werken, benodigd. De fluiddynamische krachten zijn een functie van de wandschuifspanningssnelheid, die berekend kan worden uit de tangentiële snelheid in het midden van de aan de wand grenzende cel, uit de wandschuifspanning of met behulp met van een specifieke, logarithmische functie voor het stromingsprofiel in de grenslaag. Een overzicht van de krachten wordt getoond en besproken. Voor het krachtenevenwicht worden de luchtweerstandskracht, de liftkracht voor een deeltje in een snelheidsgradient in de nabijheid van een wand, de zwaartekracht en de hechtkracht in betracht genomen.

Met behulp van wiskundige modellen wordt aangetoond dat de van der Waals energie en kracht dominant zijn voor de hechting van kalkstenen deeltjes aan de stalen wand van de cycloon. Voor de eerste grootheid worden drie natuurkundige modellen met elkaar vergeleken, die gebaseerd zijn op het contact van starre deeltjes met een correctiefactor, op het contact van zachte deeltjes en op de Lewis "acid-base" theorie. Het laatste model wordt berekend met de adhesiekaart, die de aard van het contact, voor dit geval tussen een kalkstenen deeltje en een stalen plaat, omschrijft. Dit wordt gedaan omdat de aard van het contact mogelijk afhankelijk van de diameter van het deeltje is en niet per se omschreven kan worden met één van de klassieke modellen uit de literatuur. Het overgangsgebied tussen deze modellen wordt met een ander model uit de literatuur omschreven, dat gebruik maakt van enkele empirische fits.

De hechtingsmodellen worden met behulp van het commerciële software-programma-pakket ANSYS Fluent 13.0 in computational fluid dynamics (CFD) simulaties geïmplementeerd. Het stromingsveld van de continue fase wordt berekend met Reynolds stress turbulentie model (RSM), omdat dit model het enige bestaande Reynolds Averaged Navier-Stokes (RANS) model is, waarvan uit de literatuur bekend is dat het zowel in staat is de binnenste vast-lichaam-rotatie alsook de buitenste vrije wervel in een cycloon correct te voorspellen. Deeltjesbanen worden in een onveranderlijk stromingsveld berekend met een eenzijdige koppeling middels het "discrete phase model" (DPM), gebruik makend van het direct random walk (DRW) model met een willekeurige wervelduur. De lage deeltesconcentraties maken deze aanname, waarbij de disperse fase geen invloed uitoefent op de continue fase en botsingen en andere interacties tussen deeltjes verder buiten beschouwing worden gelaten, plausibel.

Met de oorspronkelijk hechtingsmodellen gebaseerd op het behoud van energie, worden alleen bij deeltjes kleiner dan 1 μm deposities voorspeld. De modellen, die gebaseerd zijn op het krachten- en momentenevenwicht, voorspellen te hoge deposities doordat de botswaarschijnlijkheden van deeltjes aan de wand overschat worden. Eén van de redenen hiervoor is dat het gebruik van een grenslaag in complexe driedimensionale geometrieën lastig is en dat hierdoor het rekenrooster nabij de wand nog altijd relatief grof is. Een dispers deeltje kan hierdoor een tangentiële gassnelheid voelen, die geëxtrapoleerd wordt uit de waarde in het midden van de cel met behulp van de snelheidsgradient, die fysisch niet bestaat. Aan de hechtvoorwaarde, die aan de wand zou moeten heersen, wordt dus niet meer automatisch voldaan.

Daarom wordt een dempingsmodel geïntroduceerd, dat gebaseerd is op de bewegingsvergelijking van een deeltje in een lineare grenslaagstroming in de laatste aan de wand grenzende cel. Met twee voorbeelden wordt getoond dat zowel de botssnelheid alsook de -waarschijnlijkheid afhankelijk zijn van de fijnheid van het rooster nabij de wand. De simulaties met het grove rooster geven betere resultaten wanneer het dempingsmodel wordt toegepast en liggen dichter bij de resultaten die met het verfijnde rooster worden verkregen en als maatstaf gebruikt worden.

De implementatie van de dempingsfactor in de simulaties van de cycloon levert resultaten op die de experimentele waardes beter benaderen.

Samenvattend kan worden gesteld, dat het hechtingsgedrag van kalkstenen deeltjes in een cycloon zowel afhankelijk is van het debiet door de cycloon alsook van de deeltjesconcentratie in de inloopstroming. Precieze materiaaleigenschappen van het stof en de wand zijn vereist om de hechtkrachten en -energieën te omschrijven. Het is lastig om de botssnelheden en -waarschijnlijkheden in simulaties correct te voorspellen voor industriële toepassingen. Deze grootheden zijn echter van essentieel belang in de depositiemodellen. Met een eigen voorstel worden deze grootheden zo aangepast dat realistischere deposities voorspeld kunnen worden.

Acknowledgement

At last, this thesis is finished! Although after working five and half years in this field some things are still not understood and possibly more questions have arisen than have been answered. However, I hope to have made a contribution to science. Working as a PhD-student is like being a do-it-yourselfer. To cite a German do-it-yourself store: 1. "Mach es zu Deinem Projekt", 2. "Es gibt immer was zu tun" and 3. "Mach es fertig bevor es Dich fertig macht". I tried to avoid the last point.

On behalf of this I would like to thank Univ.-Prof. Dipl.-Ing. Dr.techn. Harald Raupenstrauch for giving me the possibility of making this thesis. Also I would like to thank Ao.Univ.-Prof. Dipl.-Ing. Dr.techn. Christian Weiss for all the fruitful discussions about simulating particle flows.

Without the decades of experimental research and simulations of the cyclone separator at the Technical University Graz this thesis would not have existed at all. Therefore, I would like to show my gratitude to Em.Univ.-Prof. Dipl.-Ing. Dr.techn. Gernot Staudinger, to Johann Fischer, for all the particle size distribution analyses he measured, to Hans Grubbauer and Fachoberinspektor Rudolf Hötzl for their support in the laboratory and to Lydia Fraidl for her general assistance.

Also, I would like to thank all other colleagues in Graz and Leoben especially Dipl.-Ing. Walter ("Physiker") Pölzl, Ass.Prof.i.R. Dipl.-Ing. Dr.mont. Franz Mugrauer and Ass.Prof. Dipl.-Ing. Dr.mont. Claudia Pfeiler for the interesting discussions and the wonderful working climate.

I am grateful to my parents and brother for supporting me through the first years of education. Unfortunately my grandfather and -mother cannot be present at the day of my graduation anymore but I remember them saying it was a good idea to combine working with further education. I would like thank them both in this way and also my parents in law.

As a young PhD-student it was sometimes difficult to find my way in the scientific world. Therefore, I would like to thank the unknown frustrated author who sent a letter to a journal which has been published by an editor with a relativising sense of humor [44]. Also W.F. Hermans' book "Onder Professoren" [59] was a nice reading matter for the train as variation to scientific papers or correcting own work. The only worry (or perhaps relief) is the fact that although all technical (r)evolutions in the scientific world, people still act more or less the same as others did 35 years ago.

Last but not least, I would like to thank Silvia for her great support during the last years because sometimes I had the feeling she was the only person, who understood what I was going through.

Curriculum Vitae

Joseph Johannes Hubertus Houben (Jos) was born in 1982 in Heerlen, the Netherlands. After visiting primary school "Basisschool Windekind" he visited grammar school "Bernardinuscollege", both in Heerlen, where he graduated in the year 2000 cum laude. In September of the same year he started a study mechanical engineering at the Eindhoven University of Technology. After his bachelor, he joined the chair of Process Technology in the Thermal Fluid Engineering division for his master. He got the opportunity to study abroad within the Erasmus Exchange program, which he did in the year 2005 in Graz, Austria. Also the first part of his master thesis was written there at the Graz University of Technology at the chair "Apparatebau, Mechanische Verfahrenstechnik und Feuerungstechnik". After finishing the master mechanical engineering with honour in 2006, he started as a PhD-student in Graz. In the year he performed many experiments with the test cyclone. In 2007 he then decided to change to the chair of Thermal Processing Technology at the Montanuniversiaet Leoben, where he accomplished this PhD-thesis.

Jos Houben lives together with his girlfriend Silvi. They have no children (yet) but their car is called Hermann. His hobbies are reading, cycling and classic cars.

A Cyclone's Geometry

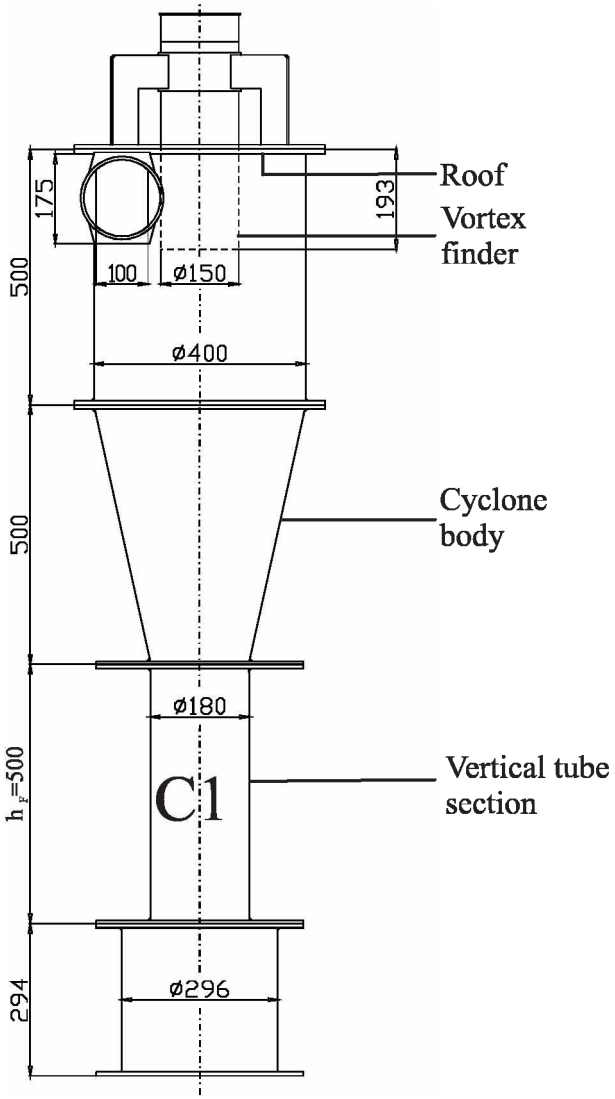

Figure A.1: *Cyclone geometry with the parts of which the depositions were extinguished.*

B Experimental Data

The experimental data for the experiments with volume flow rates of 800, 1 000 and 1 200 m^3/h are summarised in Tab. B.1, B.2 and B.3 respectively.

B.1 Student-t Hypothesis Testing

For both mean values $\mu_{e,1}$ and $\mu_{e,2}$ unknown and both variances σ_1 and σ_2 unknown and not equal, the confidence interval for the difference between the mean values is given by [17]

$$\overline{x}_1 - \overline{x}_2 - t_{\alpha/2,\nu}\sqrt{\frac{s_1^2}{n_1^2} + \frac{s_2^2}{n_2^2}} < \mu_{e,1} - \mu_{e,2} < \overline{x}_1 - \overline{x}_2 + t_{\alpha/2,\nu}\sqrt{\frac{s_1^2}{n_1^2} + \frac{s_2^2}{n_2^2}}, \tag{B.1}$$

where

$$\nu = \frac{\left(\frac{s_1^2}{n_1} + \frac{s_2^2}{n_2}\right)^2}{\frac{\left(\frac{s_1^2}{n_1}\right)^2}{n_1+1} + \frac{\left(\frac{s_2^2}{n_2}\right)^2}{n_2+1}} - 2. \tag{B.2}$$

B.2 Binomial Hypothesis Testing

The binomial distributions describes the number of succession in n independent, single experiments with a probability for succes, p [17]. The probability mass function reads:

$$P(X = k) = \binom{n}{k} p^k (1-p)^{n-k}, \tag{B.3}$$

and the variance:

$$\sigma = np(1-p). \tag{B.4}$$

The double sided confidence interval the is given by

$$\hat{p} - z_{\alpha/2}\sqrt{\frac{\hat{p}(1-\hat{p})}{n}} < p < \hat{p} + z_{\alpha/2}\sqrt{\frac{\hat{p}(1-\hat{p})}{n}}, \tag{B.5}$$

where $\hat{p}$ is the proportion of successes during the n trials and $z_{\alpha/2}$ is taken from the normal distribution function. For a 95% confidence, $z_{\alpha/2} = 1.96$, for example.

Table B.1: *Calculation procedure for the student t-test, that the total relative mass depositions during the experiments V800_μ_e1.0 (index 2) differs from those during the experiments V800_μ_e0.66 (index 1) and V800_μ_e2.0 (index 3) respectively, with a significance level of α ($\mu_{e,i}$, population mean value, $\bar{x}_i$, sample mean, n the sample size).*

Part	H_0	H_1	n_1	n_2	n_3	$\bar{x}_1$ [%]	$\bar{x}_2$ [%]	$\bar{x}_3$ [%]	s_1	s_2	s_3	t_0	α	$(1-\alpha)$ [%]
all parts	$\mu_{e,1} = \mu_{e,2}$	$\mu_{e,1} < \mu_{e,2}$	2	3	-	0.3147	1.4472	-	0.0087	1.7919	-	1.095	0.1939	80.6
	$\mu_{e,3} = \mu_{e,2}$	$\mu_{e,3} < \mu_{e,2}$	-	3	3	-	1.4472	0.4976	-	1.7919	0.5111	0.883	0.2296	77.0
vortex finder outside	$\mu_{e,1} = \mu_{e,2}$	$\mu_{e,1} < \mu_{e,2}$	2	3	-	0.0147	0.0904	-	0.0208	0.0521	-	2.263	0.0583	94.2
	$\mu_{e,3} = \mu_{e,2}$	$\mu_{e,3} < \mu_{e,2}$	-	3	3	-	0.0904	0.0754	-	0.0521	0.0616	0.321	0.3824	61.8
vortex finder inside	$\mu_{e,1} = \mu_{e,2}$	$\mu_{e,1} < \mu_{e,2}$	2	3	-	0.0412	0.0316	-	0.0583	0.0274	-	0.217	0.4285	57.1
	$\mu_{e,3} = \mu_{e,2}$	$\mu_{e,3} < \mu_{e,2}$	-	3	3	-	0.0316	0.0624	0.0583	0.0274	0.0339	1.225	0.1452	85.5
roof	$\mu_{e,1} = \mu_{e,2}$	$\mu_{e,1} < \mu_{e,2}$	2	3	-	0.0000	0.0001	-	0.0000	0.0001	-	0.735	0.2660	73.4
	$\mu_{e,3} = \mu_{e,2}$	$\mu_{e,3} < \mu_{e,2}$	-	3	3	-	0.0001	0.0000	-	0.0001	0.0000	1.000	0.2113	78.9
cyclone body	$\mu_{e,1} = \mu_{e,2}$	$\mu_{e,1} < \mu_{e,2}$	2	3	-	0.0682	0.8853	-	0.0965	1.3891	-	1.015	0.2078	79.2
	$\mu_{e,3} = \mu_{e,2}$	$\mu_{e,3} < \mu_{e,2}$	-	3	3	-	0.8853	0.2723	-	1.3891	0.4035	0.734	0.2648	73.5
vertical tube section	$\mu_{e,1} = \mu_{e,2}$	$\mu_{e,1} < \mu_{e,2}$	2	3	-	0.1906	0.4398	-	0.1668	0.3821	-	0.996	0.1981	80.2
	$\mu_{e,3} = \mu_{e,2}$	$\mu_{e,3} < \mu_{e,2}$	-	3	3	-	0.4398	0.0773	-	0.3821	0.0234	1.640	0.1209	87.9

Table B.2: *Calculation procedure for the student t-test, that the total relative mass depositions during the experiments* $V1000\_\mu_e2.0$ *(index 2) differs from those during the experiments* $V1000\_\mu_e1.0$ *(index 1) and* $V1000\_\mu_e3.0$ *(index 3) respectively, with a significance level of* α *(*$\mu_{e,i}$*, population mean value,* $\bar{x}_i$ *sample mean,* n*, the sample size).*

Part	H_0	H_1	n_1	n_2	n_3	$\bar{x}_1$ [%]	$\bar{x}_2$ [%]	$\bar{x}_3$ [%]	s_1	s_2	s_3	t_0	α	$(1-\alpha)$ [%]
all parts	$\mu_{e,1} = \mu_{e,2}$	$\mu_{e,1} < \mu_{e,2}$	3	3	-	0.90263	1.2391	-	0.2895	0.8843	-	0.626	0.2925	70.7
	$\mu_{e,3} = \mu_{e,2}$	$\mu_{e,3} < \mu_{e,2}$	-	3	4	-	1.2391	0.6927	0.2895	0.8843	0.0033	1.137	0.1858	81.4
vortex finder outside	$\mu_{e,1} = \mu_{e,2}$	$\mu_{e,1} < \mu_{e,2}$	3	3	-	0.05647	0.0833	-	0.0172	0.0467	-	0.935	0.2150	78.5
	$\mu_{e,3} = \mu_{e,2}$	$\mu_{e,3} < \mu_{e,2}$	-	3	4	-	0.0833	0.0664	0.0172	0.0467	0.0004	0.502	0.4494	55.1
vortex finder inside	$\mu_{e,1} = \mu_{e,2}$	$\mu_{e,1} < \mu_{e,2}$	3	3		0.00753	0.0821	-	0.0069	0.0567	-	2.262	0.0742	92.6
	$\mu_{e,3} = \mu_{e,2}$	$\mu_{e,3} < \mu_{e,2}$	-	3	4	-	0.0821	0.0738	0.0069	0.0567	0.0008	0.160	0.4228	57.7
roof	$\mu_{e,1} = \mu_{e,2}$	$\mu_{e,1} < \mu_{e,2}$	3	3	-	0.00004	0.0000	-	0.0001	0.0000	-	1.000	0.2113	78.9
	$\mu_{e,3} = \mu_{e,2}$	$\mu_{e,3} < \mu_{e,2}$	-	3	4	-	0.0000	0.0000	0.0001	0.0000	0.0000	-	-	-
cyclone body	$\mu_{e,1} = \mu_{e,2}$	$\mu_{e,1} < \mu_{e,2}$	3	3	-	0.04055	0.3002	-	0.0266	0.2248	-	1.986	0.0910	90.9
	$\mu_{e,3} = \mu_{e,2}$	$\mu_{e,3} < \mu_{e,2}$	-	3	4	-	0.3002	0.2391	0.0266	0.2248	0.0027	0.320	0.4584	54.2
vertical tube section	$\mu_{e,1} = \mu_{e,2}$	$\mu_{e,1} < \mu_{e,2}$	3	3	-	0.79805	0.7735	-	0.2611	0.5716	-	0.068	0.4753	52.5
	$\mu_{e,3} = \mu_{e,2}$	$\mu_{e,3} < \mu_{e,2}$	-	3	4	-	0.7735	0.3170	0.2611	0.5716	0.0026	1.415	0.1092	89.1

Table B.3: *Calculation procedure for the student t-test, that the total relative mass depositions during the experiments $V1200\_\mu_e2.0$ (index 2) differs from those during the experiments $V1200\_\mu_e1.0$ (index 1) and $V1200\_\mu_e3.0$ (index 3) respectively, with a significance level of α ($\mu_{e,i}$ population mean value, $\bar{x}_i$, sample mean, n, the sample size).*

Part	H_0	H_1	n_1	n_2	n_3	$\bar{x}_1$ [%]	$\bar{x}_2$ [%]	$\bar{x}_3$ [%]	s_1	s_2	s_3	t_0	α	$(1-\alpha)$ [%]
all parts	$\mu_{e,1} = \mu_{e,2}$	$\mu_{e,1} < \mu_{e,2}$	3	3	-	0.2383	0.4730	-	0.1632	0.2516	-	1.355	0.1288	87.1
	$\mu_{e,3} = \mu_{e,2}$	$\mu_{e,3} < \mu_{e,2}$	-	3	4	-	0.4730	0.4417	-	0.2516	0.2132	0.178	0.3716	62.8
vortex finder outside	$\mu_{e,1} = \mu_{e,2}$	$\mu_{e,1} < \mu_{e,2}$	3	3	-	0.0372	0.0609	-	0.0157	0.0308	-	1.183	0.1613	83.9
	$\mu_{e,3} = \mu_{e,2}$	$\mu_{e,3} < \mu_{e,2}$	-	3	4	-	0.0609	0.0663	-	0.0308	0.0352	0.212	0.3643	63.6
vortex finder inside	$\mu_{e,1} = \mu_{e,2}$	$\mu_{e,1} < \mu_{e,2}$	3	3	-	0.0124	0.0186	-	0.0095	0.0071	-	0.908	0.2612	73.9
	$\mu_{e,3} = \mu_{e,2}$	$\mu_{e,3} < \mu_{e,2}$	-	3	4	-	0.0186	0.0469	-	0.0071	0.0438	1.110	0.1144	88.6
roof	$\mu_{e,1} = \mu_{e,2}$	$\mu_{e,1} < \mu_{e,2}$	3	3	-	0.0000	0.0000	-	0.0000	0.0000	-	0.479	0.3332	66.7
	$\mu_{e,3} = \mu_{e,2}$	$\mu_{e,3} < \mu_{e,2}$	-	3	4	-	0.0000	0.0000	-	0.0000	0.0000	0.764	0.2604	74.0
cyclone body	$\mu_{e,1} = \mu_{e,2}$	$\mu_{e,1} < \mu_{e,2}$	3	3	-	0.0188	0.0613	-	0.0084	0.0262	-	2.674	0.0476	95.2
	$\mu_{e,3} = \mu_{e,2}$	$\mu_{e,3} < \mu_{e,2}$	-	3	4	-	0.0613	0.0992	-	0.0262	0.1686	0.386	0.2926	70.7
vertical tube section	$\mu_{e,1} = \mu_{e,2}$	$\mu_{e,1} < \mu_{e,2}$	3	3	-	0.1740	0.3322	-	0.1686	0.1892	-	1.082	0.1705	82.9
	$\mu_{e,3} = \mu_{e,2}$	$\mu_{e,3} < \mu_{e,2}$	-	3	4	-	0.3322	0.2417	-	0.1892	0.1042	0.808	0.3218	67.8

Table B.4: *Hypothesis testing methods [17].*

name	H_0	statistical testing parameter	H_1	critical region
student-t	$\mu_1 = \mu_2$	$t_0 = \frac{\bar{x}_1 - \bar{x}_1}{\sqrt{\frac{s_1^2}{n_1} + \frac{s_2^2}{n_2}}}$	H_1: $\mu_1 \neq \mu_2$	$\lvert t_0 \rvert \geq t_{\alpha/2,\nu}$
	σ_1^2 and σ_2^2 unknown	$\nu = \frac{\left(\frac{s_1^2}{n_1} + \frac{s_2^2}{n_2}\right)^2}{\frac{\left(\frac{s_1^2}{n_1}\right)^2}{n_1+1} + \frac{\left(\frac{s_2^2}{n_2}\right)^2}{n_2+1}} - 2$	H_1: $\mu_1 > \mu_2$	$t_0 \geq t_{\alpha,\nu}$
			H_1: $\mu_1 < \mu_2$	$t_0 \leq t_{\alpha,\nu}$
binominal	$p_1 = p_2$	$z_0 = \frac{\hat{p}_1 - \hat{p}_2}{\sqrt{\hat{p}(1-\hat{p})\left(\frac{1}{n_1} + \frac{1}{n_2}\right)}}$	H_1: $p_1 \neq p_2$	$\lvert z_0 \rvert \geq z_{\alpha/2}$
		$\hat{p} = \frac{n_1\hat{p}_1 + n_2\hat{p}_2}{n_1+n_2}$	H_1: $p_1 > p_2$	$z_0 \geq z_\alpha$
			H_1: $p_1 < p_2$	$z_0 \leq -z_\alpha$

B.3 Weibull Distribution Function

The Weibull distribution function is often used to describe physical quantities that cannot have a value smaller than zero per definition. Therefore, it is used in this thesis to describe residence times. The distribution function is defined by two parameters, β and δ whose value is always positive, and reads:

$$P = \frac{\beta}{\delta}\left(\frac{x}{\delta}\right)^{\beta-1} e^{-(x/\delta)^\beta}. \tag{B.6}$$

C Simulation Data

C.1 Energy Based Models

Table C.1: *Particle size and 95%-confidence interval of $d_{P,25}$, $d_{P,50}$ and $d_{P,75}$ for all depositions (for E_{vdW}, the depositions are only found at the cyclone body).*

	$d_{P,25}$ [μm]	$d_{P,50}$ [μm]	$d_{P,75}$ [μm]
experiment	2.78	4.20	5.96
$E_{vdW,0}$	0.00 ± 0.00	0.00 ± 0.00	0.00 ± 0.00
E_{vdW}	0.29 ± 0.00	0.33 ± 0.00	0.41 ± 0.06
E_S	0.00 ± 0.00	0.00 ± 0.00	0.00 ± 0.00

C.2 Force Based Models

Table C.2: *Particle size and 95%-confidence interval of $d_{P,25}$, $d_{P,50}$ and $d_{P,75}$ for all depositions.*

	$d_{P,25}$ [μm]	$d_{P,50}$ [μm]	$d_{P,75}$ [μm]
experiment	2.78	4.20	5.96
linear	1.03 ± 0.09	3.82 ± 0.63	5.31 ± 0.50
wall shear stress	1.04 ± 0.12	3.83 ± 0.06	5.37 ± 0.18
boundary layer	0.94 ± 0.00	2.66 ± 0.04	4.90 ± 0.09

Table C.3: *Particle size and 95%-confidence interval of $d_{P,25}$, $d_{P,50}$ and $d_{P,75}$ for the vortex finder (experimental values from the experiments with $\dot{V} = 600$ m^3/h and $\mu_e = 2.0$ g/kg).*

	$d_{P,25}$ [μm]	$d_{P,50}$ [μm]	$d_{P,75}$ [μm]
experiment inside	1.66	2.25	2.96
experiment outside	1.11	1.89	3.09
linear	0.00 ± 0.00	0.00 ± 0.00	0.00 ± 0.00
wall shear stress	0.00 ± 0.00	0.00 ± 0.00	0.00 ± 0.00
boundary layer	0.41 ± 0.00	0.48 ± 0.00	0.58 ± 0.00

Table C.4: *Particle size and 95%-confidence interval of $d_{P,25}$, $d_{P,50}$ and $d_{P,75}$ for the cyclone body (experimental values from the experiments with $\dot{V} = 600$ m^3/h and $\mu_e = 2.0$ g/kg).*

	$d_{P,25}$ [μm]	$d_{P,50}$ [μm]	$d_{P,75}$ [μm]
experiment	3.24	4.89	6.86
linear	1.03 ± 0.09	3.82 ± 0.63	5.31 ± 0.50
wall shear stress	1.04 ± 0.12	3.83 ± 0.06	5.37 ± 0.18
boundary layer	0.99 ± 0.00	3.15 ± 0.03	4.95 ± 0.08

Table C.5: *Particle size and 95%-confidence interval of $d_{P,25}$, $d_{P,50}$ and $d_{P,75}$ for the vertical tube (experimental values from the experiments with $\dot{V} = 600\ \mathrm{m^3/h}$ and $\mu_e = 2.0\ \mathrm{g/kg}$).*

	$d_{P,25}$ [μm]	$d_{P,50}$ [μm]	$d_{P,75}$ [μm]
experiment	**3.76**	5.22	7.16
linear	0.00 $\pm$ 0.00	0.00 $\pm$ 0.00	0.00 $\pm$ 0.00
wall shear stress	0.00 $\pm$ 0.00	0.00 $\pm$ 0.00	0.00 $\pm$ 0.00
boundary layer	0.64 $\pm$ 0.02	0.93 $\pm$ 0.15	1.31 $\pm$ 0.10

C.3 Energy Based Models with Correction Factor

Table C.6: *Particle size and 95%-confidence interval of $d_{P,25}$, $d_{P,50}$ and $d_{P,75}$ for all depositions.*

	$d_{P,25}$ [μm]	$d_{P,50}$ [μm]	$d_{P,75}$ [μm]
experiment	2.78	4.20	5.96
$E_{vdW,0}$	0.23 ± 0.00	0.25 ± 0.20	0.31 ± 0.04
E_{vdW}	0.28 ± 0.00	0.36 ± 0.01	0.48 ± 0.01
E_S	0.00 ± 0.00	0.00 ± 0.00	0.00 ± 0.00

Table C.7: *Particle size and 95%-confidence interval of $d_{P,25}$, $d_{P,50}$ and $d_{P,75}$ for the vortex finder (experimental values from the experiments with $\dot{V} = 600$ m^3/h and $\mu_e = 2.0$ g/kg).*

	$d_{P,25}$ [μm]	$d_{P,50}$ [μm]	$d_{P,75}$ [μm]
experiment inside	1.66	2.25	2.96
experiment outside	1.11	1.89	3.09
$E_{vdW,0}$	0.00 ± 0.00	0.00 ± 0.00	0.00 ± 0.00
E_{vdW}	0.22 ± 0.00	0.25 ± 0.19	0.33 ± 0.01
E_S	0.00 ± 0.00	0.00 ± 0.00	0.00 ± 0.00

Table C.8: *Particle size and 95%-confidence interval of $d_{P,25}$, $d_{P,50}$ and $d_{P,75}$ for the cyclone body (experimental values from the experiments with $\dot{V} = 600$ m^3/h and $\mu_e = 2.0$ g/kg).*

	$d_{P,25}$ [μm]	$d_{P,50}$ [μm]	$d_{P,75}$ [μm]
Experiment	3.24	4.89	6.86
$E_{vdW,0}$	0.23 ± 0.00	0.25 ± 0.20	0.31 ± 0.04
E_{vdW}	0.28 ± 0.00	0.36 ± 0.01	0.48 ± 0.01
E_S	0.00 ± 0.00	0.00 ± 0.00	0.00 ± 0.00

Table C.9: *Particle size and 95%-confidence interval of $d_{P,25}$, $d_{P,50}$ and $d_{P,75}$ for the vertical tube (experimental values from the experiments with $\dot{V} = 600$ m^3/h and $\mu_e = 2.0$ g/kg).*

	$d_{P,25}$ [μm]	$d_{P,50}$ [μm]	$d_{P,75}$ [μm]
Experiment	3.76	5.22	7.16
$E_{vdW,0}$	0.21 ± 0.00	0.23 ± 0.00	0.24 ± 0.00
E_{vdW}	0.27 ± 0.02	0.33 ± 0.05	0.42 ± 0.11
E_S	0.00 ± 0.00	0.00 ± 0.00	0.00 ± 0.00

C.4 Force Based Models with Correction Factor

Table C.10: *Particle size and 95%-confidence interval of $d_{P,25}$, $d_{P,50}$ and $d_{P,75}$ for all depositions.*

	$d_{P,25}$ [μm]	$d_{P,50}$ [μm]	$d_{P,75}$ [μm]
experiment	2.78	4.20	5.96
linear	1.01 ± 0.05	3.77 ± 0.55	5.55 ± 0.24
wall shear stress	1.02 ± 0.02	3.78 ± 0.59	5.38 ± 0.14
boundary layer	0.94 ± 0.02	2.64 ± 0.06	4.88 ± 0.08

Table C.11: *Particle size and 95%-confidence interval of $d_{P,25}$, $d_{P,50}$ and $d_{P,75}$ for the vortex finder (experimental values from the experiments with $\dot{V} = 600$ m^3/h and $\mu_e = 2.0$ g/kg).*

	$d_{P,25}$ [μm]	$d_{P,50}$ [μm]	$d_{P,75}$ [μm]
experiment inside	1.66	2.25	2.96
experiment outside	1.11	1.89	3.09
linear	0.00 ± 0.00	0.00 ± 0.00	0.00 ± 0.00
wall shear stress	0.00 ± 0.00	0.00 ± 0.00	0.00 ± 0.00
boundary layer	0.41 ± 0.01	0.48 ± 0.01	0.58 ± 0.02

Table C.12: *Particle size and 95%-confidence interval of $d_{P,25}$, $d_{P,50}$ and $d_{P,75}$ for the cyclone body (experimental values from the experiments with $\dot{V} = 600$ m^3/h and $\mu_e = 2.0$ g/kg).*

	$d_{P,25}$ [μm]	$d_{P,50}$ [μm]	$d_{P,75}$ [μm]
experiment	3.24	4.89	6.86
linear	1.01 ± 0.05	3.77 ± 0.55	5.55 ± 0.24
wall shear stress	1.02 ± 0.02	3.78 ± 0.59	5.38 ± 0.14
boundary layer	0.99 ± 0.03	3.14 ± 0.78	4.92 ± 0.08

Table C.13: *Particle size and 95%-confidence interval of $d_{P,25}$, $d_{P,50}$ and $d_{P,75}$ for the vertical tube (experimental values from the experiments with $\dot{V} = 600$ m^3/h and $\mu_e = 2.0$ g/kg).*

	$d_{P,25}$ [μm]	$d_{P,50}$ [μm]	$d_{P,75}$ [μm]
experiment	3.76	5.22	7.16
linear	0.28 ± 0.00	0.30 ± 0.00	0.33 ± 0.00
wall shear stress	0.00 ± 0.00	0.00 ± 0.00	0.00 ± 0.00
boundary layer	0.68 ± 0.08	1.00 ± 0.061	1.30 ± 0.08

D Particle Size Distributions

The cumulative particle size distribution functions obtained in the measurements are volume or mass distribution functions, indicated as Q_3 (Fig. D.1(a)). Since in the CFD simulations groups (i.e. a natural number) of inert particles need to be injected on the inlet surface, this Q_3-distribution has to be converted to a Q_0-distribution (number distribution). Therefore, the probability density function of the particle mass, q_3, is calculated as function of the mean particle diameter, $d_{\mathrm{P,m}}$, in interval i:

$$q_{3,\mathrm{i}}(d_{\mathrm{P,m,i}}) = Q_{3,\mathrm{i}}(d_{\mathrm{P,i}}) - Q_{3,\mathrm{i-1}}(d_{\mathrm{P,i-1}}), \tag{D.1}$$

with, $i = 0 : i_{\max}$ (the number of intervals) and $d_{\mathrm{P},0}$, the smallest, ending diameter in the particle size analysis. From the q_3-distribution, the q_0-distribution is obtained by multiplying the intervals with the factor $6/(\pi d^3_{\mathrm{P,m,i}})$ and scaling it in such a way, that the sum of the intervals equals 1 (Fig. D.1(b)):

$$q_{0,\mathrm{i}}(d_{\mathrm{P,m}}) = \frac{q_{3,\mathrm{i}}(d_{\mathrm{P,m,i}})\frac{6}{\pi d^3_{\mathrm{P,m,i}}}}{\sum_{i=1}^{i_{\max}} q_{3,\mathrm{i}}(d_{\mathrm{P,m,i}})\frac{6}{\pi d^3_{\mathrm{P,m,i}}}}. \tag{D.2}$$

The cumulative particle number distribution functions follows from the cumulative sum of the density distribution function:

$$Q_0(d_{\mathrm{P,i}}) = \sum_{1}^{i} q_{0,\mathrm{i}}(d_{\mathrm{P,m}}). \tag{D.3}$$

Knowing this q_0-distribution, the distribution of the particle relaxation time follows from its definition in Eq. 3.4-3.7.

Botto et al. [12] mention ratios between free flight and diffusional deposition particles. From experiments this ration appeared to be 90:10% for particles with an dimensionless relaxation time of $\tau_{\mathrm{p}}^{+} = 5$ and 60:40% for $\tau_{\mathrm{p}}^{+} = 15$. From Fig. D.1(c) follows that less than 1% of the particle mass distribution used in the cyclone experiments are diffusional particles with a certainty of 90%.

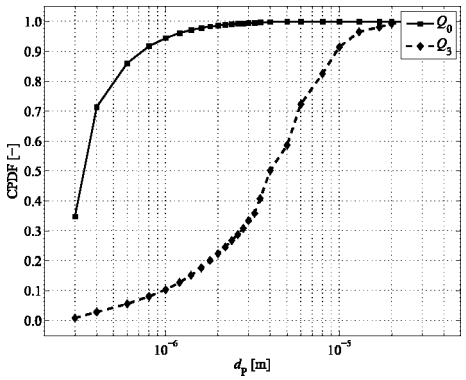

(a) Cumulative particle distribution function of number, Q_0, and volume/mass Q_3.

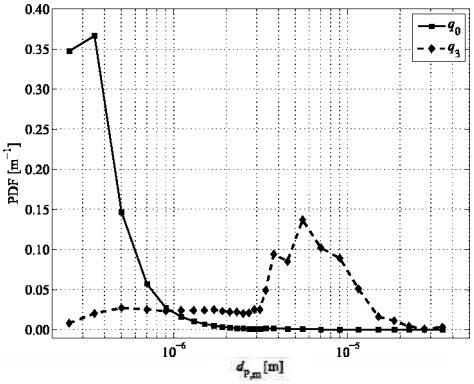

(b) Particle density distribution function of number, q_0, and volume/mass q_3.

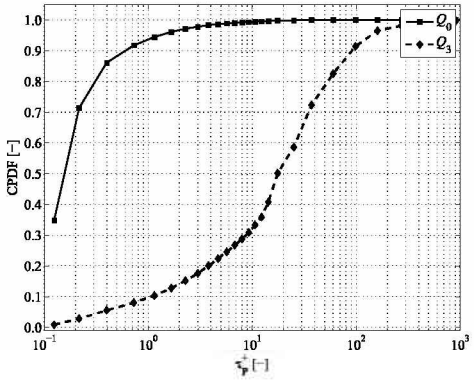

(c) Cumulative distribution of particle number (Q_0) and volume/mass (Q_3) as function of the dimensionless particle relaxation time τ_p^+.

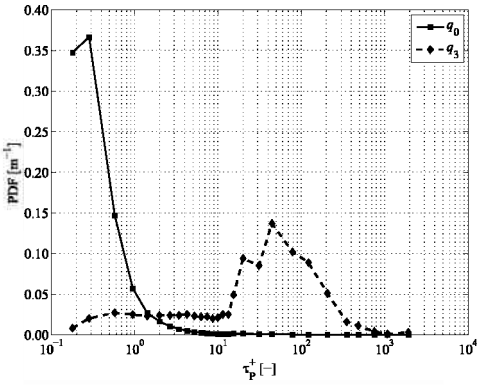

(d) Density distribution of particle number (q_0) and volume/mass (q_3) as function of the dimensionless particle relaxation time τ_p^+.

Figure D.1: *Distribution functions for* $\tau_w = 2.66$ *Pa.*

E User Defined Functions

E.1 UDF for Energy Based Wall Sticking Criterion

```
/*************************************************************/
/*            UDF: Particle wall adhesion                    */
/*          energy based deposition models                   */
/*                                                           */
/* Author: J. Houben                                         */
/* Datum: 24.05.2011                                         */
/*                                                           */
/*************************************************************/

/* UDF for computing the particle critical sticking velocity and comparing it
    with its current velocity */

#include "udf.h"
#include "dpm.h"
#include "surf.h"
#include "stdio.h"
#include "gaussrand.h"

/* Material properties */

int button=1;                   /* for activating the impact velocity correction */

#define epl       0.4           /* [-]      plastic coefficient of restitution    */
#define ppl       3.5e+8        /* [N/m2]   van der Waals pressure                */
#define z0        4.0e-10       /* [m]      distance at contact                   */
#define El        9.0e+10       /* [N/m2]   Youngs modulus limestone              */
#define Es        1.5e+11       /* [N/m2]   Youngs modulus steel                  */
#define nul       0.265         /* [-]      Poisson ratio limestone               */
#define nus       0.25          /* [-]      Poisson ratio steel                   */

#define gaml      0.38          /* [J/m2]   surface energy limestone              */
#define gams      0.046         /* [J/m2]   surface energy steel                  */
#define gamLWl    42.62e-3
#define gamLWs    37.42e-3
#define gamLWw    21.8e-3
#define gampl     1.64e-3
#define gamps     6e-5
#define gampw     25.5e-3
#define gamml     4.52e-3
#define gamms     13.94e-3
#define gammw     25.5e-3
#define eps0      8.8542e-12    /* [F/m]    relative permittivity                 */
#define epsrl     7.7           /* [-]      dielectric constant limestone         */
#define epsrs     3.0e+02       /* [-]      dielectric constant steel             */
#define rhoq      15.0e+11      /* [-]      particle resistivity limestone        */
```

```
#define rhoqs     9.7e-08     /* [-]     particle resistivity steel          */
#define lambda    0.066e-6    /* [m]     mean free path of air molecules     */

#define A12mol    15e-20      /* [J]     Hamaker constant between limestone and*/
                              /*         steel to Molerus                    */
//#define A12mol  38e-20      /* [J]     from Lifshitz acid base             */

float counter=1.0e0;

/* correction factor for 7 kg feed */

float corr1=1.65e12;              /* for 0.25 mum */
float corr2=1.93e12;              /* for 0.35 mum */
float corr3=1.13e12;              /* for 0.50 mum */
float corr4=5.09e11;              /* for 0.70 mum */
float corr5=2.37e11;              /* for 0.90 mum */
float corr6=1.21e11;              /* for 1.10 mum */
float corr7=6.43e10;              /* for 1.30 mum */
float corr8=3.70e10;              /* for 1.50 mum */
float corr9=2.32e10;              /* for 1.70 mum */
float corr10=1.53e10;             /* for 1.90 mum */
float corr11=1.08e10;             /* for 2.10 mum */
float corr12=8.03e09;             /* for 2.30 mum */
float corr13=6.10e09;             /* for 2.50 mum */
float corr14=4.91e09;             /* for 2.70 mum */
float corr15=4.98e09;             /* for 2.90 mum */
float corr16=4.09e09;             /* for 3.13 mum */
float corr17=6.47e09;             /* for 3.38 mum */
float corr18=9.16e09;             /* for 3.75 mum */
float corr19=4.69e09;             /* for 4.50 mum */
float corr20=3.94e09;             /* for 5.50 mum */
float corr21=1.23e09;             /* for 7.00 mum */
float corr22=4.98e08;             /* for 9.00 mum */

float xo1=0.3e-6;                 /* for 0.25 mum */
float xo2=0.4e-6;                 /* for 0.35 mum */
float xo3=0.6e-6;                 /* for 0.50 mum */
float xo4=0.8e-6;                 /* for 0.70 mum */
float xo5=1.0e-6;                 /* for 0.90 mum */
float xo6=1.2e-6;                 /* for 1.10 mum */
float xo7=1.4e-6;                 /* for 1.30 mum */
float xo8=1.6e-6;                 /* for 1.50 mum */
float xo9=1.8e-6;                 /* for 1.70 mum */
float xo10=2.0e-6;                /* for 1.90 mum */
float xo11=2.2e-6;                /* for 2.10 mum */
float xo12=2.4e-6;                /* for 2.30 mum */
float xo13=2.6e-6;                /* for 2.50 mum */
float xo14=2.8e-6;                /* for 2.70 mum */
float xo15=3.0e-6;                /* for 2.90 mum */
float xo16=3.25e-6;               /* for 3.13 mum */
float xo17=3.5e-6;                /* for 3.38 mum */
float xo18=4.0e-6;                /* for 3.75 mum */
float xo19=5.0e-6;                /* for 4.50 mum */
float xo20=6.0e-6;                /* for 5.50 mum */
float xo21=8.0e-6;                /* for 7.00 mum */
float xo22=1.0e-5;                /* for 9.00 mum */

DEFINE_DPM_BC(particle_v_crit,p,t,f,f_normal,dim)
```

```
{
    real NV_VEC(x);
    real vabs;              /* [m/s]    absolute particle velocity   */
    real wpn;               /* [m/s]    normal particle velocity     */
    real wpt;               /* [m/s]    tangential particle velocity */
    real wp1;
    real wp2;
    int i, idim=dim;
    real normal[3];
    real vpcrit;            /* [m/s]    critical sticking velocity   */

    real ES;                /* [J]      surface energy               */
    real EvdW, EvdW0;       /* [J]      van der Waals energy
                                         (un)deformed particle        */
    real A,A132,A131,A11,A22,A33,A12,A13,A23;/* Hamaker constants    */
    real homega;            /* [J]      Lifshitz v.d. Waals constant */

    real r0;                /* [m]      contact radius at end of collision */
    real rst;               /* [m]      averaged radius              */
    real K;                 /* [N/m2]   averaged elastic constant    */
    real kl;                /* [m2/N]   elastic constant limestone   */
    real ks;                /* [m2/N]   elastic constant steel       */
    real gam;               /* [J/m2]   energy per unit contact area */

    real Etot;              /* [J]      total energy                 */
    real Est;               /* [N/m2]   representative Young's modulus */

    real vx;                /* [m/s]    cell fluid x-velocity        */
    real vy;                /* [m/s]    cell fluid y-velocity        */
    real vz;                /* [m/s]    cell fluid z-velocity        */
    real vf;                /* [m/s]    fluid velocity               */
    real vfn;               /* [m/s]    normal component fluid velocity */
    real vft;
    real vft1;              /* [m/s]    1st tan component fluid velocity */
    real vft2;              /* [m/s]    2nd tan component fluid velocity */
    real vcell1;            /* [m/s]    1st cell fluid velocity      */
    real vcell2;            /* [m/s]    2nd cell fluid velocity      */
    real wcell;
    real Stk;               /* [-]      Stokes number                */
    real Kn;                /* [-]      Knudsen number               */
    real Cc;                /* [-]      Cunningham correction        */
    real taup;              /* [s]      particle relaxation time     */
    real s;                 /* [m]      distance cell - face midpoint */
    real sn;
    real sx;
    real sy;
    real sz;
    real alpha;
    real alfa;
    real thetac;

    real zeta;              /* [-]      damping factor               */
    real zetan;             /* [-]      normal damping factor        */
    real zetat1;            /* [-]      tan damping factor in direction 1 */
    real zetat2;            /* [-]      tan damping factor in direction 2 */
real zetat;             /* [-]      total tangential damping factor */

    real xc[ND_ND]; /* holds the cell midpoint position vector      */
    real xf[ND_ND]; /* holds the face midpoint position vector      */
```

```
        real xs[ND_ND]; /* holds the vector between face and cell midpoint      */

        real Area[ND_ND]; /* face area vector                                    */

        real m;                 /* [kg]      particle mass                       */
        real e;                 /* [-]       coefficient of restitution          */
170     real e_n;               /* [-]       normal coefficient of restitution   */
        real e_t;               /* [-]       tan coefficient of restitution      */

        real ratio;             /* [-]                                           */

        real mu;                /* [-]       Tabor parameter                     */
        real lambdap;           /* [-]       elasticity parameter                */
        real ahat, Fhat;        /* [-]       dimensionless parameters            */
        real Fc;                /* [N]       contact force                       */
        real a;                 /* [m]       contact radius                      */
180
        real G12,G12LW,G12AB;
        real g12LW,g13LW,g23LW,g12AB,g13AB,g23AB,G132tot,G11tot,G12tot,G132LW,G132AB
            ;

        real dst, fdst, k, he, corrD;     /* for the calculation of the corrected */
                                          /* van der Waals energy by Dahneke      */
        real G132tot2, G132totLW;
        real cA;                /* [-] calculation constant for Hamaker constant */

        real vfx, vfy, vfz;
190     real vft1x, vft1y, vft1z, vft2x, vft2y, vft2z;
        real wpt1x, wpt1y, wpt1z, wpt2x, wpt2y, wpt2z;
        real wpn1, wpt1, wpn2, wpt2;
        real wpt01x, wpt01y, wpt01z, wpt02x, wpt02y, wpt02z;
        real wpn01, wpt01, wpn02, wpt02;
        real vfnx, vfny, vfnz, vftx, vfty, vftz;
        real vftvecx, vftvecy, vftvecz;
        real vfsteady, vfnsteady, vfnfluc, vftsteady, vftfluc;

        real wpne,wpte,wpe,vabse, vabs0;
200     real wpn0, wpnec, wpt0, wpt0c, wpt1c, wpt2c, wpt20, wpt20c;
        real wpn0c;

        real wpnex, wpney, wpnez;
        real wptex, wptey, wptez;
        real wptevecx, wptevecy, wptevecz;
        real wpn0x, wpn0y, wpn0z;
        real wpt0x, wpt0y, wpt0z;
        real wpt0vecx, wpt0vecy, wpt0vecz;
        real xrand, yrand, zrand;
210     real corr;
        real corrf;

        real Stken, Stket,Stk0n, Stk0t, Stk0nc;
        real PI1, PI1e, PI2, PI2e, PI3, PI3e, PI4, PI4e;
        real zetatlin, zetagr ,zetatline, zetagre;
        real wptcorr;

        FILE*fpointer;
        Thread *cthread;
220
        cell_t c = RP_CELL(&(p->cCell)); /* get the cell and thread in which */
```

```
                                        /* the particle is currently        */
    cthread = P_CELL_THREAD(p);

  if ((NNULLP(t)) && (THREAD_TYPE(t) == THREAD_F_WALL)){
      F_CENTROID(x,f,t);
      for (i=0; i<idim; i++)
      normal[i] = f_normal[i];

230   vabs=NV_MAG(P_VEL(p));
      wpn=(P_VEL(p)[0]*normal[0]+P_VEL(p)[1]*normal[1]+P_VEL(p)[2]*normal[2]);
      wpt=sqrt(vabs*vabs-wpn*wpn);

      A11=24*M_PI*gamLWl*z0*z0;          /* limestone        */
      A22=24*M_PI*gamLWs*z0*z0;          /* steel            */
      A33=24*M_PI*gamLWw*z0*z0;          /* water            */

      A12=sqrt(A11*A22);                 /* limestone-steel  */
      A13=sqrt(A11*A33);                 /* limestone-water  */
240   A23=sqrt(A22*A33);                 /* steel-water      */
      cA=1.6;
      A132=cA*(A12+A33-A13-A23);
      A131=cA*(A11+A33-2*A13);

      A=A12mol;
      homega=4*M_PI/3*A;
      e=sqrt(epl*epl-A/(P_DIAM(p)*vabs*M_PI*z0*z0)*((1-epl*epl)/(6*P_RHO(p)*ppl
          )));
      e_n=epl;
      e_t=epl;
250
   /* calculation of the van der Waals surface energy in air*/

      g12LW=pow(sqrt(gamLWl)-sqrt(gamLWs),2.0);
      g13LW=pow(sqrt(gamLWl)-sqrt(gamLWw),2.0);
      g23LW=pow(sqrt(gamLWs)-sqrt(gamLWw),2.0);

      g12AB=2*(sqrt(gampl)-sqrt(gamps))*(sqrt(gamml)-sqrt(gamms));
      g13AB=2*(sqrt(gampl)-sqrt(gampw))*(sqrt(gamml)-sqrt(gammw));
      g23AB=2*(sqrt(gamps)-sqrt(gampw))*(sqrt(gamms)-sqrt(gammw));
260
      G132LW=g12LW-g13LW-g23LW;
      G132AB=g12AB-g13AB-g23AB;

      G11tot=-2*(gamLWl+2*sqrt(gampl*gamml));
      G12tot=-2*(sqrt(gamLWl*gamLWs)+sqrt(gampl*gamms)+sqrt(gamml*gamps));

      G132tot=G132LW+G132AB;
      G132tot2=
            2*(sqrt(gamLWl*gamLWw)+sqrt(gamLWs*gamLWw)-sqrt(gamLWl*gamLWs)-
               gamLWw
270           +sqrt(gampw)*(sqrt(gamml)+sqrt(gamms)-sqrt(gammw))
              +sqrt(gammw)*(sqrt(gampl)+sqrt(gamps)-sqrt(gampw))
              -sqrt(gampl*gamms)-sqrt(gamml*gamps));

      gam=A12mol/(12*M_PI*z0*z0);

    /* calculation of the van der Waals surface energy in water */

      kl=(1-nul*nul)/(M_PI*El);
```

```
        ks=(1-nus*nus)/(M_PI*Es);
        K=4/(3*M_PI*(kl+ks));
        rst=pow((1/(P_DIAM(p)/2)),-1.0);
        mu=pow(16*rst*2*gam*gam/(9*K*K*z0*z0),0.333333333);
        lambdap=1.16*mu;

    /* calculation of the contact radius from the Tabor parameter */

        if(lambdap>5){
            r0=pow((6*M_PI*gam*rst*rst/K),0.3333333333); /* according to JKR model
                */
            }

        else if(lambdap<0.1){
            r0=pow((2*M_PI*gam*rst*rst/K),0.3333333333); /* according to DMT model
                */
            }

        else{
            alfa=(1-exp(-lambdap/0.924))/1.02;
            Fhat=-1*(-0.5714+0.25*(4.04*pow(lambdap,1.4)-1)/(4.04*pow(lambdap,1.4)
                +1));
            ahat=1.54+0.279*(2.28*pow(lambdap,1.3)-1)/(2.28*pow(lambdap,1.3)+1);
            a=ahat*pow(K/(M_PI*gam*rst*rst),-0.333333);
            Fc=Fhat*M_PI*gam*rst;
            r0=pow(rst/K,0.33333333)*((1+alfa)*sqrt(Fc));
            }

    /* calculation of the correction by Dahneke */

        k=M_PI*(kl+ks);
        dst=A*A*k*k*P_DIAM(p)/(108*pow(z0,7.0));
        fdst=27*pow(dst,3.0)+36*pow(dst,2.0)+8*dst+8*sqrt(pow(dst,3.0)+dst*dst);
        he=z0*(3/8*pow(fdst,0.333333)+(24*dst+27*dst*dst)/(8*pow(fdst,0.33333))
            +9/8*dst);
        corrD=(1+he/z0+he*he/(z0*z0))+(4*sqrt(2*P_DIAM(p))/(15*k))*pow(he,2.5)/(A
            *P_DIAM(p)/(12*z0));

        ES=M_PI*r0*r0*gam;
        EvdW0=homega*homega*P_DIAM(p)/(256*pow(M_PI,3.0)*pow(z0,4.0)*ppl);
        EvdW=homega/(16*M_PI*z0*z0)*P_DIAM(p)*P_DIAM(p)*sqrt(P_RHO(p)/(6*ppl))*
            vabs*sqrt(1-epl*epl);

    /* Change model for surface energy */

        //Etot=ES;
        Etot=EvdW;
        //Etot=EvdW0*corrD;



/* calculation of the critical impact velocity */

        vpcrit=1/e*sqrt(2*Etot/(P_MASS(p)));

/* calculation of the corrected impact velocity */

        C_CENTROID(xc,c,cthread);
        F_CENTROID(xf,f,t);
```

```
            vx=C_U(c,cthread);
            vy=C_V(c,cthread);
            vz=C_W(c,cthread);

            sx=xc[0]-xf[0];
            sy=xc[1]-xf[1];
            sz=xc[2]-xf[2];
340
            s=sqrt(pow(xc[0]-xf[0],2)+pow(xc[1]-xf[1],2)+pow(xc[2]-xf[2],2));
            thetac=acos((-sx*normal[0]-sy*normal[1]-sz*normal[2])/s);

            Kn=lambda/P_DIAM(p);
            Cc=1+Kn*(2.514+0.8*exp(-0.55/Kn));
            taup=Cc*(P_RHO(p)-C_R(c,cthread))*P_DIAM(p)*P_DIAM(p)/(18*C_MU_L(c,
                cthread));

    /* calculation of the normal and tangential components */
    /* of the particle and fluid velocity                  */
350
        /* Fluid */
            xrand=gaussrand();
            yrand=gaussrand();
            zrand=gaussrand();

            vfx=C_U(c,cthread)+sqrt(C_RUU(c,cthread)/C_R(c,cthread))*xrand;
            vfy=C_V(c,cthread)+sqrt(C_RVV(c,cthread)/C_R(c,cthread))*yrand;
            vfz=C_W(c,cthread)+sqrt(C_RWW(c,cthread)/C_R(c,cthread))*zrand;

360         vfsteady=sqrt(pow(C_U(c,cthread),2.0)+pow(C_V(c,cthread),2.0)+pow(C_W(c,
                cthread),2.0));

            vf=sqrt(vfx*vfx+vfy*vfy+vfz*vfz);
            vfn=vfx*normal[0]+vfy*normal[1]+vfz*normal[2];
            vfnsteady=C_U(c,cthread)*normal[0]+C_V(c,cthread)*normal[1]+C_W(c,
                cthread)*normal[2];
            vftsteady=sqrt(pow(vfsteady,2.0)-pow(vfnsteady,2.0));
            vfnfluc=vfn-vfnsteady;
            vft=sqrt(vf*vf-vfn*vfn);
            vftfluc=vft-vftsteady;

370         vfnx=vfn*normal[0];
            vfny=vfn*normal[1];
            vfnz=vfn*normal[2];
            vftx=vfx-vfnx;
            vfty=vfy-vfny;
            vftz=vfz-vfnz;

            vftvecx=vftx/vft;
            vftvecy=vfty/vft;
            vftvecz=vftz/vft;
380
        /* Particle */

            vabse=NV_MAG(P_VEL(p));
            wpne=(P_VEL(p)[0]*normal[0]+P_VEL(p)[1]*normal[1]+P_VEL(p)[2]*normal[2])
                ;
            wpte=sqrt(vabse*vabse-wpne*wpne);
```

```
        wpnex=wpne*normal[0];
        wpney=wpne*normal[1];
        wpnez=wpne*normal[2];
        wptex=P_VEL(p)[0]-wpnex;
        wptey=P_VEL(p)[1]-wpney;
        wptez=P_VEL(p)[2]-wpnez;

        wptevecx=wptex/wpte;
        wptevecy=wptey/wpte;
        wptevecz=wptez/wpte;

    /* particle velocity component parallel to fluid velocity */
        wpt1=wptex*vftvecx+wptey*vftvecy+wptez*vftvecz;
            wpt1x=wpt1*vftvecx;
            wpt1y=wpt1*vftvecy;
            wpt1z=wpt1*vftvecz;

    /* particle velocity component perpendicular to fluid velocity */
            wpt2x=wptex-wpt1x;
            wpt2y=wptey-wpt1y;
            wpt2z=wptez-wpt1z;
       wpt2=sqrt(pow(wpt2x,2.0)+pow(wpt2y,2.0)+pow(wpt2z,2.0));


        if(cos(thetac)==0)
            {
            Stken=0;
            }
        else{
            Stken=(wpne)*taup/s*(cos(thetac));
            }

        Stk0n=Stken+2;
        wpn0=Stk0n*s/(taup*cos(thetac));
        wpn0c=wpn0+vfnfluc;
        Stk0nc=(wpn0c)*taup/s*(cos(thetac));

        Stket=(wpt2)*taup/s*(cos(thetac));
        Stk0t=Stket+2;
        wpt20=Stk0t*s/(taup*cos(thetac));
        wpt20c=wpt20+vftfluc;

        wcell=vft;
        PI2e=wcell/wpt1;

  /* put button==1 for activating velocity damping factor */

        if(Stk0nc>2 && button ==1){

            PI1=Stk0nc;
            PI4=(C_U_G(c,cthread)[0]*normal[0]+C_U_G(c,cthread)[0]*normal[1]+
                C_U_G(c,cthread)[0]*normal[2]
                +C_V_G(c,cthread)[1]*normal[0]+C_V_G(c,cthread)[1]*normal[1]+
                    C_V_G(c,cthread)[1]*normal[2]
                +C_W_G(c,cthread)[2]*normal[0]+C_W_G(c,cthread)[2]*normal[1]+
                    C_W_G(c,cthread)[2]*normal[2]
                )*taup;

/* choosing way of calculating particle velocities at entering the cell */
```

```
        //wpt0c=1/(Stk0nc-2)*(PI4*wpn0c*(2-2/Stk0nc+log((Stk0nc-2)/Stk0nc)*(
            Stk0nc-2))-2*wcell+wpt1*Stk0nc); /* from gradient */
        wpt0c=wpt1*Stk0nc/(Stk0nc-2)*(1+PI2e*(2+(Stk0nc-2)*log((Stk0nc-2)/
            Stk0nc)-4/Stk0nc)); /* from linear flow profile */

        PI2=wcell/wpt0c;
        PI3=wpn0c/wpt0c;

        zetan=1-2/PI1;
        zetatlin=PI2*(2-PI1)-PI2*(PI1-2)*log(1-2/PI1)+(1-2/PI1)*(1-2*PI2+PI2*
            PI1);
        zetagr=(PI4*PI3+1-PI4*PI3/PI1-PI2-PI4*PI3*log(1-2/PI1))*(1-2/PI1)+PI4*
            PI3/PI1-PI4*PI3+PI2;

        wpnec=wpn0c*(1-2/PI1);
        wpt1c=zetatlin/zetagr*wpt1;
        wpt2c=wpt20c*(1-2/PI1);

        corr=sqrt(pow(wpnec,2.0)+pow(wpt1c,2.0)+pow(wpt2c,2.0))/NV_MAG(P_VEL(p
            ));

      }
      else{
        corr=1;
      }

  /* Comparison of velocities */

      if (corr*vabs<vpcrit && P_POS(p)[2]>-1.0){

        C_UDMI(c,cthread,0)+=counter;    /* number of particles     */
        C_UDMI(c,cthread,1)+=P_MASS(p);   /* particle volume         */


                  if(P_DIAM(p)<xo1){corrf=corr1/2.08;}
              else if(P_DIAM(p)<xo2){corrf=corr2/2.08;}
              else if(P_DIAM(p)<xo3){corrf=corr3/2.08;}
              else if(P_DIAM(p)<xo4){corrf=corr4/2.08;}
              else if(P_DIAM(p)<xo5){corrf=corr5/2.08;}
              else if(P_DIAM(p)<xo6){corrf=corr6/2.08;}
              else if(P_DIAM(p)<xo7){corrf=corr7/2.08;}
              else if(P_DIAM(p)<xo8){corrf=corr8/2.08;}
              else if(P_DIAM(p)<xo9){corrf=corr9/2.08;}
              else if(P_DIAM(p)<xo10){corrf=corr10/2.08;}
              else if(P_DIAM(p)<xo11){corrf=corr11/2.08;}
              else if(P_DIAM(p)<xo12){corrf=corr12/2.08;}
              else if(P_DIAM(p)<xo13){corrf=corr13/2.08;}
              else if(P_DIAM(p)<xo14){corrf=corr14/2.08;}
              else if(P_DIAM(p)<xo15){corrf=corr15/2.08;}
              else if(P_DIAM(p)<xo16){corrf=corr16/2.08;}
              else if(P_DIAM(p)<xo17){corrf=corr17/2.08;}
              else if(P_DIAM(p)<xo18){corrf=corr18/2.08;}
              else if(P_DIAM(p)<xo19){corrf=corr19/2.08;}
              else if(P_DIAM(p)<xo20){corrf=corr20/2.08;}
              else if(P_DIAM(p)<xo21){corrf=corr21/2.08;}
              else if(P_DIAM(p)<xo22){corrf=corr22/2.08;}

      F_AREA(Area,f,t);
```

```
      /* Number of particles in cell          */
        C_UDMI(c,cthread,0)+=corrf*1.0;
500
      /* corrected volume of depositions      */
        C_UDMI(c,cthread,1)+=corrf*M_PI/6*pow(P_DIAM(p),3.0);

      /* corrected thickness of depositions */
        C_UDMI(c,cthread,2)+=corrf*M_PI/6*pow(P_DIAM(p),3.0)/NV_MAG(Area);

          fpointer=fopen("sticking_corr.txt","a");
            Message("%e\n",P_DIAM(p));
            fprintf(fpointer,"%d %d %d %d %8.6e %8.6e %8.6e %8.6e %8.6e\n",c,
                cthread,f,t,P_TIME(p), P_DIAM(p), P_POS(p)[0],P_POS(p)[1],P_POS(p)
                [2]);
510       fclose(fpointer);

          return PATH_ABORT;
          }



   else{
          /* calculate the normal component, rescale its magnitude by */
          /* the coefficient of restitution and subtract the change   */
520
         /* Compute normal velocity. */
          for(i=0; i<idim; i++)
          wpn += p->state.V[i]*normal[i];

          /* Subtract off normal velocity. */
          for(i=0; i<idim; i++)
          p->state.V[i] -= wpn*normal[i];

          //Apply tangential coefficient of restitution.
530       for(i=0; i<idim; i++)
          p->state.V[i] *= e_t;

          /* Add reflected normal velocity. */
          for(i=0; i<idim; i++)
          p->state.V[i] -= e_n*wpn*normal[i];

          /* Store new velocity in state0 of particle */
          for(i=0; i<idim; i++)
          p->state0.V[i] = p->state.V[i];
540
          return PATH_ACTIVE;
    }
      }
  else    {
          return PATH_ACTIVE;
          }

}

550 DEFINE_ON_DEMAND(OD_INIT_UDMI)
{

/* for resetting user defined cell memories  */
```

```
    Domain *domain;
    Thread *t;
    cell_t c;
    int i=0;

560 domain = Get_Domain(1);


    thread_loop_c(t,domain){
       begin_c_loop (c,t){
          for (i=0; i<(4);++i)     /* Number of UDMI! */
                C_UDMI(c,t,i) = 0.0;
       end_c_loop (c,t)}
       }
     Message("User defined memory per cell activated %d\n", i);
570
    }

    /* read UDM from .txt-file */
    DEFINE_ON_DEMAND(OD_UDMI_END)
    {
    Domain *domain; /* declare domain pointer since it is not passed as an
                       argument to the DEFINE macro  */

    FILE *fr;
580 FILE *fp;
    cell_t c;
    real A[ND_ND];
    real corrf;
    real relmass=0;
    float time, diam;
    float x,y,z;
    float counter=1.0e0;
    Thread *ct;
    Thread *ft;
590 int f;

    domain = Get_Domain(1);      /* Get the domain using Fluent utility */



    fr=fopen("stick.txt","r");
    /*
    File should end with "eof" !
    */
600 if((fr) == NULL){
        Message("File not found\n");
    }
    else{
        Message("File has been opened\n");

       while(fscanf(fr,"%d %d %d %d %e %e %e %e %e\n", &c,&ct ,&f, &ft, &time, &diam
           , &x, &y, &z) != 0){
             printf("%d %d %d %d %e %e %e %e %e\n", c,ct,f,ft,time,diam,x,y,z);
             Message("%d %d %d %d %e %e %e %e %e\n",c,ct,f,ft,time,diam,x,y,z);

610                    if(diam<xo1){corrf=corr1/2.08;}
                  else if(diam<xo2){corrf=corr2/2.08;}
```

```
                else if(diam<xo3){corrf=corr3/2.08;}
                else if(diam<xo4){corrf=corr4/2.08;}
                else if(diam<xo5){corrf=corr5/2.08;}
                else if(diam<xo6){corrf=corr6/2.08;}
                else if(diam<xo7){corrf=corr7/2.08;}
                else if(diam<xo8){corrf=corr8/2.08;}
                else if(diam<xo9){corrf=corr9/2.08;}
                else if(diam<xo10){corrf=corr10/2.08;}
620             else if(diam<xo11){corrf=corr11/2.08;}
                else if(diam<xo12){corrf=corr12/2.08;}
                else if(diam<xo13){corrf=corr13/2.08;}
                else if(diam<xo14){corrf=corr14/2.08;}
                else if(diam<xo15){corrf=corr15/2.08;}
                else if(diam<xo16){corrf=corr16/2.08;}
                else if(diam<xo17){corrf=corr17/2.08;}
                else if(diam<xo18){corrf=corr18/2.08;}
                else if(diam<xo19){corrf=corr19/2.08;}
                else if(diam<xo20){corrf=corr20/2.08;}
630             else if(diam<xo21){corrf=corr21/2.08;}
                else if(diam<xo22){corrf=corr22/2.08;}

      F_AREA(A,f,ft);

      /* Number of particles in cell        */
      C_UDMI(c,ct,0)+=corrf*1.0;

      /* corrected volume of depositions    */
      C_UDMI(c,ct,1)+=corrf*M_PI/6*pow(diam,3.0);
640
      /* corrected thickness of depositions */
      C_UDMI(c,ct,2)+=corrf*M_PI/6*pow(diam,3.0)/NV_MAG(A);

      }

      thread_loop_c(ct,domain){
              begin_c_loop (c,ct){
                 relmass+=2770/7*C_UDMI(c,ct,1);
              end_c_loop (c,ct)}
650   }
      Message("Data read succesfully\n");
      Message("relative deposited mass %e%%\n",relmass*100);
  }
  fclose(fr);
  }


  DEFINE_DPM_TIMESTEP(taup02,p,dt)
  {
660 real taup;
  real Kn, Cc;
  real Vc=0.13626914; /* [m3]    cyclone separator volume                          */
  real Q=600;         /* [m3/h]  volume flow rate                                  */

  real tc;            /* [s]     end time                                          */
  real dtime;
  real tmin;
  real TL;            /* [s]     time scale of turbulence (Sommerfeld (2003))      */
  real dtmin;         /* [s]     minimum from tc and TL                            */
670
```

```
FILE*fpointer;
Thread *cthread;

cell_t c = RP_CELL(&(p->cCell));     /* get the cell and thread that          */
                                     /* the particle is currently in          */
cthread = P_CELL_THREAD(p);

tc=Vc*3600/(Q);
Kn=lambda/P_DIAM(p);
Cc=1+Kn*(2.514+0.8*exp(-0.55/Kn));
taup=Cc*(P_RHO(p)-C_R(c,cthread))*P_DIAM(p)*P_DIAM(p)/(18*C_MU_L(c,cthread));

if(P_DIAM(p)!=0.0 && P_TIME(p)< 1e1*tc)
   {
    TL=0.3*C_K(c,cthread)/C_D(c,cthread);
    if(taup>TL)
     {
      tmin=TL;
     }
     else{
      tmin=taup;
    }

    dtime=0.2*tmin;
    dt=0.2*tmin;
    return 0.2*tmin;
   }
   else
   {
    Message("over time: %e\n",P_DIAM(p));
    PATH_ABORT;
    return 0;
   }
}

DEFINE_DPM_BC(bc_escape,p,t,f,f_normal,dim)
{
FILE*f2pointer;

    f2pointer=fopen("overflow_corr.txt","a");
              fprintf(f2pointer,"%8.6e %8.6e %8.6e %8.6e %8.6e\n",
                      P_TIME(p), P_DIAM(p), P_POS(p)[0],P_POS(p)[1],P_POS(p)[2])
                          ;
              fclose(f2pointer);

     return PATH_ABORT;
}
```

E.2 UDF for Force and Moment of Forces Based Wall Sticking Criterion

```
/*********************************************************/
/*                  UDF: Particle wall adhesion          */
/*                                                       */
/* Author: J. Houben                                     */
/* Datum: 24.05.2011                                     */
/*                                                       */
/*********************************************************/

/* UDF for computing forces and equilibrium of moments of forces of a particle
   in contact with the wall */

#include "udf.h"
#include "dpm.h"
#include "surf.h"
#include "stdio.h"
#include "gaussrand.h"
#include "turb.h"
#include "f_wall.h"
#include "storage.h"

/* Material properties */

int button=1;

#define epl     0.5        /* [-]     plastic coefficient of restitution   */
#define ppl     3.5e+8     /* [N/m2]  van der Waals pressure               */
#define z0      4.0e-10    /* [m]     distance at contact                  */
#define El      9.0e+10    /* [N/m2]  Youngs modulus limestone             */
#define Es      1.5e+11    /* [N/m2]  Youngs modulus steel                 */
#define nul     0.265      /* [-]     Poisson ratio limestone              */
#define nus     0.25       /* [-]     Poisson ratio steel                  */
#define Vel     0.4        /* [V]     contact potential                    */
#define gaml    0.38       /* [J/m2]  surface energy limestone             */
#define gams    0.046      /* [J/m2]  surface energy steel                 */
#define gamLWl  42.62e-3
#define gamLWs  37.42e-3
#define gamLWw  21.8e-3
#define gampl   1.64e-3
#define gamps   6e-5
#define gampw   25.5e-3
#define gamml   4.52e-3
#define gamms   13.94e-3
#define gammw   25.5e-3
#define eps0    8.8542e-12 /* [F/m]   relative permittivity                */
#define epsrl   7.7        /* [-]     dielectric constant limestone        */
#define epsrs   3.0e+02    /* [-]     dielectric constant steel            */
#define rhoql   5.0e+11    /* [-]     particle resistivity limestone       */
#define rhoqs   9.7e-08    /* [-]     particle resistivity steel           */
#define lambda  0.066e-6   /* [m]     mean free path of air molecules      */
#define fo      1.7009     /* [-]     O'Neill                              */
#define go      0.943993   /* [-]     O'Neill                              */
#define kslid   0.3        /* [-]     sliding ratio                        */
#define gr      9.81       /* [m/s]   gravity                              */
#define A12mol  15e-20     /* [J]     Hamaker constant between limestone and */
                           /*         steel to Molerus                     */
```

```
float counter=1.0e0;

/* correction factor for 7 kg feed */

float corr1=1.65e12;              /* for 0.25 mm */
float corr2=1.93e12;              /* for 0.35 mm */
float corr3=1.13e12;              /* for 0.50 mm */
float corr4=5.09e11;              /* for 0.70 mm */
float corr5=2.37e11;              /* for 0.90 mm */
float corr6=1.21e11;              /* for 1.10 mm */
float corr7=6.43e10;              /* for 1.30 mm */
float corr8=3.70e10;              /* for 1.50 mm */
float corr9=2.32e10;              /* for 1.70 mm */
float corr10=1.53e10;             /* for 1.90 mm */
float corr11=1.08e10;             /* for 2.10 mm */
float corr12=8.03e09;             /* for 2.30 mm */
float corr13=6.10e09;             /* for 2.50 mm */
float corr14=4.91e09;             /* for 2.70 mm */
float corr15=4.98e09;             /* for 2.90 mm */
float corr16=4.09e09;             /* for 3.13 mm */
float corr17=6.47e09;             /* for 3.38 mm */
float corr18=9.16e09;             /* for 3.75 mm */
float corr19=4.69e09;             /* for 4.50 mm */
float corr20=3.94e09;             /* for 5.50 mm */
float corr21=1.23e09;             /* for 7.00 mm */
float corr22=4.98e08;             /* for 9.00 mm */

float xo1=0.3e-6;                 /* for 0.25 mm */
float xo2=0.4e-6;                 /* for 0.35 mm */
float xo3=0.6e-6;                 /* for 0.50 mm */
float xo4=0.8e-6;                 /* for 0.70 mm */
float xo5=1.0e-6;                 /* for 0.90 mm */
float xo6=1.2e-6;                 /* for 1.10 mm */
float xo7=1.4e-6;                 /* for 1.30 mm */
float xo8=1.6e-6;                 /* for 1.50 mm */
float xo9=1.8e-6;                 /* for 1.70 mm */
float xo10=2.0e-6;                /* for 1.90 mm */
float xo11=2.2e-6;                /* for 2.10 mm */
float xo12=2.4e-6;                /* for 2.30 mm */
float xo13=2.6e-6;                /* for 2.50 mm */
float xo14=2.8e-6;                /* for 2.70 mm */
float xo15=3.0e-6;                /* for 2.90 mm */
float xo16=3.25e-6;               /* for 3.13 mm */
float xo17=3.5e-6;                /* for 3.38 mm */
float xo18=4.0e-6;                /* for 3.75 mm */
float xo19=5.0e-6;                /* for 4.50 mm */
float xo20=6.0e-6;                /* for 5.50 mm */
float xo21=8.0e-6;                /* for 7.00 mm */
float xo22=1.0e-5;                /* for 9.00 mm */


DEFINE_DPM_BC(particle_R,p,t,f,f_normal,dim)
{
  Domain *domain;
  real NV_VEC(x);
  real vabs;                      /* [m/s]    absolute particle velocity    */
  real wpn;                       /* [m/s]    normal particle velocity      */
  real wpt;                       /* [m/s]    tangential particle velocity  */
```

```
    real wp1, wp2;
    int i, idim=dim;
    real normal[3];

    real ES;                /* [J]      surface energy                  */
    real EvdW, EvdW0;       /* [J]      van der Waals energy            */
120                         /*          (un)deformed particle           */
    real A, A132, A131, A11, A22, A33,A12, A13, A23;
                            /* [J]      Hamaker constants               */
    real homega;            /* [J]      Lifshitz van der Waals constant*/
    real r0, r0JKR, r0DMT; /* [m]      contact radius at end of coll. */
    real rst;               /* [m]      averaged radius                 */
    real K;                 /* [N/m2]   averaged elastic constant       */
    real kl;                /* [m2/N]   elastic constant limestone      */
    real ks;                /* [m2/N]   elastic constant steel          */
    real gam;               /* [J/m2]   energy per unit contact area    */
130
    real Etot;              /* [J]      total energy                    */
    real Est;               /* [N/m2]   representative Young's modulus */

    real vx;                /* [m/s]    cell fluid x-velocity           */
    real vy;                /* [m/s]    cell fluid y-velocity           */
    real vz;                /* [m/s]    cell fluid z-velocity           */
    real vf;                /* [m/s]    fluid velocity                  */
    real vfn;               /* [m/s]    normal component fluid velocity*/
    real vft;               /* [m/s]    tan component fluid velocity    */
140 real vft1;              /* [m/s]    1st tangential component fluid velocity */
    real vft2;              /* [m/s]    2nd tangential component fluid velocity */
    real vcell1;            /* [m/s]    1st cell fluid velocity         */
    real vcell2;            /* [m/s]    2nd cell fluid velocity         */
    real Stk;               /* [-]      Stokes number                   */
    real PI2;               /* [-]      wcell/wpt0                      */
    real Kn;                /* [-]      Knudsen number                  */
    real Cc;                /* [-]      Cunningham correction           */
    real taup;              /* [s]      particle relaxation time        */
    real s;                 /* [m]      distance cell midpoint-face mid*/
150 real sn, sx, sy, sz;
    real alfa;
    real thetac;

    real thetap, thetas;
    real gn, gt;

    real zeta;              /* [-]      damping factor                  */
    real zetan;             /* [-]      normal damping factor           */
    real zetat1;            /* [-]      tan damping factor in direction 1 */
160 real zetat2;            /* [-]      tan damping factor in direction 2 */
    real zetat;             /* [-]      total tangential damping factor */

    real xc[ND_ND];         /* this will hold the cell midpoint position vector*/
    real xf[ND_ND];         /* this will hold the face midpoint position vector*/
    real xs[ND_ND];         /* this will hold the vector between face and cell */
    real Avec[ND_ND];       /* area vector of face                      */

    real e;                 /* [-]      coefficient of restitution      */
    real e_n;               /* [-]      normal coefficient of restitution */
170 real e_t;               /* [-]      tangential coefficient of restitution */

    real ratio;             /* [-]                                      */
```

```
      real mu;                /* [-]      Tabor parameter                    */
      real lambdap;           /* [-]      elasticity parameter               */
      real ahat, Fhat;        /* [-]      dimensionless parameters           */
      real Fc;                /* [N]      contact force                      */
      real a;                 /* [m]      contact radius                     */

180   real G12, G12LW, G12AB;
      real g12LW, g13LW, g23LW, g12AB, g13AB, g23AB, G132tot, G11tot, G12tot, G132LW
          , G132AB;
      real G132tot2, G132totLW;

      real FG, FGn, FGt, FTU, FL, Fa, Fvdw, FLSaff, FLLA, FLAW, FD, FDAW, FPG, FC,
         FES, Fel;
      real TD;
      real Rep, CD;

      real qp1, qp2;

190   real gamw;
      real Deltap;
      real wpabs;

      real x0, r;

      real theta;

      real vfx, vfy, vfz;
      real vft1x, vft1y, vft1z, vft2x, vft2y, vft2z;
200   real wpt1x, wpt1y, wpt1z, wpt2x, wpt2y, wpt2z;
      real wpn1, wpt1, wpn2, wpt2;
      real vfnx, vfny, vfnz, vftx, vfty, vftz;
      real vfnsteady, vftsteady;
      real vfstat, vfnstat, vftstat, vftstattot;
      real vftvecx, vftvecy, vftvecz;

      real utut;

      real dvtdn, dpdn;
210   real RH;
      real seTe;

      real wpne,wpte,wpe,vabse;
      real wpn0, wpt0;

      real xrand, yrand, zrand;
      real uac, vac, wac, uacn;
      real corr, corrf;

220   real Stken, Stk0n;
      real PI1, PI2e, PI3;
      real zetatlin, zetatlog, zetatstep;
      real wptcorr;

      real Rv, Rs, Rt;
      real wpn0c, Stk0nc;
      real Stkcritn;

      real tauw, ust, area;
```

```
230   real wcell, wcelln, wcellt;
      real up, yp;

      real Area;

      FILE*fpointer;
      Thread *cthread;

      cell_t c = RP_CELL(&(p->cCell)); /* get the cell and Thread that  */
                                       /* the particle is currently in  */
240   cthread = P_CELL_THREAD(p);

    if ((NNULLP(t)) && (THREAD_TYPE(t) == THREAD_F_WALL)){
          F_CENTROID(x,f,t);
    for (i=0; i<idim; i++)
         normal[i] = f_normal[i];

      F_AREA(Avec,f,t);
      area=NV_MAG(Avec);
      tauw=NV_MAG(F_STORAGE_R_N3V(f,t,SV_WALL_SHEAR))/area;
250   ust=sqrt(tauw/C_R(c,cthread));
      yp=P_DIAM(p)/2*ust*C_R(c,cthread)/C_MU_L(c,cthread);

      vfx=C_U(c,cthread);
      vfy=C_V(c,cthread);
      vfz=C_W(c,cthread);

      vf=sqrt(vfx*vfx+vfy*vfy+vfz*vfz);
      vfn=vfx*normal[0]+vfy*normal[1]+vfz*normal[2];
      vft=sqrt(vf*vf-vfn*vfn);
260
      xrand=gaussrand();
      yrand=gaussrand();
      zrand=gaussrand();
      uac=C_RUU(c,cthread)/C_R(c,cthread)*xrand;
      vac=C_RVV(c,cthread)/C_R(c,cthread)*yrand;
      wac=C_RWW(c,cthread)/C_R(c,cthread)*zrand;
      uacn=uac*normal[0]+vac*normal[1]+wac*normal[2];

      wcell=sqrt(pow(vfx,2.0)+pow(vfy,2.0)+pow(vfz,2.0));
270   wcelln=C_U(c,cthread)*normal[0]+C_V(c,cthread)*normal[1]
            +C_W(c,cthread)*normal[2];
      wcellt=sqrt(pow(wcell,2.0)-pow(wcelln,2.0));

    if(yp<5.0){
       up=yp;
       vft=up*ust;
       }
    else{
      Message("yp>5.0\n");
280    }
      vabs=NV_MAG(P_VEL(p));
      wpn=(P_VEL(p)[0]*normal[0]+P_VEL(p)[1]*normal[1]+P_VEL(p)[2]*normal[2]);
      wpt=sqrt(vabs*vabs-wpn*wpn);

      A=A12mol;
      homega=4*M_PI/3*A;
      e_n=epl;
      e_t=epl;
```

```
290 /* Calculation of the damping factor */

    C_CENTROID(xc,c,cthread);
    F_CENTROID(xf,f,t);

  /* calculation of the normal and tangential                    */
  /* components of the particle and fluid velocity               */

    sx=xc[0]-xf[0];
    sy=xc[1]-xf[1];
300 sz=xc[2]-xf[2];
    s=sqrt(pow(xc[0]-xf[0],2)+pow(xc[1]-xf[1],2)+pow(xc[2]-xf[2],2));

    thetac=acos((-sx*normal[0]-sy*normal[1]-sz*normal[2])/s);
    theta=acos(normal[2]);

  /* adaptation of the Stk number at impact                      */
  /* for the particle wall impact frequency                      */

    Kn=lambda/P_DIAM(p);
310 Cc=1+Kn*(2.514+0.8*exp(-0.55/Kn));
    taup=Cc*(P_RHO(p)-C_R(c,cthread))*P_DIAM(p)*P_DIAM(p)/(18*C_MU_L(c,cthread));

    vabse=NV_MAG(P_VEL(p));
    wpne=(P_VEL(p)[0]*normal[0]+P_VEL(p)[1]*normal[1]+P_VEL(p)[2]*normal[2]);
    wpte=sqrt(vabse*vabse-wpne*wpne);

        if(cos(thetac)==0)
            {
            Stken=0;
320         }
        else{
            Stken=(wpne)*taup/s*(cos(thetac));
            }

    Kn=lambda/P_DIAM(p);
    Cc=1+Kn*(2.514+0.8*exp(-0.55/Kn));
    taup=Cc*(P_RHO(p)-C_R(c,cthread))*P_DIAM(p)*P_DIAM(p)/(18*C_MU_L(c,cthread));

    Stk0n=Stken+2;
330 wpn0=Stk0n*s/(taup*cos(thetac));
    wpn0c=wpn0+uacn;

    vabse=NV_MAG(P_VEL(p));
    wpne=(P_VEL(p)[0]*normal[0]+P_VEL(p)[1]*normal[1]+P_VEL(p)[2]*normal[2]);
    wpte=sqrt(vabse*vabse-wpne*wpne);      Kn=lambda/P_DIAM(p);

    vabse=NV_MAG(P_VEL(p));
    wpne=(P_VEL(p)[0]*normal[0]+P_VEL(p)[1]*normal[1]+P_VEL(p)[2]*normal[2]);
    wpte=sqrt(vabse*vabse-wpne*wpne);
340
     if(button==1){
        Stk0nc=(wpn0c)*taup/s*(cos(thetac));
       }
    else{
        Stk0nc=Stken+2;
       }
```

```
    if(pow(thetac,2.0)>0){
        //dvtdn=vft/(yp);                          /* from boundary layer
            function */
        //dvtdn=tauw/C_MU_L(c,cthread);            /* from wall shear stress
                */
        dvtdn=wcellt/s;                            /* from cell midpoint
            velocity  */
      }
    else{
        dvtdn=0;
       }
        sn=cos(thetac)*s;

/* Particle */

    Kn=lambda/P_DIAM(p);
    Cc=1+Kn*(2.514+0.8*exp(-0.55/Kn));
    taup=Cc*(P_RHO(p)-C_R(c,cthread))*P_DIAM(p)*P_DIAM(p)/(18*C_MU_L(c,cthread))
        ;

    vabse=NV_MAG(P_VEL(p));
    wpne=(P_VEL(p)[0]*normal[0]+P_VEL(p)[1]*normal[1]+P_VEL(p)[2]*normal[2]);
    wpte=sqrt(vabse*vabse-wpne*wpne);

/* calculation of the van der Waals surface energy in air*/

    gam=A12mol/(12*M_PI*z0*z0);

/* calculation of the van der Waals surface energy in water*/

    kl=(1-nul*nul)/(M_PI*El);
    ks=(1-nus*nus)/(M_PI*Es);
    K=4/(3*M_PI*(kl+ks));
    rst=pow((1/(P_DIAM(p)/2)),-1.0);
    mu=pow(16*rst*gam*gam/(9*K*K*z0*z0*z0),0.333333333);
    lambdap=1.16*mu;

    r0JKR=pow((6*M_PI*gam*rst*rst/K),0.3333333333); /* according to JKR model */
    r0DMT=pow((2*M_PI*gam*rst*rst/K),0.3333333333); /* according to DMT model */

    if(lambdap>5){
       r0=pow((6*M_PI*gam*rst*rst/K),0.3333333333); /* according to JKR model */
      }
    else if(lambdap<0.1){
       r0=pow((2*M_PI*gam*rst*rst/K),0.3333333333); /* according to DMT model */
      }
    else{
      alfa=(1-exp(-lambdap/0.924))/1.02;
      Fhat=-1*(-0.5714+0.25*(4.04*pow(lambdap,1.4)-1)/(4.04*pow(lambdap,1.4)+1))
          ;
      ahat=1.54+0.279*(2.28*pow(lambdap,1.3)-1)/(2.28*pow(lambdap,1.3)+1);
      Fc=Fhat*M_PI*gam*rst;
      r0=ahat*pow(M_PI*gam*rst*rst/K,0.33333);
      }

   ES=M_PI*gam*pow(r0,2.0);
   Etot=ES;

/* calculation of the coefficient of restitution */
```

```
    e=pow(epl,2.0)-Etot/(0.5*P_MASS(p)*pow(vabs,2.0));
    e_n=e;
    e_t=e;

    Fvdw=Fc;

  /* Calculation of the capillar force */
410
    thetas=(5.0)/(180.0)*M_PI;
    thetap=(79.0/180.0)*M_PI;
    RH=0.5;                              /* relative humidity */
    x0=P_DIAM(p)/2*sin(thetas);
    r=(0.54e-9)/(log(RH));
    gamw=47.3e-3;
    Deltap=gamw*(1/x0+1/r);
    FC=-M_PI*pow(x0,2.0)*Deltap+2*M_PI*x0*gamw*sin(thetap+thetas);

420 /* electrical force according to Schubert                              */

    Fel=M_PI*epsrl*eps0*pow(Vel,2.0)*rst/z0;

  /* calculation of electrostatic energy accoring to Derjaguin et al. 1987 */

    seTe=1.5e6;
    qp1=0;
    qp2=15.3*pow(P_DIAM(p)/2,3.0)*pow(vabs,0.6)*seTe*pow(P_RHO(p)*(1-nul*nul)/El
        ,0.8);

430 /* electrostatic force of a particle at    */
  /* a wall after collision at a distance z0 */

    FES=qp2*qp2/(16*M_PI*eps0*epsrl*pow(P_DIAM(p)+2*z0,2));

  /* Calculation of the drag force and torque to O'Neill*/

    FD=3*M_PI*C_MU_L(c,cthread)*dvtdn*P_DIAM(p)*fo;
    TD=-2*M_PI*C_MU_L(c,cthread)*dvtdn*P_DIAM(p)*P_DIAM(p)*go;

440 /* drag force to Al-Hayes & Winterton*/

    Rep=P_DIAM(p)*dvtdn*P_DIAM(p)*C_R(c,cthread)/C_MU_L(c,cthread);

    if(Rep<20){
      CD=24/Rep;
     }
     else{
      CD=1.22;
     }
450
    FDAW=CD*C_R(c,cthread)/16*pow(P_DIAM(p),2.0);

  /* Calculation of the gravity */

    gn=gr*normal[2];
    if(normal[2]*normal[2]==1.0){
        gt=0;
    }
    else{
```

```
460         gt=sqrt(gr*gr-gn*gn);
            }

        FG=P_MASS(p)*gr;
        FGn=P_MASS(p)*gn;
        FGt=P_MASS(p)*gt;

    /* Lift force */

    /* Lift force to Leighton and Acrivos */
470
        FLLA=9.22*dvtdn*dvtdn*C_R(c,cthread)*pow(P_DIAM(p),4)/16;

    /* Saffman force for particle in contact with the wall */
        FLSaff=1.61*sqrt(C_R(c,cthread)*C_MU_L(c,cthread))*P_DIAM(p)*P_DIAM(p)*vft*(
            P_DIAM(p)/(s*cos(thetac)))*sqrt(abs(dvtdn))*abs(dvtdn)/dvtdn;

        FL=FLLA;

    /* Calculation of the pressure gradient force */

480     dpdn=C_P_G(c,cthread)[0]*normal[0]+C_P_G(c,cthread)[1]*normal[1]+C_P_G(c,
            cthread)[2]*normal[2];

    /* one iteration step needed!!! */

        FPG=-M_PI/6*pow(P_DIAM(p),3)*dpdn;

    /* Calculation of the turbophoresis force */
        utut=(C_RUU(c,cthread)*normal[0]+C_RVV(c,cthread)*normal[1]+C_RWW(c,cthread)*
            normal[2])/(C_R(c,cthread)*cos(thetac));
        FTU=-M_PI/12*P_RHO(p)*pow(P_DIAM(p),3.0)*utut;

490 /* calculation of the total adhesive force */

        Fa=Fvdw;//+FC+FES;

    /* calculation of the ratios of vertical lift off, sliding and tangential
        rolling */

        Rv=FL/(Fa+FG*cos(theta));
        Rs=(FD+FG*sin(theta))/(kslid*(Fa+FG*cos(theta)-FL));
        Rt=(0.7*P_DIAM(p)*FD+r0*FL+0.5*P_DIAM(p)*FG*sin(theta))/(r0*(Fa+FG*cos(theta))
            );

500     if (pow(Rv,2.0)<1 && pow(Rs,2.0)<1 && pow(Rt,2.0) <1 && P_POS(p)[2]>-1.0 &&
            Stk0nc>2){

                            if(P_DIAM(p)<xo1){corrf=corr1/2.08;}
                        else if(P_DIAM(p)<xo2){corrf=corr2/2.08;}
                        else if(P_DIAM(p)<xo3){corrf=corr3/2.08;}
                        else if(P_DIAM(p)<xo4){corrf=corr4/2.08;}
                        else if(P_DIAM(p)<xo5){corrf=corr5/2.08;}
                        else if(P_DIAM(p)<xo6){corrf=corr6/2.08;}
                        else if(P_DIAM(p)<xo7){corrf=corr7/2.08;}
                        else if(P_DIAM(p)<xo8){corrf=corr8/2.08;}
510                     else if(P_DIAM(p)<xo9){corrf=corr9/2.08;}
                        else if(P_DIAM(p)<xo10){corrf=corr10/2.08;}
                        else if(P_DIAM(p)<xo11){corrf=corr11/2.08;}
```

```
                else if(P_DIAM(p)<xo12){corrf=corr12/2.08;}
                else if(P_DIAM(p)<xo13){corrf=corr13/2.08;}
                else if(P_DIAM(p)<xo14){corrf=corr14/2.08;}
                else if(P_DIAM(p)<xo15){corrf=corr15/2.08;}
                else if(P_DIAM(p)<xo16){corrf=corr16/2.08;}
                else if(P_DIAM(p)<xo17){corrf=corr17/2.08;}
                else if(P_DIAM(p)<xo18){corrf=corr18/2.08;}
520             else if(P_DIAM(p)<xo19){corrf=corr19/2.08;}
                else if(P_DIAM(p)<xo20){corrf=corr20/2.08;}
                else if(P_DIAM(p)<xo21){corrf=corr21/2.08;}
                else if(P_DIAM(p)<xo22){corrf=corr22/2.08;}

      Area=NV_MAG(Avec);

      /* Number of particles in cell          */
      C_UDMI(c,cthread,0)+=corr*1.0;

530   /* corrected volume of depositions      */
      C_UDMI(c,cthread,1)+=corr*M_PI/6*pow(P_DIAM(p),3.0);

      /* corrected thickness of depositions */
      C_UDMI(c,cthread,2)+=corr*M_PI/6*pow(P_DIAM(p),3.0)/NV_MAG(Avec);

        fpointer=fopen("sticking_corr.txt","a");
                 Message("%e\n",P_DIAM(p));
              fprintf(fpointer,"%d %d %d %d %8.6e %8.6e %8.6e %8.6e %8.6e\n",c,
                  cthread,f,t,P_TIME(p), P_DIAM(p), P_POS(p)[0],P_POS(p)[1],P_POS
                  (p)[2]);
              fclose(fpointer);
540
        return PATH_ABORT;
        }
     else{
          /* calculate the normal component, rescale its magnitude by
          the coefficient of restitution and subtract the change */

          /* Compute normal velocity. */
          for(i=0; i<idim; i++)
          wpn += p->state.V[i]*normal[i];
550
          /* Subtract off normal velocity. */
          for(i=0; i<idim; i++)
          p->state.V[i] -= wpn*normal[i];

        /* Apply tangential coefficient of restitution */
          for(i=0; i<idim; i++)
          p->state.V[i] *= e_t;

          /* Add reflected normal velocity. */
560       for(i=0; i<idim; i++)
          p->state.V[i] -= e_n*wpn*normal[i];

          /* Store new velocity in state0 of particle */
          for(i=0; i<idim; i++)
          p->state0.V[i] = p->state.V[i];

          //Message("Path active\n");

      return PATH_ACTIVE;
```

```
570       }



      }
    else{
       return PATH_ACTIVE;
      }
    }

580 DEFINE_ON_DEMAND(OD_INIT_UDMI)
    {
    Domain *domain;
    Thread *t;
    cell_t c;
    int i=0;

    domain = Get_Domain(1);

    thread_loop_c(t,domain){
590    begin_c_loop (c,t){
         for (i=0; i<(4);++i)     /* Number of UDMI! */
             C_UDMI(c,t,i) = 0.0;
       end_c_loop (c,t)}
       }
       Message("User defined memory per cell activated %d\n", i);
    }

    /* read UDM from .txt-file */
    DEFINE_ON_DEMAND(OD_UDMI_END)
600 {
    Domain *domain; /* declare domain pointer since it is not passed as an
                       argument to the DEFINE macro  */

    FILE *fr;
    FILE *fp;
    cell_t c;
    real Area[ND_ND];
    real corrf;
    real relmass=0;
610 float time, diam;
    float x,y,z;
    float counter=1.0e0;
    Thread *ct;
    Thread *ft;
    int f;

    domain = Get_Domain(1);      /* Get the domain using Fluent utility */

    fr=fopen("stick.txt","r");
620  /*
     File should end with "eof" !
     */
    if((fr) == NULL){
     Message("File not found\n");
       }

    else{
        Message("File has been opened\n");
```

```
630     while(fscanf(fr,"%d %d %d %d %e %e %e %e %e\n", &c,&ct ,&f, &ft, &time, &
            diam, &x, &y, &z) != 0){
              printf("%d %d %d %d %e %e %e %e %e\n", c,ct,f,ft,time,diam,x,y,z);
              Message("%d %d %d %d %e %e %e %e %e\n",c,ct,f,ft,time,diam,x,y,z);
                        if(diam<xo1){corrf=corr1/2.08;}
                   else if(diam<xo2){corrf=corr2/2.08;}
                   else if(diam<xo3){corrf=corr3/2.08;}
                   else if(diam<xo4){corrf=corr4/2.08;}
                   else if(diam<xo5){corrf=corr5/2.08;}
                   else if(diam<xo6){corrf=corr6/2.08;}
                   else if(diam<xo7){corrf=corr7/2.08;}
640                else if(diam<xo8){corrf=corr8/2.08;}
                   else if(diam<xo9){corrf=corr9/2.08;}
                   else if(diam<xo10){corrf=corr10/2.08;}
                   else if(diam<xo11){corrf=corr11/2.08;}
                   else if(diam<xo12){corrf=corr12/2.08;}
                   else if(diam<xo13){corrf=corr13/2.08;}
                   else if(diam<xo14){corrf=corr14/2.08;}
                   else if(diam<xo15){corrf=corr15/2.08;}
                   else if(diam<xo16){corrf=corr16/2.08;}
                   else if(diam<xo17){corrf=corr17/2.08;}
650                else if(diam<xo18){corrf=corr18/2.08;}
                   else if(diam<xo19){corrf=corr19/2.08;}
                   else if(diam<xo20){corrf=corr20/2.08;}
                   else if(diam<xo21){corrf=corr21/2.08;}
                   else if(diam<xo22){corrf=corr22/2.08;}

      F_AREA(Area,f,ft);

      /* Number of particles in cell        */
      C_UDMI(c,ct,0)+=corrf*1.0;
660
      /* corrected volume of depositions    */
      C_UDMI(c,ct,1)+=corrf*M_PI/6*pow(diam,3.0);

      /* corrected thickness of depositions */
      C_UDMI(c,ct,2)+=corrf*M_PI/6*pow(diam,3.0)/NV_MAG(Area);
     }
       thread_loop_c(ct,domain){
              begin_c_loop (c,ct){
                   relmass+=2770/7*C_UDMI(c,ct,1);
670           end_c_loop (c,ct)}
              }
       Message("Data read succesfully\n");
       Message("relative deposited mass %e\n",relmass*100);
     }
     fclose(fr);
   }


   DEFINE_DPM_TIMESTEP(taup02,p,dt)
680 {
     real taup;
     real Kn, Cc;
     real Vc=0.13626914; /* [m3]   cyclone separator volume                    */
     real Q=600;         /* [m3/h] volume flow rate                            */

     real tc;            /* [s]    end time                                    */
```

```
    real dtime;
    real tmin;
    real TL;              /* [s]     Time scale of turbulence (Sommerfeld (2003)) */
690 real dtmin;           /* [s]     minimum from tc and TL                       */

    FILE*fpointer;
    Thread *cthread;

    cell_t c = RP_CELL(&(p->cCell)); /* get the cell and Thread that the particle
        is currently in */
    cthread = P_CELL_THREAD(p);



700 tc=Vc*3600/(Q);
    Kn=lambda/P_DIAM(p);
    Cc=1+Kn*(2.514+0.8*exp(-0.55/Kn));
    taup=Cc*(P_RHO(p)-C_R(c,cthread))*P_DIAM(p)*P_DIAM(p)/(18*C_MU_L(c,cthread));
        if(P_DIAM(p)!=0.0 && P_TIME(p)< 1e1*tc)
        {
         TL=0.3*C_K(c,cthread)/C_D(c,cthread);
           if(taup>TL)
             {
              tmin=TL;
710          }
           else{
               tmin=taup;
                }
        dtime=0.2*tmin;
        dt=0.2*tmin;
        return 0.2*tmin;
       }
       else
       {
720     Message("over time: %e\n",P_DIAM(p));
        PATH_ABORT;
        return 0;
       }
    }

    DEFINE_DPM_BC(bc_escape,p,t,f,f_normal,dim)
    {
     FILE*f2pointer;
        f2pointer=fopen("overflow_corr.txt","a");
730     fprintf(f2pointer,"%8.6e %8.6e %8.6e %8.6e %8.6e\n",P_TIME(p), P_DIAM(p),
            P_POS(p)[0],P_POS(p)[1],P_POS(p)[2]);
        fclose(f2pointer);

        return PATH_ABORT;
    }
```

E.3 UDF for Particle-Wall Impact Velocity

E.3.1 Original Boundary Condition

```
/*****************************************************/
/*              UDF: Particle wall adhesion          */
/*                                                   */
/* Author: J. Houben                                 */
/* Datum: 05.08.2011                                 */
/*                                                   */
/* Article: Computers and Fluids                     */
/*****************************************************/

/* UDF for calculating the particle-wall impact velocity*/

#include "udf.h"
#include "dpm.h"
#include "surf.h"
#include "stdio.h"


DEFINE_DPM_BC(damp_ratio,p,t,f,f_normal,dim)
{
  real NV_VEC(x);
  int i, idim=dim;
  real normal[2];

  real vabse, wpne, wpte;
  real vabs0, wpn0, wpt0;

  FILE*fpointer;
  Thread *cthread;
  Thread *tf;

  cell_t c = RP_CELL(&(p->cCell));/* get the cell and thread in which the
      particle is currently */
  cthread = P_CELL_THREAD(p);

  if((NNULLP(t)) && (THREAD_TYPE(t) == THREAD_F_WALL)){
    for (i=0; i<idim; i++)
    normal[i] = f_normal[i];

    vabse=NV_MAG(P_VEL(p));
    wpne=(P_VEL(p)[0]*normal[0]+P_VEL(p)[1]*normal[1]);
    wpte=sqrt(vabse*vabse-wpne*wpne);

    fpointer=fopen("no_bl_org.txt","a");
      fprintf(fpointer,"%8.6e %8.6e %8.6e %8.6e\n", P_DIAM(p), vabse, wpne, wpte
          );
    fclose(fpointer);
    return PATH_ABORT;
   }

   else{
    return 0;
   }
}
```

E.3.2 New Boundary Condition

```
/*****************************************************************/
/*                 UDF: Particle wall adhesion                   */
/*                                                               */
/* Author: J. Houben                                             */
/* Datum: 05.08.2011                                             */
/*                                                               */
/* Article: Computers and Fluids                                 */
/*****************************************************************/

/* UDF for re-estimating the particle-wall impact velocity*/

#include "udf.h"
#include "dpm.h"
#include "surf.h"
#include "stdio.h"
#include "gaussrand.h"

#define lambda 0.066e-6 /* [m] mean free path air at 20oC  */

DEFINE_DPM_BC(damp_ratio,p,t,f,f_normal,dim)
{
  real NV_VEC(x);
  int i, idim=dim;
  real normal[2];
  real xc[ND_ND];    /*this will hold the cell midpoint position vector */
  real xf[ND_ND];    /*will hold the face midpoint position vector      */
  real A[ND_ND];

  real vabse, wpne, wpte;
  real vabs0, wpn0, wpt0;
  real vabscor, wpncor, wptcor;
  real wx, wy, rmsx, rmsy;
  real dx, dy, s;
  real thetac;       /* cell midpoint face midpoint angle */

  real xrand, yrand;
  real uac, vac;

  real vfstat, vfnstat, vftstat;
  real Cc, Kn, Stkn, tau;
  real Stk0n, Stken;
  real Stk0nc, wpn0c, wpt0c;
  real wcell;

  real PI1, PI2, PI2e, PI3, PI4;

  real zetan, zetat, zetatot, zetatlog, zetatlin, zetagr, zetatstep;

  FILE*fpointer;
  Thread *cthread;
  Thread *tf;

  cell_t c = RP_CELL(&(p->cCell));/* get the cell and thread in which the
      particle is currently */
  cthread = P_CELL_THREAD(p);
```

```
  if ((NNULLP(t)) && (THREAD_TYPE(t) == THREAD_F_WALL)){
    for (i=0; i<idim; i++)
60    normal[i] = f_normal[i];

    C_CENTROID(xc,c,cthread);
    F_CENTROID(xf,f,t);

    s=sqrt(pow(xc[0]-xf[0],2)+pow(xc[1]-xf[1],2));
    dx=xc[0]-xf[0];
    dy=xc[1]-xf[1];
    thetac=acos((-dx*normal[0]-dy*normal[1])/s);

70  vabse=NV_MAG(P_VEL(p));
    wpne=(P_VEL(p)[0]*normal[0]+P_VEL(p)[1]*normal[1]);
    wpte=sqrt(vabse*vabse-wpne*wpne);

    vfstat=sqrt(C_U(c,cthread)*C_U(c,cthread)+C_V(c,cthread)*C_V(c,cthread));
    vfnstat=sqrt(C_U(c,cthread)*normal[0]*C_U(c,cthread)*normal[0]
                +C_V(c,cthread)*normal[1]*C_V(c,cthread)*normal[1]);
    vftstat=sqrt(vfstat*vfstat-vfnstat*vfnstat);

    xrand=gaussrand();
80  yrand=gaussrand();

    uac=sqrt(C_RUU(c,cthread)/C_R(c,cthread))*xrand;
    vac=sqrt(C_RVV(c,cthread)/C_R(c,cthread))*yrand;

    Kn=lambda/P_DIAM(p);
    Cc=1+Kn*(2.514+0.8*exp(-0.55/Kn));
    tau=Cc*P_RHO(p)*P_DIAM(p)*P_DIAM(p)/(18*C_MU_L(c,cthread));

    if(cos(thetac)==0){
90    Stken=0;
      return 0;
      }
    else{
      Stken=(wpne)*tau/s*(cos(thetac));
      Stk0n=Stken+2;
      wpn0=Stk0n*s/(tau*cos(thetac));
      wpn0c=wpn0+vac;
      Stk0nc=(wpn0c)*tau/s*(cos(thetac));

100   if(Stk0nc>2){
        wcell=vftstat+uac;
        PI2e=wcell/wpte;
        wpt0c=wpte*Stk0nc/(Stk0nc-2)*(1+PI2e*(2+(Stk0nc-2)*log((Stk0nc-2)/Stk0nc)
            -4/Stk0nc));
        PI1=Stk0nc;
        PI2=(vftstat+uac)/wpt0c;
        PI3=wpn0c/wpt0c;
        PI4=(C_U_G(c,cthread)[0]*normal[0]+C_U_G(c,cthread)[0]*normal[1]
            +C_V_G(c,cthread)[1]*normal[0]+C_V_G(c,cthread)[1]*normal[1])*tau;

110     zetan=1-2/PI1;
        zetatlin=PI2*(2-PI1)-PI2*(PI1-2)*log(1-2/PI1)+(1-2/PI1)*(1-2*PI2+PI2*PI1);
        zetatlog=((PI2)/(2*log(2)-1)*PI1/(PI1-4)*log(2-4/PI1)+1-log(2)*PI2/(2*log
            (2)-1))*(1-2/PI1);
        zetatstep=(PI1-1+2*PI2)*(PI1-2)/(PI1*(PI1-1));
```

```
        zetagr=(PI4*PI3+1-PI4*PI3/PI1-PI2-PI3*PI4*log(1-2/PI1))*(1-2/PI1)+PI4*PI3/
            PI1-PI4*PI3+PI2;

        fpointer=fopen("no_bl.txt","a");
          fprintf(fpointer,"%8.6e %8.6e %8.6e %8.6e %8.6e %8.6e %8.6e %8.6e %8.6e
              %8.6e %8.6e\n",
          P_DIAM(p),tau, s,zetagr, zetatlin, zetatlog, vabse, wpne, wpte, Stken,
              Stk0nc);
        fclose(fpointer);
120
        return  PATH_ABORT;
        }
      else{
        fpointer=fopen("notreached.txt","a");
          fprintf(fpointer,"%8.6e\n", P_DIAM(p));
        fclose(fpointer);
        return PATH_ABORT;
        }
       }
130  }

   else{
      return 0;
       }
   }
```